MAGNETIC RESONANCE SPECTROSCOPY AND IMAGING AS APPLIED TO THE FORESTRY SECTOR

A thesis submitted to Massey University
in partial fulfilment for the degree of

Doctor of Philosophy

by

Albert Roger Meder

Massey University
2003

ABSTRACT

The forestry sector in New Zealand ranks as the third largest export earner. The individual industries within the forestry sector have, in some cases, grown up on the basis of institutionalised knowledge, sometimes without a full understanding of the underlying fundamental physico-chemical relationships and the changes that occur during wood material processing. At the same time the commercial pressures of operating within the forestry sector have resulted in demand for more uniform, high quality, fit-for-purpose product, faster throughput and less downgrade from what is becoming a lower quality feedstock as harvest ages decline. In the 21st century, the forestry sector is being transformed into an "engineered ligno-cellulosic materials processor" and this in turn is requiring a more sophisticated knowledge of the material feedstock and the processes involved in wood products manufacture.

The aim of this work was to use magnetic resonance techniques to explore aspects of ligno-cellulosic materials processing at points along the value-added process chain, namely drying, chemical modification (preservation) and re-engineering (gluing) of wood products.

Magnetic resonance mini-imaging studies of the water transport during the drying of radiata pine boards have shown differences in the directional movement of water within the wood structure. These effects show a dependence on the surface area to volume ratio of timber and the orientation of the annual rings with respect to the larger drying face. Narrow, flat-sawn boards exhibit anomalous drying behaviour in terms of water mass transport, whereas thicker boards display more conventional core-shell drying behaviour. These restrictions to flow have been further investigated using diffusion tensor imaging *via* a modified pulsed field gradient spin-echo sequence to elucidate the nature of anisotropic diffusion in wood. The direction of least restriction to self-diffusion is in the longitudinal direction, as would be expected with it being the direction of active transport within a tree stem, whereas the direction of greatest restriction to self-diffusion is in the radial direction, with the higher density latewood acting as a barrier.

Preservation of radiata pine sapwood with novel boron-based preservatives has been investigated using magnetic resonance imaging to determine the penetration and retention of the incipient compounds. An apparent anomaly in retention for trimethylborate-treated *Pinus radiata* sapwood was investigated by ^{11}B MAS NMR spectroscopy of excised sections of latewood and earlywood, which showed hydrolytic decomposition of trimethyl borate to form boric acid. The rate of hydrolysis of trimethylborate was monitored by ^{11}B MAS NMR spectroscopy and was shown to occur very rapidly in the latewood (within 24 hours), and over a longer time scale of several days in the earlywood. The resulting publication has reported some of the first published ^{11}B MRI images.

Magnetic resonance spectroscopy has provided (in conjunction with separate mass spectrometry studies) mechanistic evidence for the accelerated curing of phenol-resorcinol formaldehyde resols, using ammonia in combination with the conventional paraformaldehyde hardener - a process known as GreenWeld™. Carbon-13 and nitrogen-15 NMR spectroscopy has shown evidence of both benzylamine and aniline type bridging structures formed during cure, compared to only methylene structures being formed under conventional curing conditions.

Poly(vinyl acetate) emulsion polymer adhesive has also been examined using NMR spectroscopic methods, with particular focus on the effect of addition of aluminium chloride, which is often commercially added to PVAc formulations as a crosslinking agent. Multinuclear magnetic resonance spectra obtained during the cure of $AlCl_3$ modified PVAc adhesive, shows a low frequency ^{27}Al shift of *ca.* 3 ppm suggesting a local change in environment as the aluminium changes from a solvated to a covalently bonded octahedral environment.

Finally, as a preliminary study, a new device for measuring uniaxial extension of visco-elastic solids was trialled on poly(vinyl acetate) hydrogels to study the effect of addition of aluminium chloride on the visco-elastic properties of the adhesive. A similar, manually operated device was used to obtain NMR spectroscopic data during compression of the gel. These studies have shown that addition of aluminium chloride as a crosslinking agent, in fact produces a cured adhesive with fewer crosslinks than the corresponding unmodified adhesive, but with increased resistance to shear-induced creep.

ACKNOWLEDGMENTS

I have learned more from my mistakes than from my successes.

Sir Humphrey Davy

During the period of research that has lead to the completion of this thesis I have certainly learned a great deal about magnetic resonance imaging and about myself. There have been a number of "practical lessons" learnt. None of it however would have been possible without the support, encouragement and assistance from a number of people.

First and foremost I owe a great deal of thanks to Prof. Paul Callaghan, FRS for allowing me to work in such a dynamic and invigorating lab as the NMR Group at Massey. Paul provided me with an opportunity to explore the arena of magnetic resonance imaging, a modality I had previously never been exposed to and at the same time explore aspects of the fundamental nature of wood and polymer systems. I am sure his efforts in attempting to convert a chemist into a physicist must at times have caused him grief and I am sincerely grateful for his perseverance, support and assistance.

To my co-supervisors, Dr Robert Franich (***Forest Research***) and Prof. Russell Howe (UNSW) I also say thank you. Robert has an undying enthusiasm for investigation and for applying non-traditional techniques to novel problems. He has been a much-appreciated source of encouragement and support and become a friend and confidante. Russell provided me with an introduction to the nuances of solid state NMR of quadrupolar nuclei in the early days of struggling with ^{11}B MAS NMR.

No vote of thanks would be complete without acknowledging the veritable United Nations that is the NMR Group. A special thanks to Dr Sarah Codd for her assistance with the idiosyncrasies of the 200 MHz widebore system, Dr Melanie Britton for an introduction to rheology NMR style, Dr Craig Eccles for his insightful development of and assistance with Prospa which was used for processing the flow images and Robin Dykstra for building the Squisher and providing often needed electronics support. Thanks too, to my fellow postgraduate colleagues Dr Elmar Fischer, Miki Komlosh, Ryan Cormier, Alexandre (Sasha) Khrapitchev, Maria Kilfoil, and to the long list of visiting academics and students who frequented the lab; Prof. Lourdes de Vargas, Dr Ana Gil, Song-I Han, Arturo Méndez, Dafnis Vargas and Céline Peurière who developed the m-code for Squisher analysis. Life in the lab was never a dull moment with so many diverse personalities.

I owe a special appreciation to ***Forest Research*** for financial assistance and particularly Dr Keith Mackie who facilitated my being able to undertake this study while maintaining a varied programme of research and commercial activity during my "day job". Keith has always been a strong supporter of my career development during my 15 years at ***Forest Research***, and I value our friendship and those semi-occasional fishing trips.

I would like to thank a number of other researchers for access to other spectrometers that were used during the course of study; Drs Tim Bastow and Mark Smith for running the ^{15}N MAS spectra on the MSL 400 at CSIRO and Dr Andrew Whittaker for letting me have access to the MSL 300 at UQ-CMR.

Special thanks go to Dr Bodo Saake (BfH, Institut für Holzchemie und chemische Technologie des Holzes, Hamburg) for the samples of cotton linters.

Some very special people supported me and put up with me during the journey; Sarah, Samuel and Kyle deserve special mention as they suffered most during the frequent trips to Massey and the lengthy writing period while they enjoyed the weather and surrounds of Brisbane.

To my mother, Betty and the memory of Adam, I say to you all ...

Kia kaha, kia tara
Have strength, have courage

TABLE OF CONTENTS

ABBREVIATIONS USED

$\boldsymbol{B}_0$	external (static) magnetic field
$\boldsymbol{B}_1$, $\boldsymbol{B}_2$	applied magnetic fields
cm	centimetre
COSY	(^{1}H-^{1}H) correlation spectroscopy
CP/MAS	cross polarisation - magic angle spinning
CPMG	Carr-Purcell-Meiboom-Gill
CSA	chemical shift anisotropy
D	diffusion coefficient
dB	decibel
DIFFSE	diffusion spin echo (pulse sequence)
DCM	dichloromethane (CH_2Cl_2)
DEPT	distortionless enhancement by polarisation transfer (pulse sequence)
FID	free induction decay
FOV	field of view
FT	Fourier transform
G	Gauss = 10^{-4} Tesla
G/cm	Gauss per centimetre (1 G/cm = 10 mT/m)
G_e	field gradient (applied in direction e)
h	Planck's constant (6.625 x 10^{-34} J s)
$\hbar$	$h/2\pi$
HMMM	hexamethylmethylolmelamine ($C_3N_3(N(OH)_2)_3$)
HMTA	hexamethylenetetramine ($C_6H_{12}N_4$)
HMBC	heteronuclear multiple bond correlation
HMQC	heteronuclear multiple quantum correlation
HSQC	heteronuclear single quantum correlation
HPDEC	high power decoupling (MAS pulse sequence)
I. S	nuclear spin quantum number
k_B	Boltzman constant (1.38 x 10^{-23} J K^{-1})
kHz	kilohertz
$\boldsymbol{L}$	angular momentum
MAS	magic angle spinning

MC	moisture content
MHz	megahertz
ML	middle lamella
mM	millimolar (concentration)
mm	millimetre
MRI	magnetic resonance imaging
MSME	multi slice, multi echo (imaging pulse sequence)
m_x, m_y, m_z	magnetisation in x, y, z axes
$\boldsymbol{M}_0$	bulk magnetisation
N_A	Avogadro's number (6.022 x 10^{23} mol^{-1})
N-MAM	*N*-methylolacrylamide
NMR	nuclear magnetic resonance
NOE	nuclear Overhauser effect
od	oven dry
PCA	principal components analysis
PFGSE	pulsed field gradient spin echo
PLS	projection to latent structures (regression)
ppm	parts per million
PVAc	poly(vinyl acetate)
PVOH	poly(vinyl alcohol)
QCC	quadrupolar coupling constant
r	radius
rf	radio frequency
R	universal gas constant (8.314 J K^{-1} mol^{-1})
S/N	signal-to-noise (ratio)
T	temperature or Tesla (magnetic flux density)
T_1	spin-lattice or longitudinal relaxation constant
T_2	spin-spin or transverse relaxation constant
T_E	echo time
T_R	repetition time
TBTO	tributyltin oxide ($((C_4H_9)_3Sn)_2O$)
THF	tetrahydrofuran (C_4H_8O)
TMB	trimethyl borate ($B(OCH_3)_3$)
TMS	tetramethylsilane ($(CH_3)_4Sn$)

Δ	"big delta" – duration between gradient ramps in diffusion sequence
δ	"little delta" – duration of gradient ramp in diffusion sequence
θ, α_E	angle, Ernst angle
π	angle of tip in radians = 180° tip
$\pi/2$	angle of tip in radians = 90° tip
η	asymmetry parameter (NMR), intrinsic viscosity (rheology)
μ	magnetic dipole moment
σ	NMR chemical shift (ppm), stress (rheology)
ρ	density
ω_o	Larmor frequency (rad s^{-1})
ν	concentration (rheology)
ν_o	Larmor frequency (Hz)
ω_Q	quadrupole frequency (rad s^{-1})
ν_Q	quadrupole frequency (Hz)
ω_{rf}	excitation frequency
ε	strain
ψ	functionality of polymer crosslinks
τ	variable delay (NMR) or stress or torque (rheology)
γ	NMR gyromagnetic ratio (rad T^{-1} s^{-1})
$\dot{\gamma}$	shear rate (rheology)
Ω	frequency of rotation of rheometer drive spindle (Hz)

LIST OF FIGURES

Chapter 2

Chapter 3

Chapter 4

Chapter 5

Chapter 6

Chapter 7

Chapter 8

Chapter 9

LIST OF TABLES

Chapter 3

Chapter 5

Chapter 6

Chapter 7

Chapter 8

Chapter 9

LIST OF PUBLICATIONS

Meder, R., Franich, R.A. and Callaghan, P.T. (1999) ^{11}B magnetic resonance imaging and MAS spectroscopy of trimethylborate-treated radiata pine wood, *Solid State Nucl. Magn. Reson.*, 15(1), 69-72.

Meder, R., Codd, S.L., Franich, R.A. Callaghan, P.T. and Pope, J.M. (2003) Observation of anisotropic water movement in *Pinus radiata* D. Don wood using magnetic resonance micro-imaging. *Holz Roh Werkst.,* 61(6), accepted, in press.

Meder, R., Franich, R.A., Witt, M., Callaghan, P.T., and Britton, M.M. (2003) Aluminium chloride crosslinking in poly(vinyl acetate) adhesive: Part 1. NMR spectroscopy and NMR-rheology. *J. Adhesion Sci. Technol.*, in prep.

Meder, R., Franich, R.A., Dykstra, R., Callaghan, P.T., and Peurière, C. (2003) Aluminium chloride crosslinking in poly(vinyl acetate) adhesive: Part 2. Visco-elastic compression studies. *J. Adhesion Sci. Technol.*, in prep.

1. OVERVIEW

Science must begin with myths and with the criticism of myths.
Karl Popper

Wood has long been used as a construction material and entire industries have been established in order to maximise the utilisation of wood fibre. Industry sectors using specialty wood adhesives for laminating solid wood or bonding fibres in composite products, or those industries using specialty chemicals and impregnation processes for preservation of lumber, have all grown up around the central forestry industry. In the 21st century these forest products industries are becoming "engineered ligno-cellulosic materials processors" as the economic pressures of higher conformity product, a lowering of quality in the raw material and development of new products requires an increased sophistication and understanding of the raw material, the processes and the process changes that occur during value-added manufacturing. These ligno-cellulosic-based industries are, however, not without their own peculiar problems and challenges.

Changes in growing (silvicultural) regimes, a lowering in the age of harvest, increases in processing speed, environmental constraints and the demand for more uniform product has lead to a number of topical issues in (particularly) the New Zealand forestry sector. Increasing environmental pressure has led to the banning in some countries, of age-old preservatives based on heavy metals. Research efforts worldwide are seeking environmentally-friendly, non-leachable compounds that offer fungicidal and insecticidal efficacy. Fully contained, closed-loop treatment processes are being developed to replace traditional vacuum-pressure treatment processes in order to minimise terrestrial contamination at treatment plants. Some of these processes involve vapour phase treatment with novel compounds, thereby avoiding the use of solvent based carriers and the consequent health and safety issues associated with the use and storage of kilolitres of solvent.

Lowering the harvest age and faster drying throughput, by using higher temperature drying schedules, has led to an increase in the incidence of drying degrade due to internal check formation (cracks and cavities appearing which visually degrade the appearance of, in particular, mouldings grade lumber).

The demand for adhesives with improved performance has lead to the development of new adhesive systems. Existing adhesives are being re-formulated to afford more desirable product performance such as resistance to creep induced failure in high humidity environments.

1.1 OBJECTIVES AND AIMS OF THIS THESIS

This thesis aims to investigate areas of application of magnetic resonance techniques in the broader forestry sector and more specifically, the potential of the method to investigate some of the long-standing questions and uncertainties that face the sector. Such fundamental questions are "What happens to timber preservatives when we impregnate radiata pine" and "Where is the preservative retained?", "What happens to water in wood during the drying process?" and "What does the addition of aluminium to poly(vinyl acetate) adhesive do?". This thesis sets out to explore the three realms of timber preservation, timber drying and timber adhesives.

Chapter two reviews the New Zealand forestry sector and some of the issues, which will be further investigated in this thesis. Chapters three through five introduce the NMR methodologies and techniques used throughout these investigations.

In chapter six we explore the nature of tin and novel boron based preservatives in radiata pine wood using the *in situ* techniques of solid state NMR spectroscopy and NMR microimaging. This has enabled investigation of not only the nature of preservatives but has provided spatial information to the penetration and retention of timber preservatives. Degradation of preservatives has been observed and in one case the rate of degradation has been determined.

The observations made in studying the degradation of timber preservatives have in turn raised questions regarding the nature of water and the movement and retention of water during drying. Is there a differential movement of water in the earlywood and latewood of radiata pine? What is the nature of water in the bound and free states in the wood structure and how does the distribution change during drying? Does wood dry differently during drying by novel methods such as azeotropic drying of wood? NMR studies relating to these issues are presented in chapter seven.

Chapter eight looks at the chemistry associated with a novel rapid curing phenol-resorcinol-formaldehyde resin (GreenWeld™) and explores the chemistry of aluminium aided cross-linking in poly(vinyl acetate) adhesives. In particular what is the mode of action of curing in GreenWeld™ accelerated curing of phenol-resorcinol-formaldehyde resins?

Finally, in chapter nine we look at the potential of novel rheology devices combined with NMR imaging and spectroscopy to provide insight into the mechanical properties of emulsion polymers used to form adhesives, both as crosslinked gels and in the liquid state. Questions which are addressed in this chapter include: "What is the role of aluminium in the curing and cross-linking of emulsion polymers such as poly(vinyl acetate)?" and "How do poly(vinyl acetate) polymers behave under shear?".

1.2 PREVIOUS NMR INVESTIGATIONS OF WOOD

During the infancy of magnetic resonance imaging (MRI) a number of studies were conducted to evaluate the usefulness of the technique to aid the processing of logs. Even today, imaging techniques that would enable sawmillers to look inside logs in order to visualise the location and size of knots and other defects *in real time* is held as one of the great hopes. While MRI is able to offer the resolution required to perform this task it is unable to accommodate logs travelling at linear speeds of several metres per second.

Early reports on application of MRI to imaging of wood dealt with observation of defects in logs and timber (Hall *et al.*, 1986a,b; Wang and Chang, 1986; Chang *et al.*, 1989) using clinical scanners in the range 0.1 – 0.5 T equipped with head coils. These studies were able to show the inner morphology of small diameter logs, clearly identifying the annual rings, rays, resin pockets and internal knots. Hall *et al.* (1986a,b) also showed variation of the spin-lattice relaxation times at different locations within the wood *viz.* T_1 = 188 – 230 ms for heartwood and 343 - 395 ms for sapwood in green (never-dried) aspen.

More recently application of the technique has branched into investigations of measuring moisture content in timber by assessment of T_1 and T_2 parameters (Hall and Rajanayagam, 1986; MacKay *et al.*, 1988; Menon *et al.*, 1989; Quick *et al.*, 1990; Flibotte *et al.*, 1990; Araujo *et al.*, 1992).

It is best to consider use of magnetic resonance imaging in these three categories:

1. Imaging of internal morphology and defects.
2. Determination of physical properties based on manipulation of T_1 and T_2 relaxation.
3. Determination of molecular migration *via* successive imaging of molecular distribution and through imaging of diffusion coefficients.

1.2.1 INTERNAL IMAGING

While the MRI technique was developed to image internal organs in the human body, the technique is equally suitable for similar investigations of whole logs or pieces of timber. Generally disks of approximately 10-50 cm length by 20-30 cm diameter have been used in clinical MRI systems using *ca.* 30 cm head coils for signal transmission and reception. The most common sequence is a spin echo image using 10-20 mm slice thicknesses, producing a transverse (cross-sectional) image through the log with in-plane resolution of *ca.* 1.0 - 1.5 mm (Hall *et al.*, 1986a, 1986b, Wang and Chang, 1986; Chang *et al.*, 1989). In the case of defect imaging, this resolution is often more than adequate, with knots, decay and resin pockets being observable with clear definition. This early work has been carried out using field strengths of 0.14 - 0.2 T (*ca.* 6 - 8 MHz ^{1}H frequency), which has limited the sensitivity and contrast of the images. Modern clinical imaging systems now operate between 1.5 and 3.0 T (65 - 130 MHz ^{1}H frequency) with 4 T systems becoming available.

The problem to be overcome for successful micro anatomical studies to take place is that of low resolution. Resolution is associated with the lower magnetic field which is available in the large bore clinical imagers (50 - 60 cm), resulting in poorer signal-to-noise ratios.

This problem can be overcome only by using research instruments, which have narrower magnet bore allowing a maximum sample size of *ca.* 5 - 8 cm diameter. The smaller (and more sensitive) rf coils combined with the much higher magnetic fields achievable (up to 11.7 T) gives increased in-plane resolution down to *ca.* 10 µm. Core samples taken from standing trees could be imaged using such a system in order to gain information on the grain orientation. While this resolution will not allow investigation of the cell wall it will allow imaging of wood rays, resin canals and defects.

Very little work has been reported on the diffusion imaging of water in plant material. While there have been some studies on the diffusion within fruit such as onions (Merboldt *et al.*, 1987), grapes (Pope *et al.*, 1993) tomatoes (Ishida *et al.*, 1994), apples (Hills and Remigereau, 1997) and kiwifruit (Clark *et al.*, 1998), there appears to be only a couple of groups investigating diffusion and flow characteristics within plant stems and no published reports of diffusion or flow imaging in wood.

The NMR group at Massey University has studied nuclear magnetic resonance microimaging of diffusion in wheat grain (Jenner *et al.*, 1988), observing bulk flow of water in the longitudinal direction of the grain, which was suggested as being associated with nutrient transport in the vascular system. The same group (Xia *et al.*, 1993; Köckenberger *et al.*, 1997) used a pulsed field gradient spin echo imaging routine to image flow in *Stachys* and *Equisetum* plant tissue (Xia) and castor bean seedlings (Köckenberger). This work clearly showed that water flow in *Stachys* and castor bean stems occurs in the xylem while flow in *Equisetum* occurs in the carinal canals. More recent work (Gil *et al.*, 2000) has investigated the penetration of water into solvent extracted cork samples (*Quercus suber*) to determine the effect of suberin removal on the uptake of water into the normally hydrophobic cork. This showed that a particular suberin species was responsible for the resistance of cork to water absorption.

The group of Van As' at Wageningen University in the Netherlands has investigated the transport of water in celery stalks and model systems of glass beads (Schaafsma *et al.*, 1992) and quantified water transport in Chrysanthemum stems by comparing actual measured water uptake in the stem with that measured by NMR flow imaging (Scheenen *et al.*, 2000).

A rapid method for quantitative NMR imaging of flow velocities in intact plants has been developed by Axel Haase's group in Würzburg. The purpose of this method is to observe dynamic changes of flow velocity in the xylem of plants after fast changes of environmental conditions. The method applies a fast gradient echo sequence (FLASH) to reduce the overall imaging time by a factor of six without significant loss of signal-to-noise (Haase, *et al.*, 1986; Haase, 1989) A complete flow measurement consisting of a set of eight different flow weighted images required a total acquisition time of only 3.5 min (Rokitta *et al.*, 1999a,b). The method has since been used to study flow velocity and solute transport in the xylem and phloem over a daily time course (Peuke *et al.*, 2001), showing that during the day sap was transported in both the xylem and phloem whereas at night the xylem showed significantly lower velocities while the phloem showed no diurnal variation in flow. The changes in xylem flow corresponded to changes in the measured transpiration rate.

1.2.2 RELAXATION STUDIES

The development of MRI has utilised the density of water protons for signal generation, and provides in fact a water density map. By manipulating the magnetic properties of water it is possible to gain information about the nature of the water within a sample, such as the local moisture content, or the differentiation of the water into "bound" and "free" states. Menon *et al.* (1989) have separated the ^{1}H NMR signal into three distinct components with differing T_2 values:

- water with short T_2 (few milliseconds) is termed the "bound"
- water with intermediate T_2 (*ca.* 50 ms) is located in the latewood tracheid and ray lumens
- water with the longest T_2 (> 100 ms) is located in the earlywood tracheid lumens

This assignment has been reviewed in the paper by Araujo *et al.* (1993) to account for the dispute over the nature of "bound" water and instead differentiates between "cell-wall" water, with short T_2, and lumen water with longer T_2 values. In this thesis the term cell-wall water will be used.

The interpretation of these differences is based on the larger cell volume in the early wood, and a model in which free water in the lumen exchanges with the surface layer of cell wall water. It is important to note that this analysis must be performed on green wood samples. A most recent study using a modified single point imaging sequence (Balcom *et al.*, 1996) has shown some success in imaging of wood below 10% moisture content (MacMillan *et al.*, 2002).

Both conventional solid state NMR and MRI techniques have been used to determine moisture content of wood (Nanassy, 1973, 1974, 1976; Quick *et al.*, 1990) with mixed success. Olson *et al.*, (1990) followed the movement of water during drying of flat-sawn white oak lumber of three thicknesses. It was shown that the thinner boards dried faster and alluded to the possibility of annual ring orientation to the drying face as playing a role in the rate of drying. This aspect is investigated further in this study. In all cases a non-linear calibration curve was produced with some species variation seen between common northern hemisphere species (Nanassy, 1973, 1976).

The advantage of deriving moisture information from image data is that the spatial distribution can be followed during the drying process. Olson *et al.* (1990) were able to show the mechanism of drying by imaging boards of different thicknesses over several days drying. It is evident from their study that water leaves the rays at the board surface by capillary action, and in doing so draws water through the pit openings into the rays within the core of the wood until all the free water within the core of the wood is removed. At this stage the rays appear to dry from the outside inward. They were also able to derive a polynomial expression to relate image density to moisture content, which was useful in the 45 to 70% moisture range.

2. FORESTRY AND WOOD PROCESSING

> *I think I shall never see,*
> *A billboard as lovely as a tree.*
> *Perhaps unless the billboards fall,*
> *I shall never see a tree at all.*
> Ogden Nash

2.1 THE NEW ZEALAND FORESTRY INDUSTRY

The forestry industry in New Zealand has been long established, with the major commercial crop (90%) being radiata pine (*Pinus radiata* D. Don) planted in 1.7 million hectares (Figure 2.1). Export of lumber and remanufactured fibre- and particleboard contributed \$1.1 billion to New Zealand's economy in 1999 with an additional \$1.2 billion earned in export of logs and pulp and paper products (NZFOA, 1999) making forestry the third largest export earner in New Zealand.

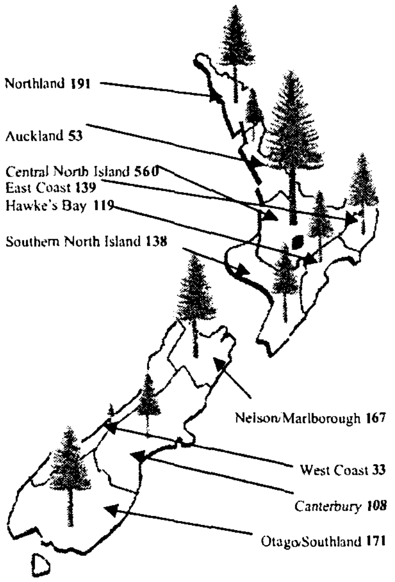

Figure 2.1. Distribution and area (in hectares x 1000) of New Zealand's plantation forests. (Adapted from NZFOA, 1999).

In 1999, 17 million m^3 of logs were harvested in New Zealand at rotation ages of 23–30 years and used in several down-stream processing industries, from solid timber framing to medium density fibreboard (MDF) and pulp and paper products. For many of these processes, very little is known about the effects of processing on the finished product. Aspects of radiata pine end-use processing have been selected for investigation by magnetic resonance techniques to better understand and characterise the effects of processing.

2.1.1 MACROSCOPIC STRUCTURE OF RADIATA PINE WOOD

The macroscopic structure of radiata pine wood is typical of softwood gymnosperms. The macroscopic structure is shown in Figure 2.2.

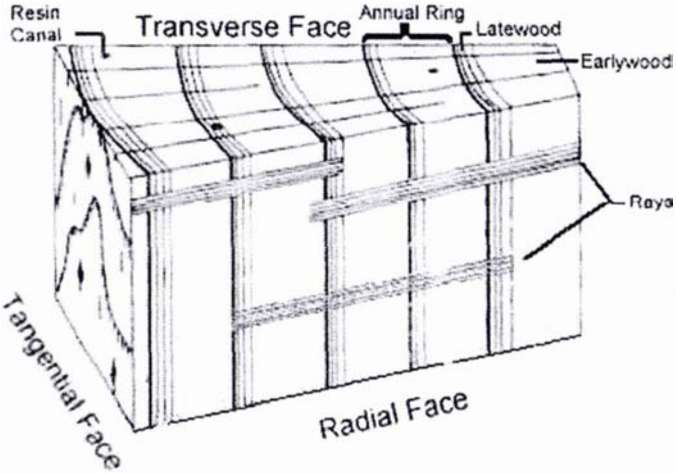

Figure 2.2. Model of softwood macroscopic structure (Fengel and Wegener, 1983).

At the centre of the tree the pith represents tissue laid down during the first year of growth. This is surrounded by the xylem, or wood, which is laid down as annual growth rings differentiated into earlywood growth and denser latewood growth. In radiata pine trees from about 10 years of age, heartwood forms in the inner growth rings. This is characterised by wood which is drier than the outer sapwood (typically 40-50 % moisture content oven-dry weight (MC od) compared with 80–150 % MC od for sapwood), contains a higher extractives content and does not transport water. The growth of a tree takes place in the cambium, a thin layer of dividing cells found between the inner bark (phloem) and the xylem. Ray cells extend radially from the bark towards the pith whereas resin canals extend vertically and are involved in storage and transport of extractives (Fengel and Wegener, 1983; Harris, 1991).

The major cellular structure of radiata pine (~95%) is tracheid cells, which are typically 1-4 mm long and 30-40 µm in diameter for earlywood sapwood cells and *ca.* 20 µm diameter for latewood cells, with the latewood cells also being thicker walled. This dramatic change in cell diameter is visible to the eye as delimiting the annual growth rings. Tracheids are oriented in the longitudinal direction of the tree stem. The cells are tapered at the ends and connect to adjacent cells *via* bordered pits, which in live sapwood allow the active transport of water and nutrients during transpiration. During drying however, these bordered pits close irreversibly (Figure 2.3 and Figure 2.4) in an attempt to protect the tree from dehydration and, once closed, they impede impregnation of dry timber with treatment solutions used for preservation against microbial attack or fire retardancy.

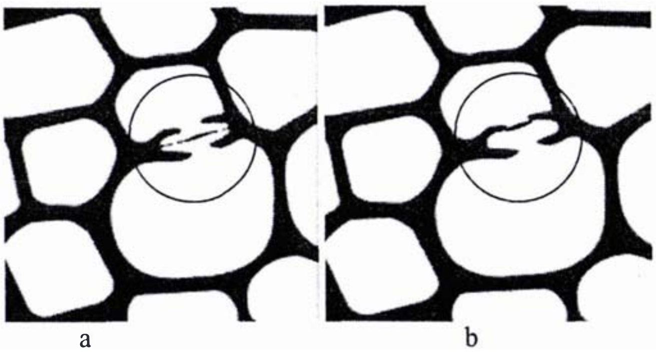

Figure 2.3. Schematic of (a) an open pit and (b) a closed (aspirated) pit.

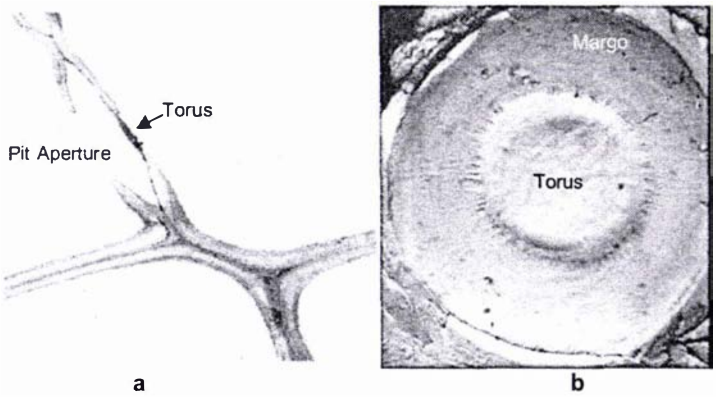

Figure 2.4. TEM of (a) an aspirated pit in cross section and (b) a pit showing the torus and margo (*Forest Research* collection #13047).

A schematic of the tracheid cell wall structure (Figure 2.5) shows several layers which differ not only in their structure but also their chemical composition. The middle lamella (ML) provides the "glue" to hold cells together. During early stages of growth the middle lamella is comprised of pectin material, namely galacturonic acids, galactans and arabinans. The middle lamella becomes increasingly lignified in mature wood. The primary cell wall (P) is the first laid down during cell growth and features an unordered mat of cellulose microfibrils. The secondary cell wall is itself separated into three distinct layers. The S1 layer contains an ordered array of cellulose microfibrils which are at a shallow angle to the horizontal, whereas the thicker S2 layer comprises the bulk of the cell wall and has an array of cellulose microfibrils which have a steep microfibrilar angle (MFA) close to vertical and in the opposite sense to the S1 layer. The S3 layer is similar in MFA and sense to the S1 layer. The lumen of the cell contains protoplasm and is filled with water above the fibre saturation point. The photomicrograph in Figure 2.6 shows the cross-sectional structure of wood cells and shows the cell lumen, the secondary cell wall and the middle lamella.

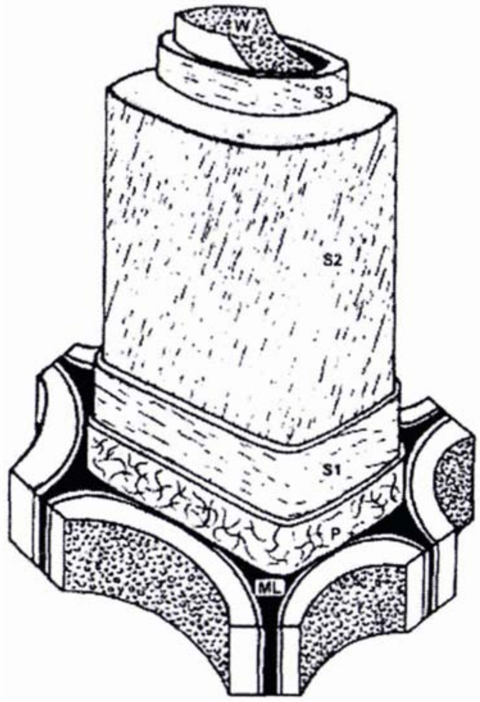

Figure 2.5. Model of tracheid cell wall structure showing the three layers of the secondary cell wall (S1-S3), the primary cell wall (P) and the middle lamella (ML) (Côté, 1983).

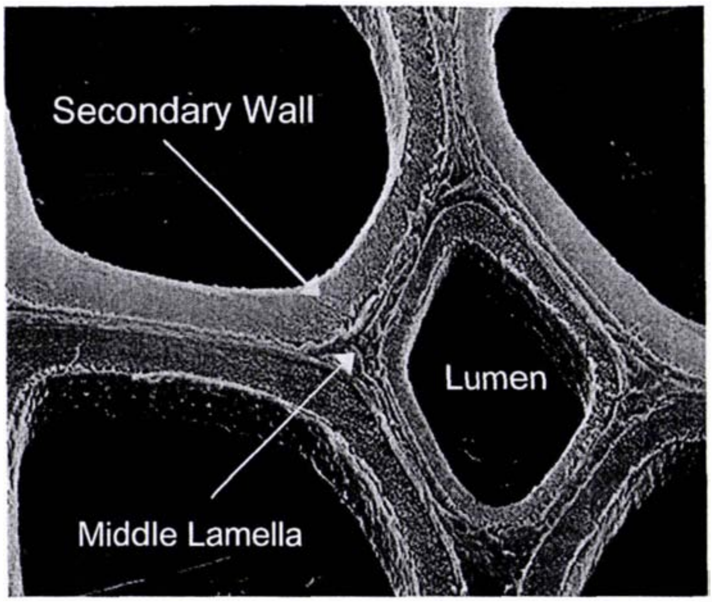

Figure 2.6. Photomicrograph of radiata cells in cross-section showing gross anatomy (*Forest Research* collection #16375).

The structural composition of the cell wall into three separate layers with differing microfibrilar angle imparts relatively high strength and stiffness to wood tracheids.

2.1.2 *TIMBER PRESERVATION*

The fast growth of radiata pine results in trees that contain a large amount of sapwood that is highly susceptible to fungal attack. The high susceptibility to biodeterioration means that treatment with a suitable preservative is required for prolonged performance of radiata pine exposed to the environment. The timber preservation industry in New Zealand uses three generic types of preservative compounds dependent on the final end-use of the product *viz.*, interior use *vs.* exterior exposed use or even ground contact. The three types are:

- water borne solutions based on salts of copper, chromium and arsenic (CCA) (such as Tanalith^{TM})
- light organic solvent preservatives (LOSP) based on organotin species (tributyltin-oxide (TBTO) or -naphthenate (TBTN))
- water borne solutions of boron based salts

Each of these preservative types has advantages and drawbacks. Those based on heavy metals (CCA and tributyltin) are suffering increased pressure from environmental agencies around the world. Changes in the Occupational Safety and Health regulations are putting pressure on the LOSP type preservatives in terms of both transport and use of the preservative compound which are often solubilised in light petroleum spirit solvents. Boron salts, applied as aqueous solutions, are prone to leaching from lumber and as such are not approved for use in exposed or ground contact situations.

Treatment of timber is generally performed on kiln-dried material. During drying, the pits, which normally allow flow of water between adjacent tracheids, close irreversibly in an attempt to prevent water loss. This presents a problem when trying to treat timber with preservative solutions, as there is active resistance to the ingress of chemical treatment solutions (Singh *et al.*, 1999). Therefore, treatment of timber is achieved using one of two generic methods:

- diffusion
- pressure treatment, often with vacuum pretreatment

Both processes are used commercially and depend on the type of preservative used and the desired level of preservative efficacy.

Once timber has been preservative treated, there is very little known about the chemical nature of the preservative chemicals. In particular it has been suggested that tributyltin oxide (TBTO) degrades in timber (Henshaw *et al.*, 1978; Barug, 1981; Jermer *et al.*, 1983), *via* debutylation reactions, forming dibutyl- and monobutyl-tin species.

The degradation of TBTO preservative in radiata pine wood has previously been investigated (Archer and Meder, 1987; Meder and Archer, 1991). NMR analysis of the extracts from TBTO-treated timber showed evidence of disproportionation of TBTO into a number of mono-, di-, tri-, and tetrabutyl tin species, predominantly esters of fatty and resin acids, including tributyltin acetate (Figure 2.7). Similar results were observed by Blunden and Hill (1988). The one obvious drawback to both of these studies was the extraction of the preservative compound out of the wood after treatment. There remains some doubt as to the cause and effect of the extraction procedure on the observed degradation of the TBTO. Ideally a solid state NMR investigation of the tin species *in situ* would be preferable.

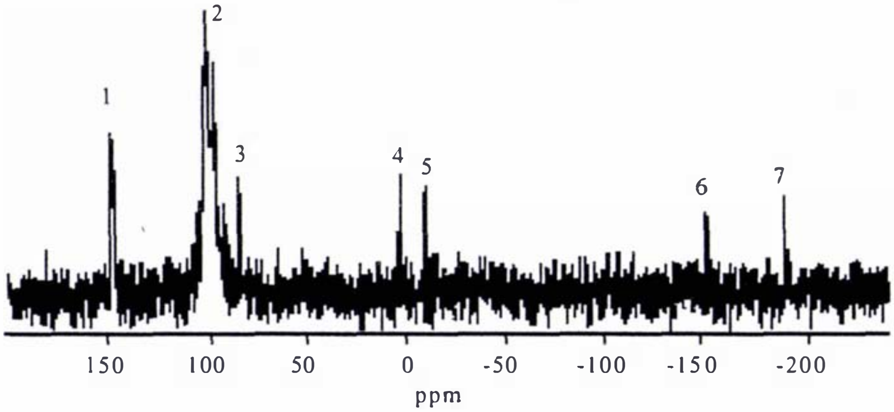

Figure 2.7. 74.5 MHz solution state ^{119}Sn NMR spectrum of $CDCl_3$ extract of TBTO treated radiata pine sapwood. 1 = Bu_3SnCl, 2 = Bu_3SnOR, 3 = TBTO, 4 = Me_4Sn (reference 0.0 ppm), 5 = Bu_4Sn, 6 = $Bu_2Sn(OBu)_2$, 7 = $Bu_2Sn(OR)_2$ where OR = fatty or resin acid ester. (Meder and Archer, 1991).

Boron salts are used to treat radiata pine sapwood to prevent borer and fungal attack in non-exposed structural lumber. Typically this is achieved by dipping freshly-sawn lumber into a solution of boric acid and borax, followed by storage in covered stacks while the preservative is allowed to diffuse into the wood, a process that can last from five to eight weeks (Harrow, 1955).

The tanalising process is a vacuum/pressure treatment process which forces a solution of copper, chrome and arsenic salts (CCA) into the wood. The freshly treated timber is stored for several days to allow fixation of the preservative. In earlier times the timber was stored on open ground and the soil often became contaminated over time from the drippings.

Vapour phase treatment of radiata pine wood with trimethylborate (TMB) was previously developed at the New Zealand Forest Research Institute (Vinden, 1990; Burton *et al.*, 1990; 1991) in an attempt to overcome such issues as pit closure and drip-pan contamination. Treated and dry lumber can be produced in as little as 30 hours using this process using a vacuum drying, pressure treatment vessel as illustrated in Figure 2.8.

Trimethylborate, produced by azeotropic distillation of boric acid and methanol, undergoes rapid hydrolysis with atmospheric moisture, reverting to boric acid. It was hypothesised that TMB would similarly rapidly hydrolyse in the presence of residual moisture in wood. However, little was actually known about the nature of the boron species in TMB-treated wood nor the degree of penetration and retention of boron in radiata pine wood at the end of the process. Boron-11 MAS NMR spectroscopy and microimaging are ideally suited to investigate the *in situ* nature of boron in TMB-treated radiata pine wood, unlike SEM/EDX which is unable to determine chemical speciation and in this case boron has too low an atomic number to be observed by X-ray techniques.

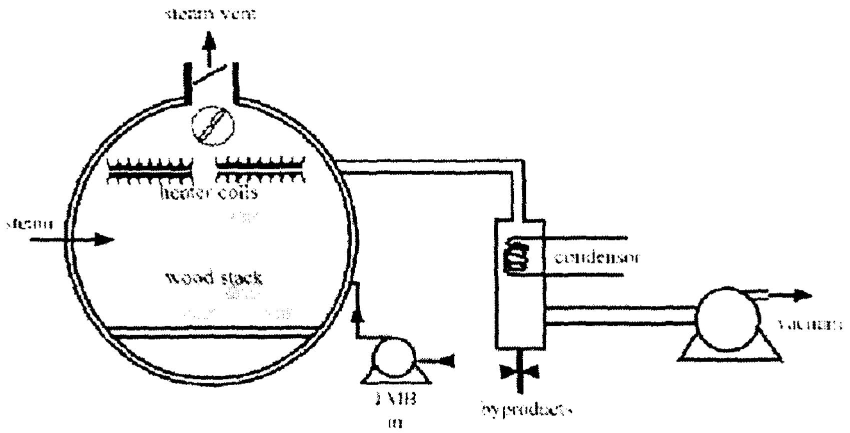

Figure 2.8. Schematic of TMB treatment vessel. The timber is first dried, the vessel evacuated of air and then TMB introduced and volatilised. After treatment the vessel is re-evacuated and the treatment solution recovered.

Previous reports of ^{11}B magnetic resonance imaging are few in number and confined to the use of ^{11}B MRI to visualise infused boron compounds in the development of Boron-Neutron-Capture-Therapies (BNCT) (Bendel *et al.*, 1990; Kabelka *et al.*, 1995). This radiotherapy technique requires the injection of a non-toxic boron compound (a substituted dodecaborane) into the bloodstream, which is selectively assimilated by the highly metabolic tumour. The infused tumour is then bombarded by low-energy thermal neutrons. The neutrons excite ^{10}B to produce ^{11}B* which rapidly undergoes fission to form an α-particle (^{4}He) and ^{7}Li recoil ion. The high energy α-particles (*ca.* 1.5 MeV) and ^{7}Li ions (*ca.* 0.8 MeV) rapidly and efficiently destroy the tumour by dissipating their energy within the volume of the tumour.

Part of the investigations discussed in this thesis cover magnetic resonance spectroscopy and microscopy of radiata pine treated with existing and novel boron based preservatives.

2.1.3 TIMBER DRYING

Approximately 3.2 million cubic metres of sawn timber is produced in New Zealand every year, the majority of which is dried at elevated temperatures by one of several processes including conventional temperatures (70 °C), high temperatures (120 °C) or vacuum drying under reduced pressure.

The moisture content in a freshly felled radiata pine tree is typically greater than 50% on an oven dry basis, and is often higher in the sapwood. Moisture in wood normally exists in three phases; water vapour, cell-wall water and liquid water and they are subject to different driving forces. Water vapour moves under a partial vapour pressure gradient whereas cell-wall water diffuses within the wood material due to a chemical potential gradient and liquid water is transported by capillary action (Stamm 1959, 1960; Spolek and Plumb, 1981; Stanish, 1986; Pang, 1996b). Each of these transport mechanisms plays a role during the drying of softwoods such as radiata pine. During drying of wood, water first leaves from the voids and lumen while the cell-wall water remains intact. The moisture content at which the cell lumens contain no free water, but at which water has not yet begun to be removed from the cell wall is known as the fibre saturation point, M_{fs}. This is typically in the range 26-32% and for radiata pine is *ca.* 30% (Kininmonth, 1991). The importance of the individual transport mechanisms may however change as drying proceeds, in particular, capillary flow of liquid water requires a continuous column of water, which is certainly the case above the fibre saturation point, but once the fibre saturation point is reached a disruption to the continuity of the liquid phase occurs so that liquid flow caused by capillary pressure is no longer possible as a transport mechanism (Spolek and Plumb, 1981). Below this point moisture transport becomes a diffusion process, which is much slower, giving rise to the development of a steep moisture gradient. The principal reason for drying lumber at elevated temperatures is to increase the rate of diffusion about 37-fold on increasing the temperature from 25 to 100 °C (Bramhall, 1979; Walker, 1993) in order to speed up the drying process below fibre saturation. Below the fibre saturation point, water must be removed from the cell wall (desorbed) in order to lower the moisture content of the wood, and will do so until an equilibrium moisture content (EMC) is reached where the moisture content in the wood attains the same moisture content as the surrounding environment.

Below fibre saturation, wood is able to absorb and desorb water in response to changes in the surrounding environment due to changes in temperature and relative humidity. The desorption isotherm for the removal of water from never-dried or green wood has been shown to be higher than the adsorption isotherm and is also higher than any subsequent desorption isotherm from previously dried and re-hydrated wood (Skaar, 1984; Figure 2.9).

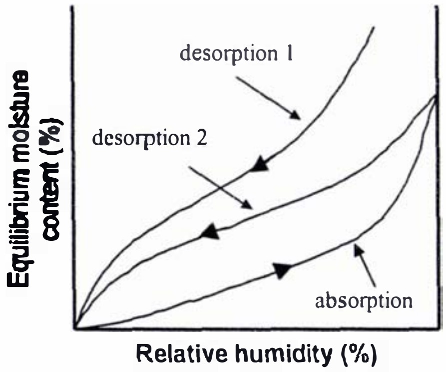

Figure 2.9. Schematic sorbtion isotherm for wood at varying EMC and relative humidity (after Skaar, 1984).

The desorption of water during drying is associated with a number of defects found in dry radiata pine *viz.* internal checking (Figure 2.10) and collapse, as well as twist, crook, cup and bow. Internal checks form in radiata pine sapwood earlywood and occur most predominantly immediately outside the heartwood/sapwood boundary. This is often the cause of radiata pine mouldings and joinery being rejected by manufacturers. In general checks do not cross the latewood between adjacent rings.

Dimensional instability such as twist, crook, cup and bow can occur on drying or more inconveniently it can occur in-service due to redistribution of moisture caused by cyclic changes in humidity. Despite the importance of drying very little is known about the nature of water movement during timber drying or about the nature of the remaining "cell-wall" water.

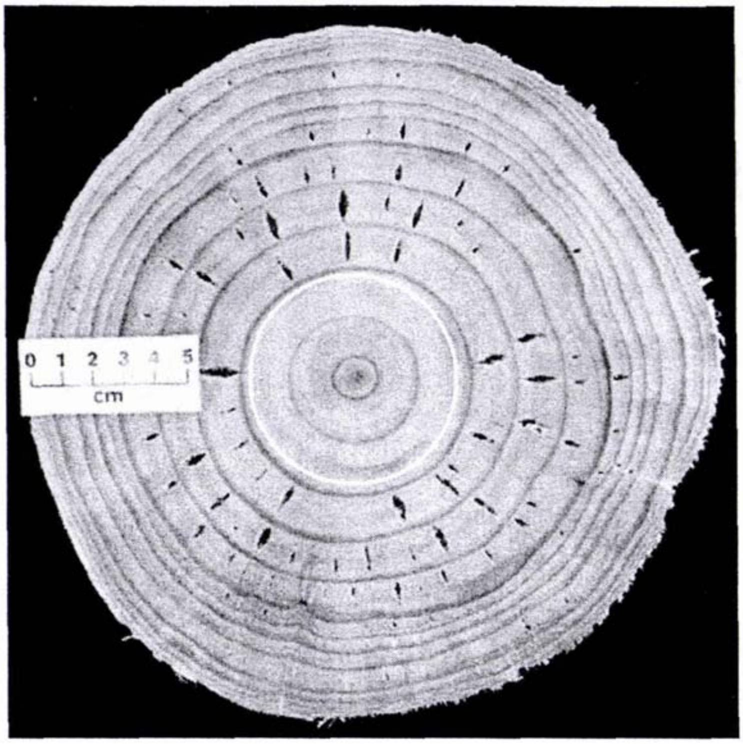

Figure 2.10. Cross-sectional image of radiata pine disk showing internal checks formed. Note that check formation takes place outside the heartwood zone (indicated by white circle) and that checks are confined within an annual growth ring. (*Forest Research* collection #20576).

Hall and co-workers (Hall and Rajanayagam, 1986; Hall *et al.*, 1986a,b) have used clinical MRI scanners to identify the inner morphology of aspen wood samples and to follow the effects of drying or preservative treatment of maple wood.

Olson *et al.*, (1990) have followed the air drying of white oak (*Quercus alba* L.) boards using the head coil of a clinical 0.5 T whole-body imaging system giving in-plane resolution of 1.2 x 1.2 mm. The rays appeared brighter in the images than surrounding tissue indicating higher relative moisture content. This indicated that the rays might play an important part in the drying of timber by providing a pathway for moisture flow during drying. Drying appeared to begin at the surface forming a shell, which progressively increased as the core began to dry. The highest area of moisture content was in the core of the timber. A study by Pang and Wiberg (1998) using computed tomography showed that drying of 100 x 40 mm radiata pine boards occurred from the outside surfaces inwards towards the core.

Several workers have used NMR to establish methods for measuring moisture content of wood (Nanassy, 1973, 1976, 1978; Sharp *et al.*, 1978; Riggin *et al.*, 1979; Menon *et al.*, 1989; Quick *et al.*, 1990; Araujo *et al.*, 1992, 1993; Thygesen, 1996).

2.1.4 TIMBER ADHESIVES

The wood products industry relies heavily on adhesive systems for the manufacture of engineered wood products such as laminated veneer lumber (LVL), medium density fibreboard (MDF), plywood, finger-jointed studs and glue-laminated beams (glulam). The adhesive system chosen must be fit for the end-use purpose. Two generic types of adhesives are used: emulsion polymer type adhesives such as poly(vinyl acetate) (PVAc) or resol type adhesives such as urea-formaldehyde (UF) or phenol-formaldehyde (PF) systems. These latter adhesives may be formulated with addition of melamine in the case of UF to form a MUF resin or resorcinol in the case of PF resins to form a "PRF" resin.

2.1.4.1 Emulsion Polymers

Emulsion polymer adhesives are an important part of the wood-working industry. Poly(vinyl acetate) (PVAc) resins are thermoplastic resins which have relatively low cost, are produced in large volume and have wide ranging application in the packaging, paper and solid wood industries, particularly the furniture and mouldings industries as it has a long pot life, is easy to use and cleans up readily in water. It is a familiar household glue that has been available since the 1930's and has the desirable property of curing to produce a clear glue line. However PVAc resins suffer from shear-induced creep and softening in moist, humid environments unless they are suitably modified to enhance cross-linking. This has lead to several formulations involving polymerisation with co-polymers and cross-linking agents.

PVAc in its simplest form is made by emulsion polymerisation of the monomeric vinyl acetate in water, along with a stabiliser (poly(vinyl alcohol), PVOH) and a polymerisation initiator (sodium persulphate). The emulsion formed is soluble as a latex colloid in a monomeric solution of vinyl acetate. The polymer particles in the latex are in the region of 0.5-2.0 μm in size. The adhesive cures by dehydration, which is aided by the dry wood drawing water from the adhesive. The polymer begins to coalesce and ultimately forms a homogeneous polymer layer (Figure 2.11).

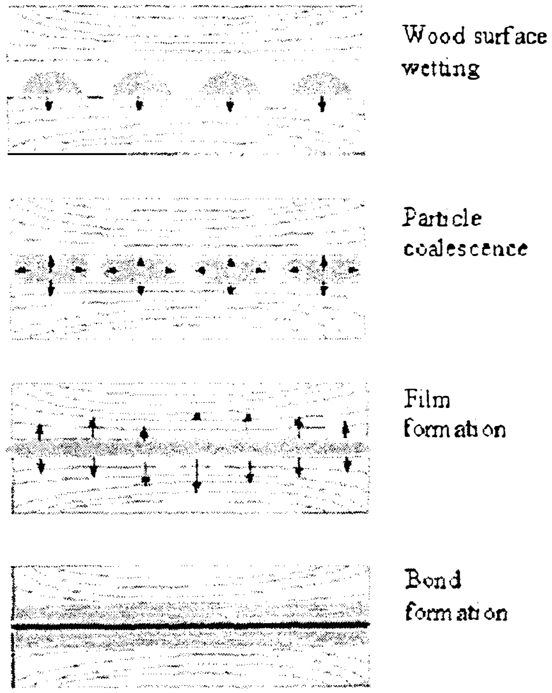

Figure 2.11. Schematic showing steps involved in adhesive-wood bond formation.

In order to impart some resistance to creep, PVAc is often co-polymerised with *N*-methylolacrylamide (*N*-MAM) (Figure 2.12) and the resulting co-polymer is often cross-linked with coordinating cations, such as aluminium, in the form of chloride or sulphate salts.

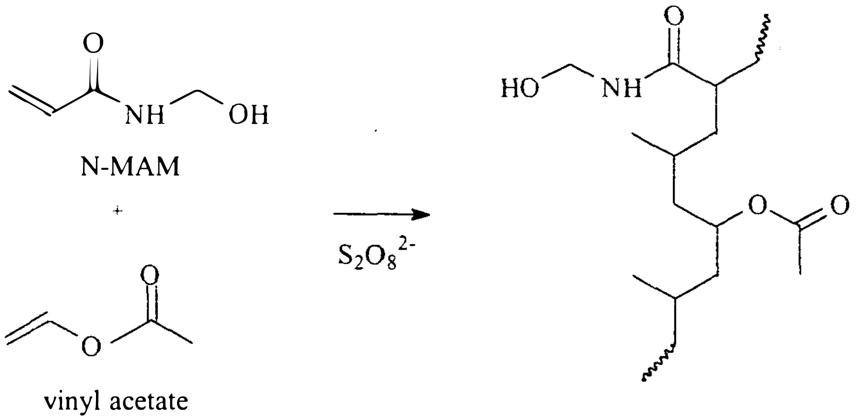

Figure 2.12. Formation of cross-linked PVAc from vinyl acetate and *N*-methylolacrylamide.

Despite the large global consumption of PVAc adhesive, very little is known about the chemical nature and mode of action of the modifiers. Much of the "art" of adhesive formulation is passed down as institutionalised recipes that work. For instance, although aluminium chloride is added to PVAc formulations to aid cross-linking and while it does impart rigidity to the cured adhesive nothing is reported in the literature about the mode of action. Crosslinking in a number of other polymer systems has been investigated by NMR and reported in a review by Whittaker (1997).

Figure 2.13 outlines three possible means by which aluminium could act as a cross-linking agent. The first is simply a solvation type complex (Figure 2.13 **1**) which may in turn form a coordination complex (Figure 2.13 **2**) on dehydration of the emulsion polymer adhesive. The third alternative is the complete removal of water whereby a coordination complex such as that shown in Figure 2.13 **3** may form.

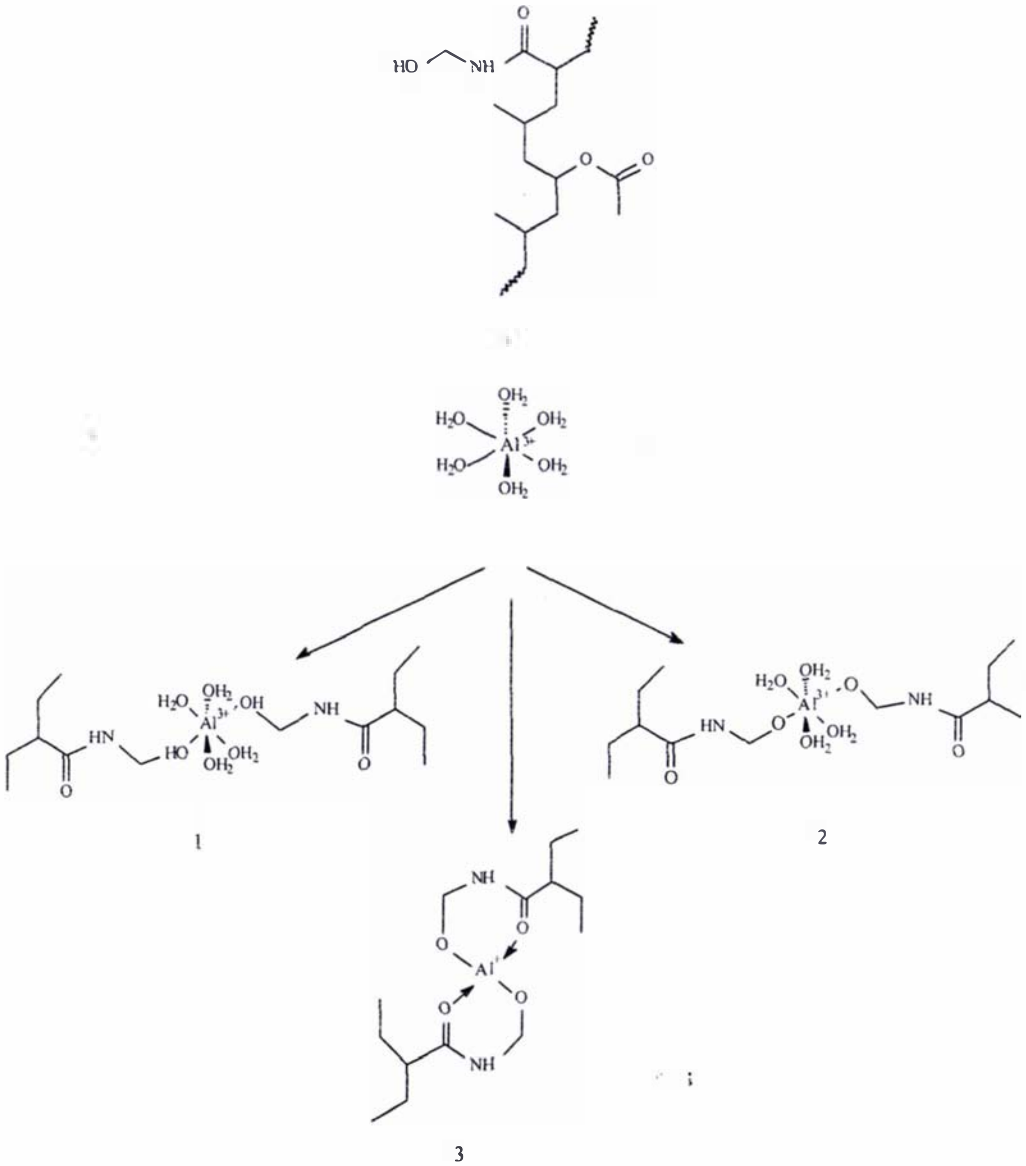

Figure 2.13. Three reaction pathway options for involvement of Al in cross-linking of *N*-MAM.

2.1.4.2 Phenolic Resins

Phenolic resins are the oldest synthetic resins, with the first commercial operation, Bakelite GmbH, starting production in 1910 (Baekeland, 1907). A large proportion of phenolic resin production (32% of European and 60% of US production) finds its way to the wood working industries, particularly in the production of laminated products such as plywood or laminated veneer lumber (LVL) (Knop and Pilato, 1985).

Phenol-formaldehyde (PF) and phenol-resorcinol-formaldehyde (PRF) adhesives are moisture resistant and can be used for bonding wood material in products to be used in load bearing situations. However they cure to a dark brown colour, which becomes obvious in the glue line of, say, a finger-jointed moulding.

In general there are two types of phenolic resins, with the difference being the amount of formaldehyde added and the pH of the preparation.

2.1.4.2.1 Novolak Resins

Novolak resins are obtained from the reaction of phenol and formaldehyde under acidic conditions with a molar excess of phenol. Formaldehyde is added slowly to the cook and as such, novolaks do not contain many reactive methylol groups and so cannot readily condense by themselves on heating. Novolak resins contain methylene linkages between phenolic rings with the linkages being either *ortho* or *para* to the hydroxyl group of the phenol (Figure 2.14). They are generally cured by addition of a "hardener" such as paraformaldehyde of hexamethylenetetramine (HMTA) which crosslink the resin (Figure 2.15).

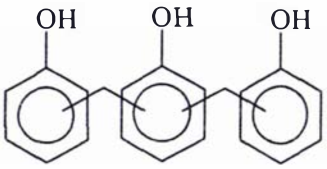

Figure 2.14. Generalised structure of a novolak-type resin.

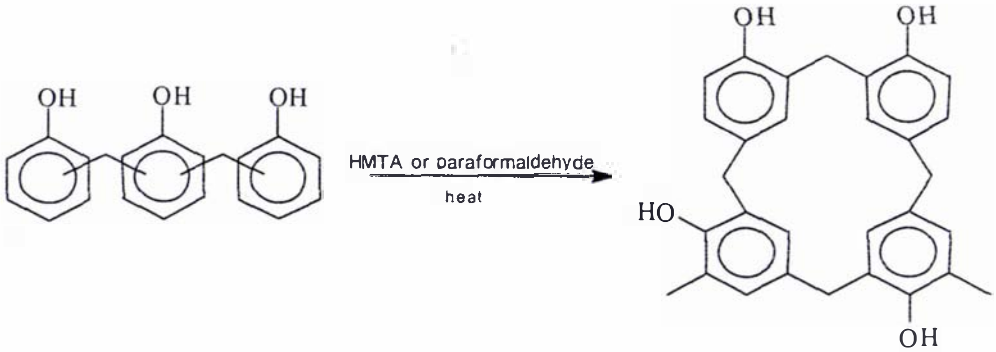

Figure 2.15. Generalised structure of HMTA or paraformaldehyde cured novolak-type resin.

2.1.4.2.2 Resol-type Resins

Resols are produced from reaction of phenol and formaldehyde under basic conditions with an excess of formaldehyde. Whereas novolaks contain only *ortho* or *para* methylene linkages, resols contain both methylene and dimethylene ether linkages as well as methylol groups *ortho* or *para* to the hydroxyl of the phenol (Figure 2.16). Resol-type resins are cured by heat or addition of acid (Figure 2.17).

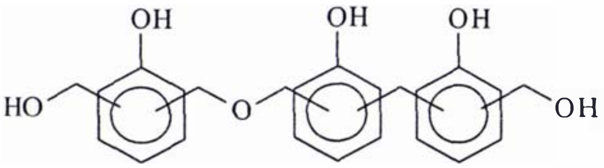

Figure 2.16. Generalised structure of a resol-type resin.

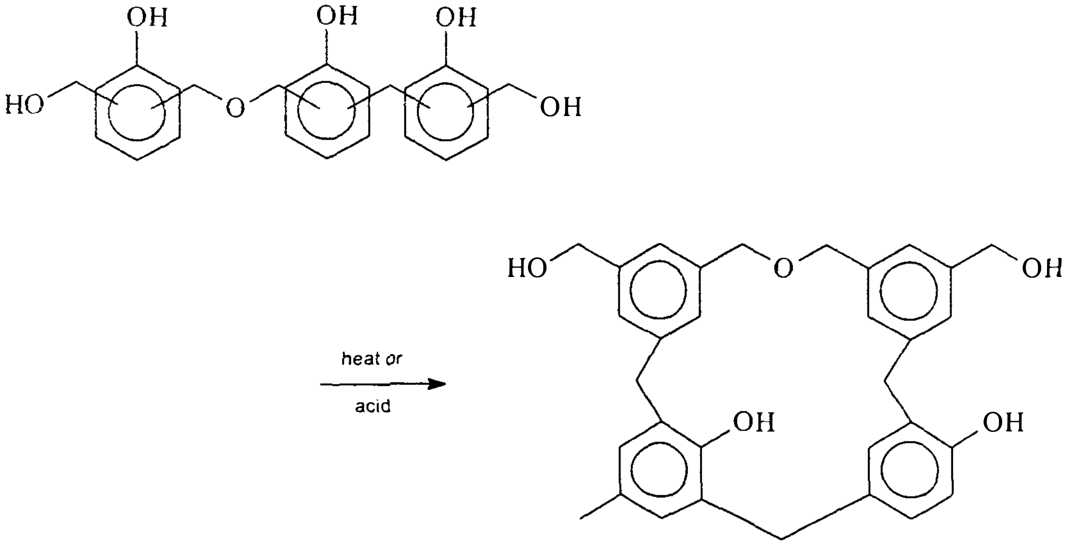

Figure 2.17. Generalised structure of heat or acid cured resol-type resin.

It is the accelerated curing of these types of resins where GreenWeld™ plays an important role (Parker *et al.*, 1999).

Several studies have investigated the cure of phenolic resins using solid state NMR (Fyfe *et al.*, 1980; Pizzi and Teleky, 1986; Hatfield and Maciel, 1987; Chuang and Maciel, 1994; Zhang *et al.*, 1997). In particular Hatfield and Maciel (1987), Pizzi and Teleky (1996) and Zhang *et al.* (1997) have studied the curing of PF resins with hexamethylenetetramine (HMTA) at elevated temperatures to form hardened resins. They all report formation of benzylamine bridges, thought to be one of the linkages possible in the GreenWeld™ cured resin.

2.1.4.3 GreenWeld™

The GreenWeld™ process grew from a desire to finger-joint green (never-dried) pieces of radiata pine. Finger-jointing involves cutting out the defect regions of long lengths of lumber and then reassembling by end gluing the defect-free sections or *shooks* to form a long section of lumber that is knot and defect free. To facilitate a stronger joint and to provide a greater surface area for glue bonding, fingers are cut into the end of the shook so that the fingers fit into the finger gaps of an adjacent shook. Figure 2.18 shows a schematic of a finger-joint along with a finger-jointed pole. Note the glueline is clearly obvious from the dark coloured PRF resin.

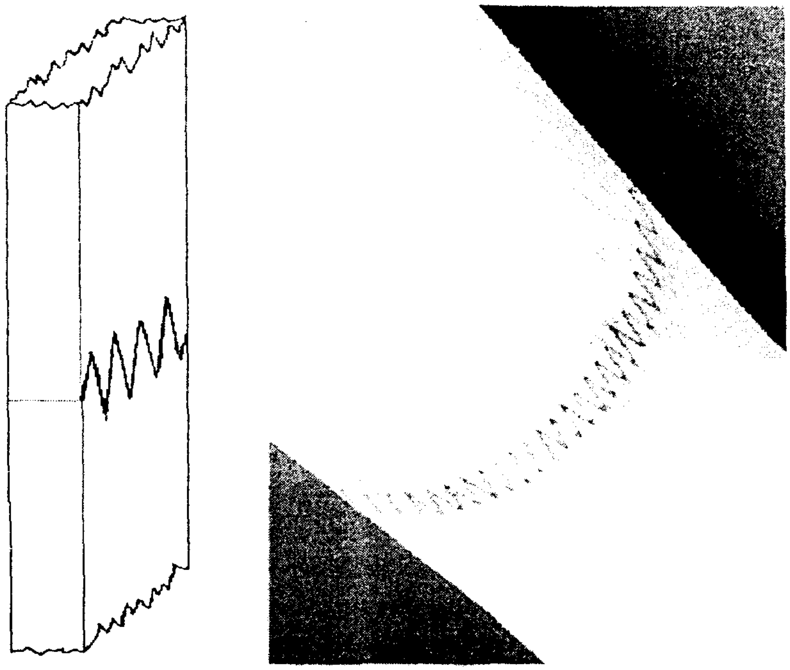

Figure 2.18. Schematic of finger-joint (left) and a finger-jointed pole (right) showing the glueline.

While finger-jointing allows a lumber processor to recover high value products (defect free structural lumber) from otherwise low value or even reject lumber, there is a cost associated with the process. Conventionally, the defect zones are not cut from the lumber to produce the shooks until after drying. Consider a medium size sawmill producing in the vicinity of 100,000 m^3 of sawn-out lumber a year (meaning that approximately 165,000 m^3 of logs come in the gate while 100,000 m^3 goes out again as sawn product, assuming a 60% conversion rate). The defects could amount to 1 – 2% of the total sawn-out volume meaning that each year a sawmill could be drying 2,000 m^3 of product that it will never get to sell.

What if the sawmiller was able to undertake defecting before drying and then engineering a structural length stud so that only the final product was being dried? That is where GreenWeld™ is able to assist. Using the patented GreenWeld™ process (Parker *et al.*, 1997), the defecting can be done on green, rough-sawn lumber and the defect-free shooks finger-jointed in the green state. The assembled, green, finger-jointed studs can then dried and finally gauged to final dimensions. The process requires no major change to existing machinery and simply utilises a modification to the conventional PRF resin hardening system by addition of one extra compound, ammonia, to accelerate hardening. Furthermore, unlike HMTA curing, the GreenWeld™ process operates at ambient temperature.

Since its development, which is proven to work empirically, there have been a number of investigations at ***Forest Research*** to understand the mechanism by which it works (Franich *et al.*, unpublished data). Several directions have been taken utilising a number of analytical methods. Nuclear magnetic resonance spectroscopy of both the liquid and cured resins has played a major part in the characterisation of the GreenWeld™ chemistry.

3. NUCLEAR MAGNETIC RESONANCE THEORY

The electron is not as simple as it looks.
Sir William Lawrence Bragg

Observations of nuclear magnetic resonance signals were independently made in 1946 by two groups of researchers at Stanford University (Bloch, 1946; Bloch *et al.*, 1946) and at Harvard University (Purcell *et al.*, 1946). The significance of this discovery was such that in 1952, Bloch and Purcell were jointly awarded the Nobel Prize for Physics. Since then two other Nobel Laureates have been awarded (in chemistry, 1991) to Richard Ernst of ETH, Zürich for his pioneering development of NMR studies in 2 and 3 dimensions and Kurt Wütrich (in chemistry, 2002) for his development of NMR as a tool for determining the three-dimensional structure of biological macromolecules in solution.

The primary field of application of NMR is the characterisation of chemical structures and as such it has been the domain of the chemist for a number of years. Advances in technology and continual development by physicists have seen the advent of imaging techniques to enable *in situ* studies of materials and biological samples.

3.1 NUCLEAR MAGNETISM

The principle behind all magnetic resonance technologies is the interaction of electronic or nuclear spin with an external magnetic field. To understand this we need to consider the forces at work.

3.1.1 THE MAGNETIC DIPOLE

Nuclei possess a magnetic dipole moment, μ, and angular momentum, $\mathbf{L}$, which is described by quantum mechanics as:

$$\mu = \gamma \mathbf{L} \qquad \text{eqn 3.1.}$$

where γ is the nuclear gyromagnetic ratio and $|L| = \hbar\sqrt{I(I+1)}$ where I is the nuclear spin quantum number and $\hbar = h/2\pi$ and h is Planck's constant (6.625×10^{-34} J s).

Angular momentum is proportional to the magnetic moment *via* the gyromagnetic ratio (γ), which is constant for each isotopic nucleus (Table 3.1).

Table 3.1. NMR properties of nuclides used in this study (Bruker, 2000).

Nuclide	Spin (I)	Natural abundance (%)	Relative sensitivity	Gyromagnetic ratio, γ (10^7 rad T^{-1} s^{-1})	NMR frequency (MHz) at B_0 =		
					4.7 T	7.1 T	9.4 T
^{1}H	½	99.98	1.00	26.75	200.13	300.13	400.13
^{2}H	1	1.5×10^{-2}	9.6×10^{-3}	4.11	30.70	46.05	61.40
^{11}B	$^{3}/_{2}$	80.42	0.17	8.58	64.17	96.27	128.34
^{13}C	½	1.11	1.6×10^{-2}	6.73	50.33	75.63	100.61
^{15}N	½	0.37	1.04×10^{-3}	-2.71	20.26	30.40	40.53
^{27}Al	$^{5}/_{2}$	100	0.21	6.97	52.17	65.14	104.23
^{119}Sn	½	8.58	5.2×10^{-2}	-10.03	74.54	111.82	149.09

3.1.2 NUCLEAR PRECESSION

Since the dipole comprises two opposite poles, there are two opposite forces acting on the dipole as it tries to align with the external field, creating a torque, τ, which is proportional to the strength of the applied field.

Consider for a moment the analogy of a spinning gyroscope. The mass moment is analogous to the dipole moment and the earth's gravitational field is analogous to the magnetic field. It precesses as the torque continually re-aligns the angular momentum vector. The torque experienced by the magnetic dipole in the external field equally causes the magnetic dipole to precess about the magnetic field at a resonant frequency proportional to the magnetic field, $\boldsymbol{B}_0$, (Figure 3.1) with the torque given by equation 3.2.

$$\tau = \mu \times \boldsymbol{B}_0 \qquad \text{eqn 3.2.}$$

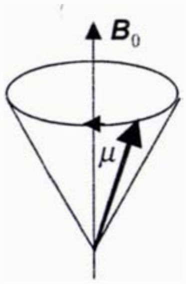

Figure 3.1. Precession of a magnetic dipole moment in a magnetic field.

By equating the torque to the rate of change of angular momentum, the equation of motion of the nuclear magnetic moment vector is described according to equation 3.3.

$$\frac{d\boldsymbol{\mu}}{dt} = \gamma(\mu \times \boldsymbol{B_o}) \qquad \text{eqn. 3.3.}$$

The frequency of precession, also called the Larmor frequency, ω_o, is given by

$$\omega_o = \gamma B_0 \qquad \text{eqn 3.4.}$$

where B_0 is the magnitude of the magnetic field.

3.1.3 THE MAGNETIC MOMENT

Consider the proton nucleus with spin quantum number, $I = ½$. The magnitude of the angular momentum is given as

$$|\boldsymbol{L}| = \hbar\sqrt{I(I+1)} \qquad \text{eqn 3.5.}$$

such that $|\boldsymbol{L}| = \hbar\frac{\sqrt{3}}{2}$

When the magnetic dipole is placed in a static, external magnetic field of amplitude, B_0, the dipole tries to align itself with the field. This can occur in a parallel or anti-parallel fashion according to magnetic quantum number, m_z, which can take values $-I, -I+1, \ldots, 0, \ldots, I-1, I$ (Ziessow, 1990). In the case of the proton nucleus, $m_z = \pm\frac{1}{2}$.

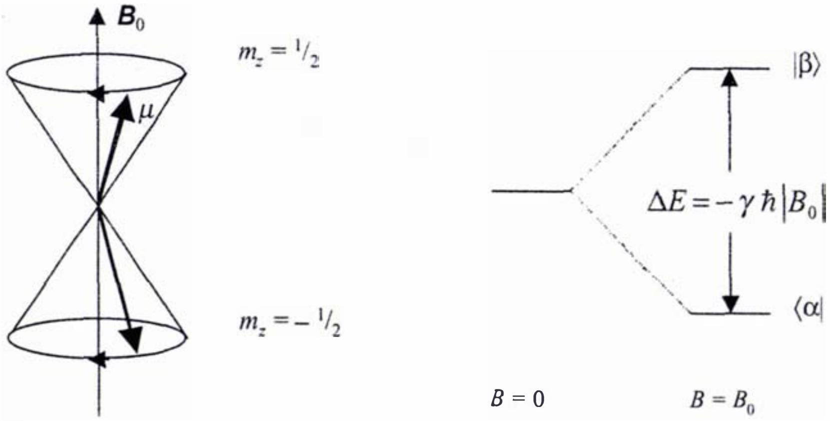

Figure 3.2. Possible spin orientations of a proton magnetic dipole moment in a magnetic field and the corresponding quantum mechanical energy states.

The energy difference between the two states can be given by equation 3.6.

$$\Delta E = \gamma\,\hbar\,|B_0| \qquad \text{eqn 3.6.}$$

Provided that the energy of corresponding photons, $\hbar\omega$, matches the difference in energy between the two spin states it is possible to meet the resonance condition, $\omega = \omega_o = \gamma B_0$, whereby the transition from the lower energy state to the higher is possible.

3.1.4 THERMAL EQUILIBRIUM

The energy differences between individual spin states gives rise to the nuclear magnetic resonance phenomenon when we consider what happens to the bulk magnetisation, $\boldsymbol{M}_0$, within a sample. At equilibrium we can represent the population of nuclei in the upper energy level N_β and the population in the lower energy level N_α. Then for nuclei with $I = ½$;

$$\frac{N_\beta}{N_\alpha}=e^{-\Delta E/k_BT}\approx 1-\frac{\Delta E}{k_BT}=1-\frac{\gamma\hbar B_0}{k_BT}$$ eqn 3.7.

where k_B is the Boltzman constant (1.38 x 10^{-23} J K^{-1}). The energy difference is very small compared to the average energy of thermal motion, such that the populations are nearly equal. The excess in the lower energy level is only in the region of parts per million. However without this minute excess of energy there would be no nuclear resonance phenomenon. At equilibrium the ensemble average of all the individual magnet moments results in a net magnetisation being observed in the direction of the field B_0. The trick is to measure the bulk magnetisation throughout the full volume of the sample, and in particular, the perturbation of the magnetisation which occurs under the resonance condition.

3.1.5 B_1 AND THE ROTATING FRAME

To allow for the precession of the spin, we use a frame of reference that itself rotates at the same frequency as the Larmor frequency. The new coordinate system defined by "the rotating frame" is described by the new axes *x'*, *y'* and *z'*. Application of a second magnetic field, $\boldsymbol{B}_1$, perpendicular to the first, and oscillating at the same frequency, has the effect of "tipping" the magnetisation out of the *z'* axis and into the *x'*-*y'* plane, through an angle θ (Figure 3.3). The $\boldsymbol{B}_1$ field is applied by means of a radiofrequency pulse of short duration (typically a few microseconds). Because $\boldsymbol{B}_1$ oscillates in the laboratory frame, in the rotating frame it provides a field which is stationary and perpendicular to $\boldsymbol{B}_0$. If the amplitude of the laboratory frame oscillating field is $2B_1$, then the amplitude of the stationary component in the rotating frame is B_1. Consequently the spins nutate around $\boldsymbol{B}_1$ at frequency γB_1 (Abragam, 1983).

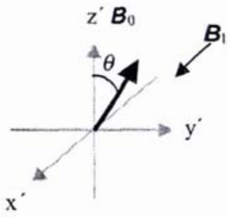

Figure 3.3. The effect of applying a $\boldsymbol{B}_1$ field along *x* on the bulk magnetisation.

The angle, θ, through which the magnetisation is tipped, is determined by two factors, namely the power level at which the $\boldsymbol{B}_1$ field is applied and the duration for which it is applied. It is common practice to set the power level and vary the duration in order to effect varying degrees of tip. As the resonant frequency for NMR operation is typically in the MHz or radiofrequency (rf) range, the $\boldsymbol{B}_1$ magnetic field pulses are commonly referred to as rf pulses. Most applications of NMR spectroscopy or imaging require the magnetisation to be tipped into the transverse plane, in which case 90° rf pulses are used, or that the magnetisation be inverted onto the $-z$ axis by using a 180° rf pulse.

Most applications of magnetic resonance require a series of rf pulses to be applied in order to manipulate the nuclear spins. These pulse sequences can also include magnetic field gradients, which are used for spatial selection of nuclear spins. This will be covered in section 3.4.

3.2 RELAXATION

Following the pulse train, the magnetisation vector, which has been perturbed, seeks to realign with the external field and re-establish equilibrium. It is this process, the so-called *free induction decay* or FID that is observed in the receiver coil. Bulk magnetisation is re-established *via* one of the two following relaxation mechanisms.

3.2.1 SPIN-LATTICE OR LONGITUDINAL RELAXATION (T_1)

The longitudinal or spin-lattice relaxation time measures the rate at which the magnetisation component *parallel* to the external field, $\boldsymbol{B}_0$, approaches thermal equilibrium. The major contributing factor to spin-lattice relaxation is dipole-dipole coupling due to energy exchange between excited nuclei (or 'spins') and their environment (the 'lattice').

The spin-lattice relaxation time for solution state NMR is defined (Bloch, 1946; Bloch *et al.*, 1946) by the equation:

$$\frac{dM_z}{dt} = -\frac{(M_z - M_o)}{T_1} \qquad \text{eqn 3.8.}$$

Variation of T_1 with inverse temperature, will typically describe a 'V' shaped curve (Figure 3.4), which is dependent on the spectrometer frequency (lower frequencies shifting the minimum to lower temperature) (Bloembergen *et al.*, 1948).

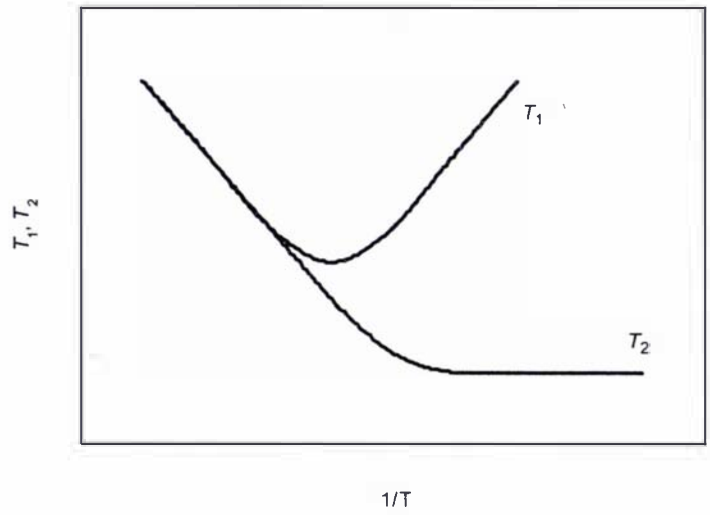

Figure 3.4. Variation of relaxation time constants T_1 and T_2 with inverse temperature.

Measurement of spin-lattice relaxation time constants can be achieved *via* an inversion recovery experiment of the type $180°_x$ - τ - $90°_x$ - FID and is shown schematically in Figure 3.5.

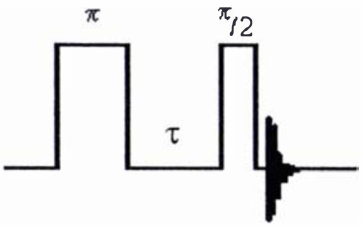

Figure 3.5. Pulse sequence for inversion recovery for measurement of T_1.

The 180° pulse tips magnetisation into negative *z'*-axis. Longitudinal relaxation occurs along the *z'*-axis for a time τ when the 90° pulse tips the remaining magnetisation into the *x'*-*y'* plane where the magnetisation can be measured (Figure 3.6).

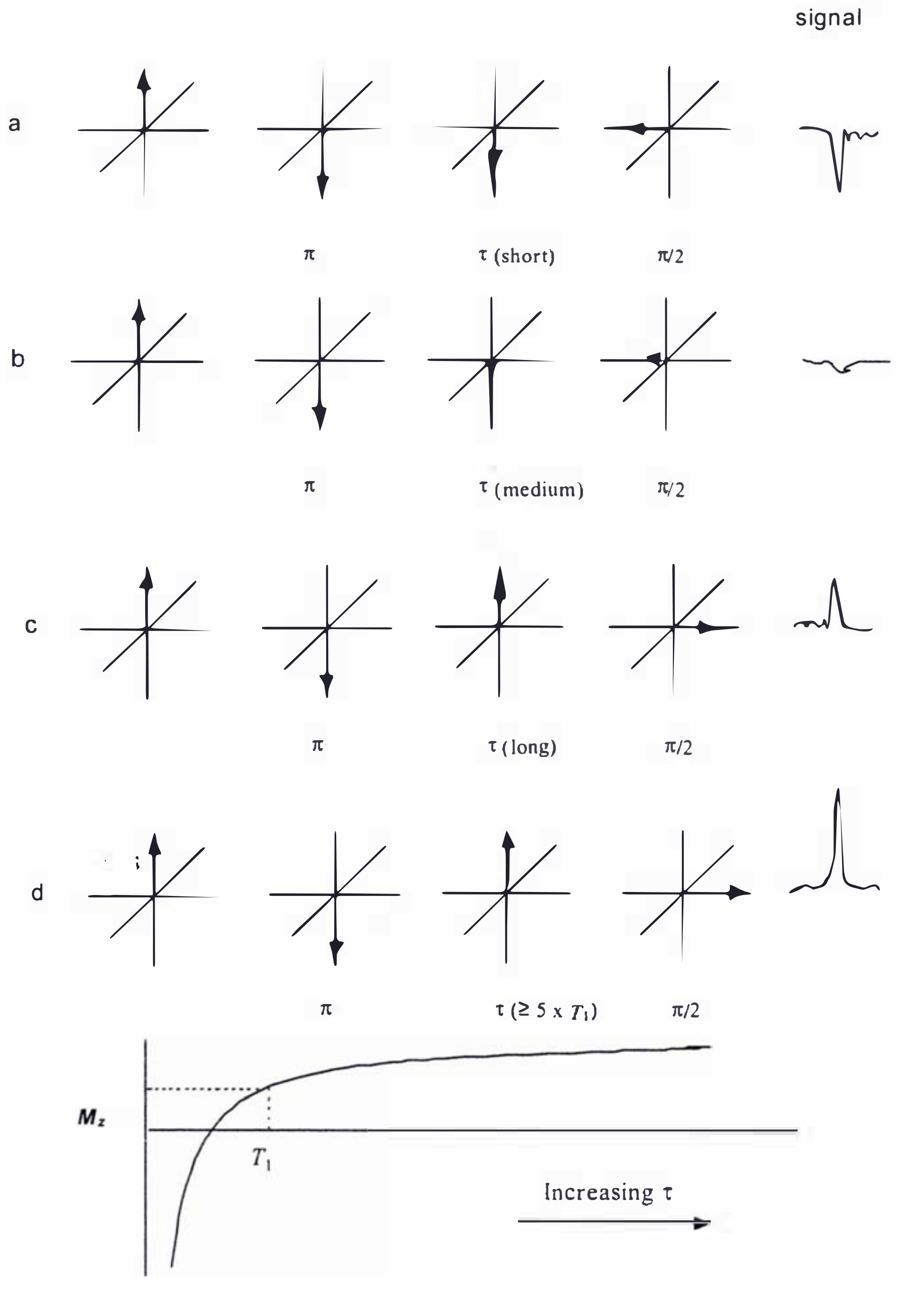

Figure 3.6. Schematic showing the inversion recovery sequence used for determining T_1 with increasing τ delay (a-d), the resultant signal in the frequency domain and a generalised T_1 relaxation curve.

The intensities of the resonances can be plotted with respect to the tau value and the decay can be analysed using standard non-linear least squares curve fitting of equation 3.9 in order to determine T_1.

$$S(t) = S_0\,(1 - \exp(-t/T_1)) \qquad \text{eqn 3.9.}$$

where S is the signal intensity at time t and time zero.

In this study proton spin-lattice relaxation was performed using a modified inversion recovery sequence according to Xu *et al.* (1996) and as shown in Figure 3.7 (MacKay, 2000). In this sequence the signal received from the inversion recovery sequence is subtracted from the signal received from the Bloch decay following a standard 90° pulse. This results in a exponential that decays to zero at long values of T_1.

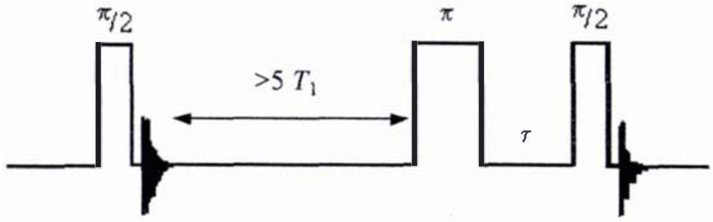

Figure 3.7. Modified inversion recovery sequence for measurement of T_1 (after Xu *et al.* 1996).

When a series of spectra are acquired using this sequence, the intensity of signal for a given resonance decreases exponentially with increasing τ values.

3.2.2 SPIN-SPIN OR TRANSVERSE RELAXATION (T_2)

The transverse or spin-spin relaxation time measures the rate at which the magnetisation component in the plane *perpendicular* to the external field approaches thermal equilibrium due to interactions between neighbouring spins. The main contribution to decay of the free induction signal is in fact field inhomogeneity since in any practical magnet $\boldsymbol{B}_0$ is not homogeneous throughout the volume. Thus not all nuclei experience the same magnetic field. This gives rise to the observed time constant T_2^* which has contribution both from the intrinsic relaxation, T_2, and from field inhomogeneity relaxation, $T_{2(mi)}$, and so T_2^* can be given by:

$$\frac{1}{T_2^*} = \frac{1}{T_2} + \frac{1}{T_{2(mi)}} \qquad \text{eqn 3.10.}$$

These magnetic field inhomogeneities cause nuclei to precess with slightly different Larmor frequencies, *even if they are chemically equivalent*. In solid state spectroscopy, T_1 can be very long (10^{-1} – 10^{-3} s) whereas T_2 is very short (10^{-5} s) since the magnetic coupling to adjacent spins is very large.

Generally the shape of the resonance line can be described as a Lorentzian function such that the width at half-height is given by

$$\Delta\nu_{½} = \frac{1}{\pi T_2^*} \qquad \text{eqn 3.11.}$$

where T_2^* is the observable time constant, which is generally shorter than the value that would be obtained if the $\boldsymbol{B}_0$ was truly homogeneous. The effect of field inhomogeneities ($\Delta\boldsymbol{B}_0$) must be removed in order to obtain the true or natural spin-spin relaxation time, T_2. This latter rate gives information about molecular interactions.

$$\frac{1}{\pi T_2^*} \approx \frac{1}{\pi T_2} + \frac{\gamma \Delta B_0}{2} \qquad \text{eqn 3.12.}$$

The standard method used to remove field inhomogeneity effects is the Meiboom-Gill modification (Meiboom and Gill, 1958) of the Carr-Purcell spin echo sequence (Carr and Purcell, 1954). In order to understand this we first need to consider what happens to the magnetisation in the transverse *x'-y'* plane.

Transverse relaxation occurs *via* the nuclear spins 'dephasing'. This occurs due to small differences in the precessional frequency of equivalent nuclei, causing the spins to "fan out", or put another way the spins are prevented from precessing in phase. These differences are due to minute changes in the local magnetic field experienced by one particular nucleus compared to that experienced by an adjacent nucleus. The true T_2 relaxation is due to interactions between nuclei which depend on local molecular dynamics. As it is really the true T_2 that we want to measure, we need to remove the effects of $\boldsymbol{B}_0$ inhomogeneity. The key to this removal is the spin echo.

3.2.2.1 The Hahn Spin Echo

The spin echo (Hahn, 1950) can be used to show the effect on the transverse magnetisation due to dephasing and is illustrated in Figure 3.8. In the rotating frame, the net magnetisation $\boldsymbol{M}_0$ lies parallel to the magnetic field $\boldsymbol{B}_0$. A 90° pulse applied by a $\boldsymbol{B}_1$ field parallel to the x'-axis has the effect of rotating the magnetisation along the y'-axis. Immediately the spins begin to dephase due to local field inhomogeneity such that the individual *isochromats* precess at different frequencies (either faster or slower than the resonant frequency). After an initial period, τ, the spins are out of phase in the rotating frame. At this point a 180° pulse is applied which flips the magnetisation about the x'-axis. The spins still precess at the same frequency and sense, so that after an additional period, τ, the spins "refocus" along the y'-axis causing a coherent "echo" to be observed. The period 2τ is referred to as the echo time (T_E) and becomes an important parameter in imaging sequences.

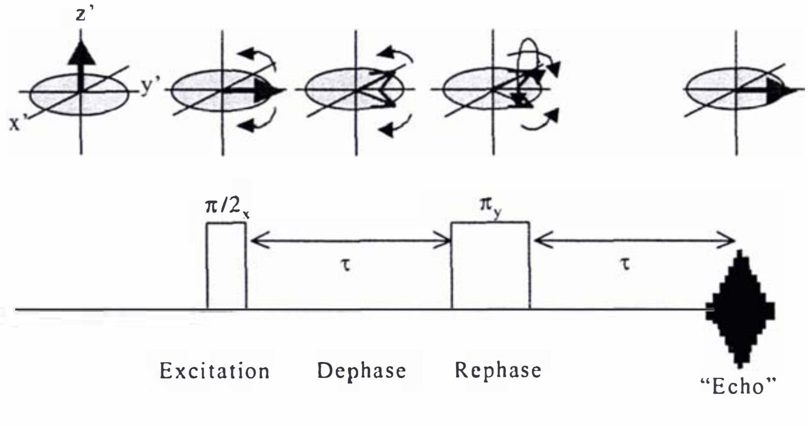

Figure 3.8. Schematic of the Hahn spin echo experiment, showing the dephasing of transverse magnetisation after a 90° excitation pulse and the refocussing of the magnetisation to produce an echo following a 180° pulse.

Measurement of spin-spin relaxation time constants is typically made *via* a Carr-Purcell-Meiboon-Gill spin echo pulse sequence (Carr and Purcell, 1954; Meiboom and Gill, 1958). The Meiboom-Gill modification of the Carr-Purcell spin-echo sequence applies the 180° pulse train (separated by 2τ), at a 90° phase shift to that of the 90° excitation pulse (Figure 3.9).

$$90°_x - \tau - 180°_y - \tau - (\text{echo}) - \tau - 180°_y - \tau - (\text{echo}) \ldots$$

The effect of this on the 180° pulse train is to refocus the echoes into the positive *x'-y'* plane during which time transverse relaxation takes place and decreases the signal intensity (Figure 3.10).

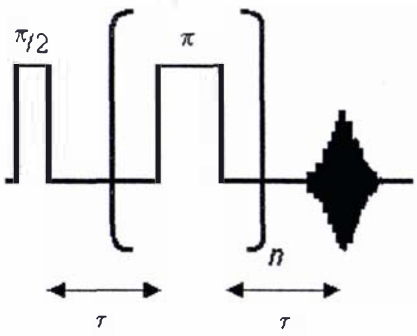

Figure 3.9. Pulse sequence for Carr-Purcell-Meiboom-Gill (CPMG) experiment.

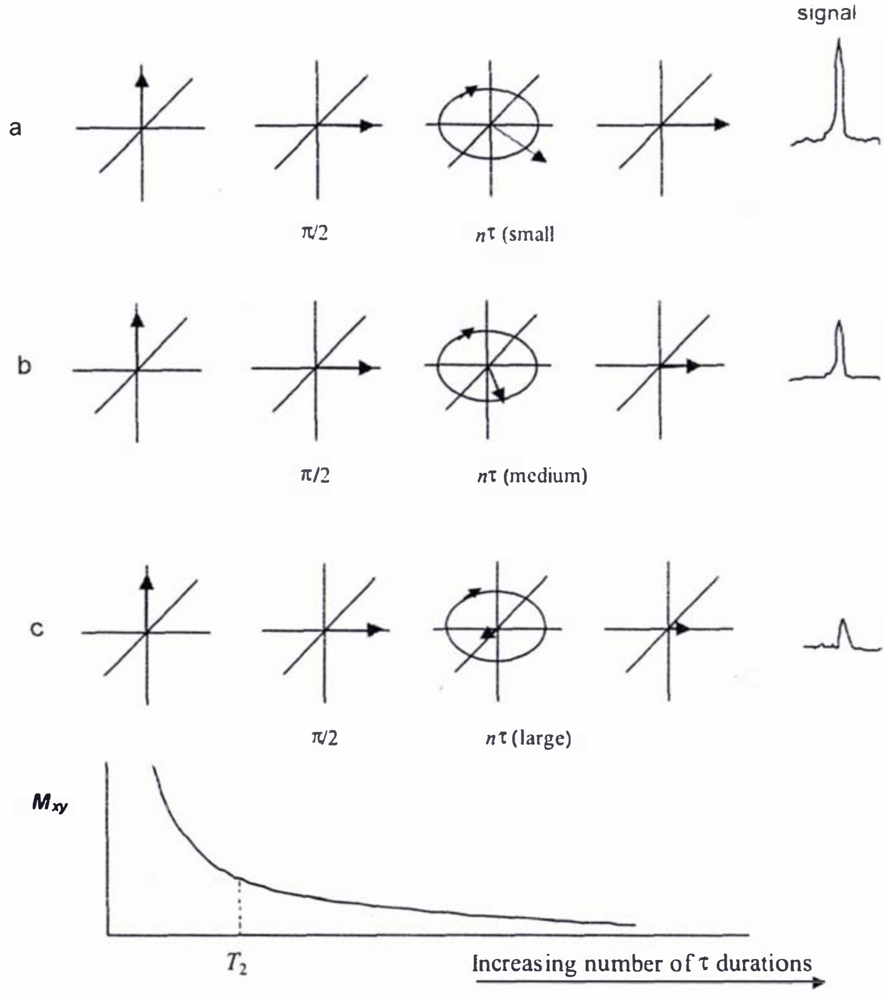

Figure 3.10. Schematic showing the evolution of the magnetisation under the CPMG sequence used for determining T_2 with respect to increasing number of τ durations (a-c), the resultant signal and a generalised T_2 relaxation curve.

A series of spectra are acquired with a varying length CPMG pulse train from which the signal intensities for the resonances of interest are extracted. From the plot of intensity *vs* time a line can be fitted through the points using equation 3.13 to solve for T_2.

$$S(t) = S_0 \exp(-t/T_2) \qquad \text{eqn 3.13.}$$

3.2.3 FOURIER TRANSFORM

In most NMR or MRI experiments there are many protons with different Larmor frequencies so that the signal is more readily viewed in the frequency domain. This requires a Fourier transform (FT) of the time domain data. A detailed description of the FT process can be found in Callaghan (1991). The FT works by extracting the component frequencies from the FID by multiplying them by a series of sinusoids of differing frequencies and then integrating as given by:

$$G(\omega)=\int_{-\infty}^{\infty} g(t)\cos(\omega t)dt + i\int_{-\infty}^{\infty} g(t)\sin(\omega t)dt \qquad \text{eqn. 3.14.}$$

3.2.4 THE NUCLEAR OVERHAUSER EFFECT

The nuclear Overhauser effect (NOE) comes about from a disturbance to a resonance of one class of nucleus due to a perturbation of resonant transitions of another class of nuclei to which the first class of nuclei is coupled. Principally the method is used to enhance ^{13}C magnetisation by polarisation transfer from coupled protons. This is generally brought about while trying to eliminate a population difference across some transition(s), by the application of a weak rf field, while observing the signal from another transition (Derome, 1987). This is certainly the case during power gated decoupling techniques whereby a low power, broadband rf field is applied to the proton spins during the relaxation delay period prior to a ^{13}C NMR signal acquisition. In the case of ^{13}C, there is a positive nuclear Overhauser effect from the proton spins, which significantly aids sensitivity, unlike the case of ^{15}N, which has a negative NOE so that any attempt to generate NOE during the relaxation delay period has the effect of reducing sensitivity.

The effect is not uniform across all resonances so that protonated carbons are enhanced more than quaternary carbons. The upshot of this is that if quantitative spectra are required an inverse gated decoupling sequence must be employed whereby there is no rf field applied during the relaxation delay period. This same sequence is required for ^{15}N observation.

3.3 CROSS POLARISATION AND MAGIC ANGLE SPINNING

There are two primary sources of line broadening in NMR spectra of solids. Very strong ^{1}H-^{13}C dipolar coupling can cause broadening of a line by more than 50 kHz. As in solution state NMR spectroscopy this effect is removed by ^{1}H decoupling, although in solid state experiments the decoupling power required is much stronger by at least an order of magnitude.

The second source of line broadening is the result of the chemical shift of a molecule being dependent on its orientation with respect to the static magnetic field. In a powdered sample all possible orientations of the molecule occur with an equal probability and therefore a range of chemical shifts is observed. The resulting spectrum is a combination of all possible chemical shifts for all the atomic environments.

For a specific carbon environment, the difference between the highest and lowest frequency chemical shift is the chemical shift anisotropy (CSA). The shape of the spectrum, for axially symmetric tensors, can be described by:

$$\sigma_{obs} = \sigma_{iso} + \sigma_{aniso}\ \tfrac{1}{2}\,(3\cos^2\theta - 1) \qquad \text{eqn 3.15.}$$

where;

σ_{obs} is the observed chemical shift
σ_{iso} is the isotropic chemical shift that would be observed in solution
σ_{aniso} is the magnitude of the anisotropic component
$\tfrac{1}{2}(3\cos^2\theta - 1)$ is the angular dependence of the chemical shift with respect to the external field, θ being the angle between the magnetic field and the principal axis of the chemical shift tensor.

When several atomic environments exist, the overlap of CSA powder patterns results in a broad, uninterpretable spectrum.

3.3.1 *THE MAGIC ANGLE*

In order to remove the anisotropic component the anisotropy is "projected" along an axis inclined at θ to the magnetic field, such that $3\cos^2\theta - 1$ equals zero. This projection is achieved by spinning the sample at the "magic angle" ($\cos\theta = \frac{1}{\sqrt{3}}$ or $\theta = 54.7°$) and, provided that the spinning rate exceeds the chemical shift frequency spread due to σ_{aniso}, this process reduces the anisotropic component to zero so that only the isotropic component remains (Andrew *et al.*, 1960). However spinning the sample at finite frequencies introduces artefacts called spinning sidebands, which appear about the isotropic line at frequencies equal to an integral number of the spinning speed. In practice these are removed from the spectrum by spinning at high speeds (several kHz) so as to place the sidebands outside the region of interest. As CSA is proportional to field strength the spinning speed required to remove sidebands increases with higher field strengths.

3.3.2 CROSS POLARISATION VIA HARTMANN-HAHN MATCH

Cross-polarisation is used to transfer magnetisation from the proton nucleus to the carbon nucleus during the CP pulse sequence (Figure 3.11). This is achieved *via* the Hartmann-Hahn match of transmitter amplifiers (Hartmann and Hahn, 1962).

In the case of ^{13}C which is a low sensitivity and low natural abundance spin system, *S*, there is much to be gained by transfer of energy from the neighbouring high sensitivity, high abundance proton spin system, *I*. The principle of cross polarisation involves exciting the *I* spins followed by a spin lock period, by applying a continuous rf field, $\boldsymbol{B}_1$. During this time a second rf field, $\boldsymbol{B}_2$, is applied to the rare *S* spins such that when the Hartmann-Hahn condition is met, thermal contact between the two spins results in cross-polarisation from the *I* to *S* spins. The Hartmann-Hahn condition is met when

$$\gamma_S B_2 = \gamma_I B_1 \qquad \text{eqn. 3.16.}$$

which is achieved by matching the amplifier outputs of the ^1H and ^{13}C transmitters.

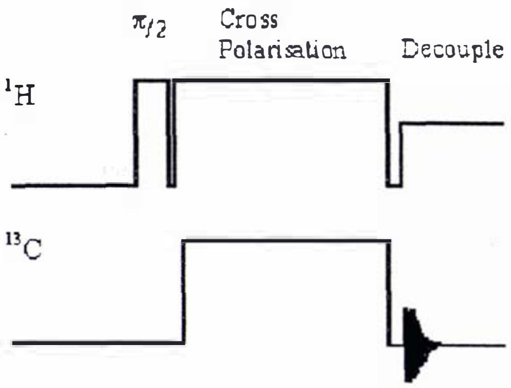

Figure 3.11. Pulse sequence for Cross Polarisation - Magic Angle Spinning (CP/MAS).

In instances where cross polarisation is inefficient it is necessary to use a direct observation sequence which can be combined with high power decoupling, and magic angle spinning, as illustrated in Figure 3.12.

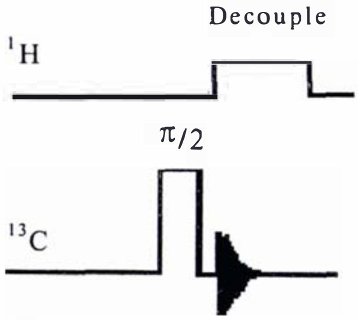

Figure 3.12. Pulse sequence for a single pulse high power decoupling experiment (HPDEC).

3.3.3 MAS OF QUADRUPOLAR NUCLEI

In the solid state, the spin interactions are dominated by dipolar effects and anisotropic chemical shifts. In the case of nuclei with spin quantum number $I \geq 1$, the NMR spectrum is further influenced by quadrupolar interactions. In this thesis we describe magic angle spinning NMR experiments of the nuclei ^{11}B ($I = {}^{3}/_{2}$) and ^{27}Al ($I = {}^{5}/_{2}$), in which quadrupolar effects dominate the line broadening. In consequence we briefly review the nature of the quadrupole interaction as it relates to experiments described in chapters six and eight.

When dealing with nuclei with spin quantum number $I \geq 1$, the solid state spectrum is dominated by quadrupolar effects, such as dipolar interactions, which give rise to line broadening, and anisotropic chemical shifts. These effects arise from the interaction of the nuclear charge with a non-spherical electric field gradient (Fyfe, 1983, Orendt, 1995). This can be expressed in terms of the quadrupole moment, *eQ*, and the electric field gradient tensor, $\mathbf{V} = \{V_{ab}\}$ where a, b = X, Y, Z (Mehring, 1982) and $|V_{ZZ}| \geq |V_{YY}| \geq |V_{XX}|$. Furthermore, the Laplace equation $V_{ZZ} + V_{YY} + V_{XX} = 0$ holds true for $\mathbf{V}$ (Man, 1995). Hence only two independent parameters are required:

$$\eta = \frac{V_{XX} - V_{YY}}{V_{ZZ}} \qquad \text{eqn 3.17.}$$

$$eq = V_{ZZ} \qquad \text{eqn 3.18.}$$

The asymmetry parameter, η, describes the deviation from axial symmetry of the electric field gradient, which in turn depends on the symmetry and chemical bonds of the quadrupolar nucleus and *eq* is the electric field gradient component in the principal axis.

If the electric field gradient is symmetric about the principal axis, V_{ZZ} will be unity, $V_{XX} = V_{YY}$ and $\eta = 0$. In solution state spectroscopy, the quadrupolar interaction is averaged to zero by the rapid tumbling of the molecule. Generally in a solid material, $V_{ZZ} \neq 0$ and hence the quadrupole interaction can provide valuable information about the symmetry of the site occupied by the nucleus.

There is an orientation dependence of the nuclear quadrupole, which is described (Fyfe, 1983) as:

$$\Delta E_Q = 3/8\left(\frac{e^2qQ}{h}\right)(3\cos^2\theta - 1 + \sin^2\theta\cos 2\varphi) \qquad \text{eqn 3.19.}$$

where ΔE_Q is the energy shift due to the quadrupole interaction, *eQ* is the quadrupole moment, *eq* the magnitude of the electric field gradient (EFG) and θ is the angle between the principal component of the electric field gradient tensor and the magnetic field vector. The collective term e^2qQ/h is known as the quadrupolar coupling constant (QCC). In solid materials when the quadrupolar nucleus is situated at a cubic site, which occurs in octahedral or tetrahedral symmetry, then $eq = 0$ by symmetry such that QCC = 0.

For spin-$\frac{1}{2}$ nuclei, in which only $m = -\frac{1}{2} \leftrightarrow \frac{1}{2}$ transitions are present, no electric quadrupolar effects are possible. For spin-half nuclei with $I = {}^{n}/_{2}$ (n = 3, 5, 7, ...), such as ^{11}B, other transitions are possible (e.g. $m = -\frac{3}{2} \leftrightarrow -\frac{1}{2}$, $-\frac{1}{2} \leftrightarrow \frac{1}{2}$ and $\frac{1}{2} \leftrightarrow \frac{3}{2}$) including the $m = -\frac{1}{2} \leftrightarrow \frac{1}{2}$ transition. This central transition is independent of the quadrupolar interaction to first order in ΔE_Q but is dependent to the second order in $(\Delta E_Q)^2/\Delta E_Z$ where ΔE_Z is the much larger Zeeman energy. These second order quadrupolar shifts are also sensitive to parameters such as quadrupolar coupling and asymmetry (Abragam, 1983; Woessner, 1986; Dec and Maciel, 1990). In the case of solid state NMR spectroscopy of quadrupolar nuclei, all NMR transitions are excited but only the central transition ($m = \frac{1}{2}$ to $m = -\frac{1}{2}$) is observed and it is unshifted by quadrupole interaction. Signals from the remaining transitions are shifted and cover a very wide range of frequencies and as such become lost in the baseline. Hence it is the second order quadrupole shifts which are observed. These are given (in the special case of $\eta = 0$) by equation 3.20 (Abragam, 1983).

$$\omega_Q = \left[\frac{3e^2qQ}{2I(2I-1)\hbar}\right]^2 \left[\frac{I(I+1)-\frac{3}{4}}{12\omega_0}\right] \left(6\cos^2\theta(1-\cos^2\theta) + \tfrac{3}{4}(1-\cos^2\theta)^2\right)$$

eqn 3.20.

The lineshape for such a signal arises from contributions at all polar angles. In the case of a non-zero asymmetry parameter a more complicated expression must be used. This expression is embedded in the lineshape fitting software used to fit the MAS NMR spectra obtained in this thesis[†].

[†] WinMAS/WinFIT, Bruker Analytik, Silberstreifen, D-76287 Rheinstetten, Germany

3.4 THEORY OF MAGNETIC RESONANCE IMAGING

Paul Lauterbur (1973) first demonstrated the application of NMR imaging by use of backprojection for image reconstruction while Mansfield and Grannell (1973) observed a two-dimensional image by acquiring an NMR signal in the presence of a switched magnetic field gradient. Ernst and co-workers proposed use of frequency encoding for magnetic resonance imaging in 1975 (Ernst 1975; Kumar *et al.*, 1975), but it wasn't until 1980 when Edelstein and co-workers demonstrated the technique by imaging of a human body that the power of the technique was fully appreciated (Bottomley *et al.*, 1983).

Development of NMR imaging was based on the omnipresence of water in biological samples. The high proton density presented by the water molecule and its relaxation behaviour makes it readily available for imaging. Techniques developed using proton imaging are now applied to a number of other biologically important nuclei (^{31}P, ^{23}Na).

3.4.1 MAGNETIC FIELD GRADIENT

Up to this point we have assumed a strong static magnetic field possessing only a z component. Magnetic resonance imaging techniques apply a linear or "constant" gradient to the static field so that it will change as a function of spatial coordinate (Figure 3.13). These gradients (of the order of tens of milliTesla per metre) are superimposed on the larger magnetic field (of the order of several Tesla). Due to the several orders magnitude difference in their field strengths, only those gradients with field components parallel to the static magnetic field impart spatial resolution to the resonance frequency (Kuhn, 1990).

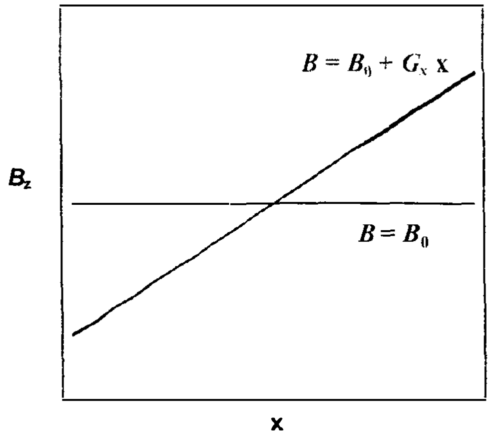

$$G_x = \frac{\delta B_z}{\delta x}$$

Figure 3.13. Magnetic field strength as observed in the *z*-axis as a result of an applied gradient.

A one-dimensional magnetic field gradient along the x-axis in a magnetic field, $\boldsymbol{B}_0$, indicates that the magnetic field is increasing in the x direction.

3.4.2 SLICE SELECTION

Slice selection in NMR imaging involves the selection of spins in a plane through the object and is achieved by applying a linear field gradient during the period that the excitation pulse is applied. Consider an object or body oriented along the z-axis parallel to the $\boldsymbol{B}_0$ field. A 90° pulse applied in conjunction with a z gradient will rotate spins, which are located in a slice or plane through the object. The width of the slice is proportional to the bandwidth of the rf pulse and the slope of the gradient, and is given by (Talagala and Lowe, 1991):

$$\Delta z = \Delta\omega / \gamma\, G_{slice} = \frac{2\pi\,\Delta f}{\gamma\, G_{slice}} \qquad \text{eqn 3.21.}$$

Note that the slice plane is normal to the gradient field direction.

The greater the bandwidth of the rf pulse or the weaker the gradient the wider the slice will be (Figure 3.14) for a fixed gradient strength (G_{slice}). Alternately, the greater the gradient strength, the greater the rf pulse bandwidth required for a similar thickness slice.

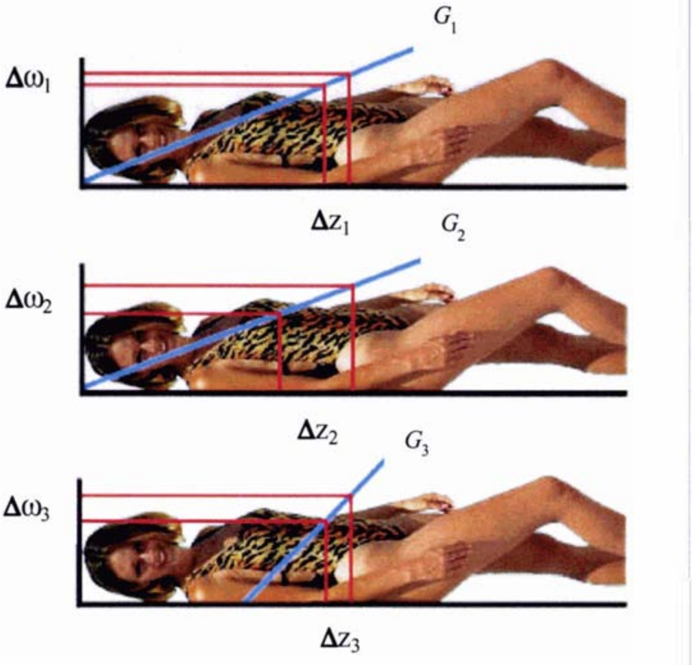

Figure 3.14. Schematic showing the relationship between excitation pulse bandwidth ($\Delta\omega$), gradient strength (G) and slice thickness (Δz).

3.4.3 FREQUENCY ENCODING

Frequency encoding uses a constant gradient during the acquisition of the NMR signal. Therefore the FID shows a regular off resonance behaviour (i.e. the phase of the signal evolves with constant angular velocity). This is demonstrated by considering three tubes of water placed along the x axis. If no gradient is applied each sample will experience the same external field. This results in three identical FIDs which would result in a spectrum with a single resonance. If a gradient, G_x, is applied, each tube will experience a different "local" external field, with the centre one on-resonance while the tube to the left experiences a smaller magnetic field and the one on the right a larger field. The resulting spectrum would show 3 resonances representing the 1D image of the samples separated in space (Figure 3.15).

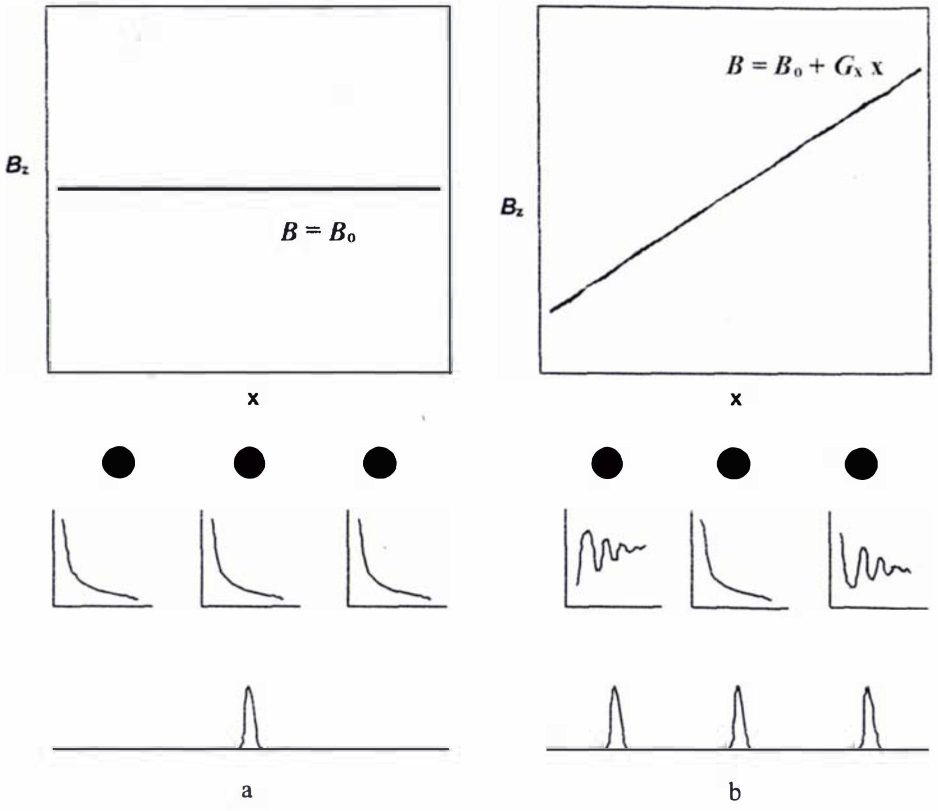

Figure 3.15. Signal observed from three spatially separated water-filled tubes (black dots), the individual FID for each tube and the resulting signal (a) without and (b) with an applied field gradient.

The result is a NMR spectrum with more than one signal. The amplitude of the signal is proportional to the number of spins in a plane perpendicular to the gradient. This procedure is called frequency encoding and causes the resonance frequency to be proportional to the position of the spin. This principle forms the basis behind most magnetic resonance imaging methods.

3.4.4 PHASE ENCODING

In a phase encoding experiment, the gradient amplitude is incremented prior to signal acquisition while the duration of the applied gradient is kept constant (Figure 3.16). The evolution of phase is now measured in a series of experiments where the phase shift increases with increasing gradient strength. With each change in gradient strength the field strength across the sample increases so that the angular velocity increases. If the gradient increment is chosen to be constant the phase evolution will show constant angular velocity in a manner similar to the frequency encoding experiment so that the result after Fourier transform will be the same.

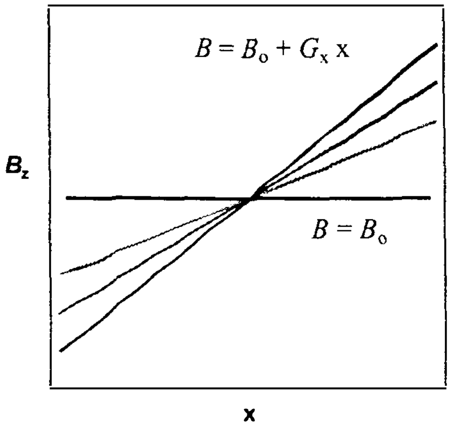

Figure 3.16. Schematic of a phase gradient ramp showing three varying gradient strengths.

While phase encoding takes longer to perform than frequency encoding, it does have the advantage of being able to introduce the additional gradient directions necessary for 2D and 3D imaging.

Consider the two dimensional case of a spatially separated 3 x 3 array of spins once the slice selection has removed the third dimension. After the initial slice selective pulse a phase encoding gradient is applied. This has the effect of changing the phase of the spins in one dimension. If another gradient, orthogonal to the first, is applied, the frequency encoding gradient, this has the effect of altering the frequency of precession according to the gradient strength experienced with the net effect of dephasing the spins in a second dimension (Figure 3.17).

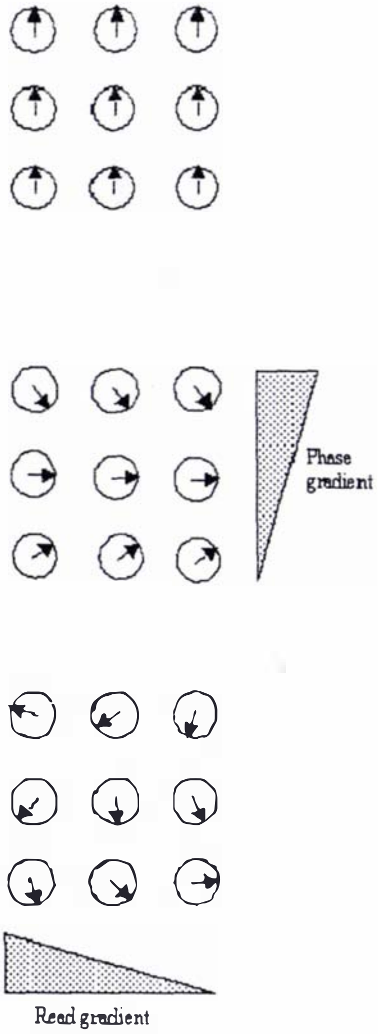

Figure 3.17. Schematic showing effect of orthogonal read and phase gradients on the angular momentum of spatially separated spins.

3.4.5 IMAGE CONTRAST

In order to visualise morphological structures in a magnetic resonance image there must be image contrast brought about by a difference in signal intensity between the adjacent structures. In the case of NMR imaging this contrast is brought about by differences in the spin density and the relaxation times T_1 and T_2 between adjacent morphological structures. Judicious selection of certain acquisition parameters enables image contrast to be maximised. The signal intensity, S, is determined by the signal equation for the specific pulse sequence used (Kuhn, 1990).

In the case of the spin-echo experiment:

$$S = \rho\left(1-\exp\frac{-T_R}{T_1}\right)\exp\frac{-T_E}{T_2} \qquad \text{eqn. 3.22.}$$

Appropriate choice of values for the echo time (T_E) and repetition time (T_R) should enable image weighting in favour of either the spin density (ρ) or one of the relaxation times T_1 and T_2.

For the gradient echo experiment:

$$S = \rho\frac{\left(1-\exp\frac{-T_R}{T_1}\right)\exp\frac{-T_E}{T_2}\sin\theta}{1-\exp\frac{-T_R}{T_1}\cos\theta} \qquad \text{eqn 3.23.}$$

Once again varying the echo time (T_E), repetition time (T_R) or the excitation angle (θ) it is also possible to produce images of varying image contrast.

The spin density is the concentration of signal producing spins of a certain species such as water protons or lipid protons in a defined volume element. Images showing spin density contrast can reflect the relative concentration of species.

Magnetic resonance images are often referred to according to the weighting applied to produce the contrast in an image. Images whose contrast is predominantly caused by differences in T_1 are referred to as T_1-weighted images. Similarly for T_2 and ρ, the images are called T_2-weighted and spin density weighted images. Table 3.2 contains the set of conditions necessary to produce weighted images.

Table 3.2. Relationship between T_R and T_E values and image weighting.

Weighting	T_R Value	T_E Value
T_1	$\leq T_1$	$<< T_2$
T_2	$>> T_1$	$\geq T_2$
ρ	$>> T_1$	$<< T_2$

3.4.6 GENERIC IMAGING SEQUENCES

3.4.6.1 Spin-Echo Imaging

An advantage of using a spin-echo sequence (Figure 3.18) is that it introduces T_2 dependence to the signal. A slice-selective 90° pulse is applied in conjunction with a slice selection gradient, followed by a delay time ($T_E/2$) after which a 180° pulse is applied in conjunction with a slice selection gradient. During the period between the 90° and 180° pulses a phase encoding and frequency encoding gradient are applied for spatial selection. A further period $T_E/2$ elapses at which time the echo is refocussed and the signal acquired.

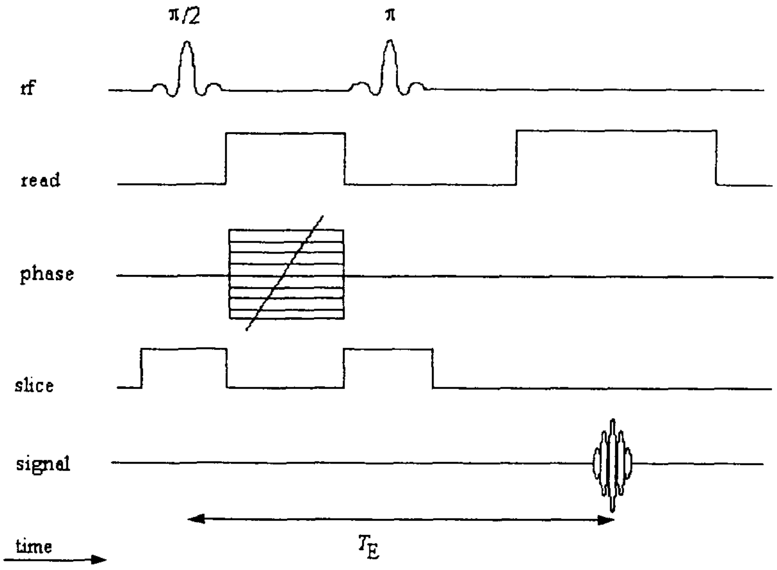

Figure 3.18. Generalised pulse sequence for spin echo imaging.

The entire sequence is repeated after a recycle delay (T_R) until all the phase encoding steps have been recorded.

3.4.6.1.1 T_2 Mapping via Multi Echo Sequence

An extension of the spin echo sequence enables collection of a series of images taken from a series of equally spaced echoes that decay over time. A standard multi-slice, multi-echo (MSME) sequence is employed whereby a series of 180° pulses are applied in a pulse train which refocusses the echo with diminishing intensity (Figure 3.19). A series of images are produced with increasing echo times (they increase as a multiple of the primary echo time). A T_2 map can be produced by fitting the decay for each pixel in the image with respect to the series of decaying intensity images.

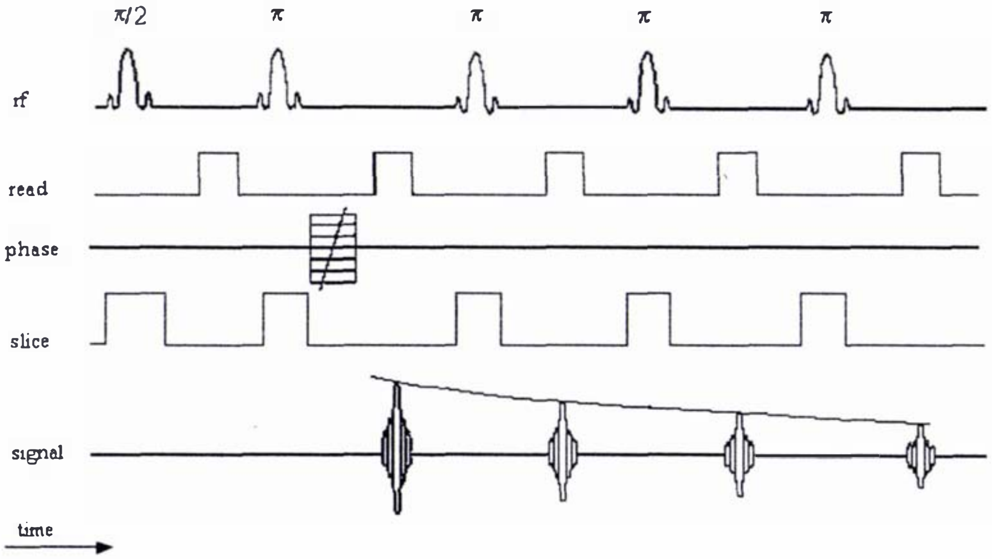

Figure 3.19. Multi slice multi echo imaging sequence for T_2 mapping (illustrated for a single slice).

3.4.6.2 Gradient Echo Imaging

Spin echo imaging sequences suffer from one major disadvantage. For maximum signal, they require the transverse magnetisation to recover to its equilibrium position along the z axis before the sequence is repeated. If T_1 is long, this can significantly lengthen the imaging sequence. If the magnetisation does not fully recover to equilibrium the signal is less than if full recovery occurs. If the magnetisation is rotated by an angle, θ, less than 90° its $\boldsymbol{M}_z$ component will recover to equilibrium much more rapidly, but there will be less signal since the signal is proportional to $\sin\theta$. Therefore there is a trade-off between signal intensity and the time taken for image acquisition.

In order to obtain the optimum signal to noise ratio within the minimum time period it is possible to use low angle excitation pulses according to the Ernst angle (Ernst, 1966). If an approximate T_1 value is known then equation 3.24 can be used to optimise the repetition time for a given angle of tip.

$$\cos \alpha_E = \exp(-T_R/T_1) \qquad \text{eqn 3.24.}$$

While a distribution of T_1 values are present in a sample undergoing imaging, the Ernst angle is useful in deriving approximate settings for pulse angle and recycle times. The spin echo sequence however is reliant on a 90° excitation pulse in order to enable refocussing of the echo *via* the π pulse and as such cannot take advantage of low tip angle optimisation. Gradient echo imaging overcomes these limitations. In the gradient echo imaging sequence (Figure 3.20) a slice-selective rf pulse is applied along with a slice selection gradient.

Following the excitation pulse, a phase encoding gradient and a dephasing frequency encoding gradient are simultaneously applied. In order to refocus the spins to produce an echo, rather than using a π refocussing pulse as per the spin echo sequence, a second frequency encoding gradient is applied *in the negative sense to that which was earlier applied.* An echo is produced when the frequency encoding gradient is turned on because this gradient refocuses the dephasing which occurred from the dephasing read gradient. The phase encoding gradient is varied in equal steps between G_{max} and $-G_{max}$ during the full course of the experiment.

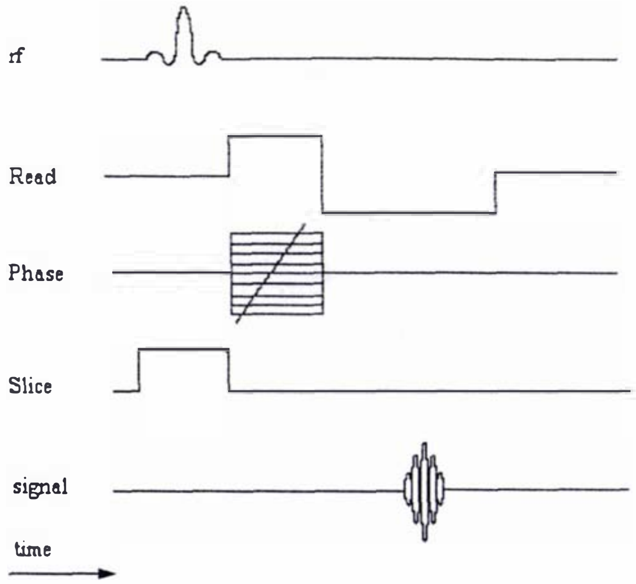

Figure 3.20. Gradient echo imaging pulse sequence.

In this instance the refocussing is not dependent on magnetisation being in the x-y plane and so low tip angle excitation pulses can be used and optimised according to the Ernst angle. This allows a much more rapid repetition rate to be used and as such the T_R period could be as short as tens of milliseconds.

3.4.6.3 3-D Imaging

In order to perform 3D imaging a second phase encoding gradient, orthogonal to the read gradient and the first phase gradient is applied (Figure 3.21). No slice selective pulse is employed.

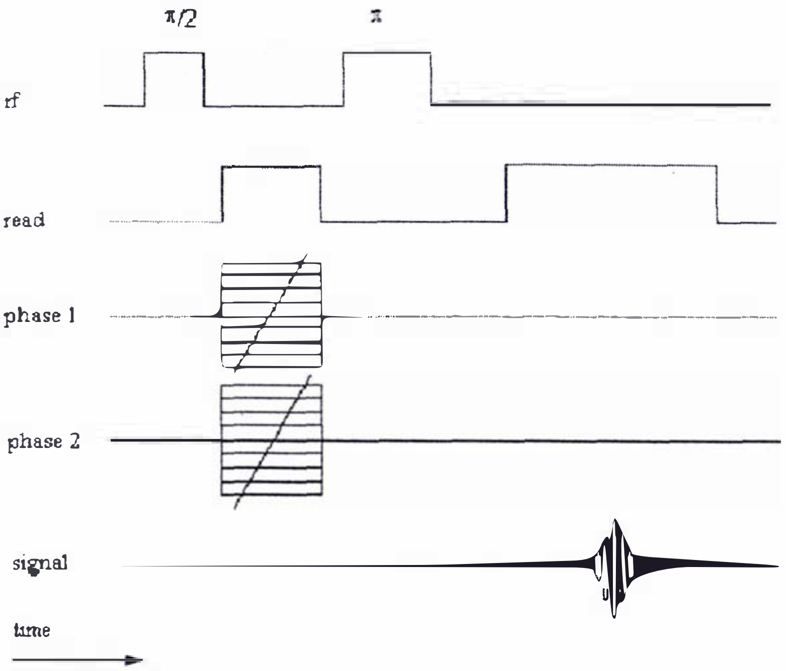

Figure 3.21. Generic pulse sequence for 3D spin echo imaging.

A volume selective rf pulse and gradient rotates only those spins in the imaged volume of the object. This combination of pulses is equivalent to a slice selection combination except the slice thickness can be of the order of 10 or 20 cm. The volume selection pulse is followed by a phase encoding gradient in first dimension and another one in the second dimension. They are applied simultaneously and are cycled through all possible combinations. The frequency-encoding gradient has its dephasing lobe negative to cause the spins to be in phase at the centre of the echo. A frequency-encoding gradient is then applied and a signal recorded.

3.4.6.4 T_1, T_2 and ρ Images

The spin-lattice relaxation time (T_1), spin-spin relaxation time (T_2), and the spin density (ρ) are properties of the spins in a sample. The calculation of T_1, T_2, or ρ starts with the collection of a series of images. For example, if it was required to produce a T_2 image, a spin-echo pulse sequence is used and a series of images are recorded with varying T_E. The signal intensity for a given pixel can be extracted and plotted for each T_E value and the best fit from the T_2 relaxation equation drawn through the data to find T_2.

A T_1 image can be created from the same pulse sequence using a series of images with varying T_R. The signal for a given pixel can be plotted for each T_R value and the best fit line from the T_1 relaxation equation drawn through the data to find T_1. The spin density can be calculated once T_1 and T_2 are found using the spin echo signal equation and any spin echo signal.

3.5 DIFFUSION

3.5.1 MOTION OF WATER

We must first understand the types of motion that water molecules are able to undergo. One type of motion is simply the tumbling of water molecules caused by rotational motion (rotational diffusion). The second type is that of translational movement (translational diffusion) of the molecule. Rotational diffusion modulates both intra- and inter-molecular dipolar interactions whereas translational diffusion *only* affects the inter-molecular dipolar interactions between protons of different water molecules. The Einstein-Smolumchowski relation (Einstein, 1905, 1908, von Smoluchowski, 1906) describes the 3-dimensional diffusion of a molecule according to:

$$D = \frac{L^2}{6t} \qquad \text{eqn 3.25.}$$

Where L = mean square displacement or diffusion length and t = time since start of the diffusion.

3.5.2 DIFFUSION MEASUREMENT VIA PFGSE

In a pulsed field gradient spin echo (PFGSE) experiment (Stejskal and Tanner, 1965), two gradient pulses of duration δ and amplitude G are applied respectively in the dephasing and re-phasing periods of the spin echo sequence (Figure 3.22). As a result the echo is encoded with phase shifts which reflect the displacements of the spins over the time (Δ) between the gradient pulses. Diffusion causes a spread in the phase and hence attenuation of the echo intensity.

The resulting echo decay curve is then fitted using a non-linear least-squares fitting procedure. For bulk water at normal temperatures, the PGSE method works well with moderate gradients. However, when the diffusion coefficient, D, is significantly lower, higher gradient magnitudes, longer gradient pulses or longer gradient pulse separations are needed to attenuate successive echoes significantly and hence fit the data with confidence. Thus the gradient duration eventually needs to be increased also, resulting in an increased echo time and loss of signal due to T_2 relaxation. Since samples with low diffusion coefficients also commonly have low T_2 values, the PGSE technique quickly becomes impractical.

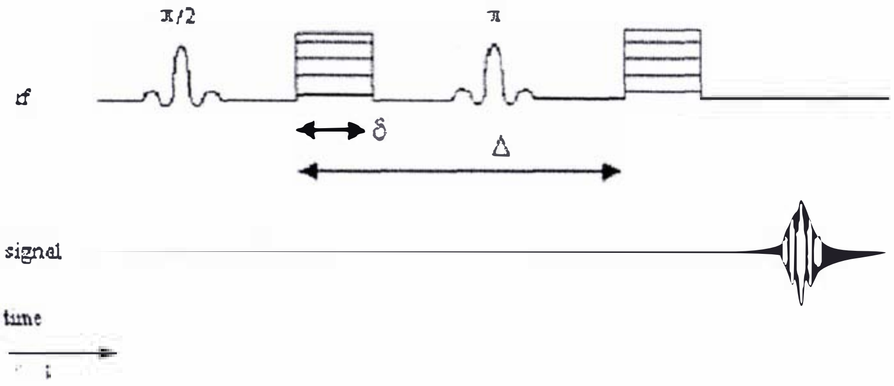

Figure 3.22. Pulsed field gradient spin echo (PFGSE) pulse sequence.

Assume two spins are at positions at z_1 and z_2 during the first gradient and second gradient respectively. This sharp definition requires that the gradient pulse duration δ is very short. In this case the phase shifts occurring during the gradient pulses are:

$$\phi_1 = \gamma G \delta z_1 \quad \text{and} \quad \phi_2 = \gamma G \delta z_2 \qquad \text{eqn 3.26.}$$

Then the resulting signal is:

$$S = S_0 \exp(i(\phi_2 - \phi_1)) \qquad \text{eqn 3.27.}$$

In free diffusion the probability of finding a spin initially at position z_1, at position z_2 after time Δ is given by:

$$P(z_1 - z_2) = \frac{1}{\sqrt{4\pi D\Delta}} \exp\left(\frac{-(z_1 - z_2)^2}{4D\Delta} \right) \qquad \text{eqn 3.28.}$$

where D is the self diffusion coefficient.

Integrating across all values of z gives rise to

$$S(G) = S_0 \exp(-(\gamma\, G\, \delta)^2\, D\, \Delta) \qquad \text{eqn 3.29.}$$

For finite durations of δ, the Stejskal and Tanner equation (1965) can be expressed as;

$$S(G) = S_0\, e^{-\gamma^2 G^2 D \delta^2 (\Delta - \frac{1}{3}\delta)} \qquad \text{eqn 3.30.}$$

Allowing for relaxation effects during the period T_E, this equation can be rewritten:

$$S(T_E, G) = S_0\, e^{-T_E/T_2}\, e^{-\gamma^2 G^2 D \delta^2 (\Delta - \frac{1}{3}\delta)} \qquad \text{eqn 3.31.}$$

If the echo time is kept constant, incrementing the amplitude of G, enables the measurement of the self-diffusion coefficient, D. The Stejskal-Tanner equation can then be simplified to:

$$S(b) = S_0'\, e^{-bD} \qquad \text{eqn 3.32.}$$

where $b \equiv \gamma^2 G^2 \delta^2 (\Delta - \frac{1}{3}\delta)$ eqn 3.33.

and $S_0' = S_0\, e^{-T_E/T_2}$ eqn 3.34.

3.5.3 DIFFUSION WEIGHTED IMAGING

Diffusion weighted imaging investigates the self diffusion of water during the period between two narrow gradient pulses. The generic pulse sequence used for diffusion imaging is shown in Figure 3.23.

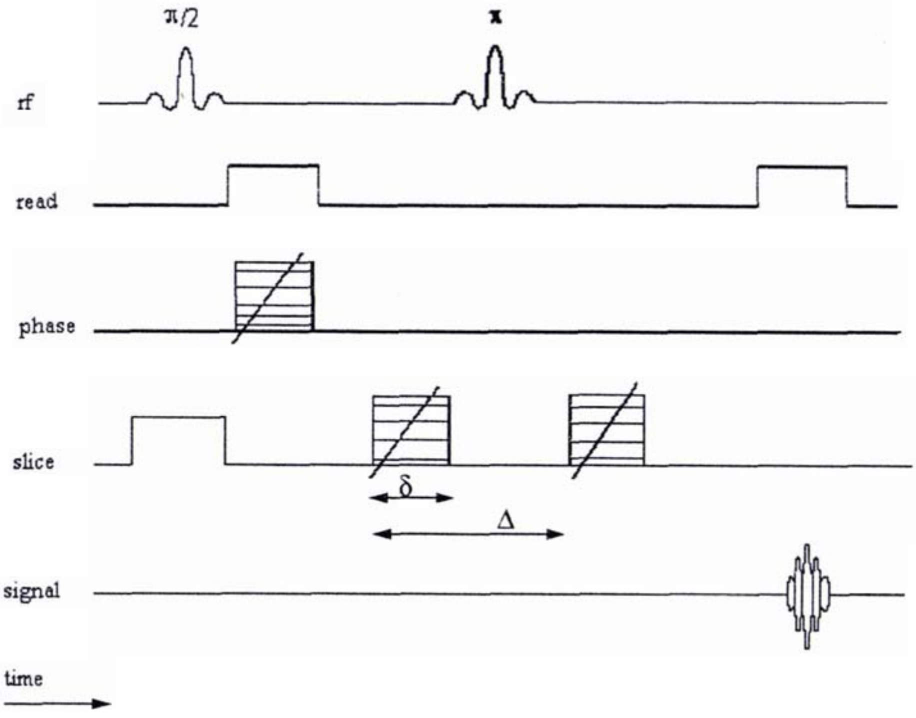

Figure 3.23. Diffusion weighted imaging pulse sequence.

This sequence is not however the sequence used in this study as it interleaves both the diffusion and imaging gradient pulses. The actual sequence used in this study is that shown in Figure 3.24, where the spin excitation is achieved by initial diffusion weighting using a standard PFGSE sequence. The diffusion weighted spins are then spatially encoded using a slice selective 180° soft refocussing pulse and phase and frequency encoded readout.

This second approach to diffusion weighted imaging has the advantage that it separates the imaging gradients from the diffusion gradients, thereby reducing cross-term effects, and allowing independent variation of the experimental parameters associated with diffusion imaging. While it is possible to calculate the contribution of the cross-terms, the approach taken is considered more robust and quantitative.

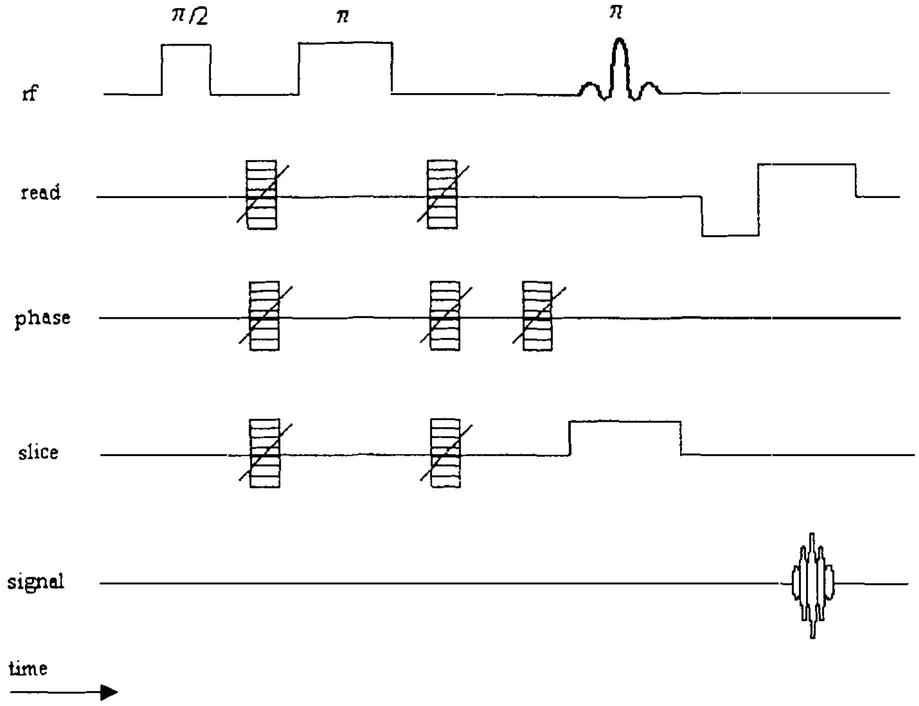

Figure 3.24. Modified dffusion weighted imaging pulse sequence showing the diffusion editing sequence separated from the spatial imaging sequence. The diffusion editing gradients are applied as linear combinations according to Table 3.3.

3.5.3.1 Diffusion Tensor and Diffusion Anisotropy Imaging

When the diffusion is anisotropic, the Stejskal-Tanner equation is modified so that the term G^2D in the exponent becomes $\underline{G}\cdot\underline{\underline{D}}\cdot\underline{G}$, where $\underline{G}$ is the gradient vector and $\underline{\underline{D}}$ is the diffusion tensor. Generally diffusion anisotropy is reflected in different diffusion coefficients D_{11}, D_{22} and D_{33} in some orthogonal principal axis frame of the sample. In this case the diffusion tensor is given by:

$$\boldsymbol{D}_p = \begin{bmatrix} D_{11} & 0 & 0 \\ 0 & D_{22} & 0 \\ 0 & 0 & D_{33} \end{bmatrix} \qquad \text{eqn 3.35.}$$

However, when imaging gradients are applied, the x, y, z axes of the gradients will not necessarily be coincident with the 1,2,3 axes of the sample, but will instead be related by a rotation matrix $\boldsymbol{R}$. Thus $\boldsymbol{D}$ must be rewritten in the gradient axis frame as

$$\boldsymbol{D} = \underline{R} \cdot \underline{\underline{D}} \cdot \underline{R}^{-1}$$

$$= \begin{bmatrix} D_{xx} & D_{xy} & D_{xz} \\ D_{yx} & D_{yy} & D_{yz} \\ D_{zx} & D_{zy} & D_{zz} \end{bmatrix} \qquad \text{eqn 3.36.}$$

Note that $\boldsymbol{D}$ is now off-diagonal.

There are many factors influencing the rate of diffusion. In structured material such as wood, these barriers are largely due to the nature and alignment of the tracheid cells themselves. In living wood cells there is active transport of water along the length of the cell during transpiration, whereas there are barriers to transverse movement. As such the diffusion rates are not equal in all directions, so the diffusion is said to be *anisotropic*. Measurement of the diffusion anisotropy can highlight restriction to diffusion, which may in turn be related to structural morphology and function.

The tracheid cells found in *Pinus radiata* are long (1-4 mm) with cell diameters *ca.* 20-30 μm. If the time over which diffusion is measured in a PFGSE sequence were sufficiently short, so that diffusion is not restricted by encounters with physical barriers, then the observed diffusion coefficient would become dependent on other factors such as the viscosity of the cell protoplasm (η), the temperature (T) and the radius (r) of the diffusing molecules as given by the Stokes-Einstein equation:

$$D = \frac{k_B \mathrm{T}}{6\pi \,\mathrm{r}\eta} \qquad \text{eqn 3.37.}$$

where k_B is the Boltzman constant. However, restrictions resulting from cell boundaries will cause D to differ according to the direction of diffusion. In wood, diffusion along the length of the cell D_{33} is likely to be less restricted than diffusion in the transverse directions D_{11} and D_{22}. The signal from the PFGSE diffusion sequence will thus be dependent on the direction of the diffusion-encoding gradient relative to the cell orientation.

In a practical PFGSE experiment, gradients applied along the x, y and z directions will sample respectively the diagonal elements D_{xx}, D_{yy} and D_{zz} of the diffusion tensor. In order to sample the off-diagonal elements, gradients need to be applied in oblique directions *via* linear combinations of G_x, G_y and G_z. As the diffusion tensor is symmetric about the leading diagonal (D_{xy} = D_{yx} *etc.*) only six combinations of gradients G_e need to be determined, while a seventh provides the average of all the gradients. They are presented in Table 3.3.

Table 3.3. Coefficients of gradient amplitude for linear combination of gradients applied to generate a series of diffusion weighted images for diffusion tensor imaging.

Diffusion Tensor	G_x	G_y	G_z
D_{xx}	1	0	0
D_{yy}	0	1	0
D_{zz}	0	0	1
D_{xy}, D_{yx}	$1/\sqrt{2}$	$1/\sqrt{2}$	0
D_{xz}, D_{zx}	$1/\sqrt{2}$	0	$1/\sqrt{2}$
D_{yz}, D_{zy}	0	$1/\sqrt{2}$	$1/\sqrt{2}$
D_{xy}, D_{xz}, D_{yz}	$1/\sqrt{3}$	$1/\sqrt{3}$	$1/\sqrt{3}$

3.6 INSTRUMENTATION

All Fourier transform NMR spectrometers, whether they are used for spectroscopy or imaging, utilise a common design. Observation of a NMR signal relies on interaction between the atomic nucleus and applied radio frequency pulses in an external magnetic field. This section will examine the key components of a NMR system.

3.6.1 THE MAGNET

The heart of all NMR spectrometers is the magnet. While earlier systems were based on resistive magnets which approached 1.5 T in field strength, today's modern spectrometers are based on cryogenic superconducting technology with field strengths reaching an order of magnitude higher field. A cut-away schematic of a cryogenic magnet is shown in Figure 3.25.

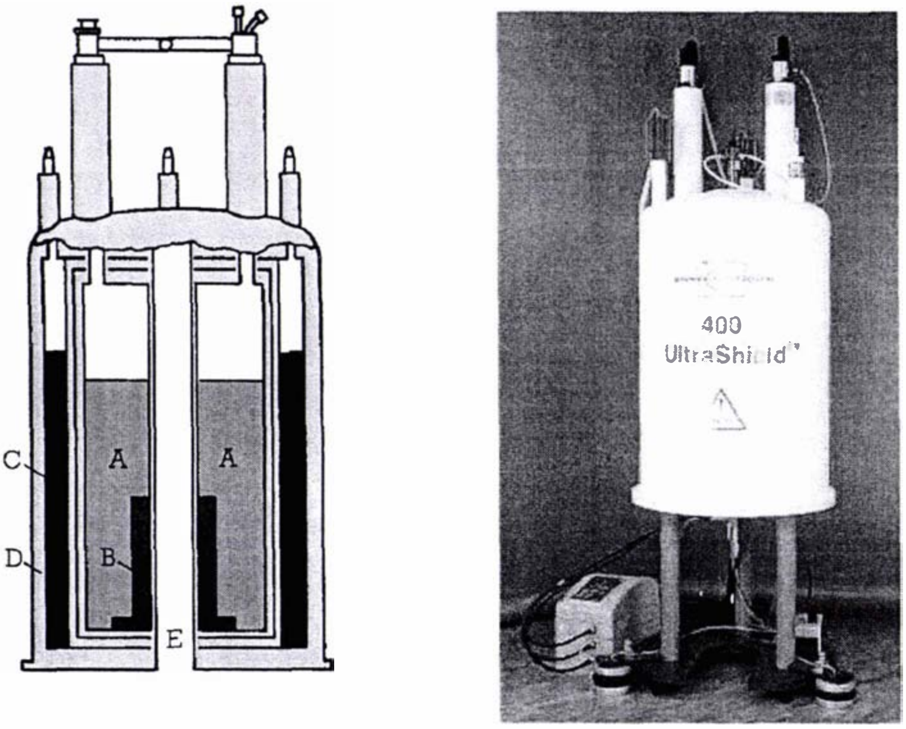

Figure 3.25. Schematic cut-away of a cryogenic magnet (left) showing (a) the liquid helium can, (b) the superconducting coil, (c) the liquid nitrogen can, (d) the vacuum space and (e) the room temperature bore into which the room temperature shim coils and probehead fit. The right hand figure shows a commercial 400 MHz (9.4 T) magnet.

3.6.2 NMR PROBE

The NMR probe is designed to sit in the centre of the $\boldsymbol{B}_0$ magnetic field. It houses the rf coil assembly and has provision to contain the sample, generally in a tube or rotor in the case of spectroscopy or contained inside the coil assembly itself in the case of imaging.

The coil must be capable of generating a $\boldsymbol{B}_1$ field and of observing the resultant signal or free induction decay (FID). This requires that once the transmit pulse train is completed, the rf coil must be switched from transmit to receive mode which is achieved by a fast-switching duplexor.

3.6.2.1 Radio-frequency Coils

The rf coil is central to the selectivity and sensitivity of a NMR spectrometer and can be one of two generic types, the solenoid type and the larger saddle coils which are found on most spectrometers where larger sample size is required.

3.6.2.1.1 Solenoids

The simplest form of rf coil is a solenoid of the type shown in Figure 3.26, although its use is limited in modern NMR spectrometer systems equipped with cryogenic superconducting magnets. The one application where it is still found is in microimaging of small samples (typically 2 – 5 mm) as they are simple to construct in comparison to other coil designs (Peck *et al.*, 1995).

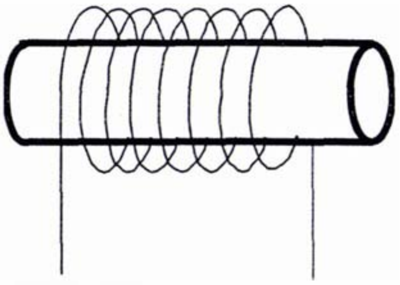

Figure 3.26. Schematic of a solenoid coil.

Today, solenoid coils are also commonly found in solid state stator systems as shown in Figure 3.27.

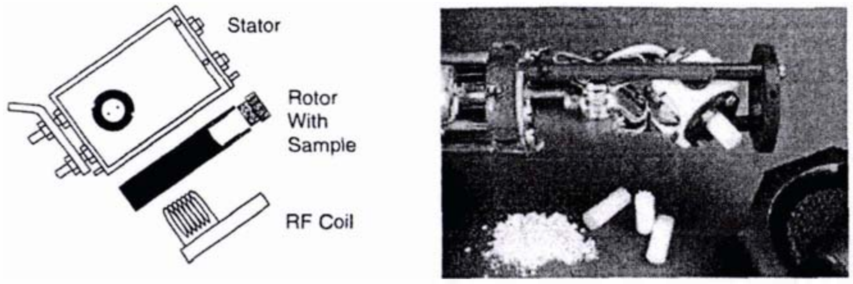

Figure 3.27. Schematic of a solid state rotor system (left) and probehead assembly (right).

3.6.2.1.2 *Saddle Coils*

Saddle coils (Figure 3.28) are commonly used in NMR spectroscopy and imaging due to the fact that the sample volume is parallel to the magnet bore in superconducting magnets, enabling ease of sample loading.

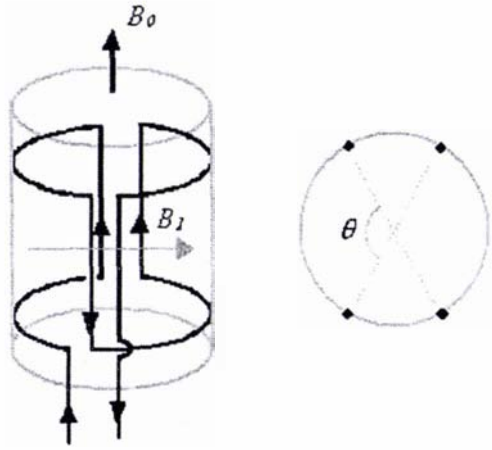

Figure 3.28. Schematic of a saddle coil showing direction of the B_1 field. The optimum performance of the coil is achieved when angle $\theta = 120°$.

In order to maximise homogeneity in the B_1 field the current density around the cylinder should vary as $J = J_0 \cos\theta$. This condition is only met at four points where the vertical sections of the coil are located. More typically in imaging situations this design of coil is made using sheet copper or aluminium for the vertical elements.

3.6.2.1.3 *Bird Cage Resonators*

Bird Cage resonators aim to describe a larger number of points on the cosine curve describing the current density and are commonly found in use on larger volume imaging systems (as is the case on the Tecmag/Oxford 200 system).

Flat sheet elements are arranged in parallel, separated by capacitors, which act to generate a phase shift between adjacent elements. If the total phase shift around the coil sums to 360° then constructive interference occurs and the device resonates (Hayes *et al.*, 1985).

3.6.3 SPECTROMETER CONSOLE

The console contains frequency generators and amplifiers for the generation of the rf pulses needed to perturb the nuclear spins. It also contains modules to generate accurate timing signals to trigger the pulse sequences, gradient amplifiers and controllers to generate the gradients required for imaging, temperature control units and shim control units. It is however the generation of pulses that is essential to the operation of NMR and a schematic showing the components of the observe channel is shown in Figure 3.29.

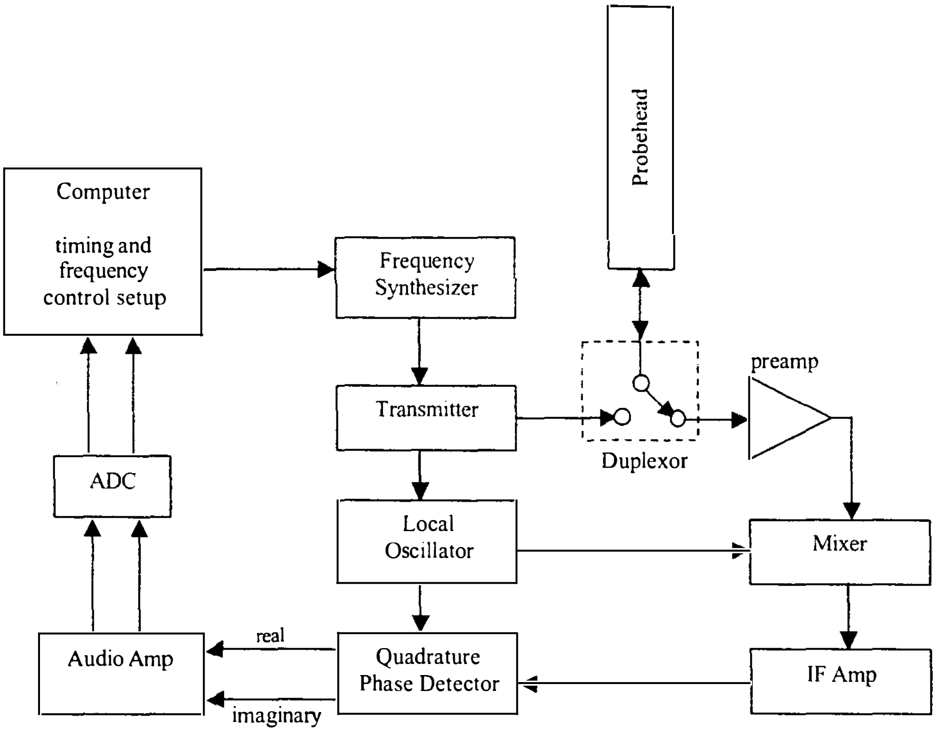

Figure 3.29. Schematic showing operational modules of the observe channel (adapted from Braun *et al.*, 1996).

4. MULTIVARIATE ANALYSIS

The purpose of models is not to fit the data but to sharpen the question.
Samuel Karlin

An attempt will be made during the course of this study to use NMR spectral and relaxation data to predict certain drying behaviour of radiata pine wood. Analysis of the spectral data requires some means of reducing the spectra to a manageable size. This is achieved by use of multivariate statistics, in particular principal component analysis (PCA) and projection to latent structures (PLS). The results of application of PLS regression to predicting the propensity for internal check formation in radiata pine will be presented in section 7.5.

4.1 PRINCIPAL COMPONENT ANALYSIS AND PROJECTION TO LATENT STRUCTURES

The purpose of using any multivariate analysis method is to reduce the degree of complexity in a data set to a more manageable size and aid interpretation. Calibration of spectral data from FTIR, NIR or NMR requires the correlation of the intensity of spectral responses (be they absorbances or resonances) with known data from classic reference methods such as concentration. In order to handle the large number of spectral responses a statistical approach must be adopted. The general prediction notation $Y = f(X)$ will be adopted where Y is the estimated or predicted variable and X is the predicting variable. The matrix containing the digitised spectra for all the samples becomes the **x**-matrix against which we regress the matrix containing the analytical results for a range of properties (variables) on all the samples (objects); this becomes the **y**-matrix.

Simple linear regression of single responses in spectra should not be used as it presupposes that the remaining spectral data do not contribute to the variation in absorbance intensity. Likewise, stepwise linear regression suffers from the limitations that (i) spectral absorbances must be linearly dependent on the analyte concentration (or property value) and (ii) the spectral absorbances may not overlap. The most constraining feature however, is that the number of calibration samples ***must*** be greater than the number of spectral bands used.

By using data-reducing multivariate techniques such as principal component analysis and projection to latent structures it is possible to use all the spectral data in the analysis. Furthermore there is no restriction on the sample size, which may be less than the number of absorbances used.

Principal components analysis (PCA) is a well documented procedure (Hotelling, 1937; Wold *et al.*, 1983; Wold, 1987; Martens and Næs, 1989; Everitt and Dunn, 1991) by means of which the variation in a set of multivariate data is described in terms of a new set of uncorrelated linear combinations of the original, uncorrelated variables. The aim is to simplify the sources of variation, by grouping correlated variables within a data matrix into a new set of variables termed principal components.

The original data matrix X can then be expressed as

$$X = 1 \cdot \bar{x} + TP' + E \qquad \text{eqn 4.1.}$$

where X is the original data matrix containing n_s samples (or objects) each with n_v variables, $\bar{x}$ is the mean, T is the scores matrix, P′ is the transpose of the loadings matrix and E is the residuals matrix representing the noise in the data. The scores matrix contains information about relationships among the objects and the loadings matrix contains information about relationships among the variables.

The first step in multivariate analysis is to minimise the data set by means of Z-scoring the data by first column-centreing and then (auto)scaling the data matrix. That is to say, the individual elements of the matrix are firstly mean centred (by subtracting the column/variable mean from the value) and then scaled by dividing each element's value by its standard deviation (Meglen, 1992). For example the following matrix transformation would arise from Z-scoring the X matrix:

$$X = \begin{pmatrix} 0.0002 & 1.0 \\ 0.0003 & 2.0 \\ 0.0004 & 3.0 \end{pmatrix}$$

For the first variable (column) the mean is 0.0003 and the standard deviation is 0.0001, and the second variable has a mean of 2.0 and a standard deviation of 1.0. Then the corresponding Z-scored matrix will be

$$Z = \begin{pmatrix} -1.0 & -1.0 \\ 0.0 & 0.0 \\ 1.0 & 1.0 \end{pmatrix}$$

Next the eigenvalues of the matrix are extracted. This is performed by finding the transformation matrix, which will rotate the coordinate system such that the new primary axis lie along the maximum variance, with successive, orthogonal axes describing further variance Figure 4.1.

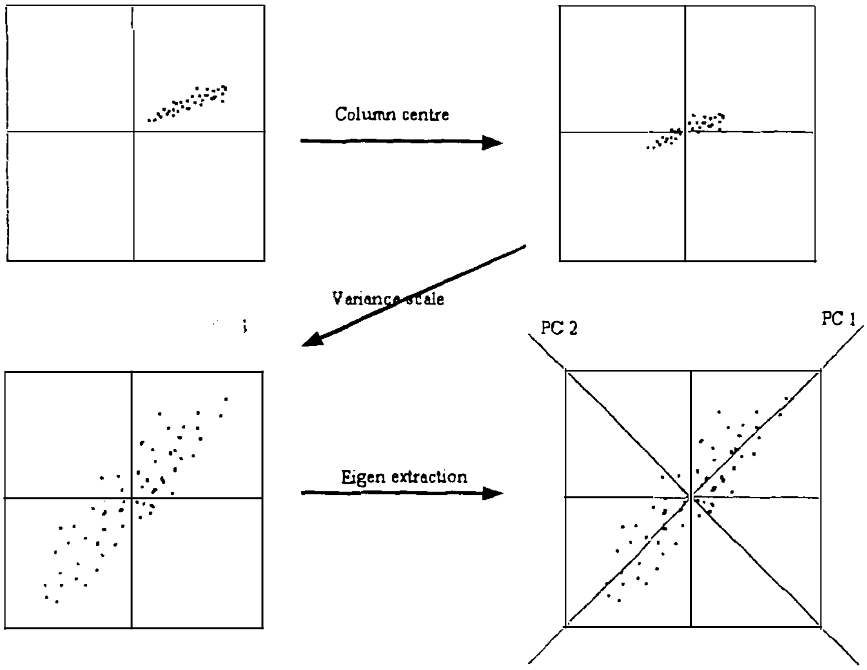

Figure 4.1. Graphical representation of Z-scoring and Eigen extraction during principal component analysis. (Adapted from Meglen, 1991).

The majority of the variance in the data is explained in the first principal component, the next greatest amount of variance is explained in the second principal component and so on.

The resultant prediction equation is a linear combination of the principal components (Meglen, 1991).

$$x_i = b_0 + b_1 \cdot t_{i1} + b_2 \cdot t_{i2} + \ldots + b_k \cdot t_{ik} + e_1 \qquad \text{eqn 4.2.}$$

where t_{ik} is the k^{th} score associated with the i^{th} object, and b_k is the model parameter estimated by the calibration (Thomas, 1994). Knowledge of the causal relationship between **x** and **y** is not necessary as the model is based on calibration only.

Projection to latent structures (PLS) regression results in a linear prediction equation, which projects into a space determined by both regressor and dependent variables. This space contains the information in the regressor variables that is relevant for explaining variation in the dependent variable while leaving the remaining potential regressor variation unused. In PLS regression both the X and Y matrices are decomposed separately in order to describe the key variances within the individual matrices as principal components (or latent variables). In this case the X matrix contains the spectral or measured variables with the signal intensity at individual chemical shifts being the variables, and Y contains the dependent variables for prediction, usually concentration or a physical property.

Once the individual matrices have been decomposed the resultant latent variables can be regressed. More detailed information about PLS and its comparison with PCR can be found in Wold *et al.* (1983), Naes *et al.* (1986), Martens and Næs, (1989) and Tabachnik and Fidell (1989).

The absolute error in the predicted value is given by the standard error of prediction (SEP), which is defined as:

$$\mathrm{SEP} = \sqrt{\frac{\sum_{i=1}^{n}(c_i - \hat{c}_i)^2}{n}} \qquad \text{eqn 4.3.}$$

where c_i is the actual property value and $\hat{c}_i$ is the predicted property value for n samples.

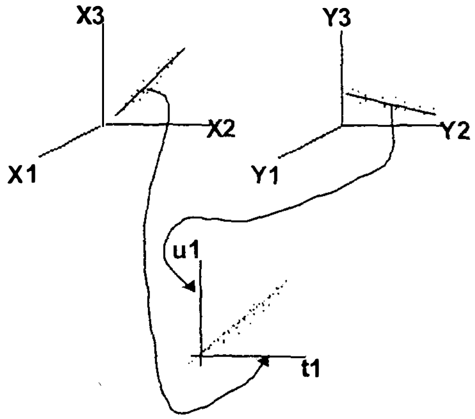

Figure 4.2. Graphical representation of PLS regression. In each of X and Y space the principal components of the data are related by a linear model. (adapted from Wallbäcks, 1991).

NB In keeping with increasing convention the term PLS-2 will be used to describe partial least squares projection to latent structures (or simply projection to latent structures) as this better describes the method than partial least squares regression. The reason for this is to avoid confusion with the older statistical method (partial least squares - PLS-1), which is just a stepwise linear regression *that does not* take colinearity into consideration and is therefore less robust.

4.2 APPLICATION OF PCA AND PLS TO WOOD PROPERTY PREDICTION

Multivariate analysis is rapidly gaining acceptance as an analytical method. Both PLS and PCA of NIR spectra is considered by the Association of Official Analytical Chemists (AOAC) as an official method for the analysis of crude protein and acid detergent fibre in forage analysis (Barton and Windham, 1988; Barton, 1991).

Most literature dealing with the development and application of multivariate analysis for wood related systems, has concentrated on the prediction of pulp properties from FTIR, NIR and NMR spectroscopy (Wallbäcks *et al.*, 1991a-c, Meder *et al.* 1994). The majority of work has focused on the comparatively rapid techniques of FTIR and NIR (Easty *et al.*, 1990; Backa and Brolin, 1991; Michell 1994, 1995; Meder *et al.*, 1999 to cite but a few).

It is most likely due to the homogeneity of the sample that the majority of work has been performed on the pulp matrix.

Very little work has been reported on the application of multivariate spectral analysis to the determination of chemical or physical constituents of solid wood based products (Hoffmeyer and Pedersen, 1995; Thumm and Meder, 2001; Meder *et al.*, 2002). Nor has much work utilised NMR spectroscopy. It is the qualitative edge to NMR spectroscopy that can provide greatest insight into understanding the fundamentals behind the largely empirical correlations that are found with NIR.

Some of the first work to make use of NMR for the prediction of pulp properties was undertaken by Wallbäcks *et al.* (1989, 1991a-c). A large number of physical and chemical properties (22 in total) were considered and by using PLS-2 modelling of all three spectroscopic techniques combined (FTIR, NIR, NMR) they were able to describe 98.8% of the variation in chemical properties. The earlier paper (1989) considered the predictive power of ^{13}C CP-MAS NMR spectra in isolation. They were able to predict 99.7% of the variation in lignin including unknown samples of particularly low lignin content.

PLS modelling has been used to determine solid wood moisture content and basic density (Thygesen, 1996) to a high degree of accuracy. Instead of the lengthy CPMG sequence, Thygesen simply performed a PLS calibration using the first 150 data points of the FID collected (corresponding to the first 170 μs of acquisition) using a 0.63 T homebuilt spectrometer. Prediction of a separate test set showed an error of ± 9.3 % (10 % of the mean) in the determination of moisture content with a correlation coefficient of 0.99 and an error of ± 29.6 kg m^{-3} (8 % of the mean) in the determination of basic density ($r = 0.87$).

The determination of cellulose I_α and I_β in lignocellulosic materials using PLS modelling of ^{13}C CP/MAS NMR spectroscopy has been reported by workers at the Swedish Pulp and Paper Institute (Lennholm *et al.*, 1994; Larsson *et al.*, 1995). A complementary method for characterisation of cellulose is to use a delayed contact spin-diffusion experiment as utilised by Newman and Hemmingson (1990, 1995) and Newman (1991, 1992, 1998, 1999).

5. NMR EXPERIMENTAL METHODS

The number you have dialled is imaginary, please multiply by i *and dial again.*
MIT phone exchange (attributed)

5.1 SPECTROSCOPY

5.1.1 SOLUTION STATE NMR

Solution state NMR spectroscopy was performed on either Bruker AC (latterly Avance) 200 or Bruker Avance 400 NMR spectrometers operating at 4.7 T and 9.4 T respectively. The 200 MHz system was equipped with a 10 mm broadband direct observe probehead and was used for solution state ^{11}B, ^{27}Al and ^{119}Sn spectroscopy. The 400 MHz system was equipped with a 5 mm broadband inverse probehead with z-gradient and was used for ^1H and ^{13}C 2D and some multinuclear spectroscopy. Two good references for solution state NMR spectroscopy and experimental setup are Derome (1987) and Braun *et al.* (1996).

Typically spectra were acquired using a power-gated WALTZ decoupling sequence (Shaka *et al.,* 1983; Figure 5.1.a), which applies a low power, broadband decoupling field during the relaxation delay in order to enhance NOE. Alternately an inverse-gated decoupling sequence (Figure 5.1.b) was used whereby the decoupler is switched off during the relaxation delay period to avoid nuclear Overhauser enhancement (NOE). This is particularly the case where nuclei exhibit a negative NOE effect (such as ^{15}N) or when quantitative spectra are required.

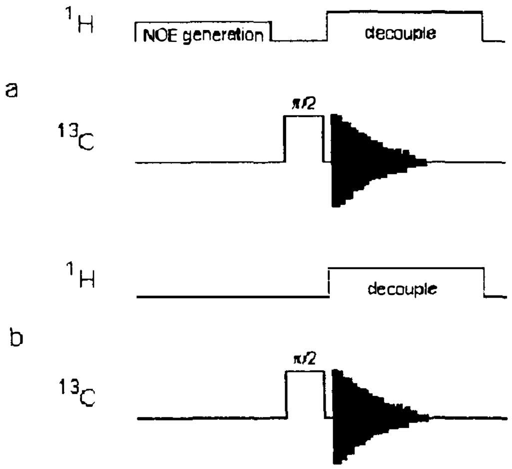

Figure 5.1. Pulse sequences for (a) power gated and (b) inverse gated decoupling.

A data size of 32K was typically used over a spectral window of 300 ppm. In order to improve the signal to noise ratio, exponential line broadening of 1 Hz was applied prior to Fourier transformation, albeit at the expense of a small loss in resolution. Spectra were referenced to TMS (^1H, ^{13}C, 0.0 ppm), $BF_3.OEt$ (^{11}B, 0.0 ppm), 2M $Al(NO_3)_3$ (^{27}Al, 0.0 ppm), KNO_3 (^{15}N, 0.0 ppm) or Me_4Sn (^{119}Sn, 0.0 ppm). In the case of neat liquid PRF resins the spectra were acquired using an inverse gated decoupling sequence and referenced to the internal methanol resonance (49.3 ppm wrt TMS).

Assignment of ^{13}C NMR spectra was assisted by use of DEPT spectral editing. Distortionless Enhancement by Polarisation Transfer (Doddrell *et al*, 1982), uses variable angle editing pulses to effect selective polarisation transfer from proton to carbon *via* ^1J coupling Figure 5.2. The variable pulse angle θ, is chosen to maximise signal depending on the number of attached protons on the carbon atom. Acquiring spectra with editing pulse values of 45°, 90° and 135° produces spectra which are respectively: a spectrum containing methine (CH), methylene (CH_2) and methyl (CH_3) resonances; a methine only spectrum; and a spectrum with the methylene resonances inverted while the methine and methyl resonances remain unaffected. In all cases quaternary carbons are suppressed since they do not have any attached protons to effect polarisation transfer.

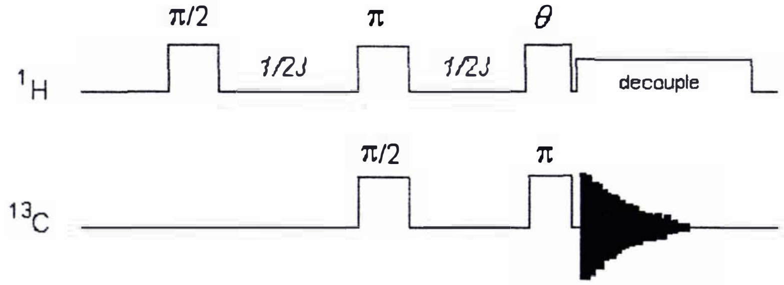

Figure 5.2. Pulse sequence for DEPT. Subspectra editing *via* the variable angle pulse, θ, is described in the text.

Simple ^1H-^1H correlated COSY spectra (as proposed by Jeener, 1971; Aue *et al.*, 1975) were acquired using two 90° pulses, over a spectral window of 3.5 kHz using a 2K x 256 matrix zero-filled to 512 in the F_1 domain. An excellent reference for multi-dimensional NMR spectroscopy is Ernst *et al.* (1987).

Phase sensitive ^1H-detected HMQC spectra (Bax and Subramanian, 1986), utilising the bilinear rotation (BIRD) sequence (Summers *et al.,* 1986) and GARP decoupling (Shaka *et al.*, 1985), were acquired over an F_2 spectral window of 4 kHz and an F_1 window of 10 kHz using a 2K x 128 matrix (zero-filled to 256 in F_1). A $\pi/2$ shifted sine-bell window function was applied in both domains prior to the 2D Fourier transform. The delay for polarisation transfer assumed a $^1J_{\text{C-H}}$ coupling constant of 145 Hz and the delay between the BIRD sequence and the HMQC portion was set to 400 ms.

Long range ^{1}H-^{13}C correlations were acquired using a gradient selected HMBC sequence (Bax and Summers, 1986; Hurd, 1990; Hurd and John, 1991) over an F_2 spectral window of 4 kHz and an F_1 window of 10 kHz using a 1K x 256 matrix (zero-filled to 512 in F_1). A $\pi/2$ shifted sine-bell window function was applied in both domains prior to the 2D Fourier transform. The delay for polarisation transfer assumed a $^nJ_{\text{C-H}}$ coupling constant of 10 Hz (Figure 5.3).

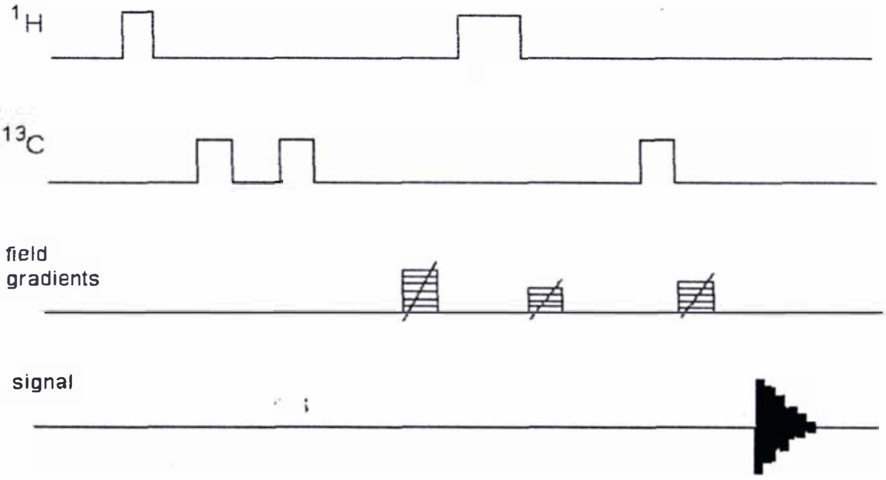

Figure 5.3. Pulse sequence for gradient selected HMBC.

5.1.2 SOLID STATE NMR

Solid state NMR spectroscopy was performed on a Bruker AC/Avance-200 equipped with a 7 mm double air-bearing MAS accessory. The MAS accessory was fitted with a custom MgO stator to minimise boron background from the standard BN stator material. The rotors were made from ZrO and fitted with Kel-F caps.

Typically samples were spun at the magic angle (54°42') at rotor speeds of 4 to 5 kHz. Cross polarisation (Hartmann and Hahn, 1962) with magic angle spinning (CP/MAS) was generally employed for spectral acquisition, or alternately a high power decoupling sequence (HPDEC) was used when cross polarisation was not possible. Good background to solid state spectroscopy can be found in Fyfe (1980), Mehring (1982) or Diehl *et al.*, (1994a,b).

The data size was typically 4K with spectral windows in the region of 300 – 350 ppm being used for all nuclei. Exponential line broadening of 20 Hz was applied prior to Fourier transformation. Chemical shifts were referenced to external adamantane (^{13}C, 38.3 ppm), BPO_4 (^{11}B, -3.60 ppm (Hayashi and Hayamizu, 1989)), 2M $Al(NO_3)_3$ (^{27}Al, 0.0 ppm), KNO_3 (^{15}N, 0.0 ppm (Witanowski and Webb, 1972)) or $(C_6H_{11})_4Sn$ (^{119}Sn, -97.4 ppm (Harris and Sebald, 1987)).

5.1.3 RELAXATION STUDIES

Relaxation studies were performed on solid wood samples using the Bruker Avance 200 with MAS accessory. Proton spin-lattice relaxation was performed using a modified inversion recovery sequence according to Xu *et al.* (1996). In this sequence the signal received from the inversion recovery sequence is subtracted from the signal received from the Bloch decay following a standard 90° pulse (see section 3.2.1).

Spin-spin relaxation was measured on bulk samples using a CPMG pulse sequence. The preparative 90° pulse is followed by a train of 180° pulses which continually refocus the transverse magnetisation until the partially relaxed signal is acquired (see section 3.2.2).

5.2 IMAGING

5.2.1 SPIN ECHO IMAGING

Magnetic resonance microimaging (^{1}H and ^{11}B (Kabalka *et al.*, 1992)) of small samples of wood (< 10 mm diameter) was undertaken on the Massey University Physics Department Bruker AMX-300 or ***Forest Research*** Bruker Avance 200 spectrometer using a microimaging accessory. A single slice spin-echo sequence (Figure 5.4) was used with the conditions as outlined in Table 5.1.

Table 5.1. Imaging conditions employed for spin echo imaging of wood samples (Bruker Avance 200 and AMX 300).

	^{1}H	^{1}H	^{11}B
Frequency (MHz)	200.13	300.13	96.29
Natural abundance	99.98 %	99.98 %	80.42 %
Absolute sensitivity (*cf* ^{1}H)[1]	1.00	1.00	0.13
Spin	$^{1}/_{2}$	$^{1}/_{2}$	$^{3}/_{2}$
Matrix size	128x128	128x128	128x128
Internal coil diameter (mm)	10	15	14
Field of view (FOV, mm)	10	15	15
In-plane resolution (μm)	78	117	117
Slice thickness (mm)	1	1	2
Offset from centre (mm)	0	0	0
Spectral width (kHz)	40	50	20
Duration of 90° hard pulse (μs)	n.a[2]	~20.0	~22.5
Attenuation of 90° hard pulse (dB)	n.a	0	0
Soft pulse waveform	sinc3.512	sinc3.512	sinc3.512
Duration of 90° soft pulse (μs)	2000	n.a	n.a
Attenuation of 90° soft pulse (dB)	~19	n.a	n.a
Duration of 180° soft pulse (μs)	2000	2000	2000
Attenuation of 180° soft pulse (dB)	~25	~27	~20
Spectral width of soft pulse (Hz)	2500	2500	2500
Gradient stabilisation delay (ms)	0.5	1.0	0.5
T_E (echo time - ms)	9.0	6.5	10.6
T_R (repetition time - ms)	500	250 or 500	250
L1 (number of acquisitions)	8	8	32
Read/phase/slice sequence	xyz	xyz	xyz
Gradient strength (G/cm)	20.0	35.0	11.2
Window function	sine-bell	sine-bell	sine-bell

Magnetic resonance imaging of larger samples (up to 80 mm diameter) was undertaken using the Massey University TecMag system interfaced to an Oxford 110 mm horizontal wide bore magnet at 200 MHz (Figure 5.5, Eccles *et al*, 1998). Parameters are shown in Table 5.2.

---

[1] Absolute sensitivity is the product of relative sensitivity and natural abundance (*cf* ^{13}C 1.76 x 10^{-4})

[2] The sequence used on the Avance 200 employed soft 90°/soft 180° pulses whereas the sequence used on the AMX 300 employed hard 90°/soft 180° pulses.

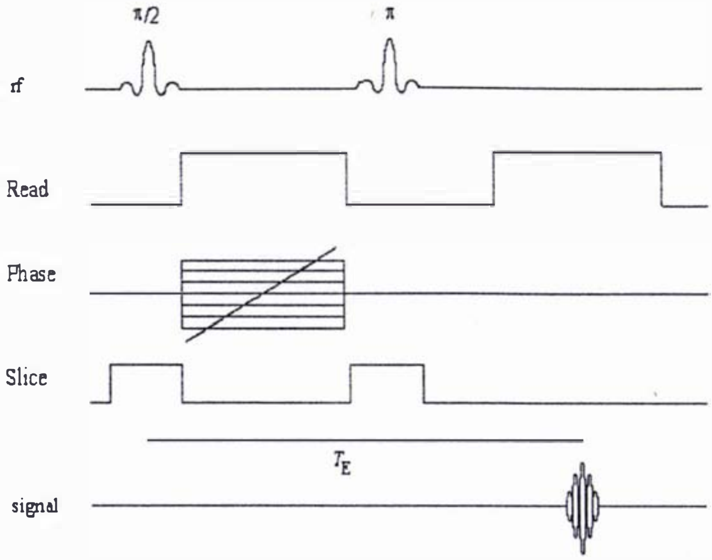

Figure 5.4. Spin echo imaging pulse sequence.

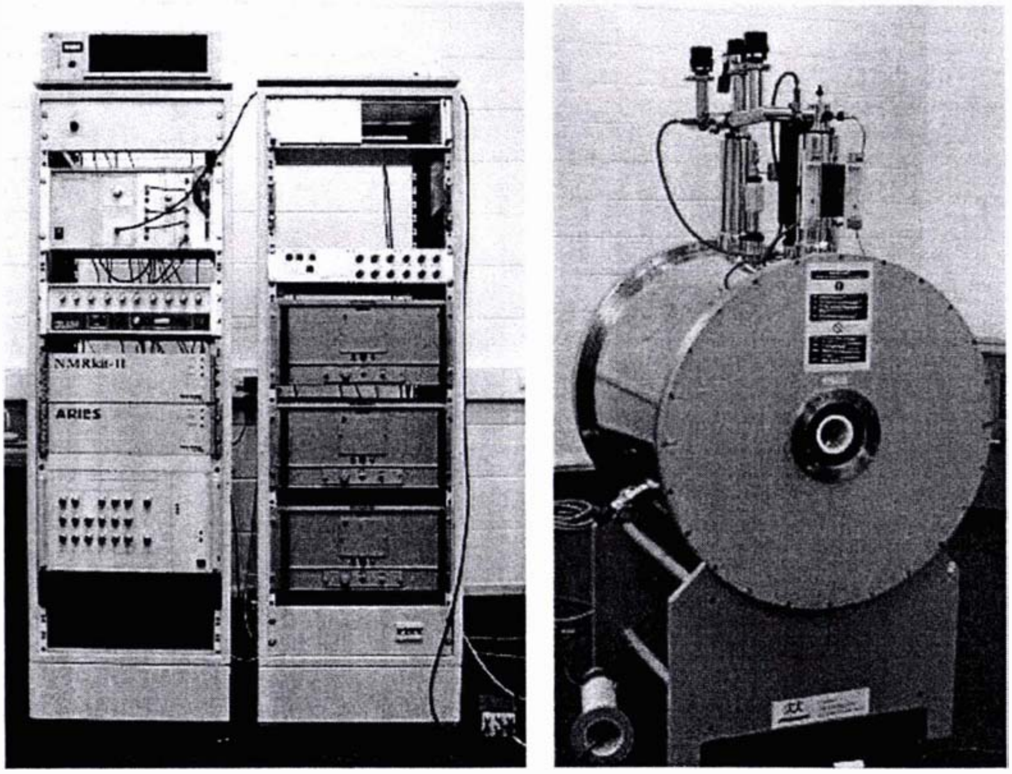

Figure 5.5. Photographs of the Tecmag Aries rf rack and Oxford 200 MHz horizontal magnet.

Table 5.2. Imaging conditions employed for spin echo imaging of large wood samples (TecMag/Oxford 200).

	^{1}H
Frequency (MHz)	200.13
Natural abundance	99.98 %
Absolute sensitivity (*cf* ^{1}H)	1.00
Spin	$^{1}/_{2}$
Matrix size	128x128
Internal coil diameter (mm)	65 or 80
Field of view (FOV, mm)	60 or 80
In-plane resolution (μm)	470 or 625
Slice thickness (mm)	1 or 2
Offset from centre (mm)	0
Spectral width (kHz)	25
Duration of 90° hard pulse (μs)	~230
Attenuation of 90° hard pulse (dB)	0
Soft pulse waveform	P4000.full
Duration of 180° soft pulse (μs)	4000
Attenuation of 180° soft pulse (dB)	0 - 4
Spectral width of soft pulse (Hz)	2500
Gradient stabilisation delay (ms)	0.5
T_E (echo time - ms)	10 - 15
T_R (repetition time - ms)	500 - 1000
L1 (number of acquisitions)	8 or 16
Read/phase/slice sequence	xyz
Gradient strength (G/cm)	20
Window function	sine-bell

5.2.2 DIFFUSION IMAGING

Diffusion images used for calculating diffusion anisotropy (Le Bihan, 1991) in radiata pine were acquired using a diffusion weighted imaging sequence as shown in Figure 5.6 (Callaghan, 1999). Seven images were acquired using all combinations of the field gradients (Table 5.3) using the conditions outlined in Table 5.4. A standard single slice spin echo image was also acquired as a reference image.

Table 5.3. Coefficients for linear combination of gradients applied to generate a series of diffusion weighted images for diffusion tensor imaging.

x	y	z
1	0	0
0	1	0
0	0	1
$1/\sqrt{2}$	$1/\sqrt{2}$	0
$1/\sqrt{2}$	0	$1/\sqrt{2}$
0	$1/\sqrt{2}$	$1/\sqrt{2}$
$1/\sqrt{3}$	$1/\sqrt{3}$	$1/\sqrt{3}$

Table 5.4. Imaging conditions employed for diffusion weighted imaging of wood samples.

	^{1}H
Matrix size	256x256
Internal coil diameter (mm)	15
Field of view (FOV, mm)	15
In-plane resolution (µm)	59
Slice thickness (mm)	0.5
Offset from centre (mm)	0
Spectral width (kHz)	50
Duration of 90° hard pulse (µs)	16.0
Attenuation of 90° hard pulse (dB)	0
Soft pulse waveform	sinc3.512
Duration of 180° soft pulse (µs)	2000
Attenuation of 180° soft pulse (dB)	30
Spectral width of soft pulse (Hz)	2500
Diffusion gradient duration, δ (ms)	2 or 3
Inter-diffusion gradient duration, Δ (ms)	10 or 12
Gradient stabilisation delay (ms)	0.5
T_E (echo time, ms)	6.5
T_R (repetition time, ms)	500
L1 (number of acquisitions)	2
L4 (number of diffusion expts = TD1)	8
Diffusion gradient strength (%)	100
Diffusion gradient mode	linear interpolation
100 % gradient strength (G/cm)	35.0

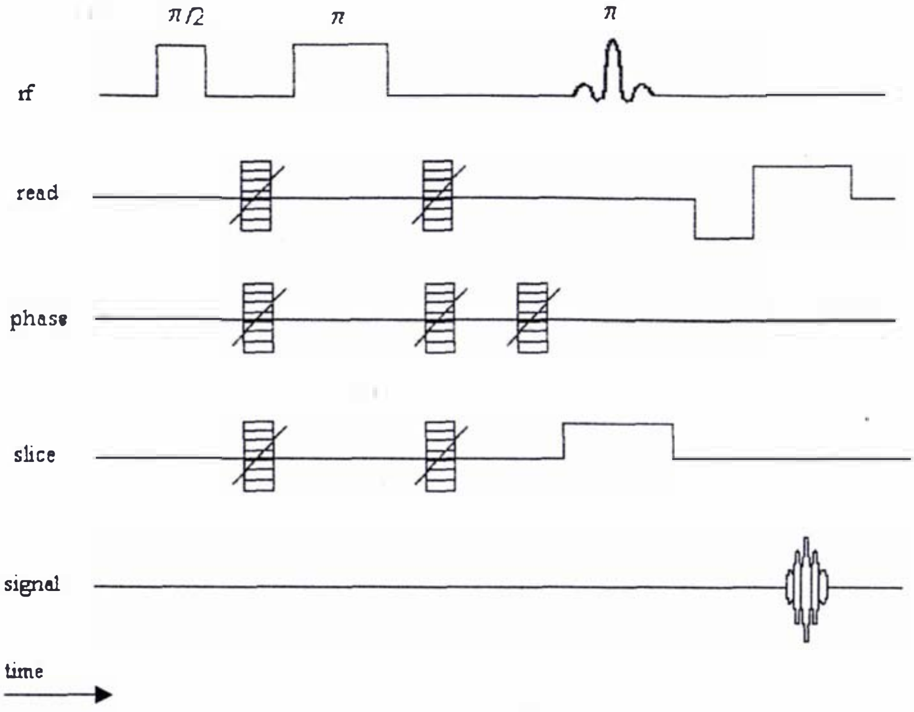

Figure 5.6. Diffusion weighted imaging pulse sequence (DIFFSE) showing the diffusion editing sequence as separated from the spatial imaging sequence.

5.2.3 CONSTRUCTION OF AN ^{11}B IMAGING COIL

A saddle coil was designed and built to operate at 96.29 MHz (the Larmor frequency of ^{11}B at 9.1 T) for use in the AMX-300 imaging probehead (Figure 5.7). The inner diameter of the coil was 12 mm.

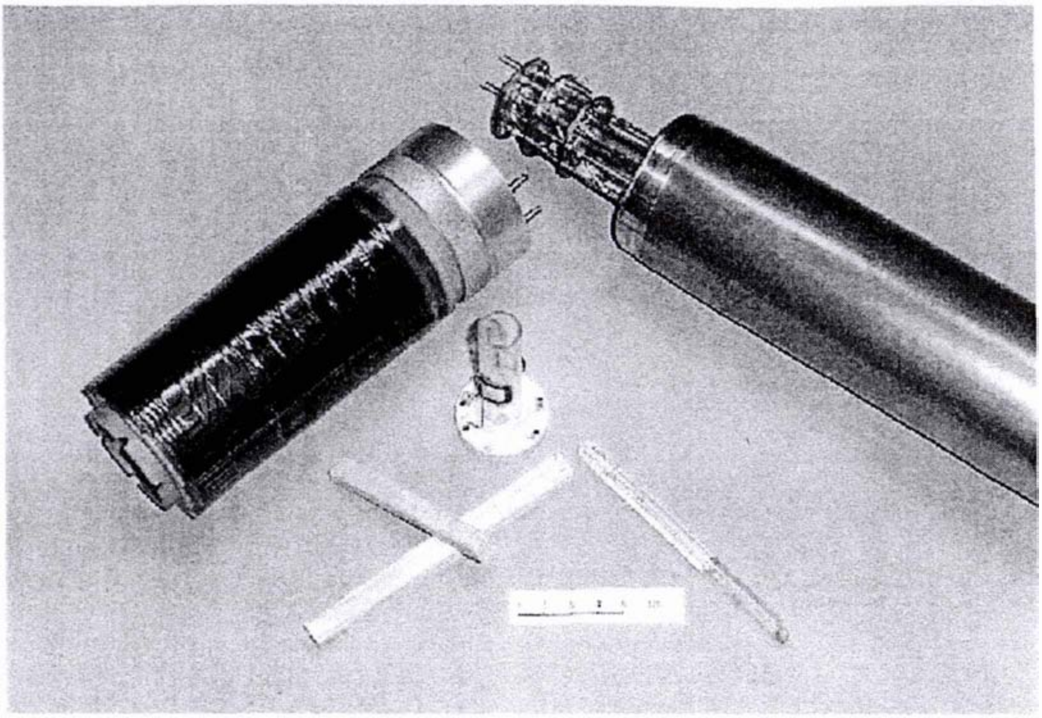

Figure 5.7. Photograph of ^{11}B imaging coil, probehead, gradient coil, phantom and samples.

5.2.4 CONSTRUCTION OF A BORON IMAGING PHANTOM

An imaging phantom was prepared to test the ^{11}B coil and to determine the direction of imaging. A 10 mm NMR tube was filled to a level of 20 mm with 3 mm glass beads. On top of this was placed two glass tubes (0.8 mm ID, 6.8 mm OD and 0.9 mm ID, 1.6 mm OD) and a sealed glass capillary (1.6 mm OD) (Figure 5.8). The tube was filled to a depth of *ca.* 40 mm with trimethyl borate (TMB) and sealed.

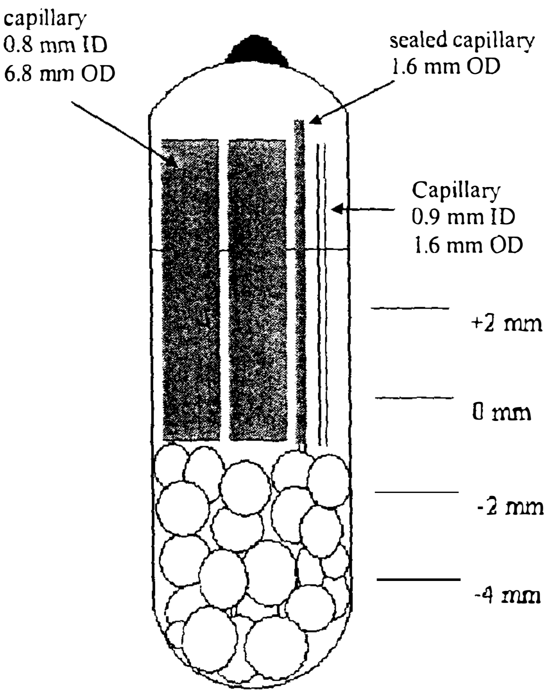

Figure 5.8. Schematic of TMB filled phantom for ^{11}B NMR imaging, showing glass beads, one open and one sealed capillary and one glass tube. The levels refer to the approximate position of the transverse ^{11}B NMR images in Figure 6.4.

Imaging was undertaken on the phantom using a 90° hard pulse, 180° soft pulse slice selective spin echo sequence as outlined previously in Table 5.1.

6. CHARACTERISING TIMBER PRESERVATIVES BY NMR SPECTROSCOPY AND IMAGING

The whole of science is nothing more than refinement of everyday thinking.
Albert Einstein

In order for radiata pine lumber to withstand fungal and microbial decay during service, it is treated with preservative compounds to a level dependent on the lumbers final end-use. As has been discussed in introductory chapters, very little is known about the *in situ* nature or distribution of some of these preservatives. This chapter will investigate both the *in situ* distribution and nature of existing and novel preservative compounds in use in New Zealand.

6.1 TIN COMPOUNDS

One tin compound used commercially for preservative treatment of timber was selected for this study (tributyltin oxide, (TBTO) ex Schering AG). Previous investigations (Blunden and Hill, 1988; Meder and Archer, 1991) on extracts of TBTO treated Scots or radiata pine have shown TBTO to disproportionate in contact with wood to form various alkylbutyltin esters. A critical question remains from both these studies - does the nature of the extract reflect the nature of TBTO *in situ* or does the extraction procedure affect the observed disproportionation of TBTO? The *in situ* nature of TBTO in TBTO-treated radiata pine was studied by solid state ^{119}Sn NMR spectroscopy, in order to confirm the observed degradation of TBTO in radiata pine wood.

6.2 BORON COMPOUNDS

Six boron-based compounds were selected for study, *viz* boric acid, **I**, trimethyl borate (TMB), **II**, 2,8,9-trioxa-5-aza-1-boratricyclo(3.3.3.0(1,5))undecane (triethanolamine borate, LIB-555), **III**, 2,9,10-trioxa-6-aza-1-boratricyclo(4.3.3.0(1,6))dodecane (tripropanolamine borate, LIB-666), **IV**, boron-biguanide chelate (BBC), **V** and bis-biguanidyl boron chloride (BGB), **VI** (Figure 6.1).

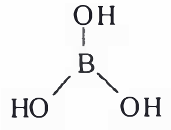

I

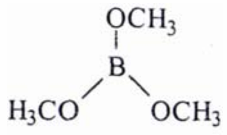

II

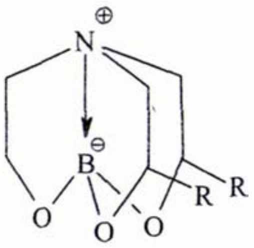

III

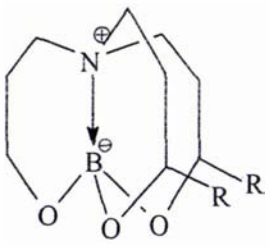

IV

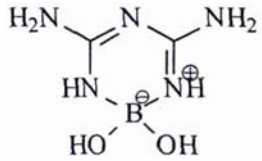

V

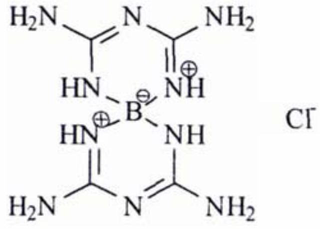

VI

Figure 6.1. Structures of preservative compounds investigated.

Compounds **I** and **II** were obtained from Aldrich Chemical Co, Milwaukee, IL, USA whereas compounds **III** and **IV** were prepared at ***Forest Research*** from boric acid and triethanolamine and tri-n-propanolamine respectively (Kelly, 1995) and compounds **V** and **VI** (R = H) were prepared at ***Forest Research*** according to Anderson *et al.* (1995; 1997). The substituted analogs of **III** and **IV** (R = $C_{22}H_{45}$) were also prepared in a similar fashion and are currently undergoing patent protection for preservative application (Franich *et al.*, 2001a).

6.3 MODEL WOOD COMPOUNDS

The two major chemical components of radiata pine are lignin (27%) and holocellulose (71%) (comprising cellulose (40%) and hemicellulose (31%)). In order to provide representative compounds for model studies the following samples were prepared: milled wood lignin (MWL), microcrystalline cellulose, cotton linters (native cellulose) and glucomannan (hemicellulose).

6.3.1 LIGNIN

6.3.1.1 Milled Wood Lignin (MWL)

The preparation of MWL is adapted from that described by Bjorkman (1956). Approximately 200 g of radiata pine wood (air dry, coarsely ground) was extracted with DCM (6 L) for 18 hours in a Soxhlet extractor. The wood was removed, air dried and subsequently extracted with 95 % ethanol (5 L) for a further 18 hours. The wood was then allowed to air dry to remove remaining solvent.

The extracted wood was then finely ground so as to pass through a 60 mesh sieve in a preparative Wiley mill. 70 g air dry of sample was loaded into a ball mill and milled for *ca.* 100 hours. The finely ground wood was recovered from the mill.

The finely ground wood recovered from the ball mill was extracted with an 80:20 acetone:water solution for 100 hours in a 800 mL beaker covered with parafilm (using approximately 5 mL of acetone:water solution per 1 g of ball milled wood). The acetone:water solvent was collected by decantation and filtration to remove traces of wood. The residual ball milled wood was then washed with a further 200 mL of solvent. The extract and washings were combined and the volume reduced under reduced pressure. The gummy deposit was then freeze dried overnight to remove water.

The extract was dissolved in 90 % acetic acid (*ca.* 20 mL of acetic acid per 1 g lignin) and the solution poured dropwise (with stirring) into a centrifuge tube. The solution was centrifuged at 3000 rpm for 15 minutes. After decantation of the supernatant, the precipitate was twice washed with 100 mL of distilled water, each washing being centrifuged at 3000 rpm for 15 minutes. The precipitate was slurried with water and transferred to a round bottom flask and the mixture freeze dried overnight.

The product was dissolved in a 2:1 mixture of DCM:ethanol (*ca.* 25 mL of solvent per 1 g lignin) filtered through glass fibre filter paper to remove insoluble material and the clear filtrate added dropwise to 200 mL of diethyl ether.

Ether was removed from the precipitate by decantation, the precipitate washed with 150 mL of ether, and dried under vacuum at room temperature. The product was then washed with 40-60 petroleum spirits, the solvent removed and finally dried under vacuum for 70 hours.

6.3.2 CELLULOSE

6.3.2.1 Cotton Linters

Cotton linters were sourced from Temming-Linters GmbH/Buckeye Cellulose, Glückstadt, Germany. Two samples were obtained representing two degrees of polymerisation (DP 1470 and DP 1900). The sample with the lower DP was used as supplied.

6.4 PRESERVATIVE TREATMENT

Samples of radiata pine sapwood were obtained green from a local sawmill before sapstain treatment had occurred. Machined samples 8 x 8 mm x 90 mm were prepared to include a chamfer on one corner to provide visual reference to sample orientation as shown in Figure 6.2. The samples were dried at 105 °C for 18 hours.

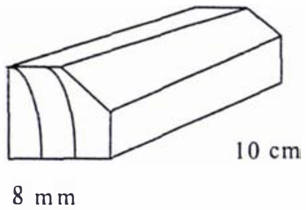

Figure 6.2. Schematic of machining of radiata pine sapwood.

The green sapwood was imaged using ^1H magnetic resonance imaging (MRI) microscopy at Massey University. This provided a base image upon which to superimpose the boron image of the treated samples. The samples were then oven dried at 105°C until constant mass was achieved.

Treatment solutions were prepared fresh (1% boric acid equivalent) in either water (boric acid) or Hexane:DCM:THF 3:7:3 (LIB compounds). Trimethylborate was used as a neat liquid for the gaseous phase treatment. All treatments were performed using the following schedule in a Parr bomb reactor. A vacuum of –0.5 bar was applied for 15 minutes, after which treatment solution/vapour was introduced, followed by a positive pressure of 1.5 bar for 20 minutes. All samples were allowed to air dry following treatment.

A subsample of the TMB-treated material was separated into earlywood and latewood for comparative NMR studies to investigate the relative rates of TMB hydrolysis.

6.5 RESULTS

6.5.1 ^{119}Sn MAS SPECTROSCOPY

The ^{119}Sn MAS NMR spectrum of TBTO-treated, kiln-dried, radiata pine sapwood 4 days after treatment is presented in Figure 6.3. It shows a single broad resonance at 104 ppm characteristic of tributyltin esters of resin and fatty acids (Smith and Tupciauskas, 1978; Wrackmeyer, 1985, 1997). This is consistent with the primary degradation product observed in $CHCl_3$ extracts of TBTO-treated radiata pine sapwood (Blunden and Hill 1989; Meder and Archer 1991).

A smaller resonance at 87 ppm is barely visible and is attributed to residual TBTO. There is no real evidence of any other tin species (dibutyl- and monobutyl-tin species) as identified in the solution state extracts.

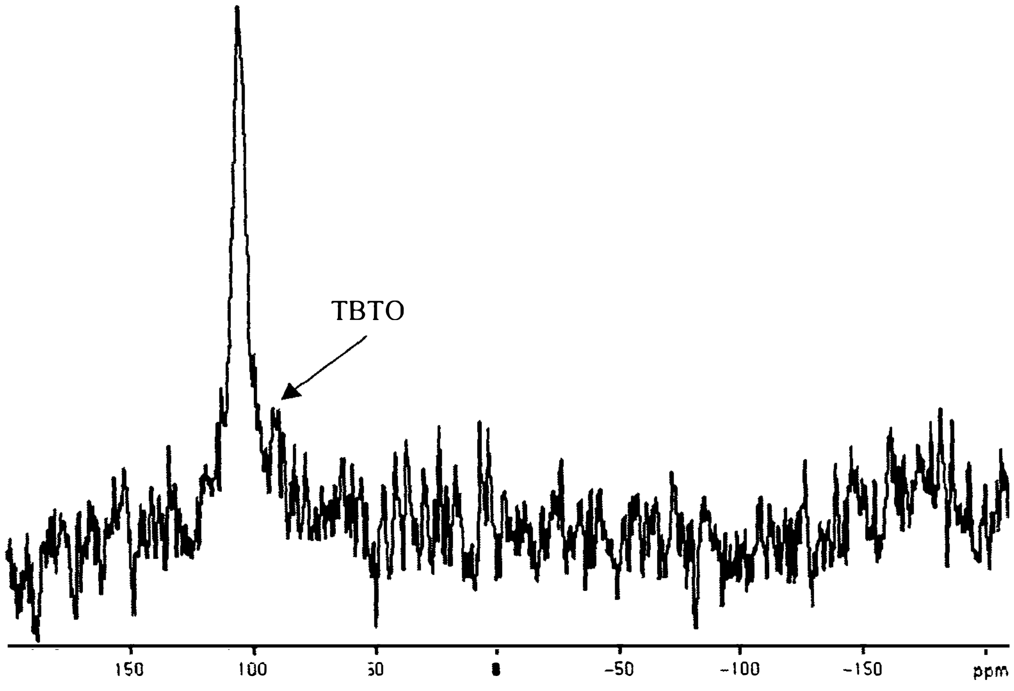

Figure 6.3. 74.5 MHz ^{119}Sn MAS NMR spectrum of TBTO-treated radiata pine sapwood 2 weeks after treatment. [Avance-200, HPDEC, rotor speed 4.5 kHz, relaxation delay 4 s, 6 μs 90° pulse, LB 40 Hz, referenced to external $(C_6H_{11})_4Sn$ (-97.4 ppm)].

6.5.2 ^{11}B NMR IMAGING

In order to improve the signal-to-noise ratio (S/N) on the Bruker AMX 300, an additional bandpass amplifier was used. An AR^2 (Advanced Receiver Research, Burlington, CT) GaAsFET preamplifier tuned to 96.3 MHz was added in series with the existing broadband amplifier and tested using a single pulse acquisition on the TMB phantom solution. The S/N ratio without the amplifier was 65:1 versus 70:1 with the amplifier. There was consequently no distinct advantage in using the preamp to maximise the S/N ratio. However, as will be shown, the S/N ratio of the system was sufficient to enable ^{11}B imaging to be performed.

A multislice spin echo sequence was used to acquire ^{11}B images (2 mm thick slices) at 0, ±2 and ±4 mm offsets from centre. The slices at +2, 0, -2 and -4 mm offset are shown in

Figure 6.4 and clearly show the features present in the phantom. This also confirms the direction of the offset as being positive in the positive *z* axis.

6.5.3 BORON TREATED RADIATA PINE SAPWOOD

Samples of dry radiata pine sapwood, treated with compounds **I** – **VI**, were imaged using a spin-echo sequence according to the previous conditions.

Only radiata pine wood samples treated with compound **II** (TMB) showed any signal in the spin echo images. Furthermore there was initial concern regarding the apparent lack of penetration of TMB in the latewood of the samples. This initially suggested a difference in the vapour phase porosity between the latewood and the earlywood.

Light micrographs of the samples are shown in Figure 6.5 along with ^{1}H NMR images of the samples before treatment with TMB (earlywood and latewood are clearly visible) and the corresponding ^{11}B NMR images after treatment. Note in particular the absence of signal in the ^{11}B images in the latewood section of the images.

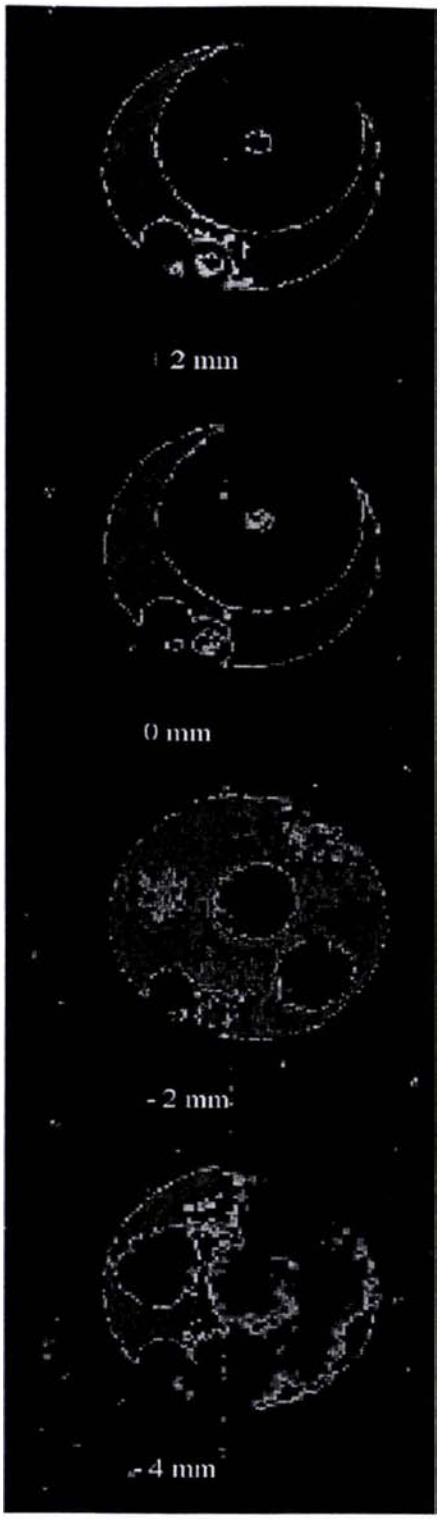

Figure 6.4. 96.3 MHz ^{11}B NMR images of TMB filled phantom at +2, 0, -2 and -4 mm offset from centre. [AMX-300, spin echo, 128x128, 15 mm FOV, 2 mm slice, T_E 10.6 ms, T_R 250 ms].

300 MHz ^{1}H magnetic resonance image of wood samples in transverse section

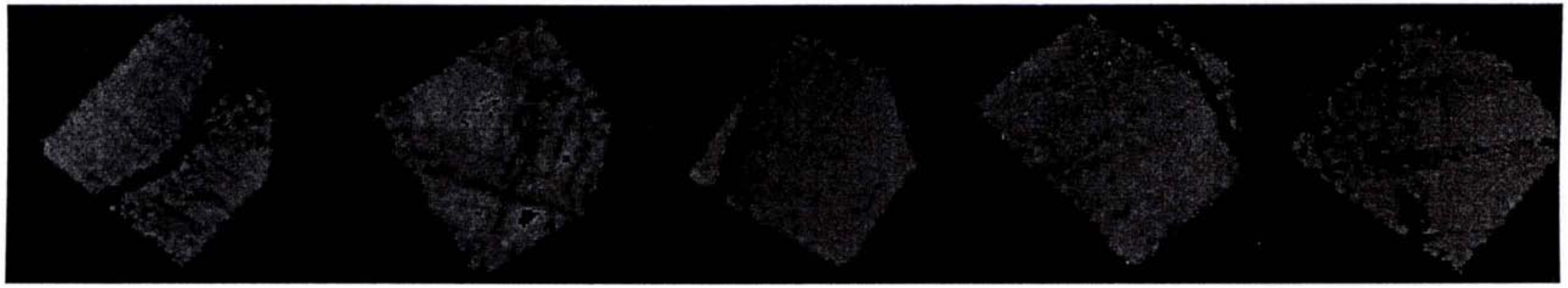

96 MHz ^{11}B magnetic resonance image of TMB treated wood samples from above (in transverse section)

Figure 6.5. ^{1}H and ^{11}B NMR images of TMB treated radiata.

One sample was chosen for a more in-depth study. Figure 6.6 shows the optical image, ^{1}H image before drying and TMB treatment and the ^{11}B image after drying and TMB treatment of a 8 mm^2 x 90 mm sample of radiata pine (Meder *et al.*, 1999).

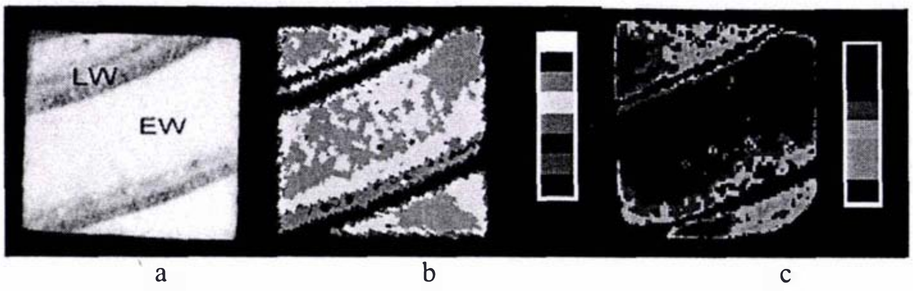

Figure 6.6. (a) Optical image of radiata pine cross section showing dark latewood (LW) and lighter coloured earlywood (EW), (b) ^{1}H NMR image of green (wet) sample before TMB treatment and (c) ^{11}B NMR image two days after drying and TMB treatment. [AMX-300, spin echo, 128x128, 15 mm FOV, 2 mm slice, T_E (^{1}H) 6.5 ms, T_E (^{11}B) 10.6 ms, T_R (^{1}H) 500 ms, T_R (^{11}B) 250 ms].

The loss of signal in proton NMR imaging experiments is most often due to the transverse relaxation time for the nuclear species of interest being much shorter than the spin echo imaging time T_E. In the case of boron NMR imaging it is possible that the absence of signal might arise from two possibilities. First it is possible that the T_2 of the boron compound present in the latewood is very short. Secondly, it is possible that the TMB has not penetrated the latewood and is only present in the earlywood. In order to elucidate the cause, ^{11}B MAS NMR spectroscopy was performed on excised sections of TMB-treated earlywood and latewood, and compared these results with ^{11}B MAS NMR spectra of known compounds.

6.5.4 NMR SPECTROSCOPY

6.5.4.1 Candidate Preservative Treatment Compounds

Solution and solid state NMR chemical shift data for the boron compounds as recorded are presented in Table 6.1 along with literature data for comparison.

Table 6.1. Solution state and solid state NMR chemical shift data (ppm) for candidate boron compounds.

	I	II	III	IV	V	VI
	Boric Acid	**TMB**	**LIB-555**	**LIB-666**	**BBC**	**BGB**
Solution state[a]	18.5 (D_2O)	15.2 (neat[b])	14.8 ($CDCl_3$)	2.2 ($CDCl_3$)	-1.6 (D_2O)	-5.3 (D_2O)
Literature	19.2[c]	?	10.5[d]	4.4[d]	n.a.	n.a.
Solid state[e]	18.9	-	13.9, 10.4	1.5	n.d.	-10.7
Literature	~18[f]	-	n.a.	n.a.	n.a.	n.a.

a. solution state data obtained on ***Forest Research*** AC/Avance-200 referenced to external $BF_3.Et_2O$ (0.0 ppm)
b. neat solution (Aldrich Chemicals)
c. Coddington and Taylor (1989) (in D_2O referenced to $BF_3.Et_2O$)
d. Sun *et al.* (1986) (in D_2O referenced to $BF_3.Et_2O$)
e. solid state data obtained on ***Forest Research*** AC/Avance-200 referenced to BPO_4 (-3.60 ppm, Hayashi and Hayamizu, 1989)
f. Wang *et al.* (1996)
n.a. not available
n.d. not determined

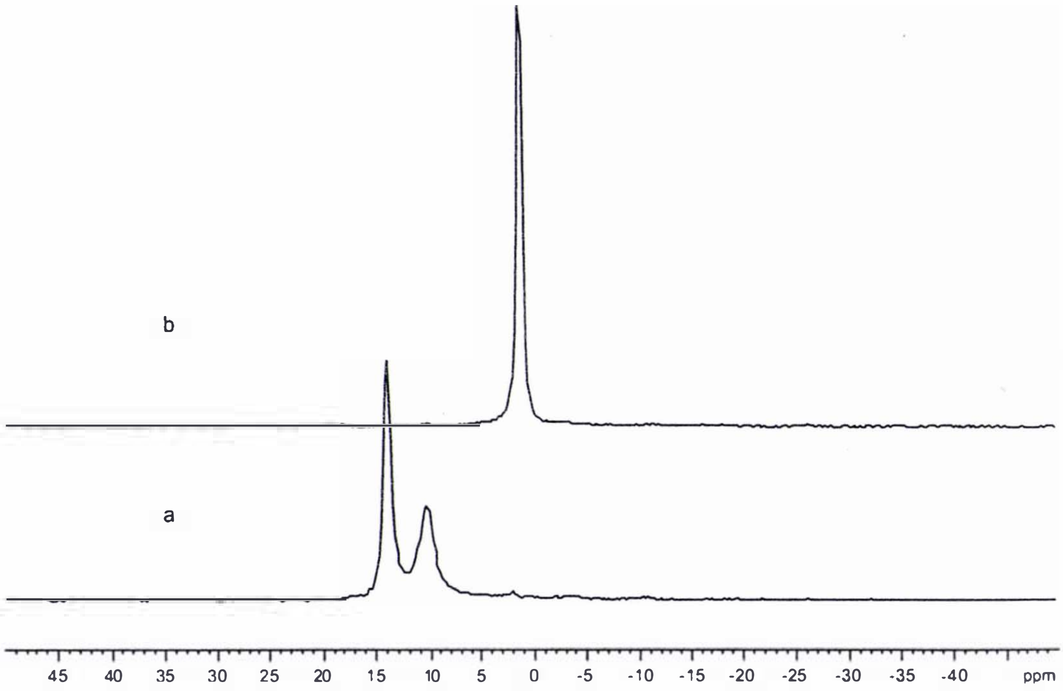

Figure 6.7. 64.2 MHz ^{11}B MAS NMR spectra of (a) LIB 555 and (b) LIB 666. [AC-200, HPDEC, rotor speed 4 kHz, relaxation delay 5 s, 6.5 μs 90° pulse, LB 10 Hz, referenced to external BPO_4 (-3.60 ppm)].

6.5.4.2 Treated Radiata Pine

The ^{11}B solution state NMR spectrum of boron biguanide chelate, **V**, (Figure 6.8) showed a resonance at –1.65 ppm which was found to be dependent on pH. At pH 3 the solution contained both boric acid (~19 ppm) and the BBC, **V**, resonance at –1.65 ppm. Hence compound **V** (BBC) was considered unsuitable for wood treatment due to its poor hydrolytic stability. Table 6.2 shows the solid state ^{11}B NMR chemical shifts observed in samples of radiata pine treated with the candidate boron compounds.

Table 6.2. Solid state ^{11}B NMR chemical shift data (ppm) for candidate boron compounds in radiata pine.

	I **Boric Acid**	**II** **TMB**	**III** **LIB-555**	**IV** **LIB-666**	**V** **BBC**	**VI** **BGB**
Solid state	19.0	18.4	18.2	n.d.	u.s.	-10.5 -5.5
Literature	18.9[1]	n.a	n.a.	n.a.	n.a.	n.a.

1. Wang *et al.*, 1996.
n.d. not determined
u.s. hydrolytically unstable

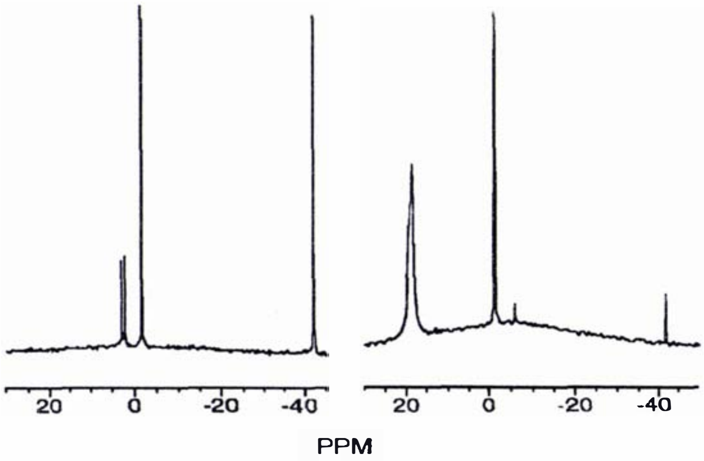

Figure 6.8. 64.2 MHz ^{11}B solution state NMR spectrum of boron biguanide chelate, **V**, in aqueous solution (left) and after adjusting to pH 3 (right). [AC-200, single pulse, relaxation delay 2 s, 9.5 µs 90° pulse, LB 2 Hz, referenced to internal concentric BH_4^+ (-42.2 ppm)].

Bis(biguanadyl)boron chloride **VI** showed one major resonance in both solid and solution state ^{11}B NMR spectra at –5.3 ppm, indicative of a tetrahedral boron environment (Figure 6.9). Unlike compound **V**, compound **VI** was not affected by change in solution pH.

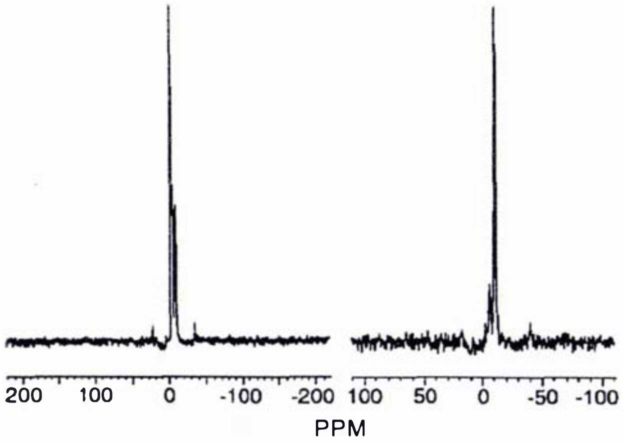

Figure 6.9. 64.2 MHz ^{11}B solution state NMR spectrum of bis-biguanadyl boron, **VI**, (left) and ^{11}B CP/MAS NMR spectrum of the copolymer formed by condensation of **VI** with hexamethyl-methylolmelamine (right). [Solution state: conditions as per Figure 6.8. Solid state: conditions as per Figure 6.7].

Figure 6.10 shows the solid state ^{11}B CP/MAS NMR spectrum of radiata pine sapwood treated with bis(biguanadyl)boron chloride **VI** and hexamethylmethylolmelamine (HMMM) *via* an *in situ* polymerisation. Primary resonances are observed at –10.5 ppm and at –5.5 ppm, both of which are seen in the solid state spectrum of the pure condensation polymer, along with resonances at 1.5, 5.5 and 12.5 ppm.

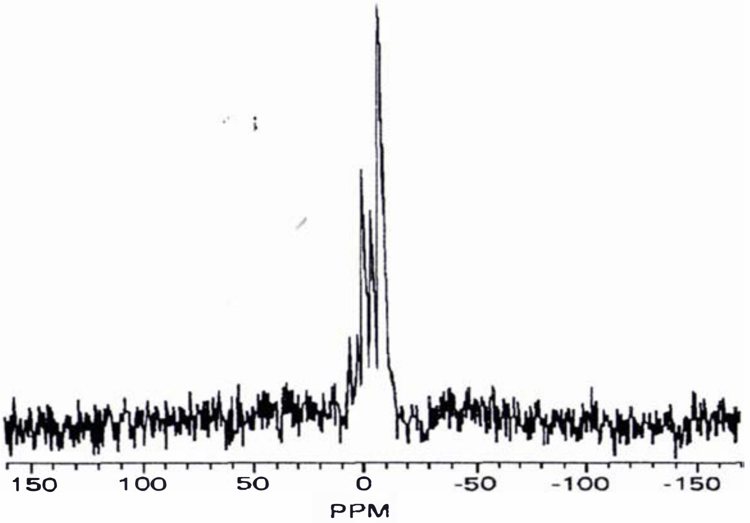

Figure 6.10. 128.3 MHz ^{11}B CP/MAS NMR spectrum of bis-biguanadyl boron **VI** /HMMM polymer formed in radiata pine sapwood. [MSL-400, CP/MAS, rotor speed 3.6 kHz, relaxation delay 10 s, contact time 1 ms, 3.8 μs 90° pulse, LB 20 Hz, reference BPO_4 (-3.60 ppm)].

The resonances observed can possibly be explained as hydrolysis products of BGB **VI** and subsequent chelation with wood sugars and/or hydrolysed HMMM. The resonance at 12.5 ppm is similar to that observed for LIB 555 **III** suggesting hydrolytic breakdown and reaction to form reaction products as proposed in Figure 6.11.

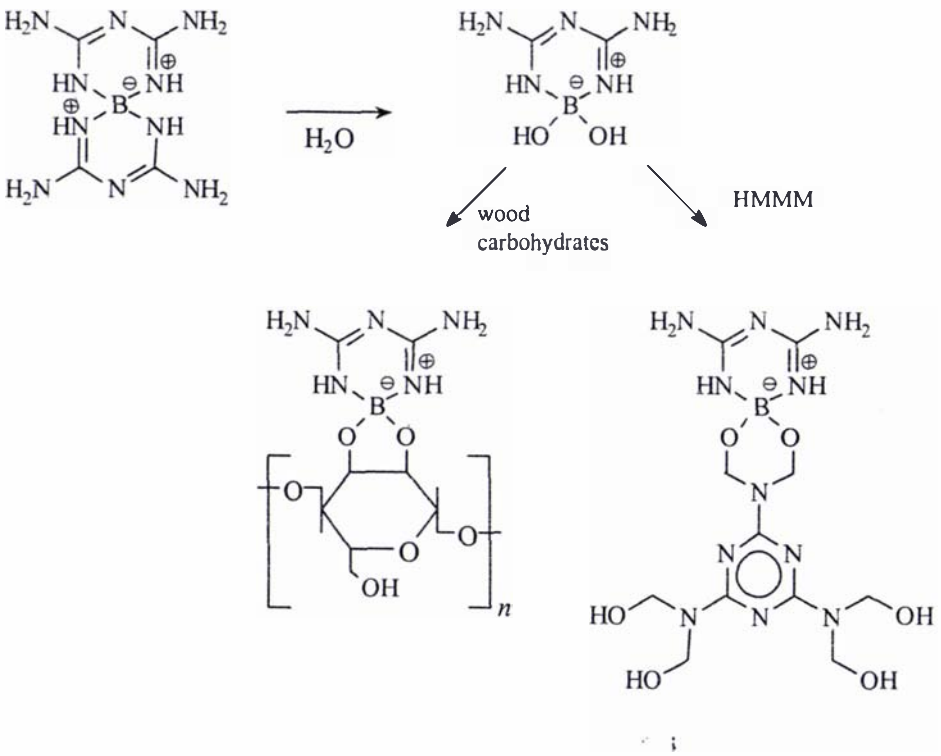

Figure 6.11. Possible reaction scheme for reaction of BGB hydrolysis product with wood carbohydrates and/or hexamethylmethylolmelamine (HMMM).

Treatment of radiata pine with vapour phase trimethyl borate (TMB) was shown by magnetic resonance imaging to have anomalous retention characteristics in the latewood. TMB-treated radiata pine was sectioned to provide latewood and earlywood samples, which were analysed by ^{11}B MAS NMR spectroscopy (Figure 6.12). The spectrum of boric acid has been included for direct comparison. Figure 6.13 shows the simulated lineshape fit, as produced using WinFit[†], for the ^{11}B MAS NMR spectrum of boric acid. It suggests a trigonal boron species with quadrupolar coupling constant

---

[†] Bruker Analytik, Silberstreifen, D-76287 Rheinstetten, Germany

of 2.26 MHz, an assymetry parameter, $\eta = 0$ and an isotropic shift of 18.5 ppm, compared with reported values of 2.48 MHz, 0.0 and 18.9 ppm respectively (Wang *et al.*, 1996).

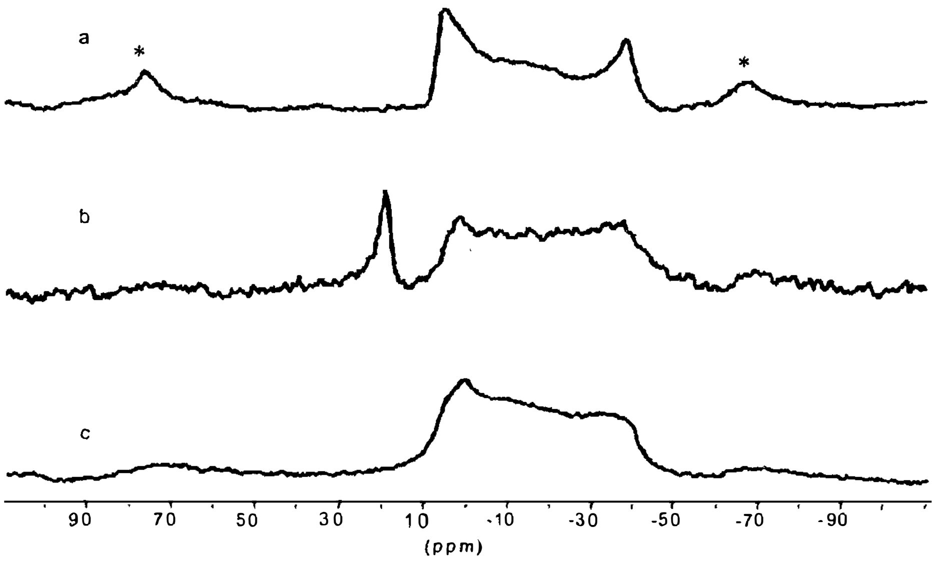

Figure 6.12. 64.2 MHz ^{11}B MAS NMR spectrum of (a) boric acid, (b) TMB-treated earlywood, and (c) TMB treated latewood sectioned from a radiata pine wood sample. The position of spinning sidebands are indicated by an asterisk. [AC-200, HPDEC, rotor speed 5 kHz, relaxation delay 2 s, 5 μs 90° pulse, LB 10 Hz, reference external BPO_4 (-3.60 ppm)].

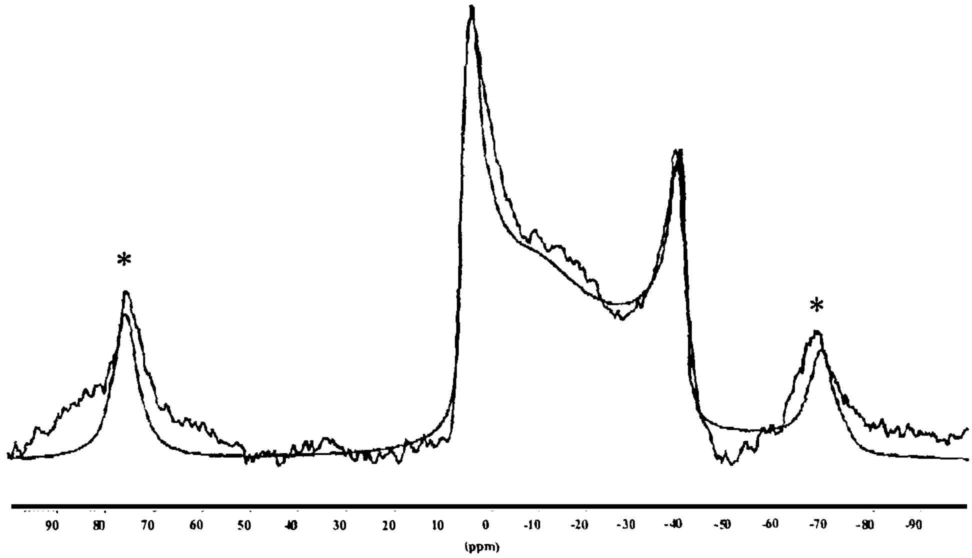

Figure 6.13. 64.2 MHz ^{11}B MAS NMR spectrum of boric acid and simulated fit (smooth line). Spinning sidebands are indicated by an asterix. [AC-200, HPDEC, rotor speed 5 kHz, relaxation delay 2 s, 5 μs 90° pulse, LB 10 Hz, reference external BPO_4 (-3.60 ppm). [Conditions as per Figure 2.12].

The spectrum of TMB-treated radiata pine earlywood shows not only boric acid but also residual TMB (sharp resonance at 18.4 ppm) being present (Figure 6.12). This indicates that the TMB undergoes hydrolysis with residual water in the wood but that the rate of hydrolysis differs from the earlywood to that of the latewood with the rate of hydrolysis of TMB following preservative treatment being faster in the latewood than in the earlywood. It has previously been reported that in wood samples with moisture content below the fibre saturation point the latewood has a higher water density (Quick *et al.*, 1990). In kiln or oven dry wood the higher water density observed in the latewood would give rise to a higher rate of hydrolysis of TMB, as observed.

Figure 6.14 shows the rate of TMB hydrolysis for radiata pine earlywood and latewood following treatment. A single component exponential decay fit to the data was unsatisfactory for both the earlywood and latewood, so a two component fit was undertaken and the results presented in Table 6.3.

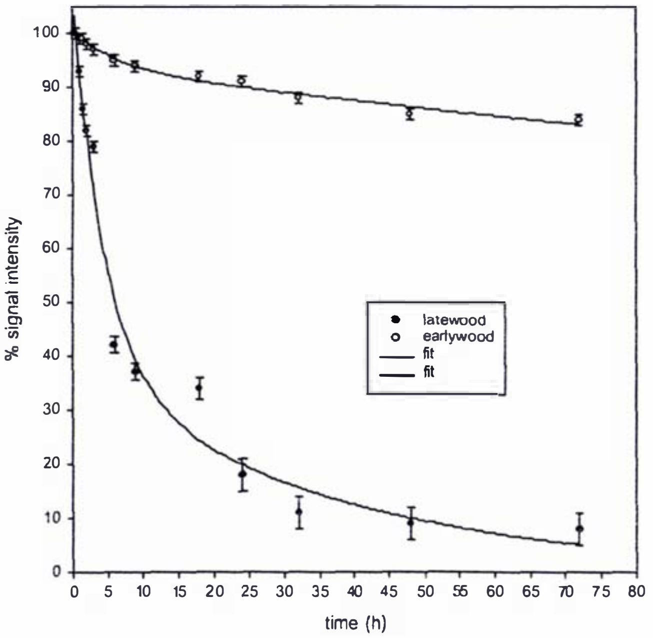

Figure 6.14. Relative rates of hydrolysis of TMB as followed by disappearance of the ^{11}B NMR signal for TMB (18.0 ppm).

Table 6.3. Time constant data for decay of TMB signal from TMB-treated radiata pine sapwood earlywood and latewood.

	Latewood	Earlywood
Time constant 1 (hr)	3.7	7.6
Time constant 2 (hr)	55	100

The results of NMR spectroscopy suggest that the TMB in latewood was extensively hydrolysed to boric acid and that the reason it was not observed in the ^{11}B image is that the T_2 relaxation was too short for it to be observed on the NMR timescale. The minimum T_2 value for a chemical species to be observable in an image is determined by the echo time, which in the case of the ^{11}B image is 10.6 ms. The very short T_2 relaxation times of the boric acid in conjunction with strong quadrupolar broadening leads to a broad linewidth of the boric acid resonance. This results in there being no observable ^{11}B signal in the latewood region where only boric acid is present. In the earlywood region the observed signal in the image is from the residual TMB which has a longer T_2 value.

Attempts to image the samples four weeks after treatment were impossible due to the fact that the residual TMB observed in the earlywood two days after treatment being completely hydrolysed to boric acid (as seen in subsequent solid state NMR spectra) and as such was "invisible" on the NMR imaging timescale (Meder *et al.*, 1999).

6.5.4.3 Treated Model Compounds

6.5.4.3.1 Chemical Shift Data

Table 6.4 shows the ^{11}B NMR chemical shifts observed in samples of model compounds treated with the candidate compounds. The spectrum of TMB-treated cotton linters shows quadrupolar coupling similar to the TMB-treated radiata pine samples whereas the TMB-treated milled wood lignin shows a single resonance at 19.2 ppm evident of TMB (Figure 6.15) along with the boric acid degradation product.

Table 6.4. Solid state ^{11}B MAS NMR chemical shift data for TMB treated model compounds.

	Cotton linters	MWL	
Solid state			
δ (ppm)	18.5	19.2	18.3
η	0	0	0
QCC (MHz)	2.2	0	2.2
Assignment	Boric acid	TMB	Boric acid

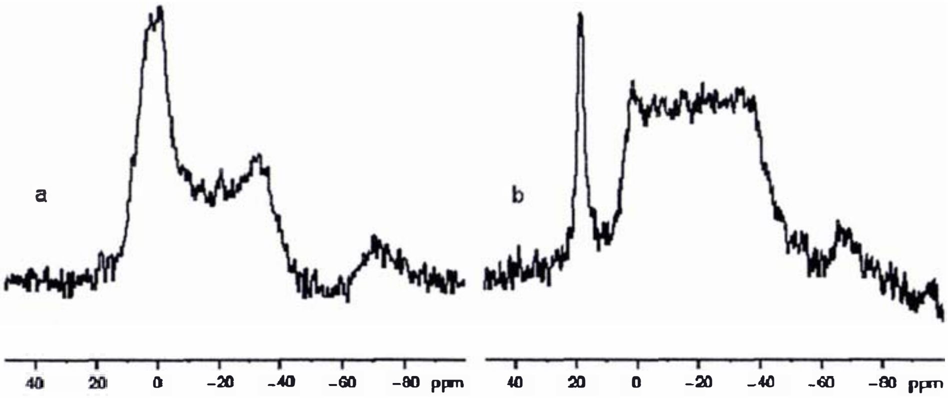

Figure 6.15. ^{11}B MAS NMR spectra of TMB-treated (a) cotton linters and (b) milled wood lignin, 1 day after treatment. [Conditions as per Figure 2.12].

6.6 SUMMARY OF CHAPTER

Solid state ^{119}Sn NMR spectroscopy of TBTO-treated radiata pine wood has shown tributyltin esters to be present *in situ*, supporting previous observations of tributyltin esters in solution state ^{119}Sn NMR spectra of extracts of TBTO-treated radiata pine wood.

The work undertaken in this section presents some of the first ^{11}B NMR images outside of the area of boron-neutron-capture-therapy imaging. This has included successfully imaging the penetration and retention of trimethylborate in radiata pine wood after vapour phase treatment. The apparent loss of signal in the latewood bands is explained by the rapid hydrolysis of TMB to boric acid in the latewood. Quadrupolar broadening of the boric acid resonance gives rise to a signal that is too broad to be observed in the imaging of treated wood.

The rate of hydrolysis of TMB in treated radiata pine latewood and earlywood has been studied by solid state ^{11}B NMR spectroscopy and shows rapid hydrolysis of TMB in radiata pine sap latewood with a rate constant of 3.7 hr.

Solid state ^{11}B NMR analysis of radiata pine wood treated with a range of boron based preservative candidates has been instrumental in determining the *in situ* nature of the boron species. It has also been able to determine the nature of the boron species after water leaching and exposure to decay fungi.

7. NMR IMAGING OF TIMBER DRYING

> *The most exciting phrase to hear in science, the one that heralds the most discoveries, is not 'Eureka!' but 'That's funny...'.*
>
> Isaac Asimov

The measurement of moisture content gradients during drying of lumber is extremely difficult. Several methodologies have been developed, requiring sub-sampling during drying runs and their individual merits have been reviewed by Gu and Zink-Sharp (1999). Rosenkilde and Jesper (1997) measured the moisture content gradient of Scots pine (*P. sylvestris*) dried at 60 °C, using small samples (30 x 30 x 30 mm), which were insulated against heat and moisture movement on four faces so that moisture movement could only occur in one direction in each sample. Samples were prepared to allow measurement of moisture gradient in either the radial, tangential or longitudinal direction. The moisture contents were determined by either direct measurement on 3 mm slices (Samuelsson and Arfvidsson, 1994) or by computed tomography (CT) using the technique of Lindberg (1992). The moisture content gradient was low during the period of drying above fibre saturation, at which point a steep gradient was established. In the radial direction the drying gradient appeared to be lower than that in the tangential direction.

Avramidis and Siau (1987) investigated drying in the radial direction of Western white pine (*P. monticola*) samples of varying thickness (0.5, 1.0 and 2.0 cm). Their results showed that as the thickness of the sample increased the ratio of internal to total resistance decreased. The ratio was calculated from the apparent diffusion coefficient and the surface emission coefficient. In both of these previous studies the influence of earlywood and latewood composition was not known.

This section of work investigated the drying of radiata pine wood and the influence of annual ring orientation and physical dimensions as a result of differing sawing patterns. Before venturing further it is necessary to present the various orientations of annual ring that result from adopting different sawing patterns. Two extreme geometries can be adopted. Flat-sawn lumber is characterised by the annual rings running parallel to the wide face of lumber, when viewed end on, whereas quarter-sawn lumber has annual rings that are oriented perpendicular to the wide face (Figure 7.1). These extremes of orientation were used in the preparation of large-scale samples for drying studies.

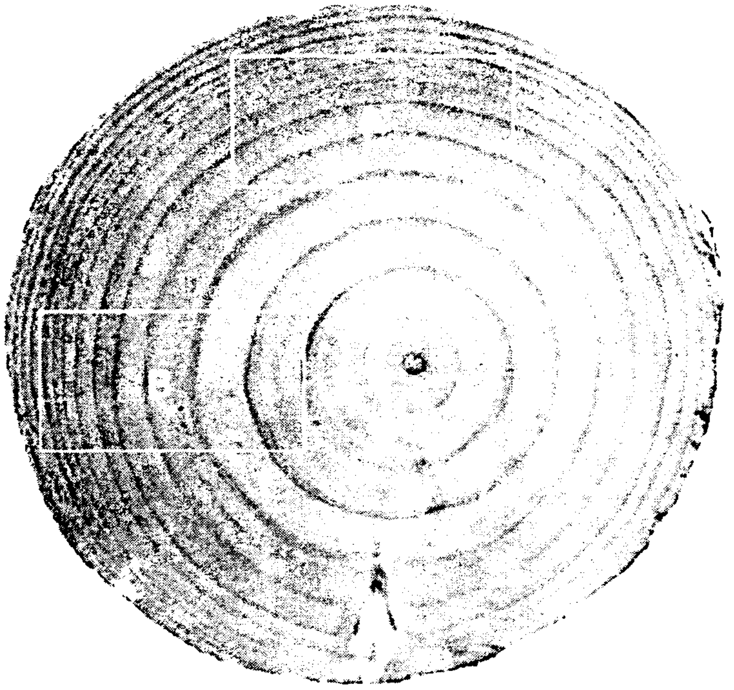

Figure 7.1. Illustration of the two extremes in orientation of annual rings resulting from (A) flat-sawn and (B) quarter-sawn cutting patterns.

7.1 SMALL SCALE SAMPLES

Radiata pine sapwood was selected in a green state and machined to 8 x 8 mm x 90 mm (longitudinal) dimensions (Figure 7.2). For drying studies the samples were end-sealed with an aluminium-based two-pot resin (Altra Shield™ 546[†]) to minimise longitudinal drying from occurring and thus simulating the situation known to occur in a long length of lumber.

[†] Altex Coatings, 215 Oropi Rd, Tauranga, New Zealand

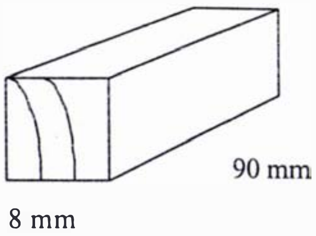

Figure 7.2. Schematic of machining of radiata pine sapwood.

With the sample placed axially in the imaging coil (15 mm ID) of the AMX-300, a flow of heated air (60°C, 500 L/hr) was passed over the surface of the sample. Proton images of the sample were obtained approximately every 7 minutes according to the conditions described previously (Table 5.1), with the following exceptions:

L1 (number of acquisitions)	4
T_E (echo time - ms)	8
T_R (repetition time - ms)	1000

7.2 LARGE SCALE SAMPLES

Assessment of the drying of larger pieces of timber (50 x 30 and 50 x 20 mm x 100 mm long, end-sealed) was undertaken using the Massey University 200 MHz, 10 cm horizontal widebore 4.7 T, Oxford magnet interfaced to a TecMag system running MacNMR (Eccles *et al.*, 1998).

Samples were dried at 80 °C in a drying oven, removed and imaged at intervals during the drying. Every effort was made to replace the sample in a similar orientation inside the coil for each imaging run.

7.2.1 AZEOTROPIC DRYING

A sample of 30 x 50 mm radiata pine (end-sealed) was azeotropically dried at 84 °C in refluxing toluene using a Dean and Stark apparatus to measure loss of water. For imaging the sample was removed from the refluxing toluene, the surface toluene allowed to evaporate and then the sample wrapped in GladWrap® (a polyethylene lunch wrap) and placed in the 200 MHz horizontal bore magnet for imaging.

7.3 DIFFUSION TENSOR IMAGING

Diffusion tensor imaging was performed on the 8 mm^2 x 90 mm samples of green radiata pine sapwood in order to visualise any restriction to diffusion. Diffusion weighting was applied *via* a quantitative PFGSE preparative pulse train separated from the spatial selection component, comprising of a standard spin echo imaging sequence (section 5.2.2). This was done to minimise artefact generation by cross-terms between the imaging and diffusion gradients.

7.4 MOVEMENT AND NATURE OF WATER DURING DRYING OF RADIATA

7.4.1 BULK MOVEMENT OF WATER

7.4.1.1 Small Scale Samples

The result of using ^{1}H NMR imaging to follow the mass transport of water during drying is shown in Figure 7.3. High water density appears bright white and regions of low water density (drier regions) appear as black.

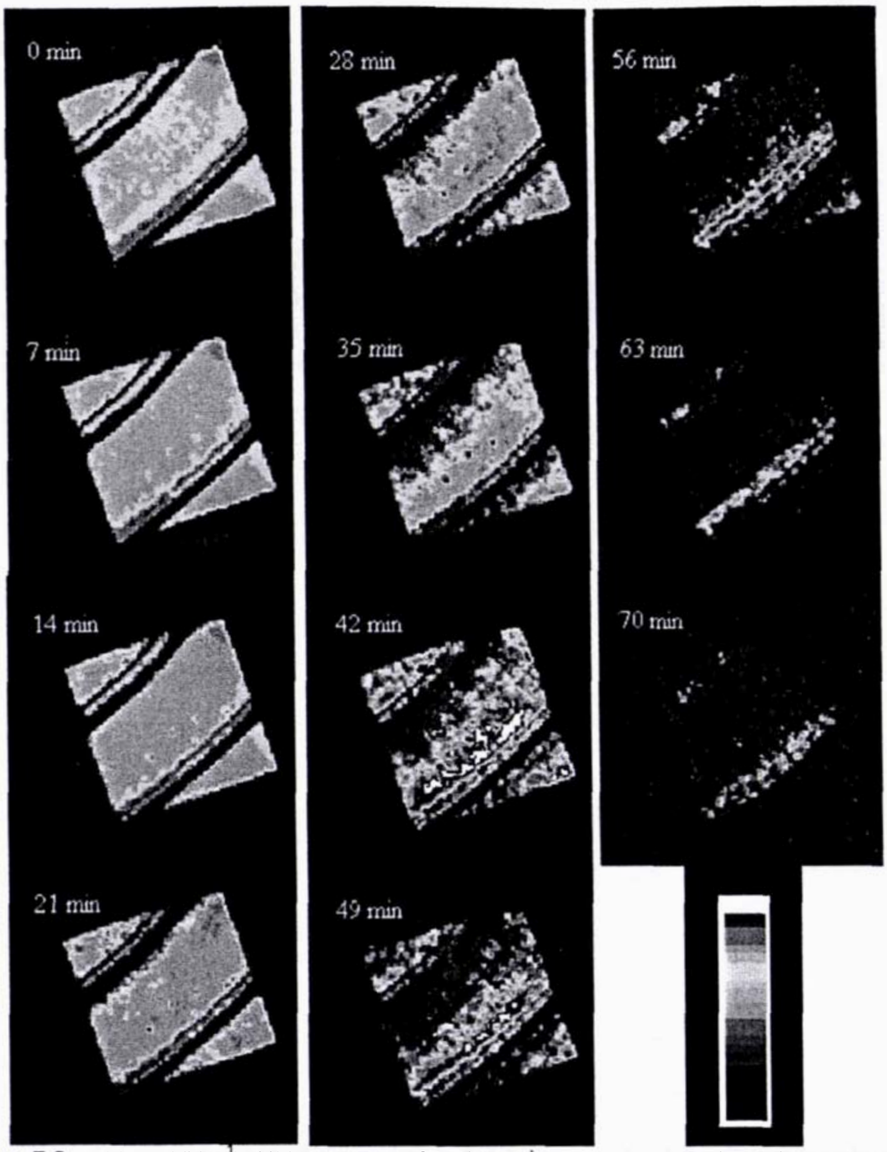

Figure 7.3. 300.13 MHz ^{1}H NMR images of radiata pine sample at 7 minute intervals during drying at 60°C. (The direction of the pith is located upper left of the image). [AMX-300, spin echo, 128x128, FOV 15 mm, 1 mm slice, T_E 6.5 ms, T_R 500 ms].

The drying process evident in Figure 7.3 is indicative of anisotropic migration of water. In particular the images suggest that water does not move from earlywood into the latewood of the previous annual ring nor does water move tangentially within the earlywood to the nearest drying surface. If this were the case it would be observed in the ^{1}H NMR image as uniform drying from the edges of the sample towards the core (i.e. the dry region of low water density, (black in image) would appear to form at the edge of the image and extend inwards to the core). A schematic representation of this situation is shown in Figure 7.4.

One possible model that would be consistent with Figure 7.3 is as follows. Once water begins to be removed from the surface of the sample, water is drawn radially from the earlywood towards the associated latewood (that latewood which occurs immediately after the earlywood within an annual ring). Water leaves the sample *via* the latewood causing more water to be drawn towards the latewood. This is evidenced in the time series from 14 minutes through to 70 minutes. The dry zone (black) within the middle annual ring appears to move as a uniform front towards the latewood in the lower right of the sample. The earlywood immediately bordering the associated latewood is always high in water density (appearing white) indicating that while water is lost from the latewood ring there is a constant renewal of water density as water is drawn to the latewood.

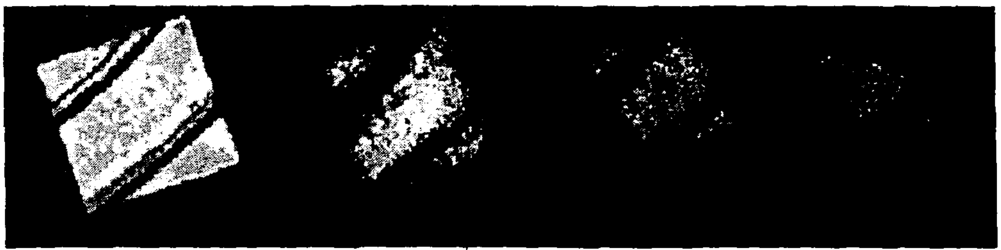

Figure 7.4. Schematic representation of ^{1}H NMR images during drying of radiata pine wood if water movement was multi-directional to all drying surfaces via a core-shell model.

7.4.1.2 Large Scale Samples

7.4.1.2.1 Conventional Drying

The phenomenon observed on the 8 x 8 x 90 mm samples could in part be due to the scale of sample. To investigate this phenomenon further, larger samples with differing surface area/volume (SAV) ratios and with differing orientation of the annual rings were imaged. Olsen *et al.* (1990) showed a faster rate of drying for thin white oak boards and alluded to a dependence on the annual ring orientation, although it was difficult to determine, as they were unable to recover thick boards showing true flat-sawn orientation from the small diameter logs used. Large diameter radiata pine logs are able to produce large volume boards with true flat-sawn orientation as used in this study. Figure 7.5 shows ^{1}H NMR images obtained at intervals during the 80° drying of 20 x 50 mm radiata pine sapwood (surface area to volume ratio = 0.140 mm^{-1}) sawn in flat or quarter-sawn fashion (Olsen, 1986) while Figure 7.6 shows the similar drying of 30 x 50 mm flat or quarter-sawn radiata pine sapwood (surface area to volume ratio = 0.106 mm^{-1}). By comparison the surface area to volume ratio for the smaller 8 x 8 x 90 mm samples is 0.5 mm^{-1}.

While it would be desirable to model the movement of water with respect to the time series it is not possible in the present study as the samples were removed for further drying between images. While every attempt was made to replace the sample in the same orientation, small differences in the orientation render pixel-by-pixel analysis impossible.

Due to the long echo times used on the 200 MHz imaging system (10 – 15 ms) it is difficult to obtain images as the moisture content of the samples approaches the fibre saturation point (~30 % MC od for radiata pine (Kininmonth, 1991)) since the T_2 value of the water bound in the cell wall is very short (10^{-3} s, Araujo *et al.*, 1992).

By following the loss of water in 20 x 50 mm radiata pine sapwood samples (Figure 7.5), it is seen that in the flat-sawn boards there is again evidence of oriented flow of water. The latewood appears to act as a boundary to flow, channelling the water tangentially along the latewood/earlywood boundary towards the drying surface. This behaviour is not what is expected from core-shell drying models.

By comparison, the loss of water in the quarter-sawn 20 x 50 mm boards show more of a conventional core-shell drying regime. Water still flows to the latewood boundary and is channelled towards the drying surface. In this instance however the annual rings are perpendicular to the larger of the drying faces and there does not appear to be as great a restriction to flow.

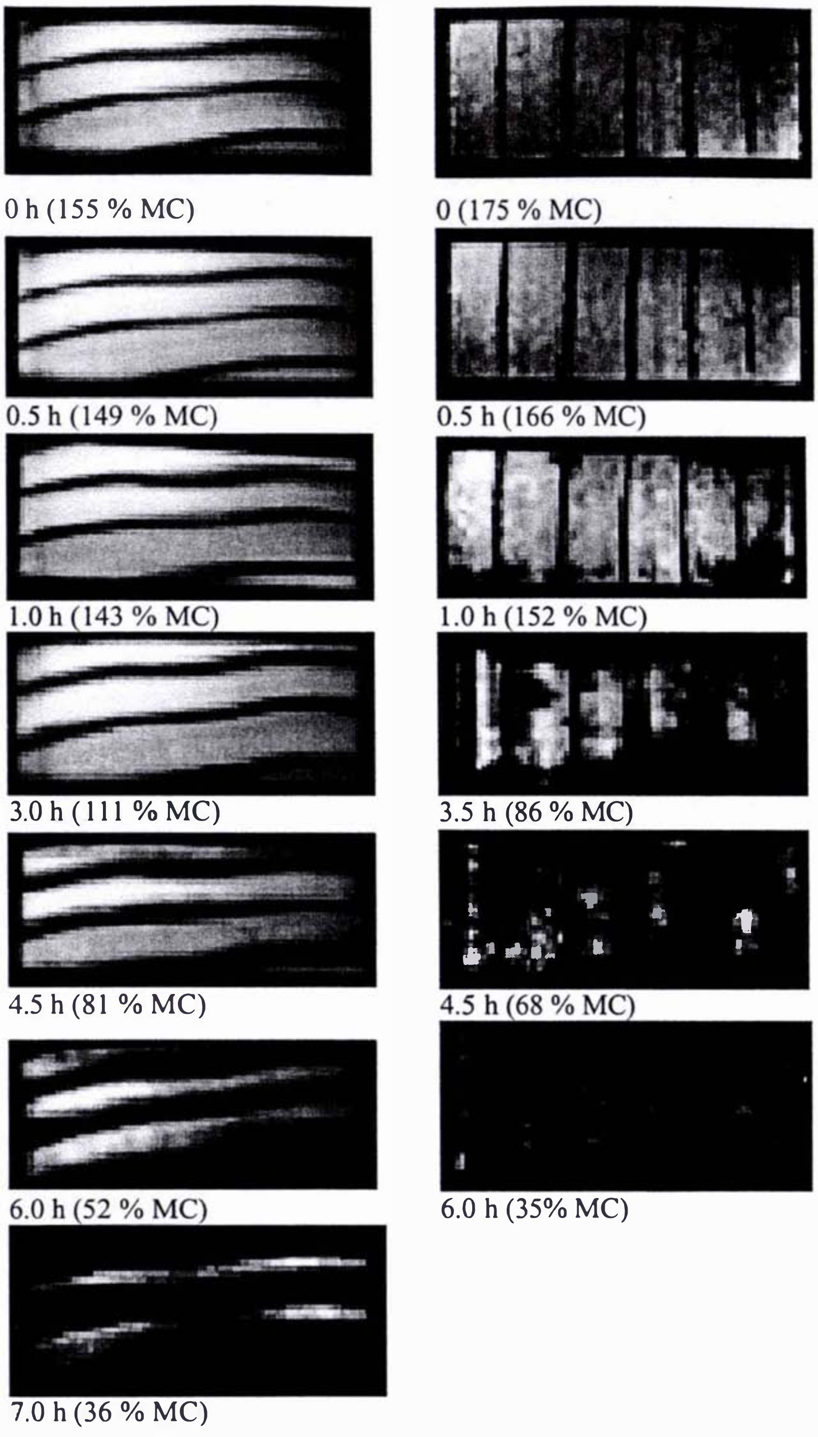

0 h (155 % MC)

0 (175 % MC)

0.5 h (149 % MC)

0.5 h (166 % MC)

1.0 h (143 % MC)

1.0 h (152 % MC)

3.0 h (111 % MC)

3.5 h (86 % MC)

4.5 h (81 % MC)

4.5 h (68 % MC)

6.0 h (52 % MC)

6.0 h (35% MC)

7.0 h (36 % MC)

Figure 7.5. ^{1}H NMR images of flat-sawn (left) and quarter-sawn (right) 20 x 50 mm radiata during drying at 80°C. [Oxford/TecMag 200, spin echo, 128x128, FOV 70 mm, 2 mm slice, T_E 10 ms, T_R 500 ms].

In further contrast to that observed for the drying of 20 x 50 mm boards (SAV = 0.140 mm^{-1}), the drying of 30 x 50 mm boards, which have a lower surface area to volume ratio (SAV = 0.106 mm^{-1}) shows a more conventional type of core-shell drying for both quarter-sawn and flat-sawn boards (Figure 7.6).

Pang (1996a) has shown from experimental and modelling data on large radiata pine samples that a large moisture gradient is developed across the thickness of flat-sawn 100 x 50 mm radiata pine (SAV = 0.060 mm^{-1}), with the moisture content in the outer 5 mm layer being 6-7% while the moisture content from a depth of 5 mm into the core is in the range of 70-100%. From the results obtained in this study it would be concluded that the larger 100 x 50 mm boards, having a low SAV ratio, would display a core-shell drying profile, which was indeed what was observed (Pang, 1996a).

In this current study, the thinner 20 x 50 mm flat-sawn board shows anomalous drying behaviour attributed to a greater restriction to water transport than the thicker 30 x 50 mm board, as evidenced by the apparent barrier at the earlywood/latewood boundary. The denser latewood is less permeable than the earlywood by a factor of ~12 (Booker, 1991, 2001), forming a barrier to diffusive transport. During initial drying of sapwood, the outer and core temperatures are similar and it is not until drying progresses that a drying gradient develops (Pang *et al.*, 1994). When the temperature increases the rate of diffusion also increases (Bramhall, 1979; Walker, 1993) such that the barrier is overcome and diffusive drying occurs across the latewood boundary. Restriction to flow in quarter-sawn boards is not an issue, irrespective of size, as the rings are oriented parallel to the plane of restriction so that the higher density latewood is not a barrier.

In order to investigate further the apparent barrier formed by the latewood boundary, diffusion tensor imaging of diffusion anisotropy was undertaken, with the results being presented in the next section.

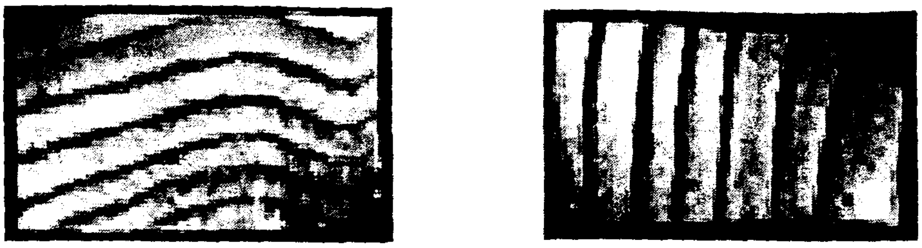

0 h (165% MC)

0 h (145% MC)

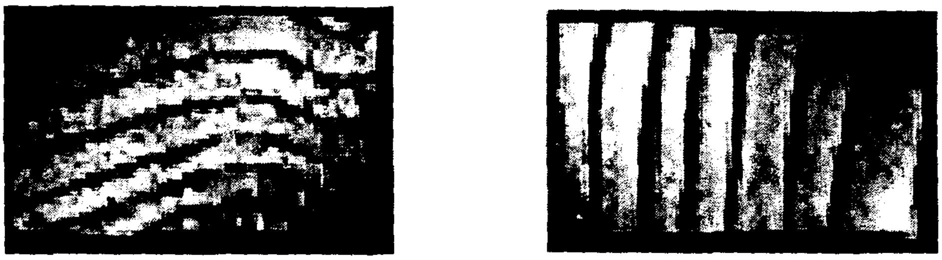

1.0 h (144% MC)

1.0 h (135% MC)

3.5 h (106% MC)

3.5 h (89% MC)

5.0 h (89% MC)

5.5 h (71% MC)

7.0 h (76% MC)

7.5 h (48% MC)

Figure 7.6. ^{1}H NMR images of flat-sawn (left) and quarter-sawn (right) 30 x 50 mm radiata during drying at 80°C. [Conditions as per Figure 8.5].

7.4.2 ANISOTROPIC DIFFUSION

The results so far indicate that there is oriented flow of water during drying of lumber. Diffusion tensor imaging would allow us to visualise the direction of greatest and least restriction to flow if diffusion is indeed anisotropic. This must be performed as a passive experiment without drying, as any dehydration of the sample during the experiment would bias the images over time as water was removed. Samples of green radiata pine sapwood 8 x 8 x 90 mm were used for this trial.

A series of seven images were acquired using a pre-weighted diffusion imaging sequence, with the PFGSE preparation separated from the spatial imaging component of the pulse sequence. Linear combinations of the diffusion gradients as outlined in section 3.5.3 were used. The seven resulting images are presented in Figure 7.7 along with the corresponding diffusion tensor images.

For the experimental conditions used, $\Delta = 12$ ms, $\delta = 2$ ms and $G = 0.35 \text{ T m}^{-1}$, then the *b*-factor in the Stejskal-Tanner equation (equation 3.32) is $b = 3.9 \times 10^{10} \text{ s m}^{-2}$.

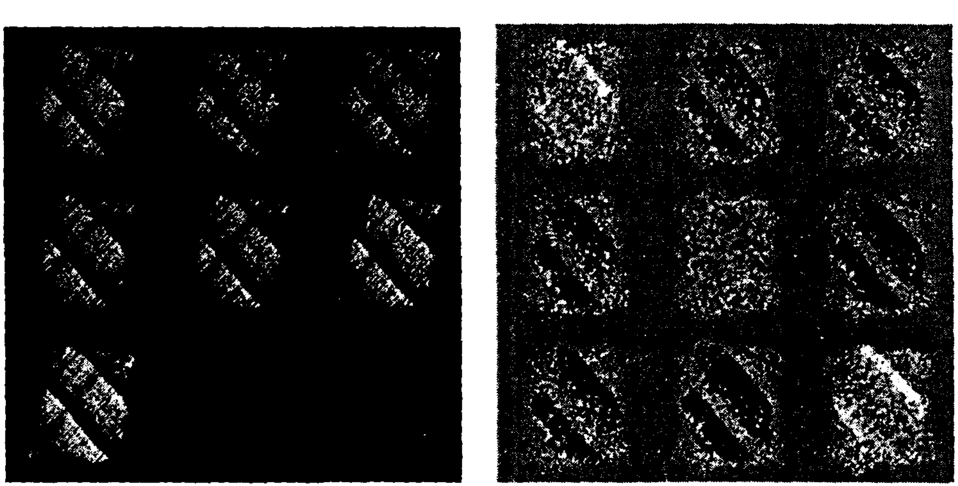

Figure 7.7. Seven diffusion images (left) corresponding to each of the diffusion gradient combinations outlined in §3.5.3. The diffusion tensor map (right) corresponds to the nine elements of the diffusion tensor (eqn 3.35). [AMX-300, DIFF-SE, 128x128, FOV 15 mm, 1 mm slice, T_E 6.5 ms, T_R 750 ms, Δ 12 ms, δ 3 ms, G 0.35 T/m].

The Eigenvalues calculated from the diffusion tensor map are presented in Figure 7.8. This figure shows the relative magnitude of the diffusion in the three axes. Not surprisingly the greatest diffusion occurs in the longitudinal (3) axis which is the long axis of the wood fibre and the direction of active transport up the stem of a tree. When the Eigenvalues are computed for the *x* and *y* directions only it can be seen that there is greater diffusion in the *y* direction. In order to visualise the direction of minimum diffusion, that is the direction with the highest restriction to self diffusion, a quiver plot was prepared from the Eigenvectors (Figure 7.9).

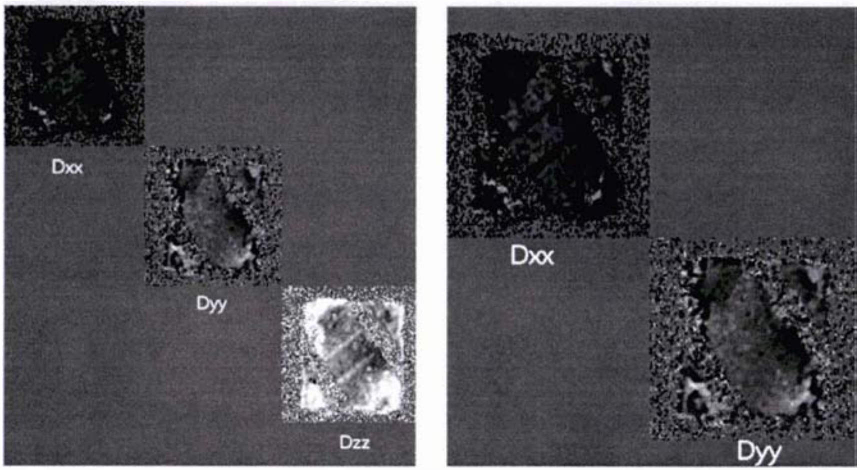

Figure 7.8. Eigenvalue maps taken from the diffusion tensor maps for (left) the three primary axes and (right) an expansion of the x and y directions only.

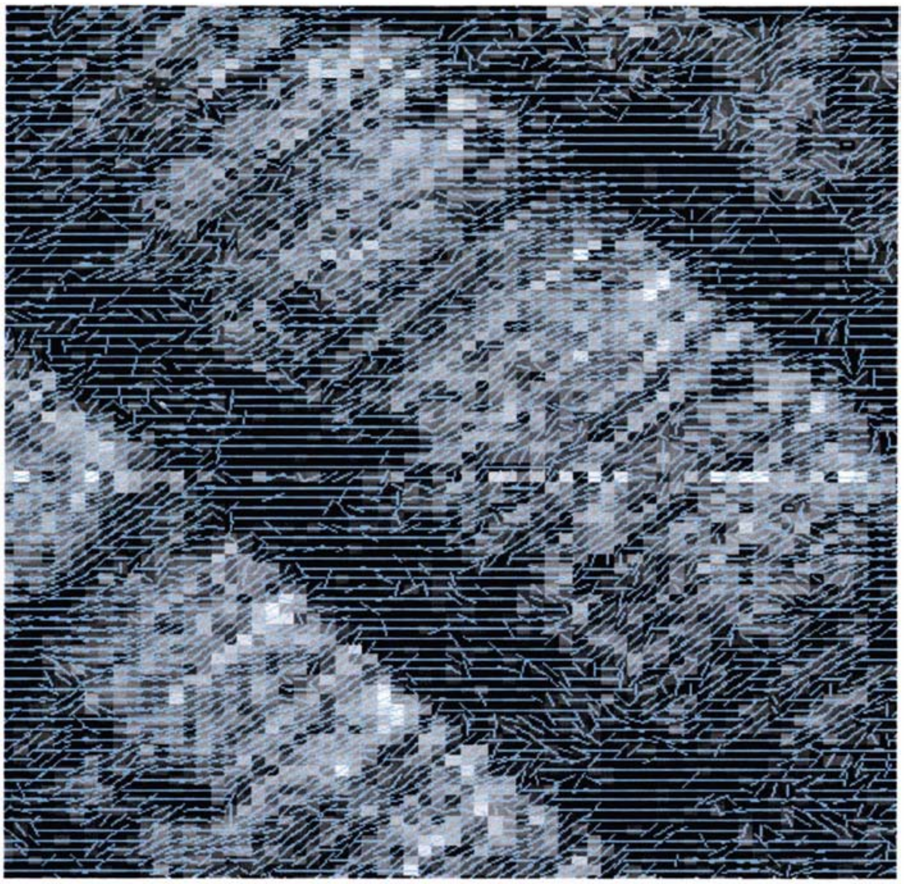

Figure 7.9. Quiver plot of Eigenvectors showing direction of minimum diffusion.

The quiver plot shows the direction of minimum diffusion (parallel to the quivers) as being across the annual ring. There is a region of indeterminate diffusion anisotropy in the centre of the central annual ring. This could be due to the presence of ray cells which facilitate trans-annular ring flow, thereby enhancing local diffusion across the ring to a point where it is comparable with the diffusion parallel to the rings. It would also indicate axial symmetry resulting in isotropic diffusion, as would be expected in the larger earlywood lumens with an internal diameter in the range 20-30 μm. The superimposition of all three diagonal elements of the diffusion tensor can provide a measure of the mean magnitude of diffusion and this is shown in Figure 7.10. The region with highest restriction to diffusion occurs at the earlywood/latewood transition (shown as purple and blue). This suggests that there is a restriction to steady state flow in this region and it is proposed that this restriction would continue to be present under a drying gradient.

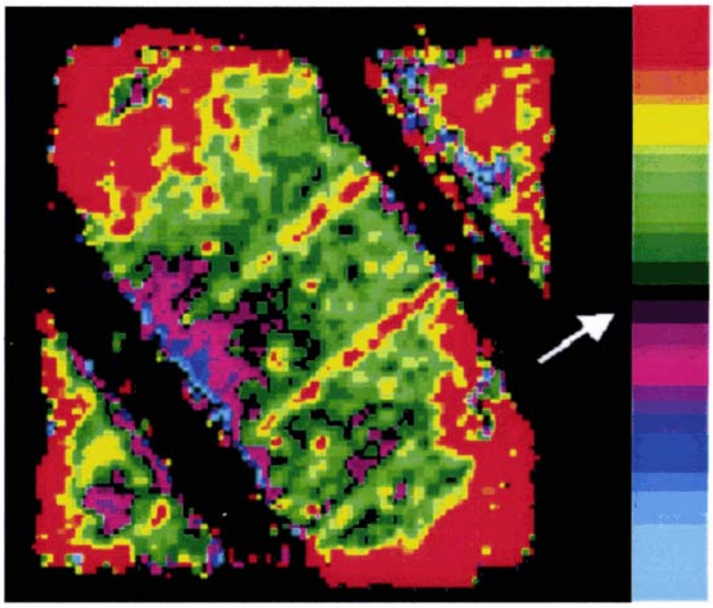

Figure 7.10. Diffusion image showing restriction to diffusion (purple to blue) adjacent to the latewood and high diffusion in the earlywood and at the surfaces and in the rays (green to red). The arrow indicates the direction of the pith.

A second sample having three latewood bands running diagonally across the sample shows similar results for the direction of minimum diffusion as being transverse across the earlywood ring (Figure 7.11).

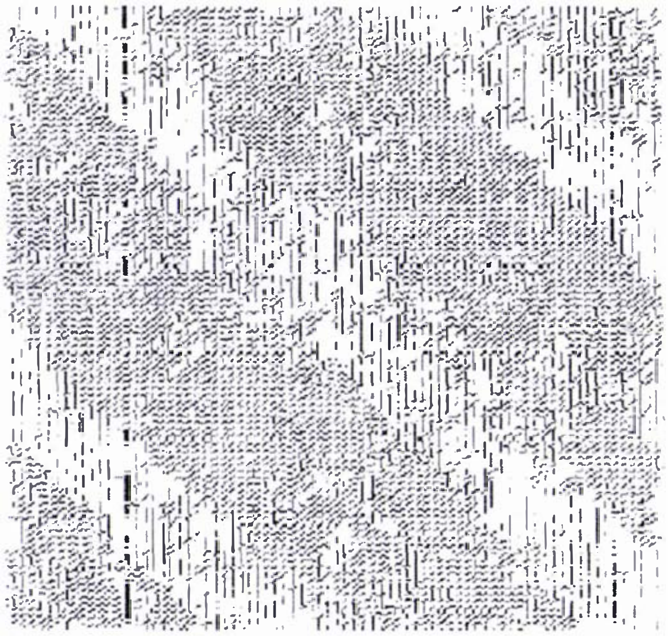

Figure 7.11. Quiver plot of Eigenvectors showing direction of minimum diffusion for a second sample.

It would be helpful to obtain similar data on larger, more representative samples, similar to those used for the large scale drying. However the gradient amplifiers on the 200 MHz horizontal imaging system were not of sufficient power to produce the gradient strengths required to perform diffusion imaging on the large samples. This is work that should and could be revisited using a more suitable system.

The results of the diffusion tensor imaging and the anisotropy observed, supports the observation of restricted water movement in flat-sawn boards, particularly those with a high surface area to volume ratio (20 x 50 mm, SAV = 0.140 mm^{-1}). The latewood provides a boundary to flow due to its increased density.

7.4.3 AZEOTROPIC DRYING

Investigations into the azeotropic drying as a means of drying wood shows some potential for not only removing water from wood, but also as a means of simultaneously impregnating wood with chemicals to impart preservative efficacy, fire retardancy or dimensional stability. By using a solvent system that azeotropes with water, such as toluene, water can be removed without causing pit closure. This ensures that it is possible to introduce chemicals into the wood without excessive use of vacuum/pressure schedules that are required when the pits close during conventional drying. Figure 7.12 shows the comparative drying of a 30 x 50 mm sample of radiata pine sapwood using a toluene azeotrope drying process.

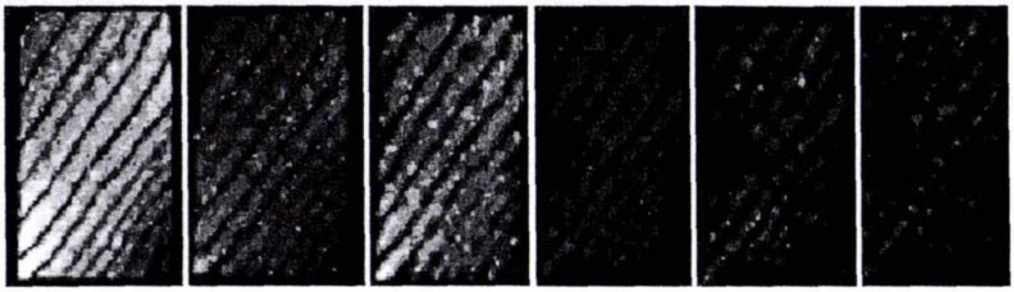

Time (min)	0	25	35	50	65	80
Water loss (mL)	0	14	23	43	58	73

Figure 7.12. 200.1 MHz ^{1}H NMR images of quarter-sawn 30 x 50 mm radiata pine taken at intervals during azeotropic drying using toluene. [Oxford/TecMag 200, spin echo, 128x128, FOV 70 mm, 2 mm slice, T_E 10 ms, T_R 500 ms].

It can be seen from the series of images that drying occurs more evenly throughout the sample and that there does not appear to be any structured movement of water as observed in samples dried by conventional means. This would suggest that there is little restriction to the movement of water in this sample.

The loss of water with respect to duration of drying for the conventionally dried and azeotropically dried samples is shown in Figure 7.13 and shows similar rates of drying for conventionally dried radiata pine samples irrespective of the SAV ratio of the samples and the orientation of the annual rings. It does however show a much more rapid loss of water from the azeotropically dried sample than from the conventionally dried samples (0.96 g/min *vs* ~0.25 g/min respectively). The reason for this could be due to the non-aspiration of the pits during the solvent based drying allowing greater mass transport (Singh, 2001) and the benefit that drying should proceed *via* a liquid transport mechanism for the entire duration of water removal as the toluene is able to provide a continuous phase allowing drying to proceed via capillary action and not depending on the slower diffusion controlled drying that occurs below fibre saturation.

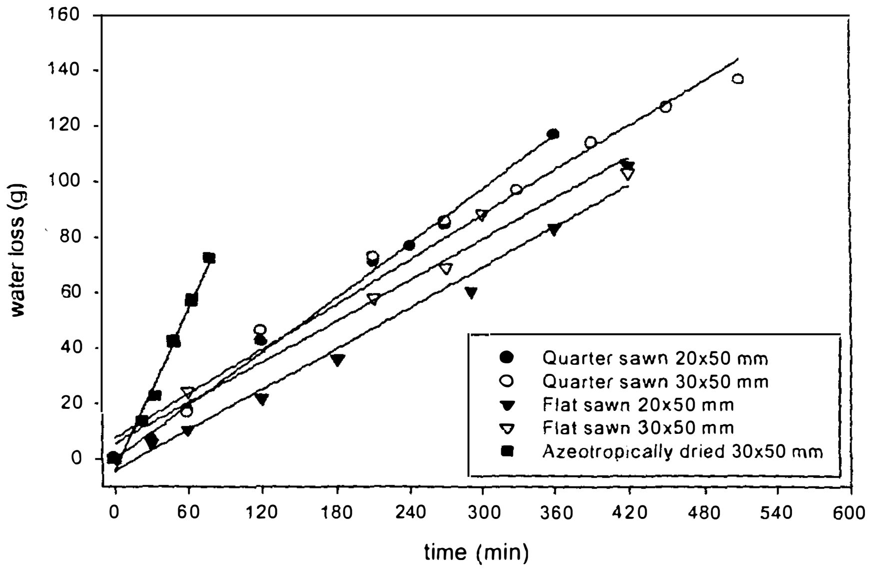

Figure 7.13. Water loss from drying samples for conventionally dried and azeotropically dried radiata pine wood.

Overall the flat-sawn 20 x 50 mm sample has the lowest loss of water, albeit at approximately the same rate of loss as the other conventionally dried samples. This too is consistent with there being a restriction to mass transport of water in flat-sawn lumber with high SAV ratios.

7.4.4 WATER RELAXATION

NMR spin relaxation measurements of water during drying were performed on the large, conventionally dried samples. The purpose of these measurements was to determine whether or not rotational mobility of the water molecules (as indicated by spin relaxation rates) differs across the annual rings. Relaxation maps were calculated using the software package Prospa[†], on an iMac computer. Below fibre saturation it was difficult to obtain images on the TecMag/Oxford 200 with sufficient signal, as the

---

[†] *Pro*cessing *Pac*kage developed by C. Eccles, NMR Group, IFS-Physics. Massey University, New Zealand. A PC version is soon to be available.

T_2 of wood below fibre saturation is very short (10^{-3} s, Araujo *et al.*, 1994) and the minimum practical echo time for imaging was 10 ms.

Unlike the relaxation measurements of Araujo *et al.* (1994) and Xu *et al.* (1996) on the bulk samples, whereby multi-exponential fits were made to the data in order to obtain the single exponentials, multi-exponential fits of the image data was not performed and as such represents the distribution of single exponentials present.

7.4.4.1 T₁

Relaxation maps for T_1 were calculated from a series of single-slice, single-echo images with increasing repetition times, T_R, using the conditions described in the caption of Figure 7.14. The T_1 maps show lower values of T_1 in the latewood regions at both 155% and 52% moisture content. The high intensity spike observed on the lower right of the T_1 map at 155% MC is due to surface water on the sample.

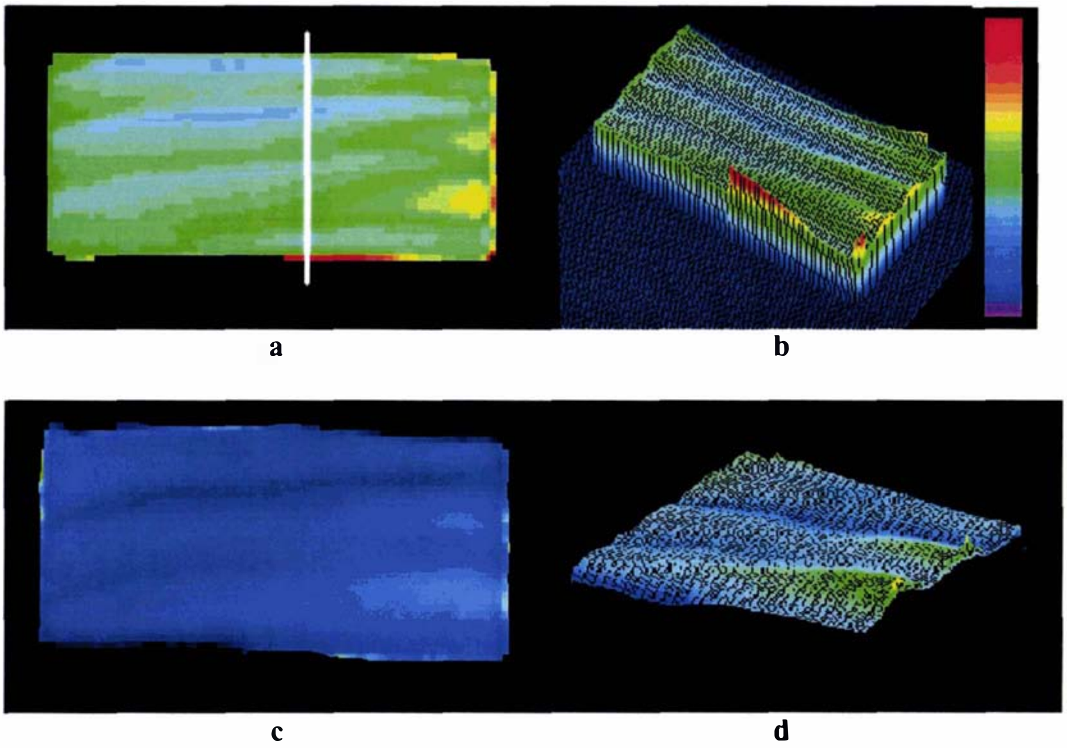

Figure 7.14. T_1 relaxation maps of flat-sawn 20 x 50 mm radiata pine sapwood during drying at 80°C: (a) intensity plot and (b) surface plot at 155% MC; (c) intensity plot and (d) surface plot at 52% MC. The white line in (a) shows the approximate transect position at which a profile of T_2 values were extracted (Figure 7.15). [Oxford/ TecMag 200, spin echo, 128x128, FOV 70 mm, 2 mm slice, T_E 10 ms, T_R 50, 100, 200, 400, 800, 1600, 3200 ms].

A transect of T_1 values across the sample at a position illustrated in Figure 7.14.a, for the two moisture contents is presented in Figure 7.15. This shows latewood T_1 values in green radiata pine earlywood to be in the range of 600-750 ms (ignoring the spike at the surface) whereas the T_1 value for green latewood is between 550 and 600 ms. This is consistent with observations by Xu *et al.* (1996) where they established a direct relationship between T_1 relaxation and the localised basic wood density in western red-cedar and western hemlock (*Tsuga heterophylla*). For radiata pine the average latewood density is 550 kg m^{-3} and that for earlywood is 350 kg m^{-3}, which is within 10% of that for western hemlock (Cown and Parker, 1978). Other studies show the same general trend for higher T_1 values in the earlywood (Hall *et al.*, 1986a,b; MacKay *et al.*, 1988, Menon *et al.*, 1989).

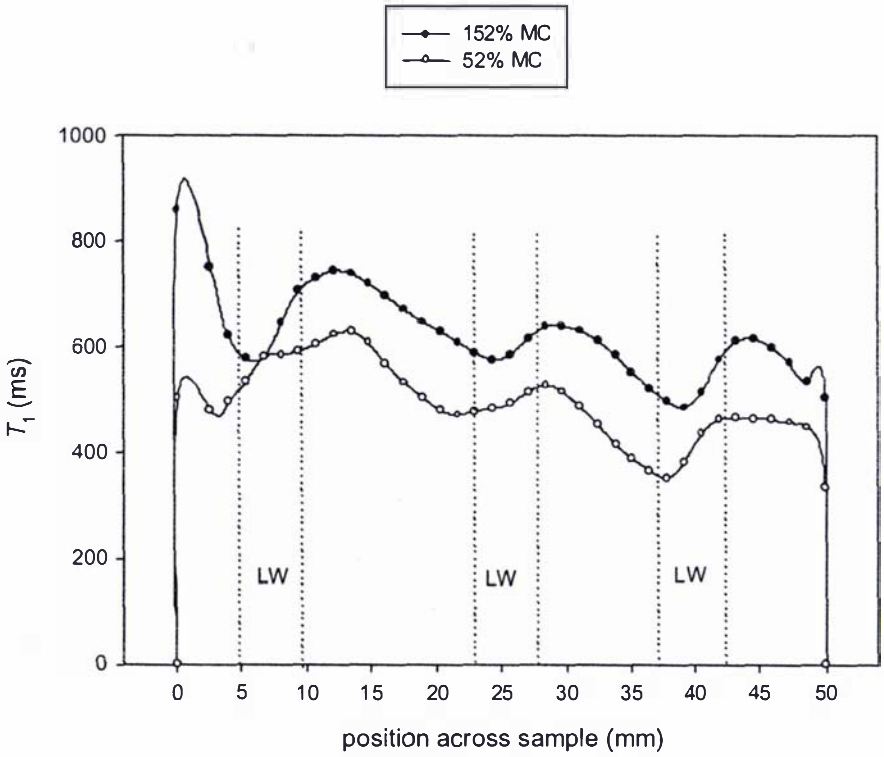

Figure 7.15. T_1 values obtained from transect position across a T_1 map of flat-sawn 20 x 50 mm radiata pine (Figure 7.14) at varying moisture contents during a drying run at 80°C. The approximate positions of the latewood (LW) bands are indicated by dotted lines.

7.4.4.2 T_2

Relaxation maps for T_2 were calculated using a series of images with increasing echo times, T_E, using the conditions outlined in the caption of Figure 7.16. Images were acquired using multiple, single-slice, single-echo acquisitions rather than a multi-echo sequence, as the multi-echo sequence was not stable on the Oxford/ TecMag 200.

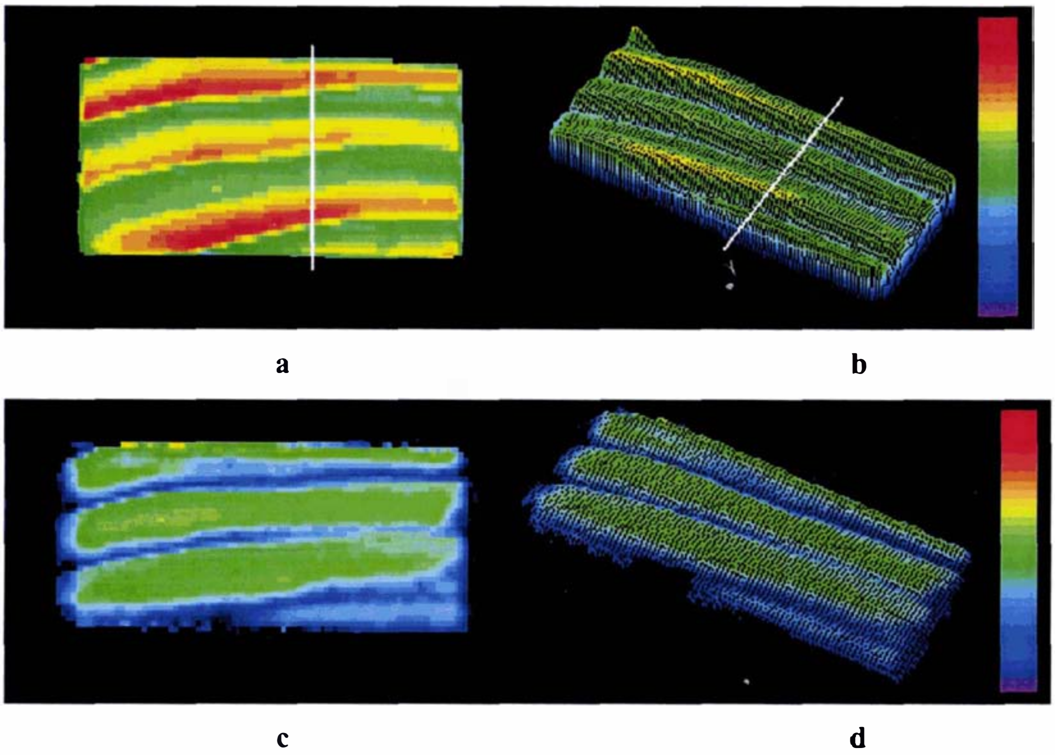

Figure 7.16. T_2 relaxation maps of flat-sawn 20 x 50 mm radiata pine sapwood during drying at 80°C: (a) intensity plot and (b) surface plot at 155% MC; (c) intensity plot and (d) surface plot at 52% MC. The white lines in (a) and (b) show the approximate transect position at which T_2 values were extracted (Figure 7.17). [Oxford/ Techmag 200, spin echo, 128x128, FOV 70 mm, 2 mm slice, T_R 3200 ms, T_E 10, 20, 40, 60, 80, 100, 120, 150 ms].

A transect of T_2 values was taken across the sample at the position indicated in Figure 7.16.a. This was performed on the fresh sample at 155% MC and again towards the end of the drying run at 52% MC. The data obtained are shown in Figure 7.17. As with the T_1 data it shows lower values for T_2 in the latewood than in the earlywood. The lower values are associated with the higher density wood cells, which have smaller lumen and thicker cell walls. This means that the corresponding proportion of cell-wall water to free lumen water is higher in the latewood.

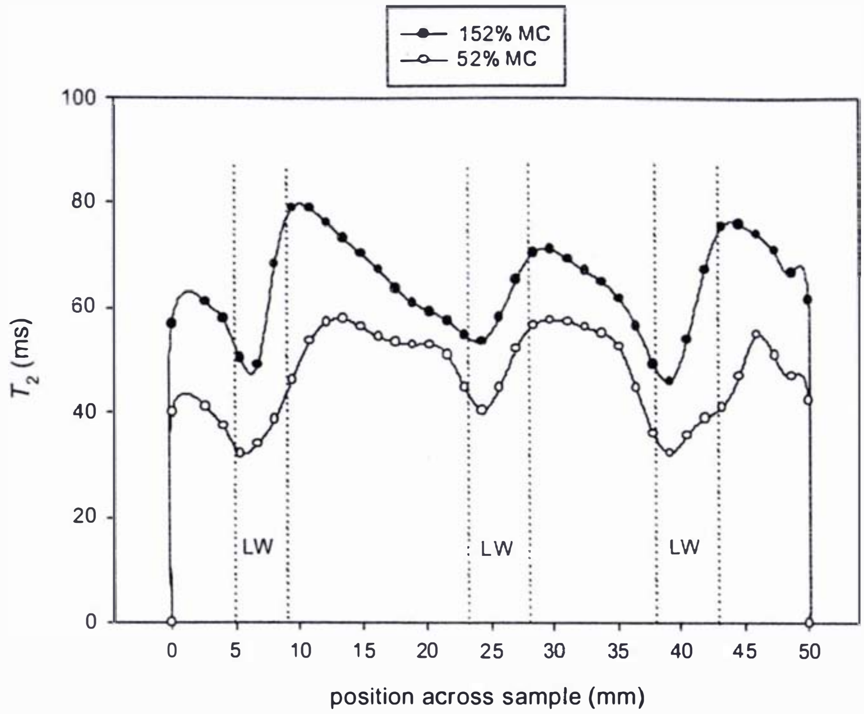

Figure 7.17. T_2 values obtained from transect position across a T_2 map of flat-sawn 20x50 mm radiata pine (Figure 7.16) at varying moisture contents during a drying run at 80°C. The approximate positions of the latewood bands (LW) are indicated by dotted lines.

The T_1 and T_2 relaxation maps show regular variation with local density in transecting the latewood and earlywood. As the lumen water is removed the relaxation values decrease as the cell-wall water becomes the more dominant exponential decay.

7.5 INTERNAL CHECK FORMATION

Pith-to-bark strips were selected from breast height half-disks of trees that were prone to internal check formation and from trees that were nominally free from checking. The half-disks were pre-selected from samples that had been assessed on the matching half-disk, using the ***Forest Research*** in-house accelerated disk drying method developed by McConchie and McConchie (1999). This test accelerates the formation of checks so that the disks can be assessed for the presence and severity of checking by tallying the number of checks per annual ring (Figure 7.18).

For NMR relaxation measurements, the matching green half disk was sub-sampled by collecting the shavings obtained from drilling a hole in the annual ring using a drill press. This enabled sampling of fresh green wood samples on an annual-ring-by-annual-ring basis from the pith-to-bark strips. The shavings were packed into 7 mm OD ZrO rotors for NMR relaxation analysis. The samples were spun at 50 Hz in the MAS accessory.

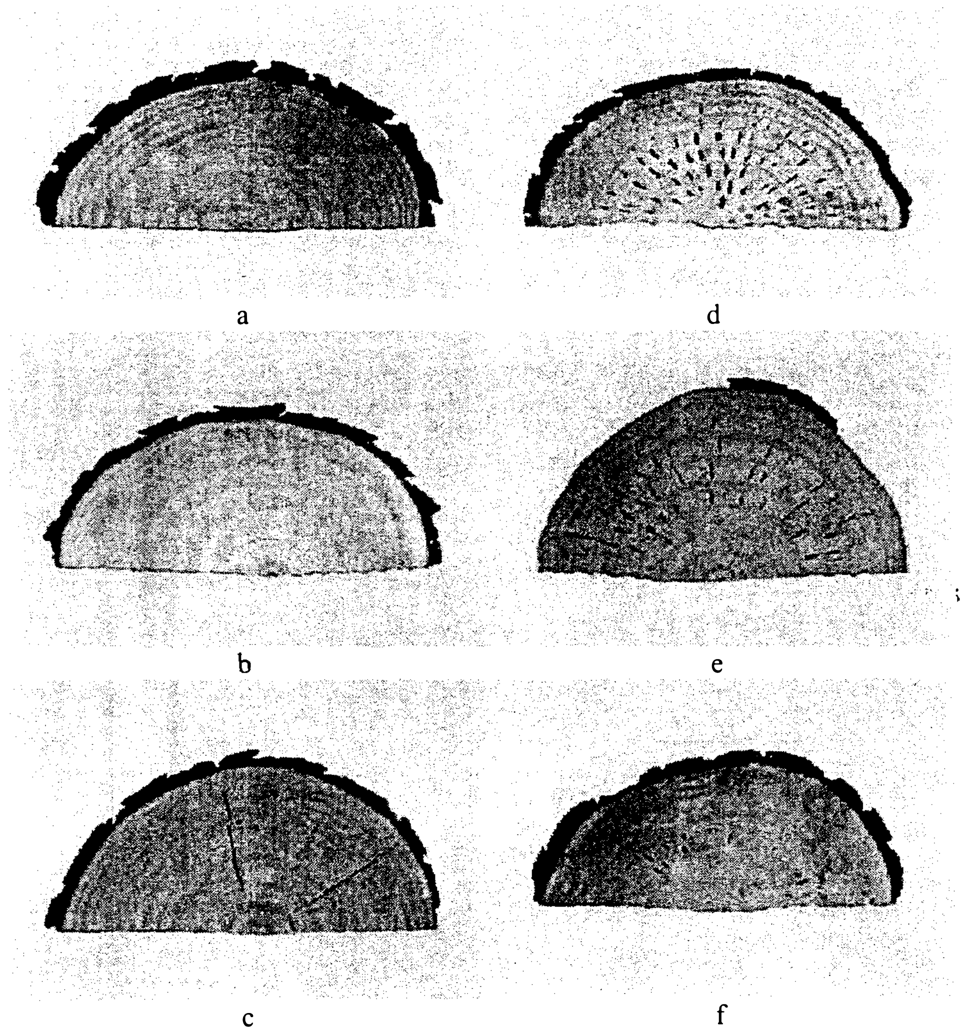

Figure 7.18. Photographs of the disks from the accelerated drying test showing samples that did not form checks (a-c) and those that did form checks (d-f). The large cracks that appear on sample c are not regarded as internal checks and have a different mechanism of formation.

Measurement of T_1 and T_2 relaxation times for each annual ring sample was undertaken using the modified inversion recovery sequence of Xu *et al.* (1996) for T_1 and a standard CPMG sequence for T_2. Table 7.1 provides the tally of checks per ring for the checked samples.

Table 7.1. Tally of internal checks per annual ring for checked samples in Figure 7.18.

	Ring Number									
	Pith	**2**	**3**	**4**	**5**	**6**	**7**	**8**	**9**	**10**
B5			1	7	14	19	19	15	15	9
B7				2	12	18	15	9		
B14						6	8			1

The one factor to be aware of when reporting the incidence of checking is that although a sample may not show evidence of checking it does not mean that the sample is not prone to check formation. Therein lies the quandary of predicting a negative event. This fact must be kept in mind when analysing the results of predicting the propensity to check by instrumental means, in particular when the level of checking is low or zero.

^{13}C CP/MAS NMR spectra were acquired on a reduced number of samples selected to represent the range of checking severity. Twelve samples were selected in total, the limiting factor being the time taken to acquire spectra of sufficient signal to noise ratio. Spectra were acquired according to standard conditions previously detailed (section 5.1.2.).

In order to reduce the size of the data matrix, and in order to extract the key variances governing any correlation of spectral data with checking intensity, projection to latent structures (PLS) regression has been employed. From chapter four it has been shown that PLS regression is able to reduce the spectral variances to a linear combination of principal components, or latent variables (eqn 4.2). In turn the resulting latent variables can be interrogated to provide an insight into chemical basis underlying the material property being investigated, in this instance the formation of internal checks on drying.

Projection to latent structures regression of ^{13}C CP/MAS NMR spectra with the number of checks per ring however shows a strong correlation as shown in Figure 7.19 (number of samples, n = 12, R^2 = 0.93, 3 latent variables). The standard error of prediction (SEP) for the validation is 2.4, indicating that the error in prediction of the number of checks is ± 2.4 checks. While this is not acceptable when trying to identify samples that are not prone to check formation, it is acceptable when predicting the severe incidence of checking. It must also be recalled that while the sample does not appear to have checked, the spectral "signature" would still indicate that it is in fact prone to check formation.

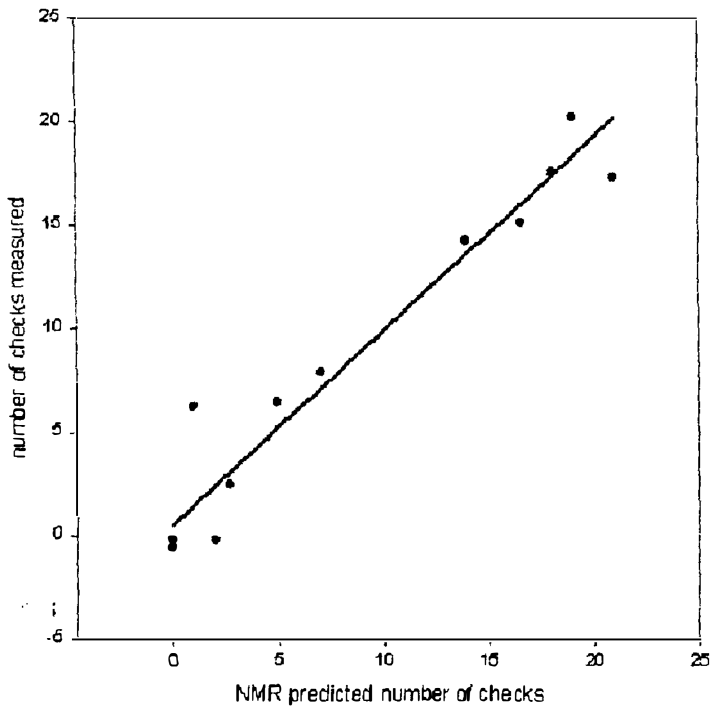

Figure 7.19. Predicted versus measured plot for the incidence of checking per ring based on ^{13}C CP/MAS NMR spectra. (number of samples, n = 12, R^2 = 0.93, 3 latent variables, SEP = 2.4).

The ability to identify material that is highly prone to checking is however, a highly useful and sought after tool, as it would allow processors to divert the highly check-prone material from processing streams that are sensitive to the presence of internal checks, namely visual grade lumber for mouldings. However, the drawback is that the instrument time is the order of hours per sample prohibiting the application of NMR as a rapid screening tool. At present this capability must remain the tool of the researcher.

As a tool for the research scientist, the information gained can be used to further our understanding of the formation of checks. Interrogation of the results from the PLS regression allows us to look at the key resonances within the ^{13}C MAS NMR spectrum (Figure 7.20) that lead to the prediction of checking. Interpretation of those resonances, as presented in the loadings weights, allows chemical meaning to be imparted to the mode of check formation. The loading weights for the first three latent variables are shown in Figure 7.21. This shows the weighting for each resonance and its contribution to the prediction model.

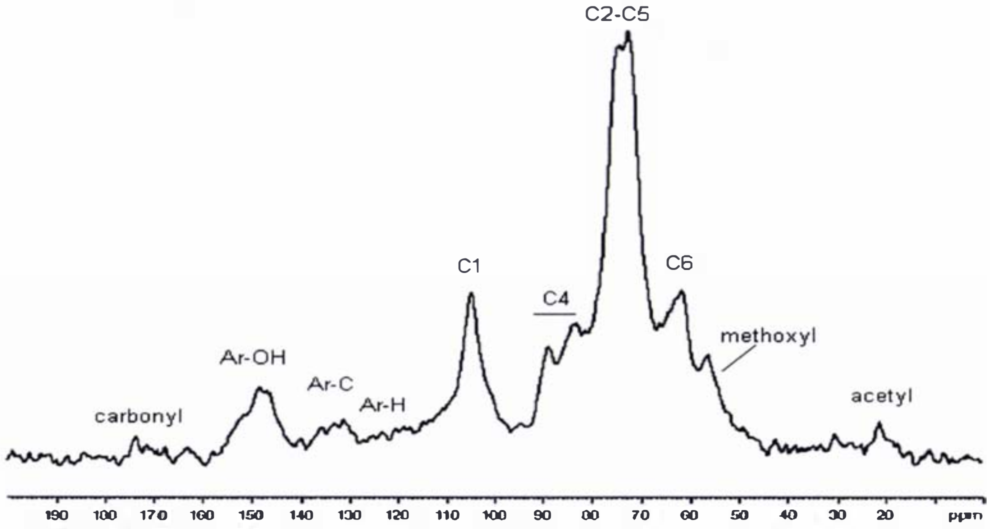

Figure 7.20. 50.3 MHz ^{13}C CP/MAS NMR spectrum of radiata pine sapwood.

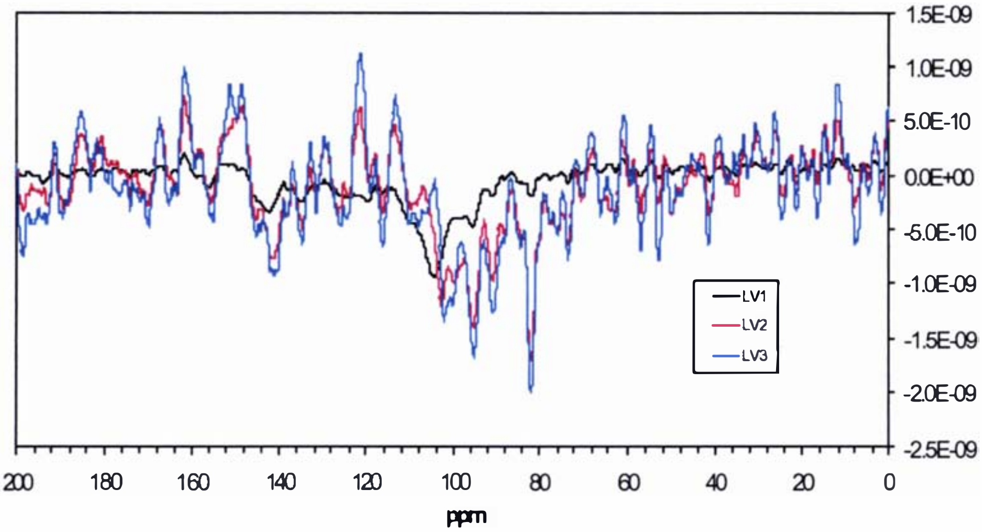

Figure 7.21. Loading weights for the first three latent variables used in the prediction of checking severity based on ^{13}C CP/MAS NMR spectra.

The first latent variable indicates that the greatest contribution towards the prediction is due to carbohydrate, specifically the anomeric carbon resonance at *ca.* 104 ppm is the primary loading. Loadings for subsequent latent variables also show carbohydrate resonances between 70 and 100 ppm but also begin to show aromatic and phenolic resonances (110-160 ppm) as contributing to the regression.

The resonance at 104 ppm is assigned as the anomeric carbon for cellulose and/or hemicellulose, which would suggest that there is some difference either in the structural nature or the composition of the cellulose/hemicellulose that correlates with the incidence of checking. From the data however, it is not possible to say what those differences might be.

It is possible that changes in the hemicellulose could be borne about by the presence of compression wood. It is known that, in particular, galactose content is elevated in samples of compression wood (Timmel, 1986). Although no chemical analysis was undertaken the samples were visually assessed to be free of compression wood, which can be identified by light microscopy by the presence of intercellular spaces that arise from tracheids that are more circular in cross section (Harris, 1991).

The degree of crystallinity (X_C) of the cellulose was determined from the ^{13}C CP/MAS NMR spectra according to the method of Newman and Hemmingson (1990). This is determined by taking the ratio of the integrated area from 81.0 to 93.0 ppm divided by the area from 84.6 to 93.0 ppm. For the twelve samples analysed, the values fell in the range 0.51-0.55 which is similar to the value of 0.54 observed by Newman and Hemmingson. From this it was concluded that there is nothing abnormal about the crystallinity of the cellulose that may be giving rise to propensity to check formation.

The proton relaxation times, ^{1}H T_1 and T_2, can be acquired much more rapidly than ^{13}C NMR spectra. In an attempt to determine whether a rapid screening test could be developed to predict the propensity for check formation, twenty samples, sampled from individual annual rings (Table 7.2), were selected for relaxation analysis as follows:

- 12 samples taken from checked rings (either slightly or severely checked)
- 3 samples taken from unchecked rings in disks that showed no checking at all within the entire disk
- 5 samples taken from unchecked rings in disks that showed evidence of checking in other rings

Table 7.2. Relaxation and checking data for individual annual rings samples from disks.

Number of checks	T1 (ms)	T2 (ms)	Comments
0	88	5.4	Unchecked disk
0	78	2.8	Unchecked disk
0	97	3.9	Unchecked disk
0	188	14.2	Adj. to checked ring
0	156	12.9	Adj. to checked ring
0	207	15.1	Adj. to checked ring
0	43	1.2	Adj. to checked ring
0	236	16.3	Adj. to checked ring
7	322	21.4	
14	234	28.6	
19	214	23.5	
19	342	26.9	
18	406	31.5	
9	258	17.3	
15	246	20.5	
12	224	14.2	
9	202	10.6	
15	187	19.6	
8	212	11.6	
6	132	9.8	

Correlation analysis of the relaxation times with the incidence and severity of checking shows no significant correlation using a simple linear correlation (Table 7.3) although there is evidence that suggests a weak correlation with the transverse relaxation time, T_2 ($r^2 = 0.61$). It would suggest that samples prone to check formation have higher values for T_2 than those that do not readily form checks. Sadly the correlation between relaxation parameters and the incidence of checking is not sufficiently strong to allow rapid screening of radiata pine wood for propensity to form checks.

Table 7.3. Correlation analysis (r) of relaxation times with incidence of check formation (n = 20).

	Number of checks	T_1	T_2
Number of checks	1.00		
T_1	0.67	1.00	
T_2	0.78	0.89	1.00

The relaxation data does however offer more information as to the fundamental mechanism behind check formation. The higher T_2 values observed in check prone samples suggest there is a difference in the bound nature of water in the wood cell. This result, coupled with the indication that there is a difference in the cellulose/ hemicellulose makeup of the cell, presents a pointer towards more fundamental chemical analysis of check prone radiata pine.

Two scenarios present themselves. The first is that there is simply a difference in the amount of cell-wall water or secondly that there is a difference in the nature of the cell-wall water. This in itself could be due to a difference in the cellulose/hemicellulose structure which may have differing crystallinity or ordering. No attempts have been made to explore this further but a likely direction would be to undertake a detailed carbohydrate analysis of both composition and conformation. It would also be interesting to more fully examine the crystallinity of the cellulose either by direct X-ray diffraction means or *via* a solid state NMR investigation along the lines of the work undertaken by Newman (1999) whereby a dipolar dephasing MAS experiment is used to extract sub-spectra corresponding to the amorphous and crystalline cellulose.

7.6 SUMMARY OF CHAPTER

The work reported in this chapter has investigated the behaviour of water in radiata pine wood substrate and its movement during drying, in particular any restriction in movement during drying.

Imaging of the drying sequence for radiata pine samples of differing surface area to volume ratio and with differing orientation of the annual rings to the major drying face has been undertaken. In particular flat-sawn boards with a high SAV ratio show an apparent restriction to flow across the latewood boundary unlike boards with a lower SAV ratio. This can be explained by considering the lower drying gradient that is used in the thinner boards and this gradient is less in magnitude than the restriction to diffusion of water so that movement of water is diffusion limited. The larger boards have a larger drying gradient which overcomes the restriction to diffusion so that movement can occur across the latewood. For quarter-sawn boards, the annual rings are perpendicular to the drying gradient and hence the latewood does not pose a restriction to the direction of water movement.

Support for this observation has been shown directly by investigation of the diffusion tensor (albeit without an applied drying gradient). There is an evident restriction to water self diffusion in the transverse direction, that is, across the latewood boundary. The latewood restricts diffusion between adjacent earlywood bands, due most likely to the higher density of the latewood. For thin flat-sawn boards, the moisture gradient during drying is insufficient to overcome this natural barrier to water movement.

When wood is dried using an azeotropic solvent, water removal is approximately four times faster than that for conventional drying and the drying adopts a conventional core-shell drying front.

While there is no conclusive correlation between NMR relaxation times of green radiata pine sapwood and the propensity for internal check formation on drying, there is a tendency for samples prone to checking to have higher T_2 values than those that are less susceptible to checking. The reason for this is not apparent and may be due to differences in the cellulose or hemicellulose structure, giving rise to differences in the bound nature of water in the cell wall.

Projection to latent structures regression of ^{13}C CP/MAS NMR spectra of green radiata pine sapwood shows a correlation with the propensity for check formation, with the first latent variable indicating that the key variance, giving rise to the correlation is the cellulose and/or hemicellulose component of the wood. It must however be noted that a small data set was used for this section of work and that a larger sample set with increased S/N ratio would be required before drawing any definitive conclusion.

8. NMR SPECTROSCOPY OF WOOD-WORKING ADHESIVES

Science clears the fields on which technology can be built.
Werner Heisenberg

The development by ***Forest Research*** scientists (Parker *et al.*, 1997) of a rapid curing phenol-resorcinol-formaldehyde adhesive system for the green gluing of radiata pine, discussed in chapter two, has required considerable understanding of the chemistry taking place. Some of this understanding has been provided by NMR and mass spectroscopy. This chapter will discuss NMR studies using model resorcinol compounds and studies on the curing of the actual resin system.

8.1 PHENOL-RESORCINOL RESINS

Three phenol-resorcinol-formaldehyde (PRF) resins with varying levels of resorcinol were sourced from ICI Resins Division (latterly Orica), which contain *ca.* 50 % (R15), 25-30 % (R25) and 25 % (R35) resorcinol respectively (although exact formulations are proprietary information). R15 is the resin currently used industrially in the Greenweld™ process.

The PRF resins used in this study contain blends of RF and PF resins formulated from resorcinol **VII** and phenol **VIII** which are partially crosslinked prior to final curing. The reported chemical shifts (Breitmaier and Voelter, 1978) for resorcinol **VII** and phenol **VIII** are given in Table 8.1.

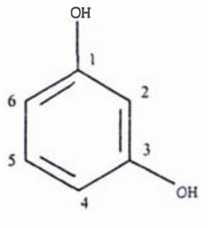

VII

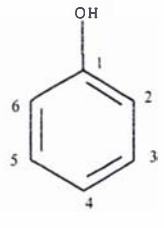

VIII

Table 8.1. ^{13}C chemical shifts for resorcinol and phenol.

Carbon No.	**Chemical Shift (ppm)**	
	Resorcinol, **VII**	Phenol, **VIII**
1	159.3	155.1
2	105.3	115.7
3	159.3	130.1
4	110.3	121.4
5	133.3	130.1
6	110.3	115.7

Figure 8.1 presents chemical shifts of resorcinol dimers bound *via* methylene or ether linkages. In the actual resin, formation of linkages will also occur between resorcinol and phenol monomers. Electronically the hydroxyl groups are *ortho* and *para* directing which means that those positions *ortho* and *para* to the hydroxyl groups are most reactive to both electrophilic and nucleophilic substitution. This means that, steric effects aside, the C2 position of resorcinol is highly reactive.

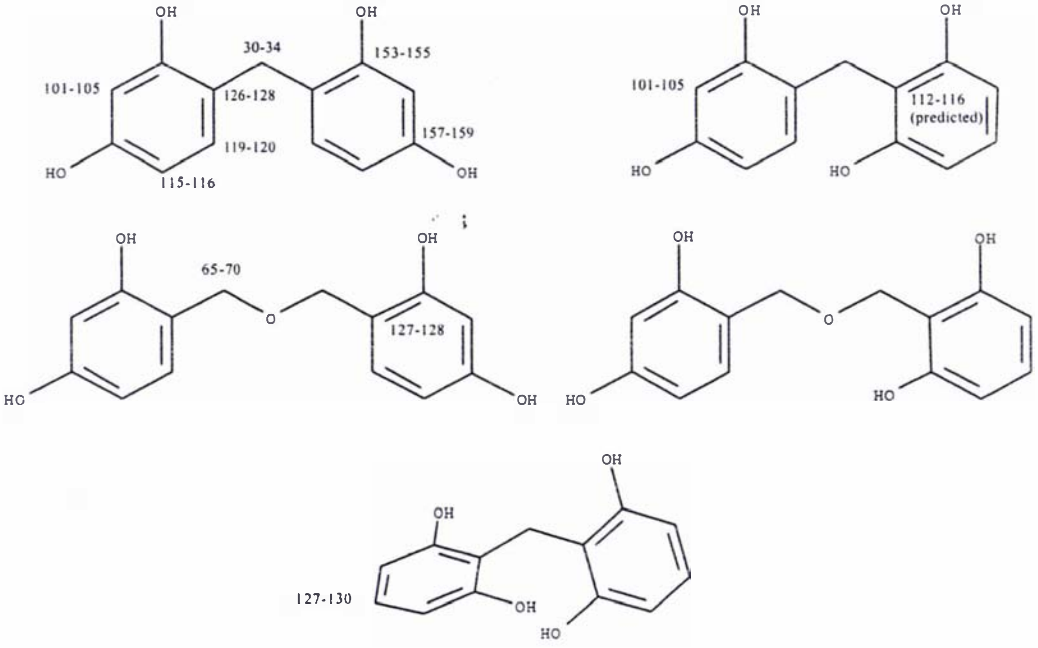

Figure 8.1. Schematic showing possible linkage formation between two resorcinol monomers indicating chemical shift values (Knop and Pilato, 1985).

8.2 CHARACTERISATION OF GREENWELD™ RESIN BY NMR SPECTROSCOPY

Nuclear magnetic resonance spectroscopy has been used to investigate the mechanism of curing for PRF resins under GreenWeld™ conditions, namely the addition of ammonia to the existing formaldehyde hardening system. Note that the cure occurs at ambient temperature. GreenWeld™ currently uses a PRF resin (R15) containing approximately 50% resorcinol. This resin has been studied along with two similar products having lower resorcinol contents.

8.2.1 LIQUID RESINS

The three liquid resins were analysed neat by ^{13}C NMR spectroscopy on a Bruker AC-200 NMR spectrometer at 50.33 MHz using an inverse gated decoupling sequence to remove the effect of nuclear Overhauser enhancement (NOE). This sequence removes the effect of NOE enhancement on the carbon signals, which would otherwise artificially enhance the signal intensity of protonated carbons to the extent that quantitative comparison would not be possible.

Solution state ^{13}C NMR spectra of the three liquid resins are shown in Figure 8.2. Assignment of the resonances is as per Table 8.2 referenced to the intense internal methanol resonance at 49.3 ppm.

Table 8.2. Integrated peak areas of resonances for the 3 resins.

Chemical shift (ppm)	Assignment		Peak Area R15	Peak Area R25	Peak Area R35
157.2	VII	C1 + C3	1.0	1.0	1.0
155.2	VIII	C1	3.2	7.3	0.8
152.7	?		3.0	14.8	1.0
131.3	VII	C5	0.8	9.8	1.9
130.4	VIII	C3 + C5	0.9	14.3	2.0
120.8	VIII	C4	5.8	13.4	0.6
115.5	VIII	C2 + C6	1.0	15.4	1.5
107.9	VII	C4 +C6	2.3	1.9	1.1
103.4	VII	C2	2.1	2.0	0.5

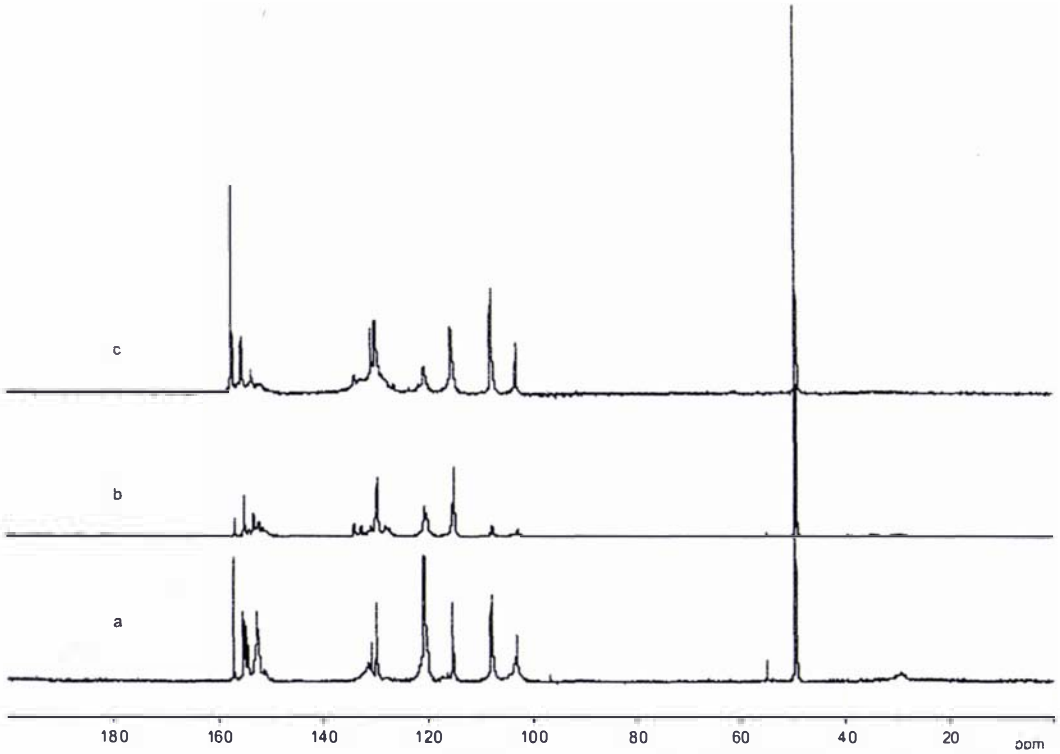

Figure 8.2. 50.3 MHz solution state ^{13}C NMR spectra of (a) R15, (b) R25 and (c) R35 resins. [AC-200, neat solutions, inverse gated decoupling, relaxation delay 10 s, 13 μs 90° pulse, no linebroadening applied, referenced to internal MeOH (49.3 ppm)].

No definitive conclusions can be drawn from the spectra of the liquid resins. This may be due to the difference in storage times before analysis of the individual resins (the R35 was fresh as opposed to the R15 having been in storage for over 1 year).

Analysis of the integrals does not provide any indication as to the relative percentages of free phenol and resorcinol.

8.2.1.1 Isotope Labelled Model Compounds

Two substituted resorcinol model compounds were prepared (Watson and Franich, 1996) in order to block either the 2 and 4, or the 4 and 6 positions of resorcinol. The diethyl substituted compounds **IX** and **X** were then reacted under GreenWeld™ conditions using ^{15}N labelled ammonia.

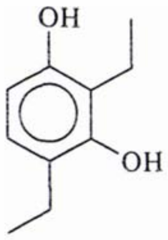

IX

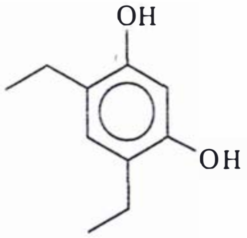

X

Solution state NMR spectroscopy was employed to determine the structure of the reaction products.

8.2.2 CURED RESINS

The resins were cured under varying conditions, with and without GreenWeld™ enhanced curing, both with and without heating to 100°C. The cured resins were ringmilled to a powder for subsequent analyses.

The spectrum of conventionally cured R25 resin is shown in Figure 8.3 and is used to illustrate the assignment of the various resonances, which are presented in Table 8.3.

Table 8.3. Assignment of ^{13}C NMR resonances in conventionally cured PRF resins.

Chemical shift (ppm)	Generic assignment	Assignment - Resorcinol	Assignment - Phenol
151.2	O substituted aromatic	C1 and C3	C1
130.0	*meta* aromatic C **OR** *ortho* aromatic C of *meta* substituted	C5	C3, C5
120.8	*para* aromatic C	-	C4
115.9	*ortho* aromatic C	C4, C6	C2, C6
102.8	*ortho* aromatic C	C2	-
88.3	$\text{-O-}\underline{\text{C}}\text{-O-}$	ether linkages	ether linkages
50-46	$(\text{Ar-}\underline{\text{C}}\text{H}_2)_2\text{-NH}$ [a]	methylene bridges in dibezylamine	methylene bridges in dibezylamine
56-53	$(\text{Ar-}\underline{\text{C}}\text{H}_2)_3\text{-N}$ [a]	methylene bridges in tribezylamine	methylene bridges in tribezylamine
38.9	*o-p* methylene bridge	methylene bridges in biphenyls	methylene bridges in biphenyls
30.8	*o-o* methylene bridge	methylene bridges in biphenyls	methylene bridges in biphenyls

[a] Hatfield and Maciel (1986); Pizzi and Teleky (1996); Zhang *et al.*, (1997)

The resonances at 65-52 ppm are assigned to methylene ether bridges and resonances around 30 ppm are assigned to methylene linkages (Knop and Pilato, 1985). For resols conventionally cured using formaldehyde these are the primary linkages formed.

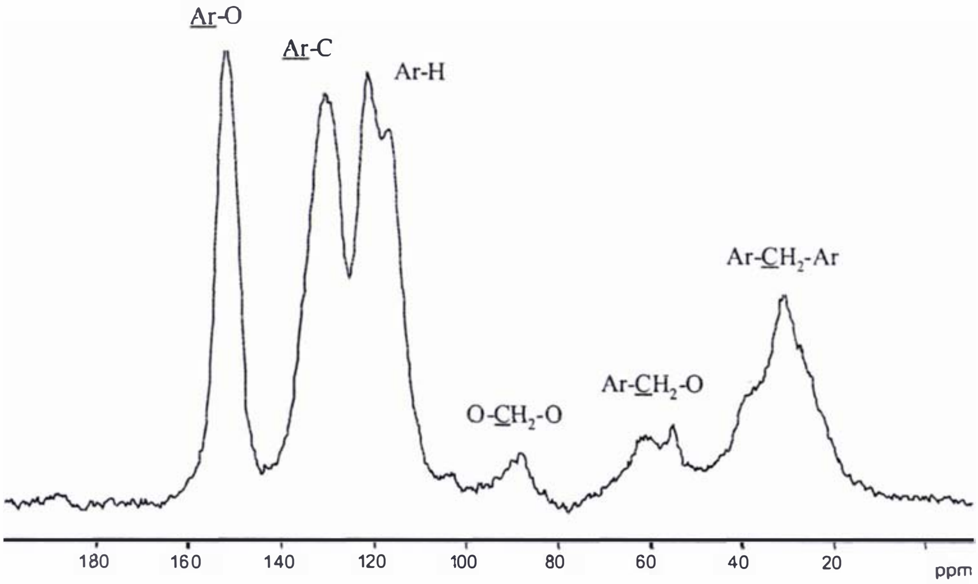

Figure 8.3. 50.3 MHz ^{13}C CP/MAS NMR spectrum of conventionally cured R25 PRF resin showing generic assignment of resonances. [AC-200, CP/MAS, rotor speed 5 kHz, relaxation delay 2 s, contact time 4 ms, 5.5 μs 90 ° pulse, LB 20 Hz, referenced to external adamantane (38.3 ppm)].

The ^{13}C CP/MAS NMR spectra of conventionally cured R15, R25 and R35 PRF resins are shown for comparison in Figure 8.4. Of note are the resonances at 103, 115 and 120 ppm (C2 resorcinol, C2, C6 phenol plus C4, C6 resorcinol and C4 phenol respectively). The spectrum of cured R35 resin shows no visible evidence of the resonance at 103 ppm indicating that either (i) there is very little resorcinol in the formulation or (ii) whatever resorcinol is in the formulation is involved in crosslinking of the resin at the C2 position of resorcinol. It is known that the resorcinol level in the R35 resin is approximately half that of the R15 resin. It is likely then that the available resorcinol has been reacted, with reaction occurring at the highly reactive C2 position of resorcinol.

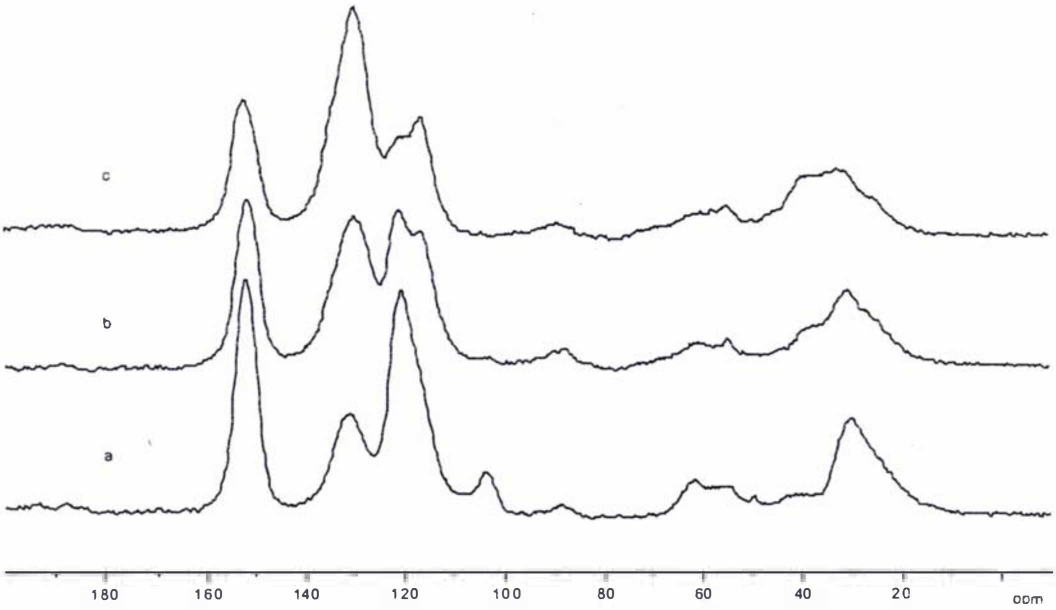

Figure 8.4. 50.3 MHz ^{13}C CP/MAS NMR spectra of conventionally cured (a) R15, (b) R25 and (c) R35 PRF resins. [Conditions as per Figure 8.3].

There is a progressive decrease in the ratio of the 151 ppm resonance with respect to the 131 ppm resonance between R15 and R35, indicating a lower ratio of hydroxyl groups present due to increased dilution of resorcinol in the resin formulation by phenol. In comparing the conventional cure there is a relative decrease in the intensity of the 120 ppm resonance (*para*-hydroxyphenol) when comparing R15 to R35 resin. This is due to in part the difference in the initial levels in the resin blend.

The spectra of GreenWeld™ cured R15, R25 and R35 resins are shown in Figure 8.5. Again there is a decrease in the intensity of the 151 ppm resonance between R15 and R35, as the amount of resorcinol present in the original formulation decreases between R15 and R35. It also shows a decrease in the resonance at 103 ppm (C2 resorcinol) again suggesting that for R35 the available resorcinol is reacted.

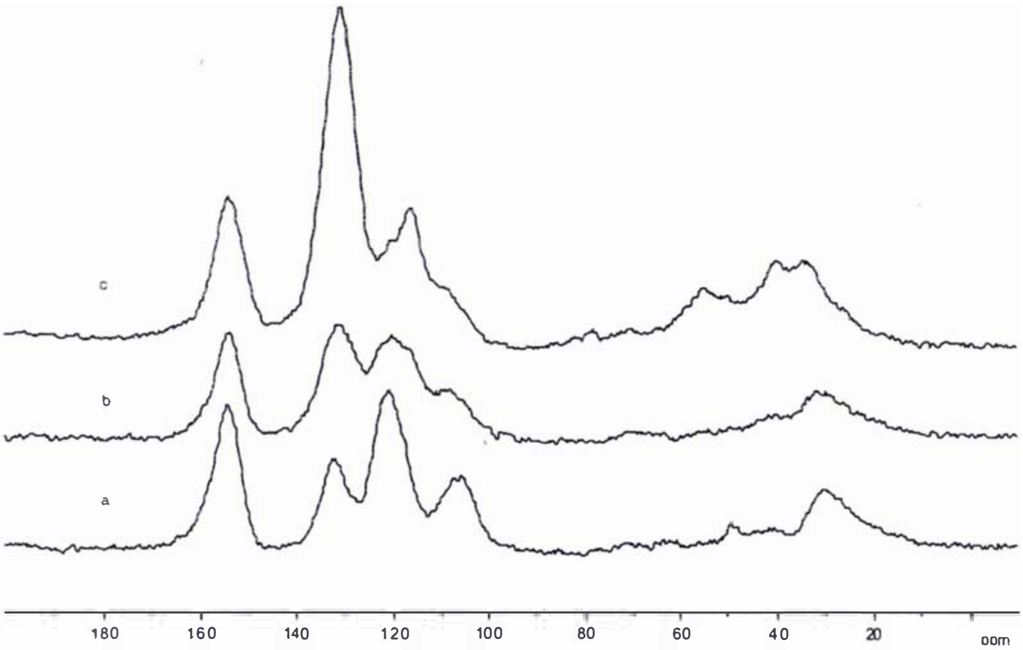

Figure 8.5. 50.3 MHz ^{13}C CP/MAS NMR spectra of Greenweld™ cured (a) R15, (b) R25 and (c) R35 resins. [Conditions as per Figure 8.3].

The spectrum of R15 resin cured under conventional conditions, GreenWeld™ conditions and GreenWeld™ conditions with subsequent curing at 100 °C is shown in Figure 8.6.

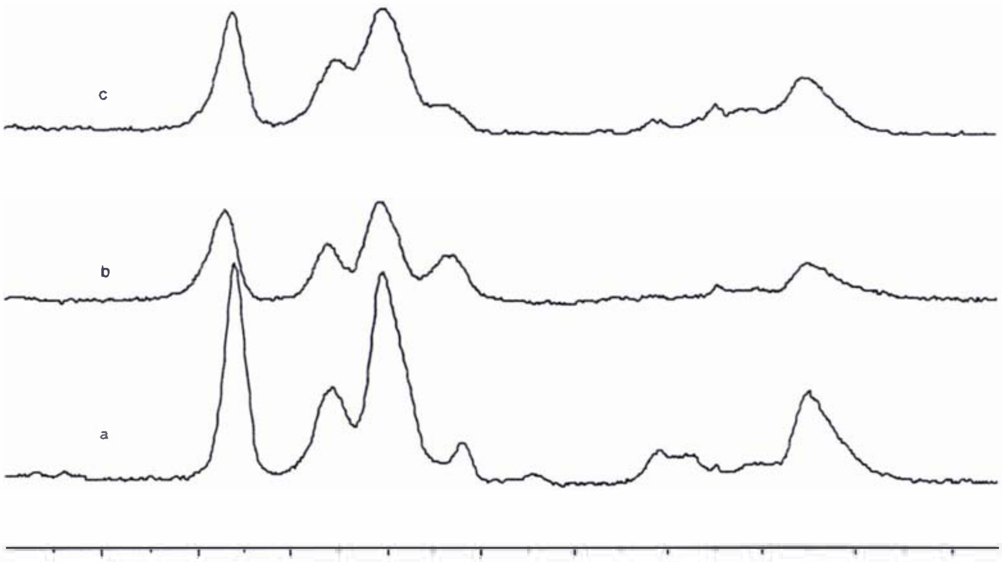

Figure 8.6. 50.3 MHz ^{13}C CP/MAS NMR spectra of R15 resin following (a) conventional cure, (b) Greenweld™ cure and (c) Greenweld™ cure followed by heating at 100°C. [Conditions as per Figure 9.3].

Note the difference in intensity of the resonance at 103 ppm (C2 resorcinol) in the conventionally cured adhesive. This suggests that cross-linking must occur at the C2 position in conventionally cured resin whereas a different mechanism is favoured under GreenWeld™ conditions. In GreenWeld™ resins cured at ambient temperatures there is a decrease in intensity of the resonance at 120 ppm relative to 103 and 130 ppm suggesting that the C4 and C6 positions on resorcinol are favoured sites for crosslinking.

In the conventionally cured resin, there is evidence of methylene ether linkages at 65-52 ppm which is largely absent in the GreenWeld™ cured resin. Instead there is evidence for methylene amine linkages at 40-53 ppm (Witanowski and Webb, 1972), which is even more prevalent in the elevated temperature cure. There is literature evidence that formaldehyde and ammonia undergo reaction to form hexamethylenetetramine, HMTA, (Neilsen *et al.*, 1979), which at ambient temperature is unreactive towards PRF resin but is known to react with phenol-resorcinol resins at elevated temperatures (Pizzi and Teleky, 1996; Zhang *et al.*, 1997).

If the GreenWeld™ curing process is carried out at elevated temperature (100°C) there is a similar change in intensity of the resonance of the C2 carbon at 103 ppm. This suggests that an alternative cross-linking mechanism is favoured under these conditions, giving rise to a more thermodynamically favoured product.

There is a noticeable difference compared with the intensity of the resonance at 103 ppm (C2) in conventionally cured R15 (Figure 8.6). It is less than 10% of the intensity of the same resonance in GreenWeld™ cured resin. This resonance corresponds to that of the carbon *ortho* to both of the hydroxyl groups (position 2), suggesting that this is the preferred site of crosslinking in the conventionally cured resin. Hydroxyl groups are *ortho* and *para* directing, so that positions 2, 4 and 6 of the resorcinol are activated towards nucleophilic aromatic substitution. Similar results are observed for R35 resin (Figure 8.7), which due to the lower resorcinol content makes these observations even more apparent for conventionally cured resin where the C2 carbon of resorcinol is totally reacted.

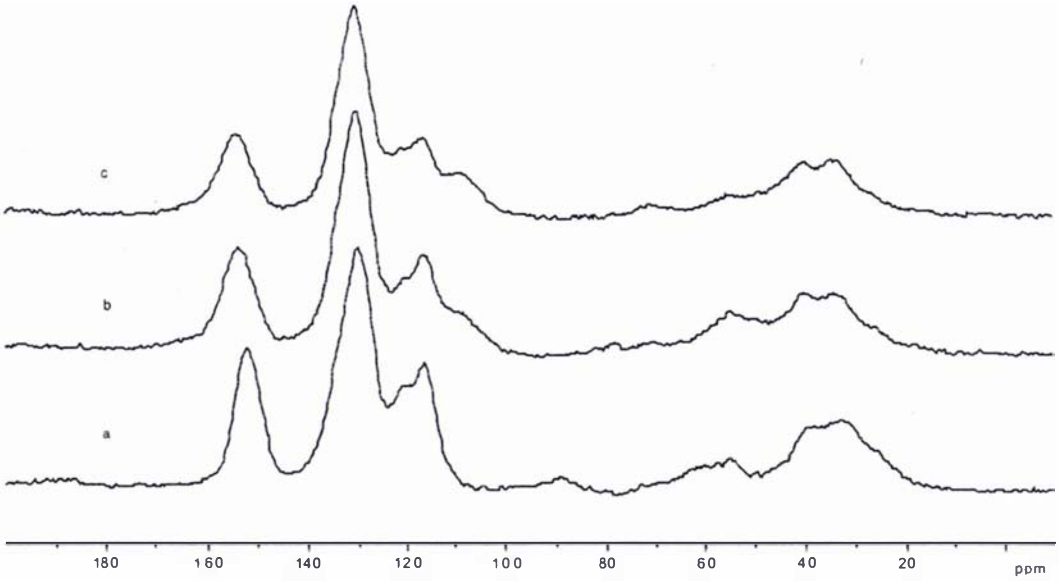

Figure 8.7. 50.3 MHz ^{13}C CP/MAS NMR spectrum of R35 resin following (a) conventional cure, (b) GreenWeld™ cure and (c) GreenWeld™ cure followed by heating at 100°C. [Conditions as per Figure 9.3].

The ^{15}N MAS NMR spectrum of R25 resin cured with ^{15}N labelled ammonia is shown in Figure 8.8 and assignments for the observed resonances are given in Table 8.4.

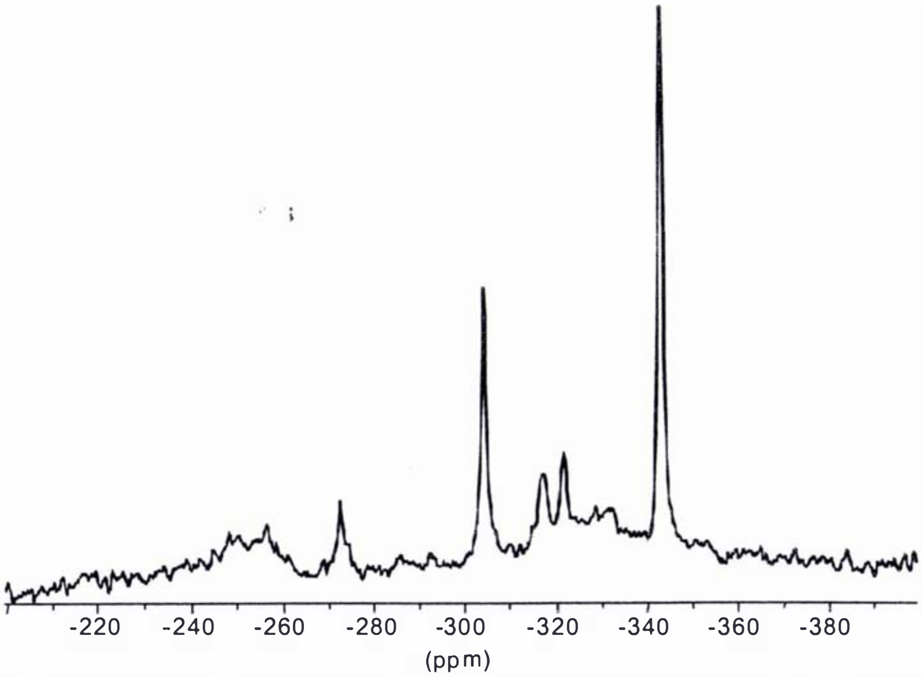

Figure 8.8. 40.5 MHz ^{15}N MAS NMR spectrum of GreenWeld™ cured R25 resin [MSL 400, HPDEC, rotor speed 4.8 kHz, relaxation delay 2 s, 2 μs 90° pulse, LB 25 Hz, referenced to external CH_3NO_2 (0.0 ppm)].

Table 8.4. Chemical shift data for ^{15}N MAS MNR spectrum of GreenWeld™ cured R25. Referenced external KNO_2 (= $\delta_N CH_3NO_2$ = 0.0 ppm = $\delta_N NH_3$ liq. (-383.0 ppm [a])).

Chemical shift (ppm)	Assignment	
-358.1	benzylamine [b]	$Ar\text{-}CH_2\text{-}\underline{N}H_2$
-344.2	dibenzylamine [b]	$(Ar\text{-}CH_2)_2\text{-}\underline{N}H$
-336.5	hexamethylenetetramine [c]	(HMTA)
-332.0	tribenzylamine [b]	$(Ar\text{-}CH_2)_3\text{-}\underline{N}$
-319.5	aminobenzene [b]	$Ar\text{-}\underline{N}\text{-}R_2$
-287.8	?	
-270.8	amides ?	$Ar\text{-}CH_2\text{-}\underline{N}R'\text{-}CO\text{-}R''$?
-266.1	amides ?	$Ar\text{-}CH_2\text{-}\underline{N}R'\text{-}CO\text{-}R''$?

[a] Witanowski and Webb, 1972

[b] Witanowski and Januszewski, 1969 referenced CH_3NO_2

[c] Hatfield and Maciel, 1986

Whereas Zhang *et al.* (1997) investigated the hexamethylenetetramine (HMTA) cure of novolac resins at elevated curing temperatures, the GreenWeld™ process involves rapid ambient temperature cure. However, similar reaction products to those observed by Zhang *et al.* were observed in the reaction of ammonia with PRF resins *via* the GreenWeld™ process. In particular the presence of benzylamines and possible amides suggests similar reaction mechanisms exist between the reaction of PRF resins with HMTA or ammonia. Reaction does not proceed between HMTA and resorcinol at ambient temperature.

8.2.3 MODEL COMPOUNDS

The solution state ^{13}C NMR spectra for the 2,4- (**IX**) and 4,6-diethyl (**X**) substituted resorcinols are shown in Figure 8.9 and Figure 8.11 respectively, with chemical shift data reported in Table 8.5.

Table 8.5. ^{13}C chemical shift data (ppm) for 2,4- (**IX**) and 4,6-diethylresorcinol (**X**). ($CDCl_3$)

	C1	C2	C3	C4	C5	C6	CH_2	CH_3
IX	152.03	116.41	152.41	121.56	126.10	107.35	16.70^{C4}	13.57^{C4}
							22.66^{C2}	14.13^{C2}
X	154.10	103.39	154.10	121.96	130.36	121.96	20.79	15.21

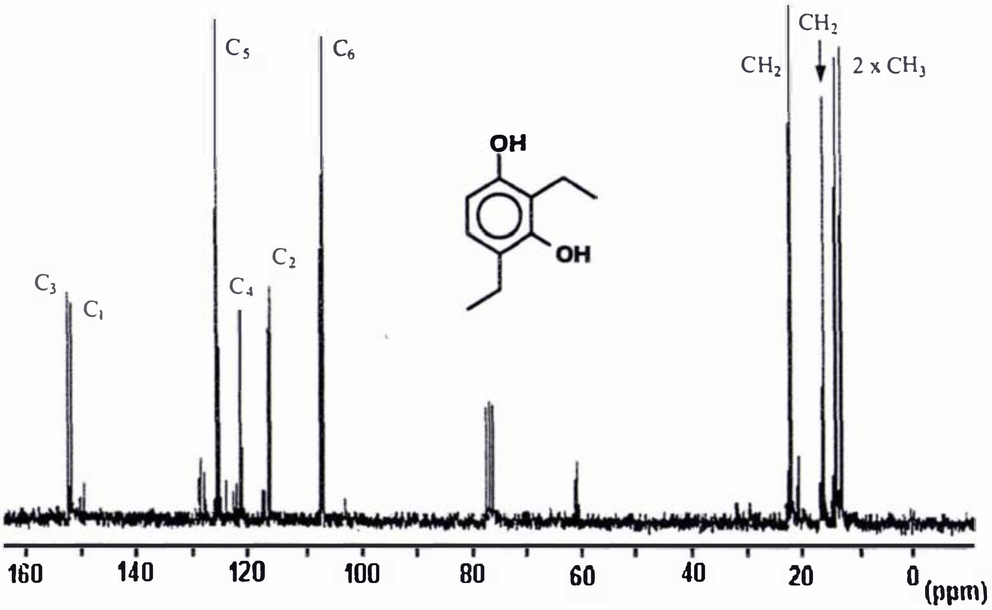

Figure 8.9. 50.3 MHz ^{13}C solution state NMR spectrum of 2,4-diethylresorcinol, **IX**. [AC 200, $CDCl_3$, power gated decoupling, relaxation delay 2 s, 13 μs 90° pulse, linebroadening 1 Hz, referenced to internal $CDCl_3$ (77.04 ppm)].

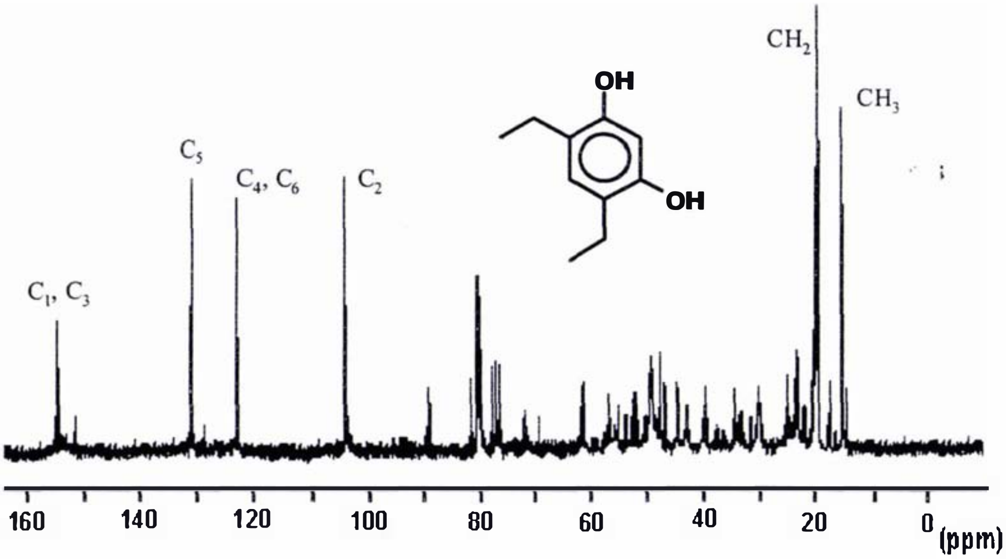

Figure 8.10. 50.3 MHz ^{13}C solution state NMR spectrum of crude 4,6-diethylresorcinol, **X**. [Conditions as per Figure 8.9].

Both of the substituted models were reacted under GreenWeld™ conditions using isotopically labelled ammonia-^{15}N. ^{13}C NMR spectra of the reaction products are shown for the 2,4- and 4,6-diethylresorcinol in Figure 8.11 and Figure 8.12 respectively. Chemical shift assignments are given in Table 8.6.

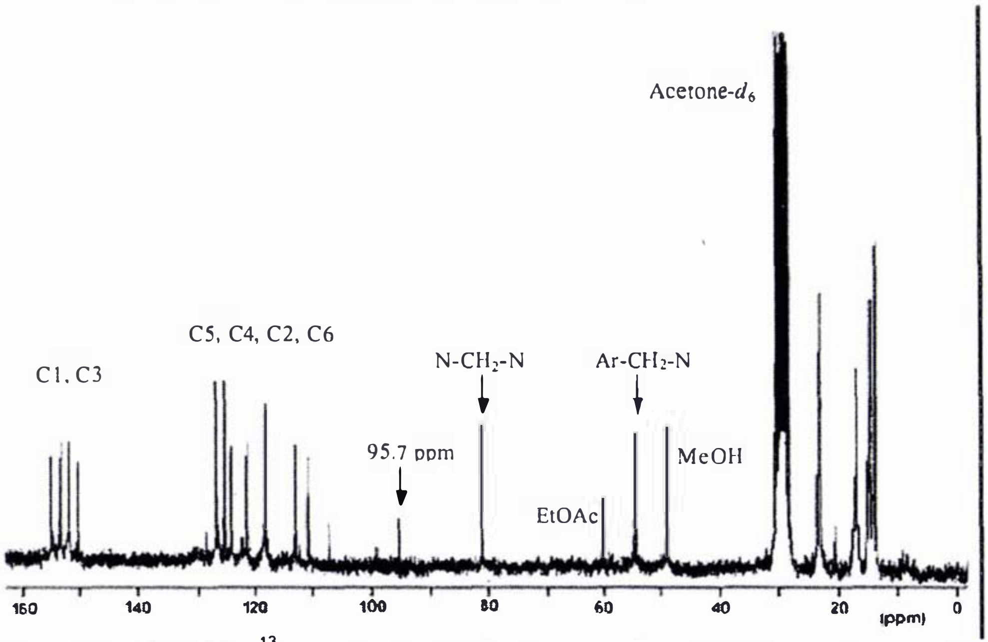

Figure 8.11. 50.3 MHz ^{13}C solution state NMR spectrum of 2,4-diethylresorcinol, **IX**, reacted with ammonia and paraformaldehyde (GreenWeld™ conditions). [Conditions as per Figure 8.9, referenced to internal acetone-d_6 (29.8 ppm)].

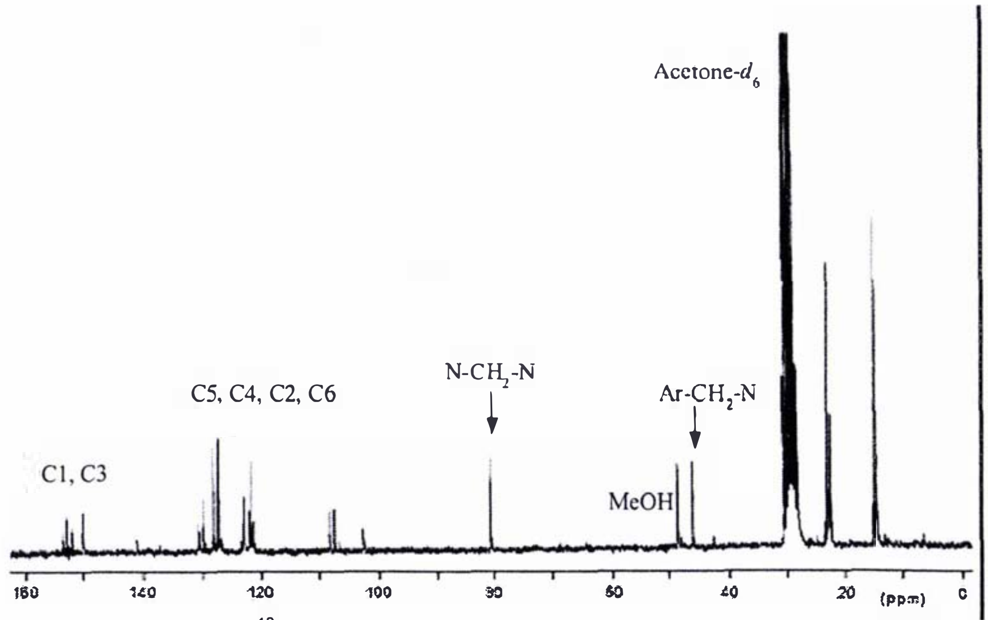

Figure 8.12. 50.3 MHz ^{13}C solution state NMR spectrum of 4,6-diethylresorcinol, **X**, reacted with ammonia and paraformaldehyde (GreenWeld™ conditions). [Conditions as per Figure 8.11].

Table 8.6. ^{13}C chemical shift data (ppm) for GreenWeld™ reaction products of diethyl substituted resorcinol models **IX** and **X**.

Chemical shift (ppm)		Assignment
~153	A̲r-OH	C1 and C3 of subst resorcinol **IX** and **X**
~128	A̲r-H	C5 of subst resorcinol **X**
~123	A̲r-C	C4 and C6 of subst resorcinol **X**
~103	A̲r-H	C2 of subst resorcinol **X**
95.7	?	
81.2	N-C̲H$_2$-N	
54.9	Ar-C̲H$_2$-N	methylene of benzylamine
23.3	C̲H$_2$-CH$_3$	methylene of ethyl
15.2	CH$_2$-C̲H$_3$	methyl of ethyl

The ^{13}C spectra of GreenWeld™ products from the two model compounds suggest the presence of benzylamine type structures as being the predominant reaction products. The corresponding ^{15}N NMR solution state spectra and chemical shift assignments are presented in Figure 8.13 and Table 8.7 respectively.

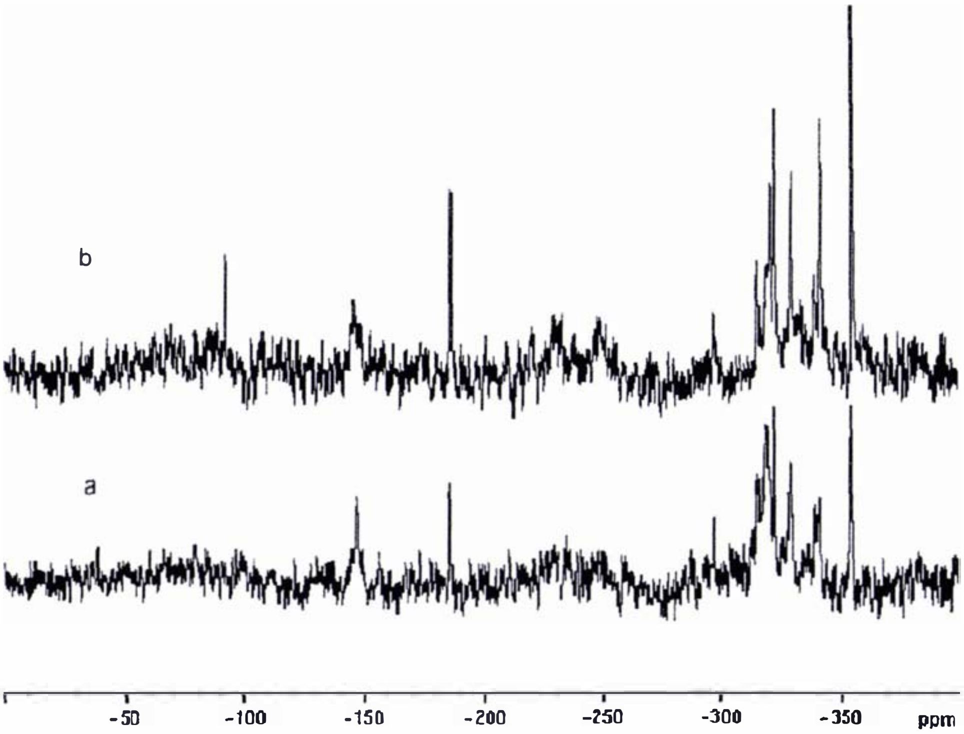

Figure 8.13. 40.5 MHz ^{15}N solution state NMR spectrum of (a) 2,4-diethylresorcinol, **IX**, and (b) 4,6-diethylresorcinol, **X**, reacted under GreenWeld™ conditions using ammonia-^{15}N. [Avance-400, $CDCl_3$, inverse gated decoupling, relaxation delay 10 s, 15 μs 90° pulse, LB 5 Hz, referenced to external CH_3NO_2 (0.0 ppm)].

Table 8.7. Chemical shift data (ppm) for ^{15}N solution NMR spectra of 2,4- and 4,6-diethylresorcinol reacted with $^{15}NH_3$ and formaldehyde. Referenced external KNO_2 (= $\delta_N CH_3NO_2$ = 0.0 ppm = $\delta_N NH_3$ liq. (-383.0 ppm [a])).

Chemical shift (ppm)	Assignment	
-355.8	$Ar\text{-}CH_2\text{-}\underline{N}H_2$	benzylamine [a,b]
-342.1	$(Ar\text{-}CH_2)_2\text{-}\underline{N}H$	dibenzylamine [a,b]
-330.0	$(Ar\text{-}CH_2)_3\text{-}\underline{N}$	tribenzylamine [a,b]
-323.0	?	
-320.5	$Ar\text{-}\underline{N}\text{-}R_2$	aminobenzene type [a]
-185.8	?	
-146.8	?	
-91.9	$Ar\text{-}\underline{N}\text{-}$	imines ? [a]

a Witanowski and Webb, 1972
b Hatfield and Maciel, 1986

The solution state ^{15}N NMR spectra of the GreenWeld™ reacted 2,4- and 4,6-diethylresorcinol model compounds **IX** and **X** support the presence of benzylamine and aminobenzene structures. They show very similar spectra with the only significant difference being the presence of a resonance at -91.9 ppm in the 4,6-diethylresorcinol reaction product.

The ^{1}H-^{15}N correlation of 4,6-diethylresorcinol *via* a HSQC experiment is shown in Figure 8.14. Correlations were only observed in the F_1 (^{15}N) domain in the region from –370 to –300 ppm, suggesting that the resonances observed at –185.8, -146.8 and –91.9 ppm are non-protonated nitrogen species. In this compound the highly reactive *ortho* position at C2 is free for reaction. The resonance at –91.9 ppm is assigned as an imine-type reaction product. The resonances at –350 to –340 correlate with methylene protons between 4.2 and 3.6 ppm, which based on chemical shift, would be consistent with methylamine type structures. To support this a ^{1}H-^{13}C HMQC correlation, shown in Figure 8.15, confirms the correlation of these protons with methylene carbons. The longer range ^{1}H-^{13}C correlation afforded by the HMBC experiment Figure 8.16, shows longer range correlation of the methylenes with aromatic protons, further supporting evidence of benzylamine stuructures.

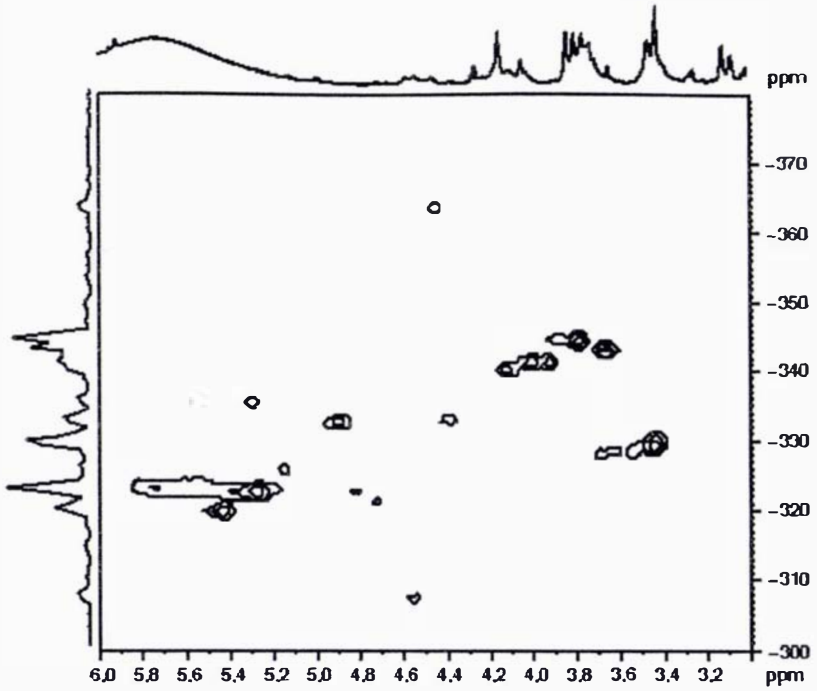

Figure 8.14. ^{1}H-^{15}N HSQC correlation spectrum of reaction product from reaction of $^{15}NH_3/(CH_2O)_n$ with 4,6-diethylresorcinol. [Avance 400, HSQC, 2K x 256 (zero filled to 512), $^1J_{NH}$ 10 Hz].

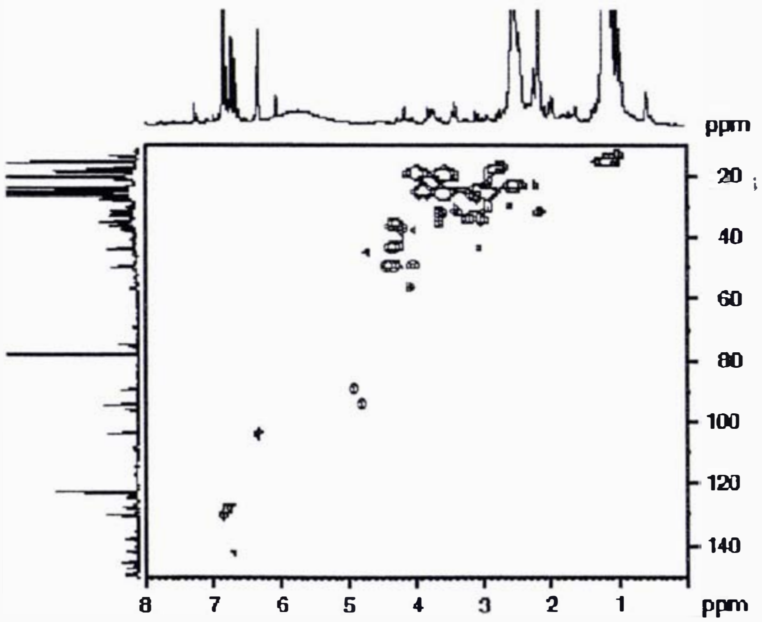

Figure 8.15. ^{1}H-^{13}C HMQC correlation of reaction product from reaction of $^{15}NH_3/(CH_2O)_n$ with 4,6-diethylresorcinol. [Avance 400, HMQC, 2K x 128 (zero filled to 256), $^1J_{CH}$ 145 Hz, mixing delay 400 ms].

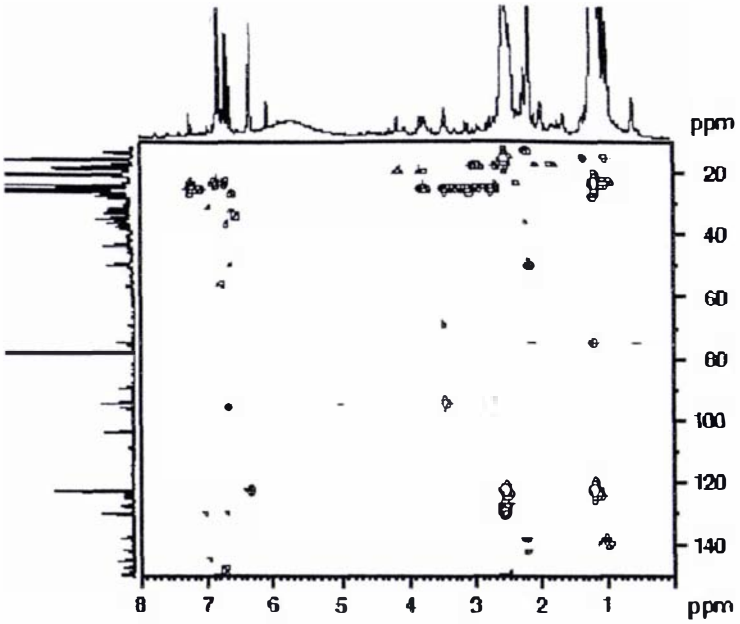

Figure 8.16. Long range ^{1}H-^{13}C HMBC correlation of reaction product from reaction of $^{15}NH_3/(CH_2O)_n$ with 4,6-diethylresorcinol. [Avance 400, HMBC, 1K x 256 (zero filled to 512), $^{n}J_{CH}$ 10 Hz].

These results suggest that the GreenWeld™ reaction proceeds *via* initial amination of the highly activated resorcinol ring by a methyleneimine. The high pH of the GreenWeld™ process, which would result in the preferential formation of phenolate anions, and the specificity of the attack at the most reactive sites on resorcinol (i.e. C2 > C4, C6) implies an electrophilic substitution mechanism. Proposed structures for the reaction of 2,4- and 4,6-diethylresorcinol with formaldehyde and ammonia are shown in Figure 8.17 and a proposed mechanism of reaction in Figure 8.18.

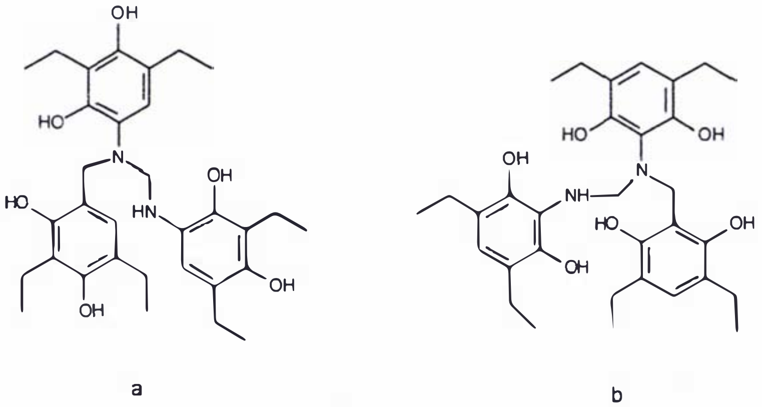

Figure 8.17. Proposed structures for reaction of (a) 2,4- and (b) 4,6-diethylresorcinol with formaldehyde and ammonia (GreenWeld™).

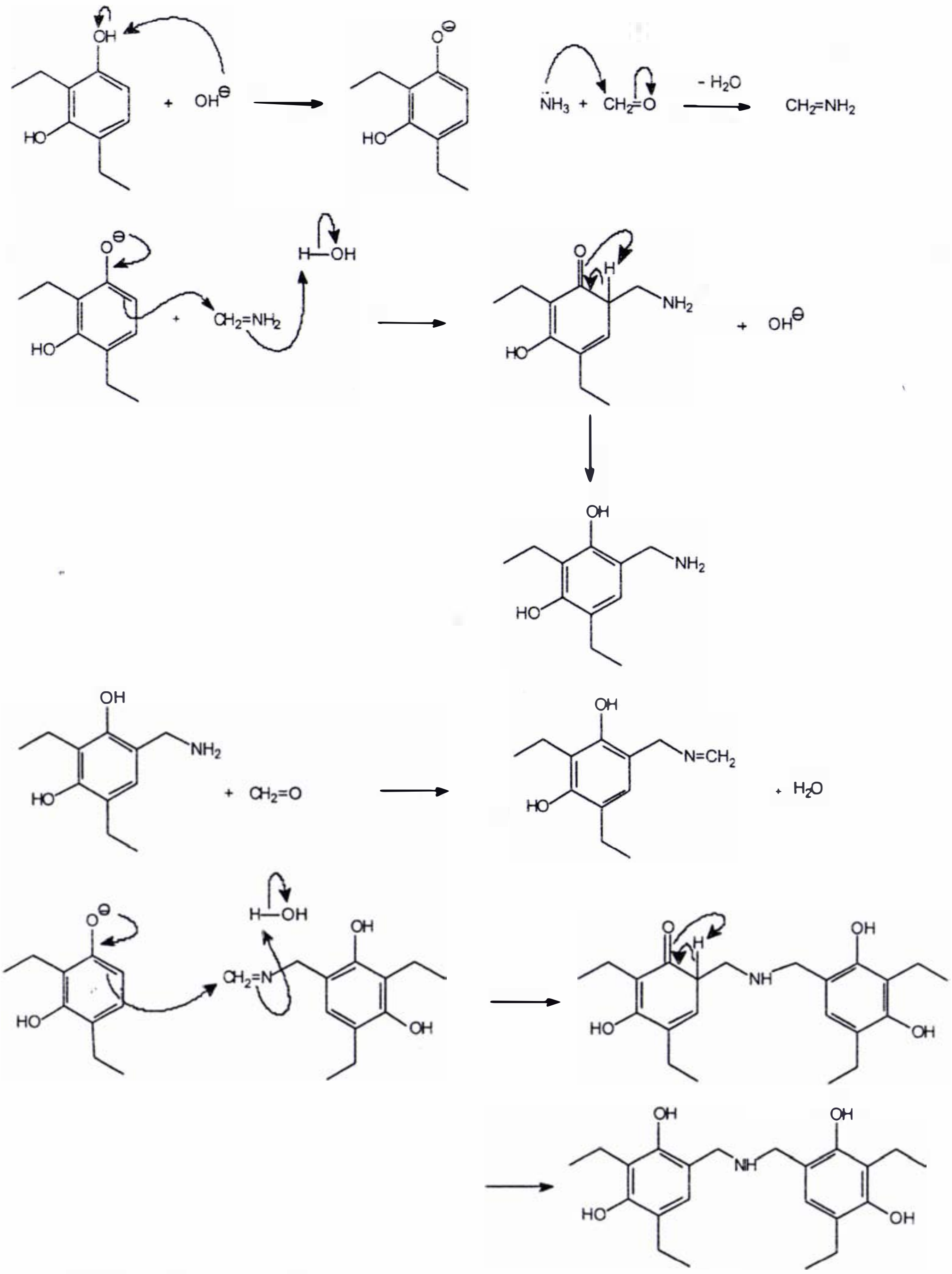

Figure 8.18. Proposed mechanism for reaction of 2,4-diethylresorcinol with ammonia and paraformaldehyde *via* methyleneimine, showing formation of benzylamine and dibenzylamine.

There is spectral evidence for aryl nitrogen compounds being formed as well. This would be possible *via* formation of HMTA, which is known to react with PRF at elevated temperature, but at lower temperatures the mechanism may involve Michael addition substituting a resorcinol hydroxyl and then subsequent reaction with resorcinol (Figure 8.19).

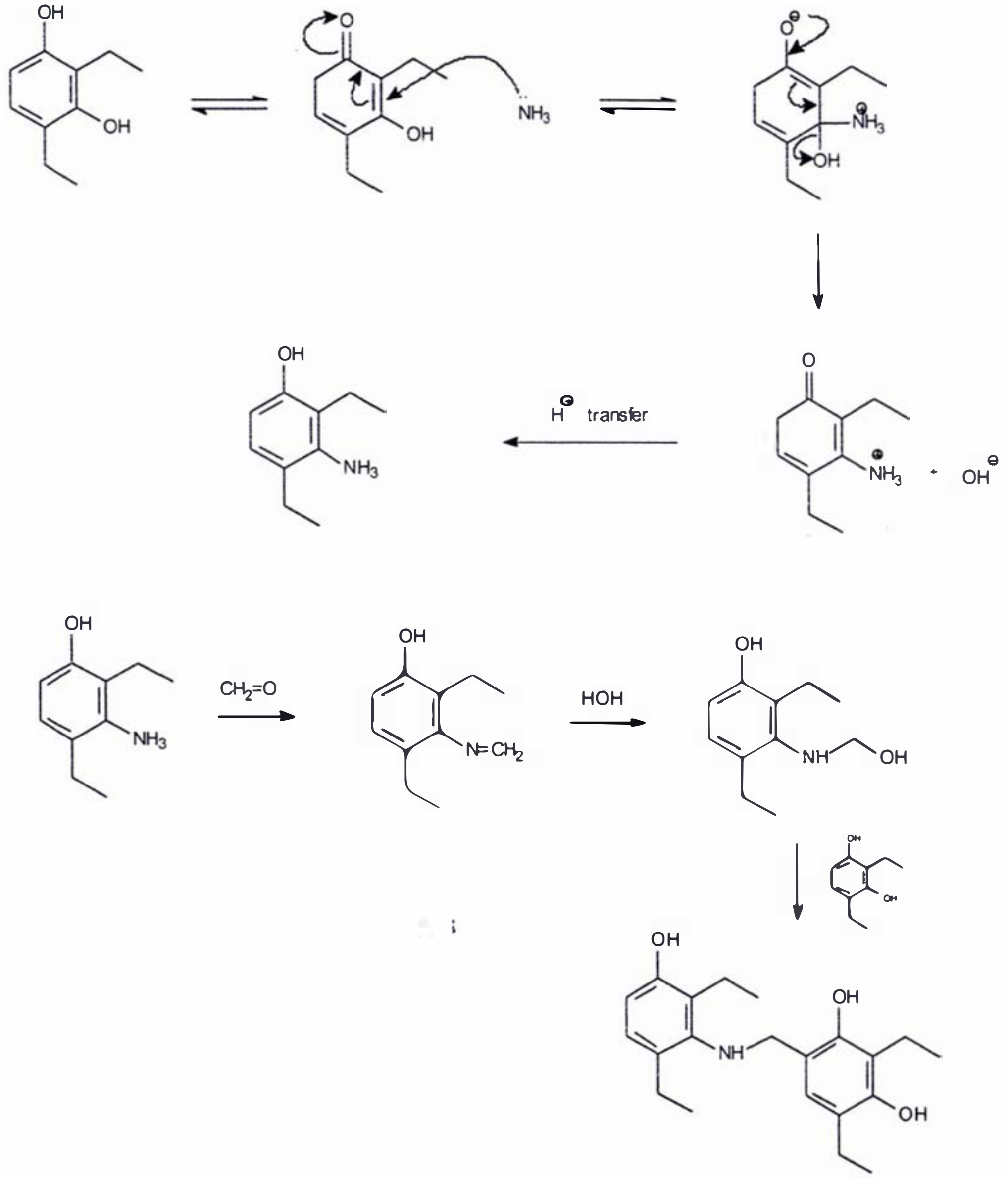

Figure 8.19. GreenWeld™ mechanism continued, showing formation of aryl nitrogen compounds.

8.3 CHARACTERISATION OF POLY(VINYL ACETATE) BY NMR SPECTROSCOPY

Emulsion adhesives are polymer colloids stabilised in water (El-Aasser and Vanderhoff, 1981). Poly(vinyl acetate) (PVAc) is probably the most well known of the emulsion polymer adhesives and it is used widely in the mouldings and furniture industries as it provides a clear glueline finish. It does however have the drawback that it is prone to shear-induced creep and failure if the product gets wet or if subjected to high humidity. Crosslinkable PVAc emulsion adhesives are known to exist commercially in which one of several additives are commonly used to crosslink the polymer backbone in an attempt to provide a more rigid structure. This is often achieved by addition of aluminium salts, normally as chloride or sulphate salt. Crosslinkable PVAc adhesive is produced from the emulsion polymerisation of vinyl acetate and *N*-methylolacrylamide (*N*-MAM) (Figure 8.20). Assignments of chemical shifts for *N*-MAM, vinyl acetate and PVAc are given in Table 8.9 along with a solution state ^{13}C NMR spectrum of a commercial PVAc adhesive in Figure 8.21. For the studies undertaken in this section of work, formulations as outlined in Table 8.8 were used.

Table 8.8. Generic formulation for *N*-MAM/PVAc formulation used in this study. Exact formulations are cited in the appropriate text or Figure captions.

Water	50%
Vinyl acetate monomer (VAM)	30-47%
N-Methylolacrylamide (*N*-MAM)	2-20%
Potassium persulphate initiator	1%
$AlCl_3$	0% or 5%

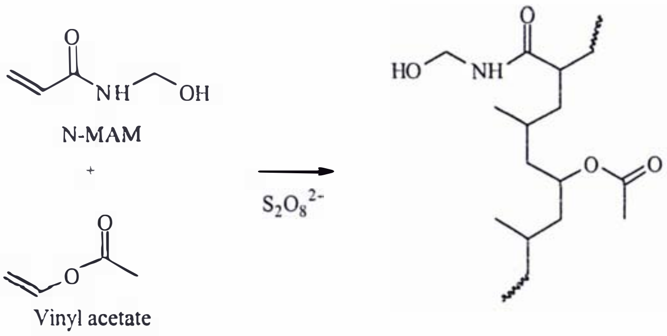

Figure 8.20. Polymer reaction scheme of *N*-MAM and vinyl acetate monomer to form poly(vinyl acetate) latex.

Table 8.9. Assignment of ^{13}C NMR resonances in PVAc latex and monomer compounds (Phan *et al.*, 1983; de Souza and Tavares, 1998).

Vinyl acetate:

δ_C ($CDCl_3$): 167.6, C=O; 141.4, $\underline{C}HCH_2$; 97.1, $CH\underline{C}H_2$; 20.3, $CO\underline{C}H_3$.

N-MAM:

δ_C (acetone-d_6): 168.9, C=O; 129.9, $CH\underline{C}H_2$; 128.4, $\underline{C}HCH_2$; 63.0, $HO\underline{C}H_2NH$.

N-MAM/PVAc:

δ_C (99% D_2O, acetone-d_6): 180.1–173.7, C=O; 68.1, $CO\underline{C}HCH_2$ (mm); 66.4-65.1, $CO\underline{C}HCH_2$ (mr); 41.8-37.0, $COCH\underline{C}H_2$; 20.9, $CO\underline{C}H_3$.

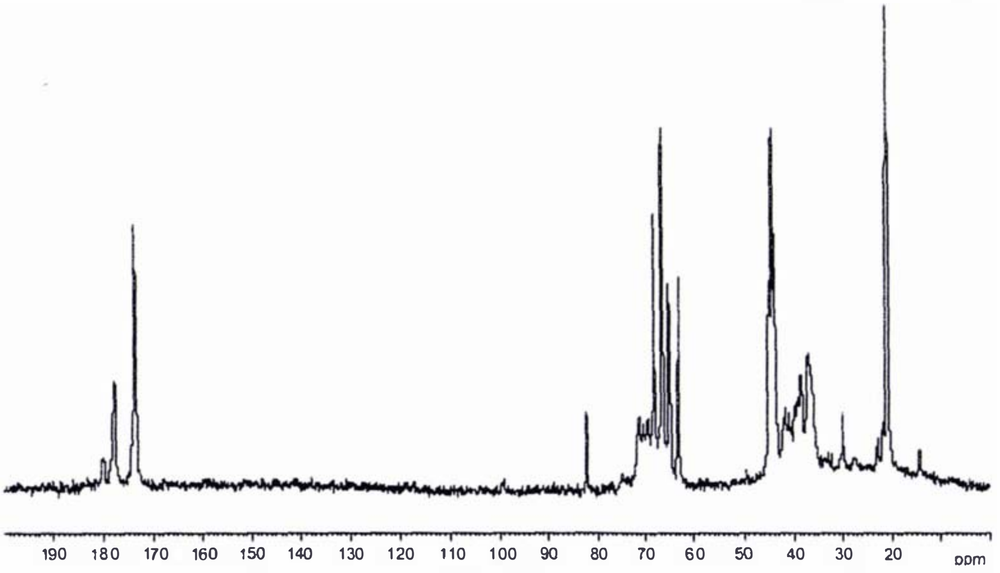

Figure 8.21. 100.1 MHz solution state ^{13}C NMR spectrum of commercial *N*-MAM/PVAc emulsion polymer (Edson Chemicals). [Avance-400, neat solution, powergated WALTZ decoupling, relaxation delay 2 s, 13 µs 90° pulse, LB 1 Hz, referenced to external acetone (29.8 ppm)].

A sample of ^{13}C-labelled *N*-MAM in which the methylol carbon at 63.0 ppm was labelled was prepared from ^{13}C-labelled paraformaldehyde and its ^{13}C NMR spectrum is shown in Figure 8.22. Residual ^{13}C-paraformaldehyde is observed at 70.3 ppm.

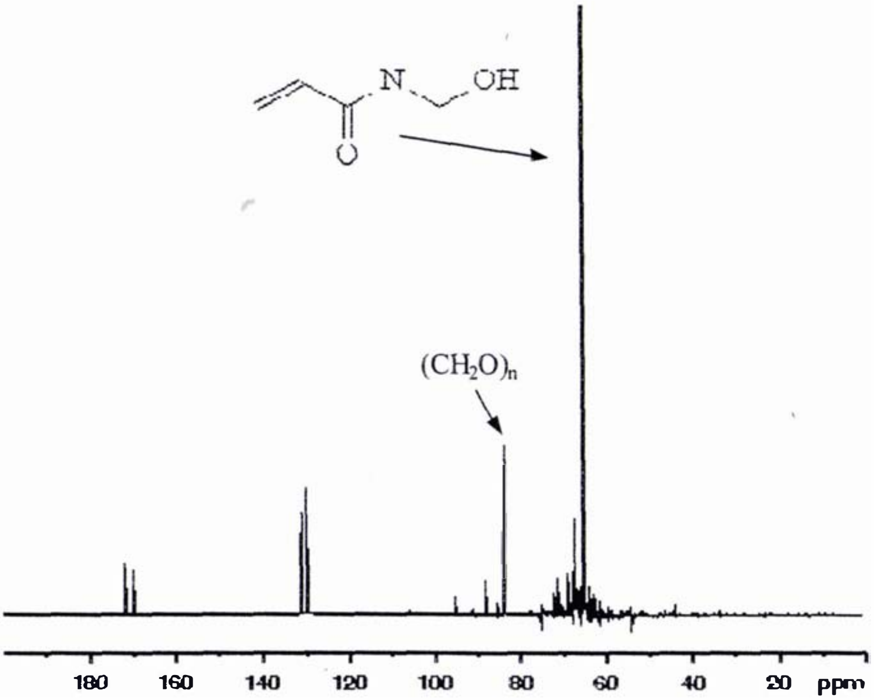

Figure 8.22. 100.1 MHz solution state ^{13}C NMR spectrum of ^{13}C labelled *N*-MAM. [Avance-400, D_2O, powergated WALTZ decoupling, relaxation delay 2 s, 13 µs 90° pulse, LB 1 Hz, referenced to external acetone (29.8 ppm)].

A PVAc was in turn formulated using the ^{13}C-labelled *N*-MAM in order to observe the incorporation of the methylol methylene in the cured resin *via* solid state NMR. The ^{13}C NMR spectrum of the labelled formulation is shown in Figure 8.23 and the formulation containing 5% addition of $AlCl_3$ is shown in Figure 8.24.

The only discernable difference between the spectra is shown in the expansion plot of the ^{13}C NMR spectrum (Figure 8.25), which shows 131 Hz ^{13}C-^{27}Al coupling in the PVAc formulation containing the added $AlCl_3$.

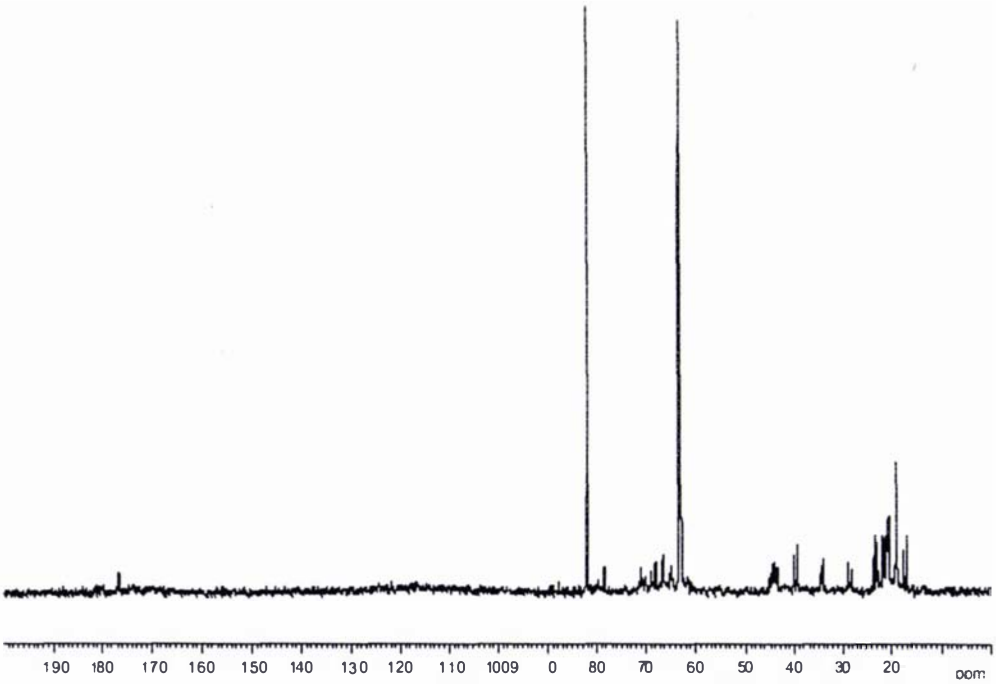

Figure 8.23. 100.1 MHz solution state ^{13}C NMR spectrum of ^{13}C labelled *N*-MAM/PVAc emulsion polymer. [Conditions as per Figure 8.20].

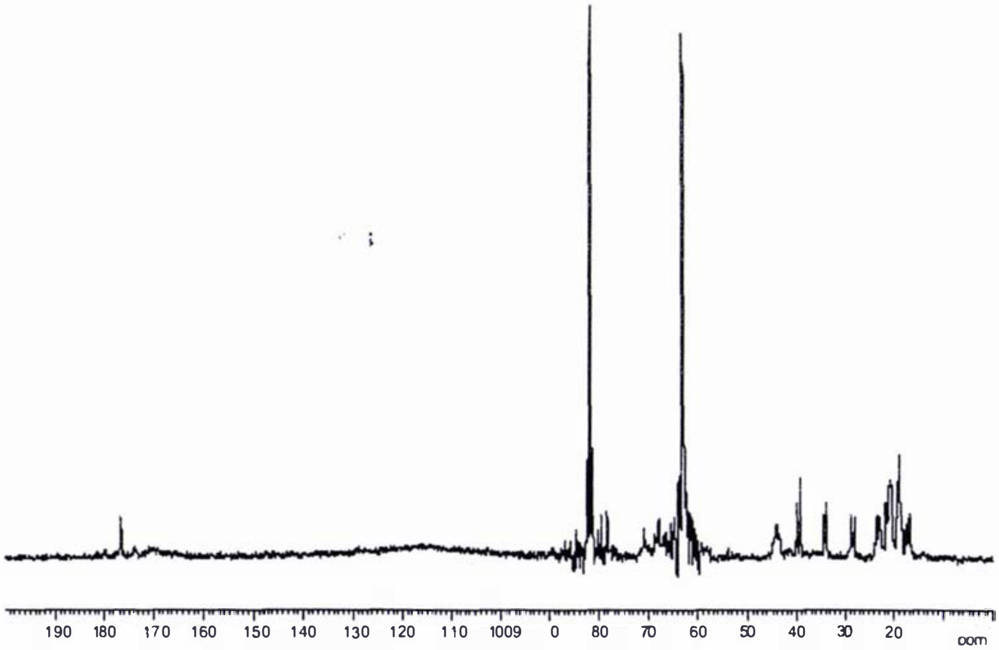

Figure 8.24. 100.1 MHz solution state ^{13}C NMR spectrum of ^{13}C labelled *N*-MAM/PVAc emulsion polymer with 5% w/v $AlCl_3$. [Conditions as per Figure 8.20].

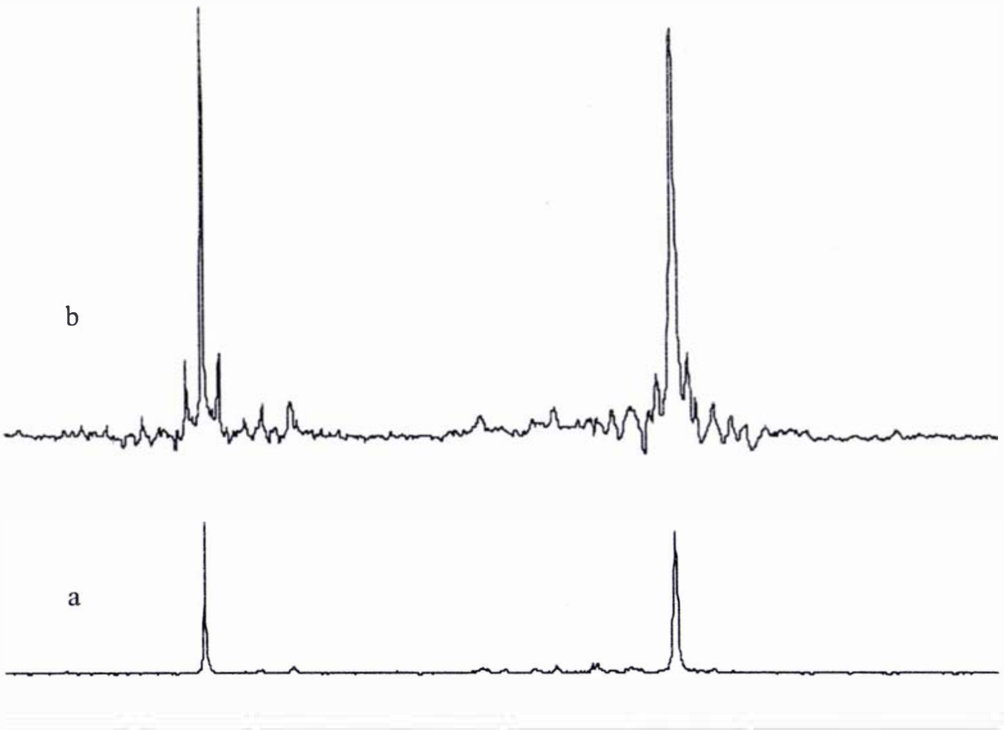

Figure 8.25. Expansion of ^{13}C NMR spectra of (a) ^{13}C labelled *N*-MAM/PVAc emulsion polymer and (b) ^{13}C labelled NMAM/PVAc emulsion polymer with 5% w/v AlCl$_3$.

Addition of AlCl$_3$ in either the *N*-MAM gel or the *N*-MAM/PVAc emulsion polymer gives rise to a change in chemical shift of the aluminium. As water is removed from the *N*-MAM gel or PVAc adhesive during cure there is a low frequency shift in the chemical shift of the ^{27}Al signal (Table 8.10, Figure 8.26). This shift suggests a change in the aluminium chemical environment from a solvated environment to a covalently bonded octahedral or sheared octahedral structure.

Table 8.10. ^{27}Al NMR chemical shifts of added AlCl$_3$ with respect to 2M Al(NO$_3$)$_3$ (0.0 ppm).

	^{27}Al Chemical Shift (ppm)
AlCl$_3$ (D$_2$O)	0.38
+ *N*-MAM (liquid)	0.05
+ *N*-MAM (gel)	0.09
+ *N*-MAM (air-dried)	-3.55
+ *N*-MAM (oven-dried)	-7.04
+ *N*-MAM/PVAc (liquid)	0.12
+ *N*-MAM/PVAc (cured)	-0.62

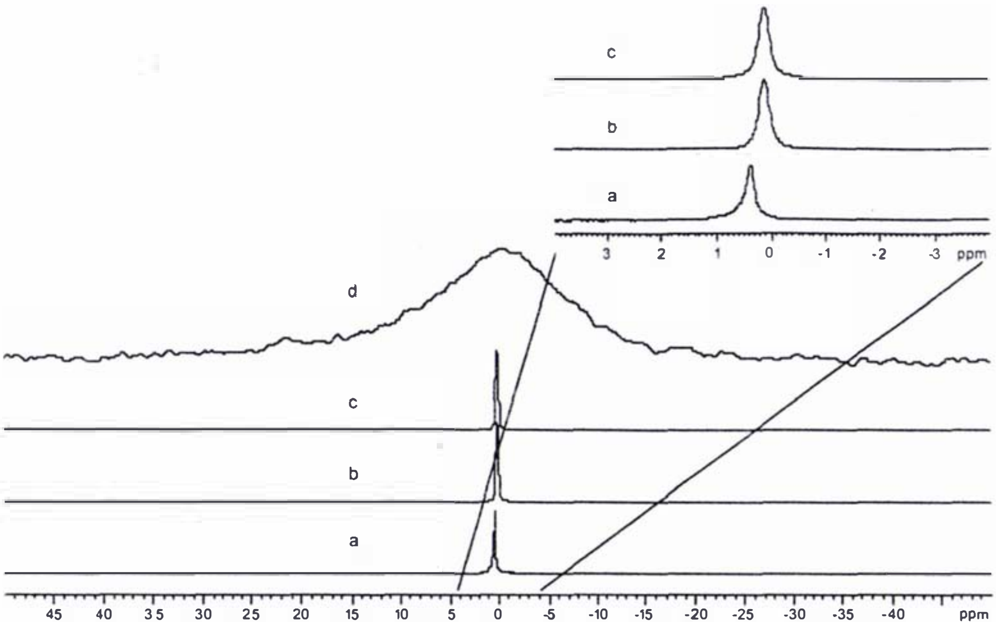

Figure 8.26. 52.2 MHz solution state ^{27}Al NMR spectra of (a) $AlCl_3$ solution, (b) PVAc + 5% w/v $AlCl_3$ 10 minutes after addition and (c) 12 hours after addition of $AlCl_3$ and (d) 52.2 MHz ^{27}Al MAS NMR spectrum of cured resin. The insert shows the expansion of the chemical shift scale for a-c. [Solution state: Avance-200, D_2O, single pulse, relaxation delay 2 s, 12 µs 90° pulse, LB 2 Hz, referenced to external 2M $Al(NO_3)_3$, (0.0 ppm). Solid state: Avance-200, HPDEC, rotor speed 4 kHz, relaxation delay 2 s, 6 µs 90 ° pulse, LB 20 Hz, referenced to external 2M $Al(NO_3)_3$, (0.0 ppm)].

The corresponding ^{13}C NMR spectra of the *N*-MAM/PVAc adhesive is shown in Figure 8.27 along with an expansion of the methine and methylene region in Figure 8.28, which also shows tacticity assignments for the diads and triads.

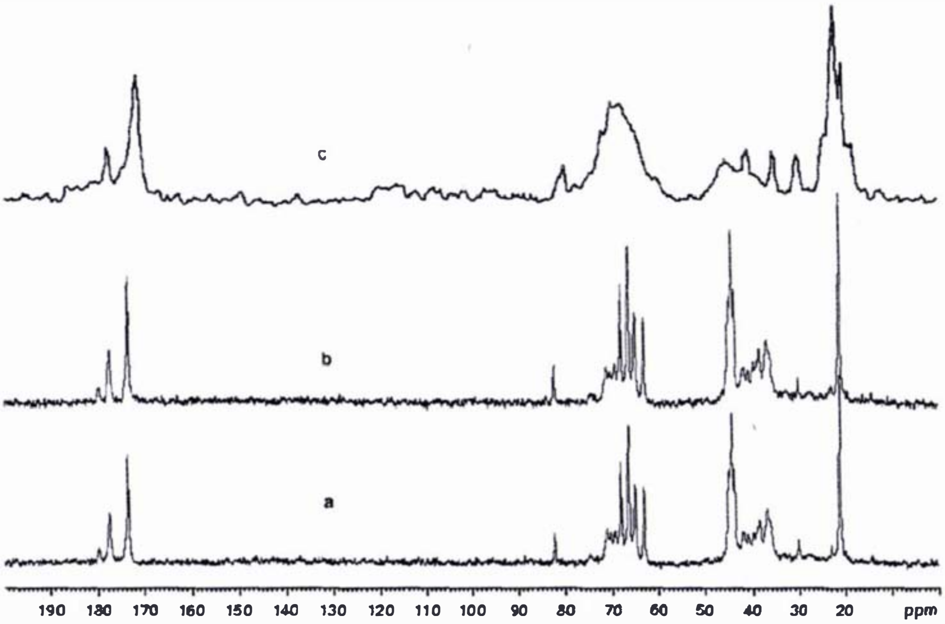

Figure 8.27. 100.1 MHz ^{13}C NMR spectra of PVAc + 5% w/v $AlCl_3$ solutions (a) 1 hour and (b) 2 hours after addition of $AlCl_3$ and (c) 75.4 MHz ^{13}C MAS NMR spectrum of cured adhesive. [Conditions as per Figure 8.20 (solution) and Figure 8.27 (solid)].

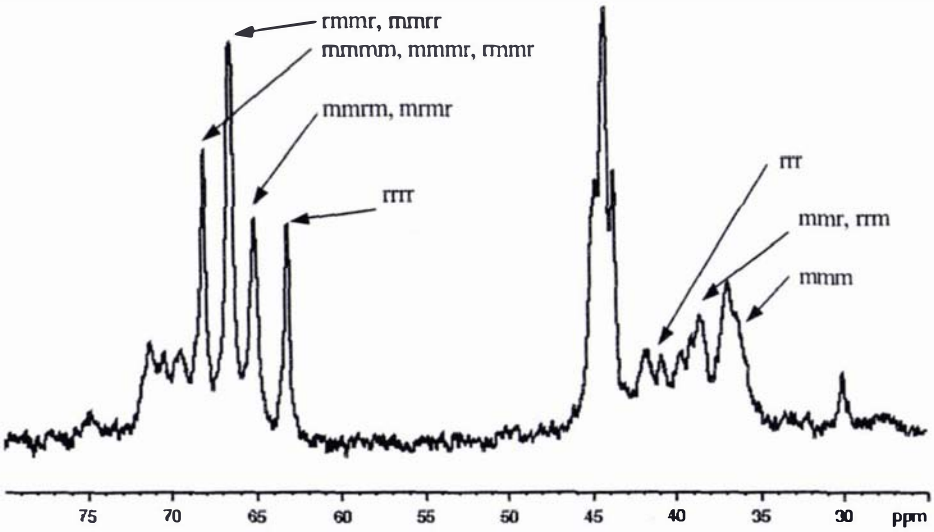

Figure 8.28. Expansion of methine and methylene region of Figure 8.26a showing tacticity assignments (Wu and Ovenall, 1974; Sung and Noggle, 1981).

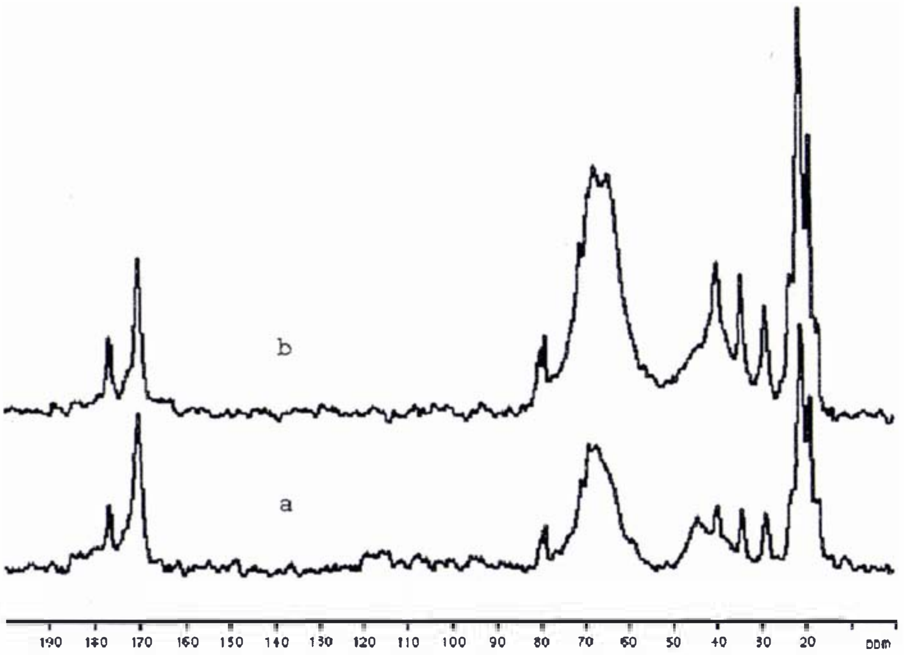

Figure 8.29. 75.4 MHz ^{13}C MAS NMR spectra of (a) cured ^{13}C-labelled *N*-MAM/PVAc + 5% $AlCl_3$ and (b) cured ^{13}C-labelled *N*-MAM/PVAc. [MSL-300, HPDEC, relaxation delay 2 s, 5.6 μs 90° pulse, rotor speed 7.5 kHz, LB 20 Hz, referenced external adamantane (38.3 ppm)].

There is very little difference between the ^{13}C MAS NMR spectra of cured ^{13}C-PVAc and ^{13}C-PVAc with addition of $AlCl_3$ (Figure 8.29). The resonance at 44.5 ppm is more pronounced in the adhesive with addition of the aluminium. At the same time the signal intensity is less in the sample with aluminium addition, suggesting a change in T_1, although relaxation studies have not been undertaken.

8.4 SUMMARY OF CHAPTER

The curing of phenol-resorcinol-formaldehyde resols under conventional conditions has been followed by ^{13}C NMR spectroscopy and compared to accelerated cure achieved under GreenWeld™ conditions with ammonia. Unlike conventional curing, use of ammonia causes the cure to proceed *via* methyleneimine intermediates resulting in both aniline-type and benzylamine-type crosslinked structures.

In a similar manner, NMR spectroscopy of poly(vinyl acetate) latex adhesive cured with and without the addition of aluminium chloride shows that the aluminium cation is involved in crosslinking *via* solvation complexes.

9. RHEOLOGY AND RHEO-NMR STUDIES OF ADHESIVES

Our knowledge can only be finite, while our ignorance must necessarily be infinite. Karl Popper

The curing of adhesives involves the formation of high molecular weight polymers from the constituent low molecular weight, monomeric and oligomeric compounds. The very nature of the polymerisation imparts physico-chemical change to the resultant polymer, the most obvious being its decreasing solubility, to a point where the polymer is no longer soluble in the original (or any other) solvent.

During the cure of a polymer adhesive, the viscosity slowly increases until the *gel point* is reached, at which point the viscosity increases sharply and a rigid polymer is formed. The gel point, while difficult to define, can, for a chemical crosslinking polymer such as PVAc, be thought of as the point in time at which each polymer chain contains an average of one crosslink to another chain (Winter, 1989). Note that the molecular weight distribution at the gel point may be broad and it may still be possible to extract low molecular weight molecules. Once crosslinking has occurred an elastic network is formed whose elastic modulus is directly related to crosslink density. In this chapter we carry out some simple measurements of elasticity using a newly developed compression cell.

Nuclear magnetic resonance techniques find themselves ideally suited to the study of adhesive polymer systems, either as low molecular weight solutions or as cured gels or resins. Solid state NMR in particular is widely used to characterise polymers and to study the nature and extent of crosslinking in polymers (Whittaker, 1997).

In this thesis a different approach is adopted in the use of NMR to characterise rheology. In particular we will use NMR imaging and spectroscopy to investigate latex adhesives under deformation. This represents a novel approach to the study of molecular properties and the results presented represent an initial investigation only. However they point the way to possible future investigations.

The structure of this chapter is as follows. First the basic principles of elastomer mechanical properties are described, with reference to both the elastic modulus and visco-elastic relaxation. Then the flow curve rheology of viscous liquids is discussed in the context of flow curve measurement using the cone-and-plate device in tandem with NMR velocimetry investigations of the deformation profile within the fluid. The elastomer discussion pertains to mechanical and rheo-NMR measurements on model gel systems, while the discussion of cone-and-plate flow curve rheology involves rheo-NMR investigations of the liquid adhesives.

9.1 POLYMER NETWORKS AND POLYMER DEFORMATION

Consider the crosslinked polymer network as shown in Figure 9.1. Assume that the network undergoes *affine deformation*, meaning that the deformation is the same at all length scales. In the affine deformation model it is assumed that:

- The network has n chains per unit volume
- Volume is conserved in deformation
- The chain segments between crosslinks can be represented by a Gaussian distribution of phantom chains (which can pass freely through one another)
- The unstressed network is isotropic

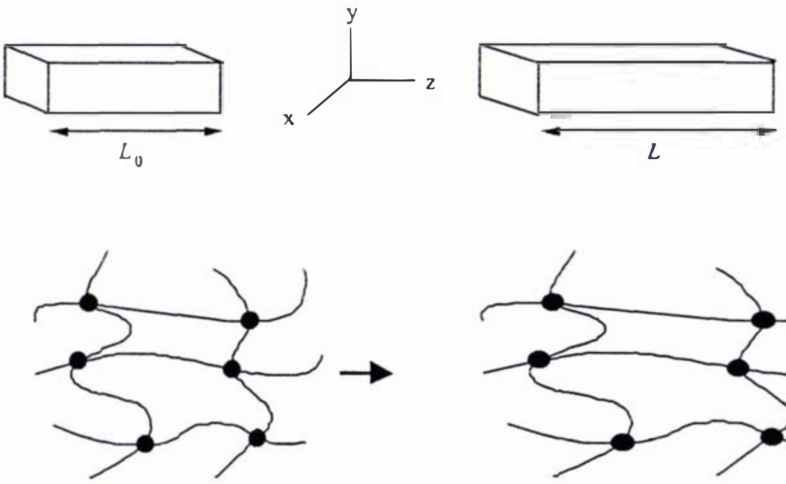

Figure 9.1. Schematic showing affine deformation of crosslinked polymer chains resulting from uniaxial extension.

Consider uniaxial extension along the z axis arising from the deformation matrix

$$\mathbf{E} = \begin{bmatrix} \lambda_1 & 0 & 0 \\ 0 & \lambda_2 & 0 \\ 0 & 0 & \lambda_3 \end{bmatrix} \qquad \text{eqn 9.1.}$$

then any distance L_0 measured along z changes to L such that the extension ratio is:

$$\lambda_3 = \lambda = L/L_0 \qquad \text{eqn 9.2.}$$

In order to conserve volume $\lambda_1 \cdot \lambda_2 \cdot \lambda_3 = 1$ and as the extension is uniaxial, $\lambda_1 = \lambda_2$, hence:

$$\mathbf{E} = \begin{bmatrix} \lambda^{-1/2} & 0 & 0 \\ 0 & \lambda^{-1/2} & 0 \\ 0 & 0 & \lambda \end{bmatrix} \qquad \text{eqn 9.3.}$$

We can define the strain, ε, to be:

$$\frac{\Delta L}{L} = \frac{L - L_0}{L_0} \qquad \text{eqn 9.4.}$$

Hence $\lambda = 1 + \varepsilon$ eqn 9.5.

9.1.1 CROSSLINK DENSITY

In an entangled polymer network the point where two chains meet will form a crosslink. The number of chain segments emanating from this point describes the *functionality*, ψ, of the crosslink. For the situation portrayed in Figure 9.2, $\psi = 4$, such that the number of chains that meet at a crosslink is $\psi/2$.

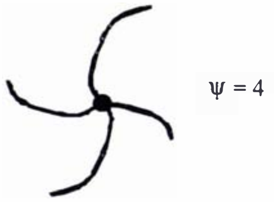

Figure 9.2. Schematic of a crosslink point between two individual polymer chains with functionality, $\psi = 4$.

The number of crosslinks, N_{XL}, per unit volume is a function of the polymer density and average molar mass of the chain segments, $\overline{M}_c$, as given by:

$$N_{XL} = \rho N_{AV} / \overline{M}_c \qquad \text{eqn 9.6.}$$

The stress-extension relationship can be written (Treloar, 1971; Doi, 1996):

$$\sigma = \frac{\psi \nu k_B T}{2} \left(\lambda^2 - \lambda^{-1}\right) \qquad \text{eqn 9.7.}$$

For small deformation this reduces to:

$$\sigma = {}^3\!/_2\, \psi \, \nu \, k_B \, T \varepsilon \qquad \text{eqn 9.8.}$$

9.1.2 UNIAXIAL COMPRESSION OF GELS

Consider a material of length L, deformed by a small amount, ΔL. The strain, ε, is defined by:

$$\varepsilon = \frac{\Delta L}{L} \qquad \text{eqn 9.9.}$$

According to Hooke's law, deformation is proportional to the applied force. For small deformations, the stress, σ (force per unit area) and strain are related *via* the elastic modulus E, given by:

$$\sigma = E \varepsilon \qquad \text{eqn 9.10.}$$

Hence, comparing equations 9.8 and 9.10, we see that E is related to the crosslink density as:

$$E = {}^3\!/_2\, \psi \, \nu \, k_B \, T \qquad \text{eqn 9.11.}$$

In this chapter an estimate of the elastic modulus is obtained by deforming the sample under compression. Consider a hydrogel cylinder under compression from force f shown schematically in Figure 9.3. A constant strain is applied to the sample and the stress is measured with respect to time.

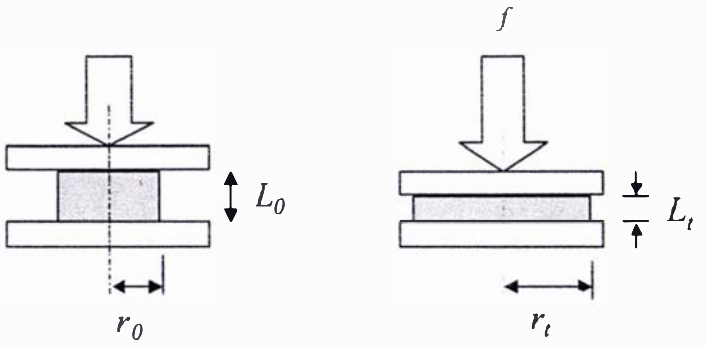

Figure 9.3. Schematic of compression of a hydrogel causing deformation.

Assuming a constant volume sample, the sample radius at time t can be determined from the thickness according to:

$$r_t = r_0\sqrt{\frac{L_0}{L_t}} \qquad \text{eqn 9.12.}$$

where r_t is the radius at any time t, r_0 is the initial radius, L_0 is the initial thickness and L_t is the thickness at time t.

From this the time dependent stress can be determined according to:

$$\sigma(\mathrm{t}) = \frac{f}{\pi r_t^2} \qquad \text{eqn 9.13.}$$

Note that, at any instant, the strain rate, $\dot{\varepsilon}$ (t), can be given by:

$$\dot{\varepsilon} = -\frac{\Delta L / \Delta \mathrm{t}}{L} \qquad \text{eqn 9.14.}$$

Hence the integrated (Hencky) strain can be determined according to:

$$\varepsilon_H = -\frac{1}{2}\ln\left(\frac{L_t}{L_0}\right) \qquad \text{eqn 9.15.}$$

Measurement of uniaxial compression was performed using "The Squisher" (shown schematically and in photograph in Figure 9.4), a device built in-house at Massey University to measure compressive force with respect to a calibrated rate of loading, to a point of fixed load, following which the strain is held constant and the stress allowed to relax to equilibrium. A Mac personal PC, which acted as a data logger, controlled the device and the resulting data was analysed using Matlab routines (Peurière, 2000) and Excel. A manually-operated version of "The Squisher" was also used in the NMR spectrometer to obtain spectra during various stages of compression.

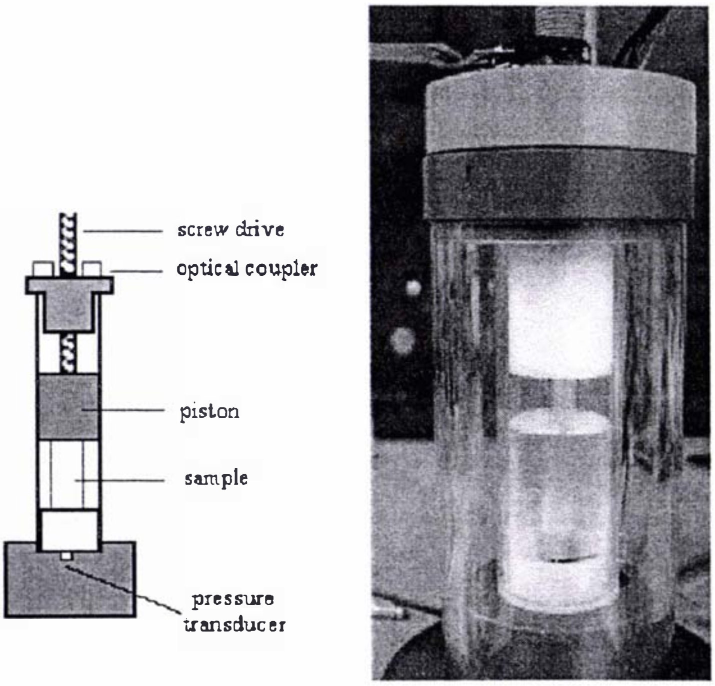

Figure 9.4. Schematic and photograph of "The Squisher" showing the sample gap between the fixed base plate, the top mounted moving piston, the screw drive, the optical coupler to register the zero point and the micro pressure transducer.

The basis of the analysis is the calculation of the instantaneous stress *via* equation 9.13 and the instantaneous "extension ratio", λ, *via* equation 9.2. Furthermore, during the process of applying the strain at a fixed rate it is possible to gain information about the elasticity through relation 9.7. During subsequent stress relaxation the data logger records the time dependence of the stress, so that a relaxation analysis can be performed.

9.1.3 STRESS RELAXATION

When a constant deformation is applied to an object, such as that experienced as a result of compression, the object undergoes internal rearrangement to relieve the stress. This can be achieved via one of three microscopic mechanisms (Lenk, 1978).

1. In a rapid elastic manner characterised by a high modulus corresponding to bond stretching and deformation of bond angles.
2. By viscous flow characterised by a low modulus corresponding to the slippage of flow units past one another.
3. In a rubber-elastic manner characterised by a low modulus but with largely reversible slippage of flow units. The flow units straighten out from their randomly coiled configuration and align along the stress axis.

These responses can be described macroscopically by using a mechanical model comprising dashpots and springs. The classic Maxwell model utilises a single dashpot and spring in series while the Kelvin or Voigt model uses a single dashpot and spring in parallel (Figure 9.5).

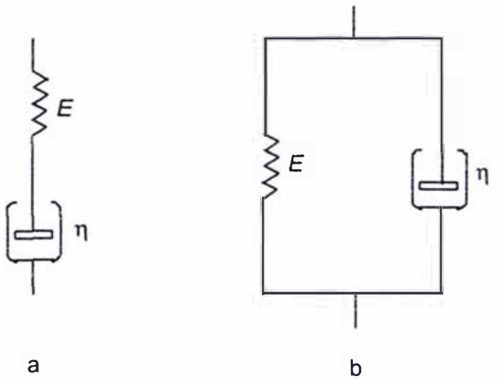

Figure 9.5. Simple spring and dashpot models (a) Maxwell model (b) Kelvin or Voigt model.

In the Maxwell model with the elements connected in series the stress in the model is equal to the stress in each element whereas the strain is equal to the sum of the strain in the two elements:

$$\sigma = \sigma_E = \sigma_\eta \quad \text{and} \quad \varepsilon = \varepsilon_E + \varepsilon_\eta \qquad \text{eqn 9.16.}$$

The subscripts E and η denote components associated with the elastic and viscous elements respectively.

The equation of strain of a Maxwell element is then given by:

$$\varepsilon = \frac{\sigma}{\eta} + \frac{\dot{\sigma}}{E} \qquad \text{eqn 9.17.}$$

For the Voigt model the constitutive equation is given by:

$$\sigma = E\varepsilon + \eta\dot{\varepsilon} \qquad \text{eqn 9.18.}$$

Neither model is able to simultaneously represent relaxation and creep of a polymer under stress, and so a combined Maxwell-Voigt model termed the *standard linear solid model* has been used (Lockett, 1972; Lenk, 1978; Figure 9.6). At low temperatures the viscosities of the dashpot, η, is high and the polymer can only respond in an elastic manner defined by the springs with moduli E_1 and E_2. At higher temperatures the viscosity of the dashpots will be lower and will enable relaxation of stress in the right hand element so that the final elastic behaviour is determined by E_2 alone. The consequence of the stress relief behaviour is that the polymer appears soft and rubbery.

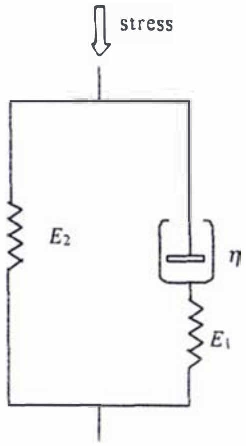

Figure 9.6. Schematic of a combined Maxwell-Voigt standard linear solid model for stress accommodation in polymers.

The equation of state for the standard linear solid model shown in Figure 9.6 is given by:

$$\left(1+\frac{E_2}{E_1}\right)\sigma+\left(\frac{\eta}{E_1}\right)\dot{\sigma}=E_2\,\varepsilon+\eta\dot{\varepsilon} \qquad \text{eqn 9.19.}$$

In the experiments undertaken with the Squisher, force is applied in order to deform the material to a point of constant strain, which is then maintained while the stress in the material relaxes. In this instance, τ_R is the relaxation time (Lenk, 1978) and is defined by:

$$\tau_R=\frac{\eta}{E} \qquad \text{eqn 9.20.}$$

For the system of springs and dashpot as shown in Figure 9.6 subjected to a sudden strain, the springs respond immediately while the dashpot is initially unstrained. As a consequence, the stress which is required to be applied to the system is the sum of the stress in the individual springs, E_1 + E_2. Subsequently the dashpot will relax so that the stress is determined by E_2 alone.

This simple model reflects the microscopic behaviour of a gel subjected to stress. The dashpot represents internal molecular reorganisation. In terms of molecular reorientation, a rapid relaxation can be attributed to the unravelling of twisted chains whereas the relaxation mechanisms with longer time constants require the breaking and formation of hydrogen bonds (weak van der Waals forces) to allow flow past adjacent polymer segments. In a real system there may be multiple time constants. Then the time constant τ_R defined in equation 9.20 directly relates to the microscopic behaviour.

In the simple model of Figure 9.6, the stress relaxes mono-exponentially as:

$$\sigma(t) = \sigma_0 \exp(-t/\tau_R) \qquad \text{eqn 9.21.}$$

However in a real system the relaxation behaviour may be much more complicated and multi-exponential behaviour may be observed.

9.2 UNIAXIAL COMPRESSION OF HYDROGELS

Cylinders of *N*-MAM or PVAc hydrogels (with and without addition of $AlCl_3$) were prepared by casting in 7 mm ID silicone tubing. The dimensions of the cylinders were measured by vernier callipers, with the height being in the range 6 – 8 mm.

The PVAc and *N*-MAM hydrogels were compressed in "The Squisher" using a protocol whereby a strain was rapidly applied to the gel and then maintained while the stress in the gel subsequently relaxed. The relaxation results will be explained in terms of the spring and dashpot model discussed previously.

9.2.1 STRESS-STRAIN RELATIONSHIPS

Stress *vs* extension ratio plots have been obtained by analysing the build-up of stress during the initial application of strain, using data taken from force *vs* time plots like that shown in Figure 9.11. Figure 9.7 shows the stress-extension ratio plot for *N*-

MAM hydrogels with and without addition of aluminium chloride at varying *N*-MAM concentrations. The expanded plot shows that for a given stress of 2000 N mm^{-2}, there is a dramatic difference in the strain experienced between a 30% *N*-MAM hydrogel and a 10% *N*-MAM hydrogel containing 5% $AlCl_3$ (Figure 9.8). Whereas the 30% *N*-MAM gel shows very little strain at high stress, the remaining gels and in particular the 10% *N*-MAM/5% $AlCl_3$ gel shows considerable strain. Furthermore the 30% *N*-MAM gel shows very little increase in strain at much higher stress levels. This is a very rigid gel suggesting that there is very little mechanism available for molecular reordering on the short time scale associated with the period of stress build-up, on the order of one second. This in turn suggests a very highly crosslinked gel.

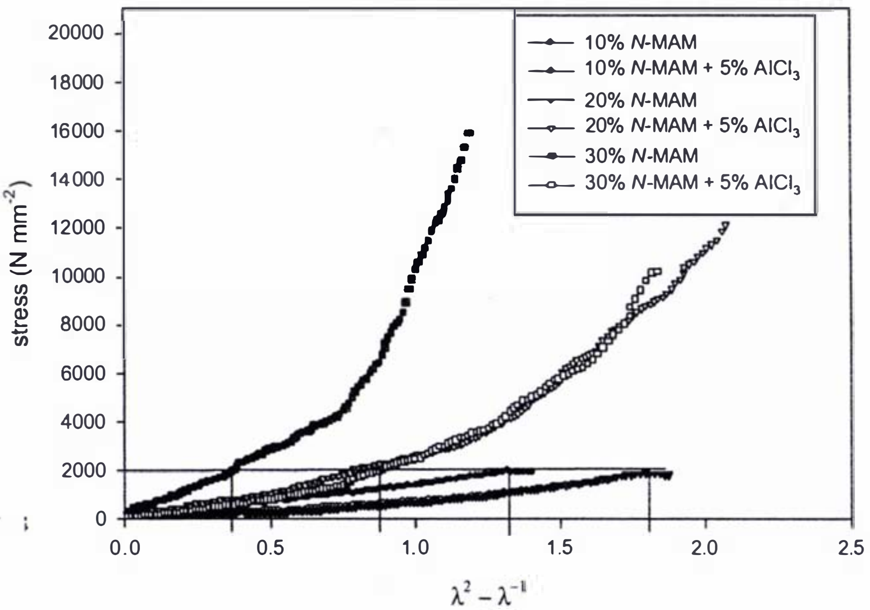

Figure 9.7. Stress *vs* extension ratio plot for gels of varying *N*-MAM concentration with and without addition of $AlCl_3$.

The 30% *N*-MAM gel shows very little strain at 2000 N mm^{-2}, compared to the 10% *N*-MAM gel which shows approximately three times the strain. Addition of aluminium chloride increases the corresponding strain for a given stress in both the 10% and 30% *N*-MAM gels.

From equation 9.7, assuming a functionality (ψ) of 4, the crosslink density, ν_c, (as measured at 21 ±2 °C) is given by:

$$\nu_c = \frac{\sigma}{k_B T(\lambda^2 - \lambda^{-1})} \qquad \text{eqn 9.22.}$$

The molar crosslink densities, ν_c, as molar amount of crosslinks per cubic centimetre, for the *N*-MAM gels at 10 and 30% concentration with and without addition of aluminium chloride are given in Table 9.1. This analysis shows that the 30% *N*-MAM gel is highly crosslinked and that addition of aluminium chloride to an *N*-MAM gel actually decreases the crosslink density in the gel.

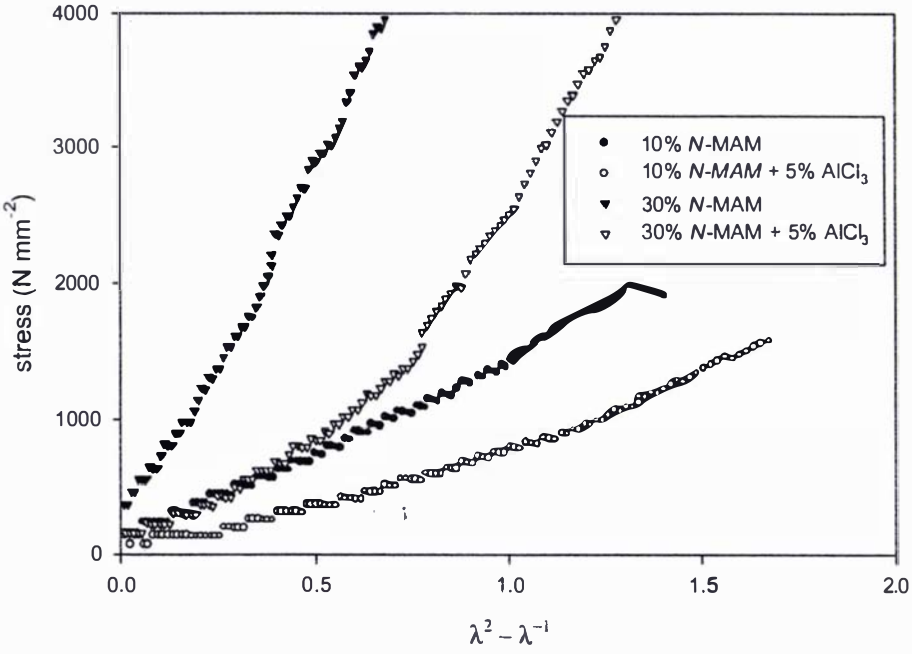

Figure 9.8. Expansion of stress *vs* extension ratio plot for gels of varying *N*-MAM concentration for 10% and 30% *N*-MAM concentration, with and without addition of AlCl$_3$.

Table 9.1. Crosslink densities for *N*-MAM gels of varying concentration with and without addition of AlCl$_3$.

	10% *N*-MAM	10% *N*-MAM +AlCl$_3$	20% *N*-MAM	20% *N*-MAM +AlCl$_3$	30% *N*-MAM	30% *N*-MAM +AlCl$_3$
ν_c (10^{-4} mol cm^{-3})	4.9	3.1	7.3	8.2	17.6	7.3

When aluminium chloride is added, at varying concentration, to 20% *N*-MAM gels there is a maximum crosslink density achieved with 5% addition (Figure 9.9, Table 9.2). Commercially, aluminium is added to PVAc/*N*-MAM adhesive formulations at around the 5% level, as it is believed to increase crosslinking. This result would suggest that 5% addition is indeed the level of addition required for maximum crosslinking to occur. However, the previous result comparing the crosslink density of *N*-MAM gels with and without addition of aluminium chloride suggests that the addition is in fact detrimental to crosslink formation.

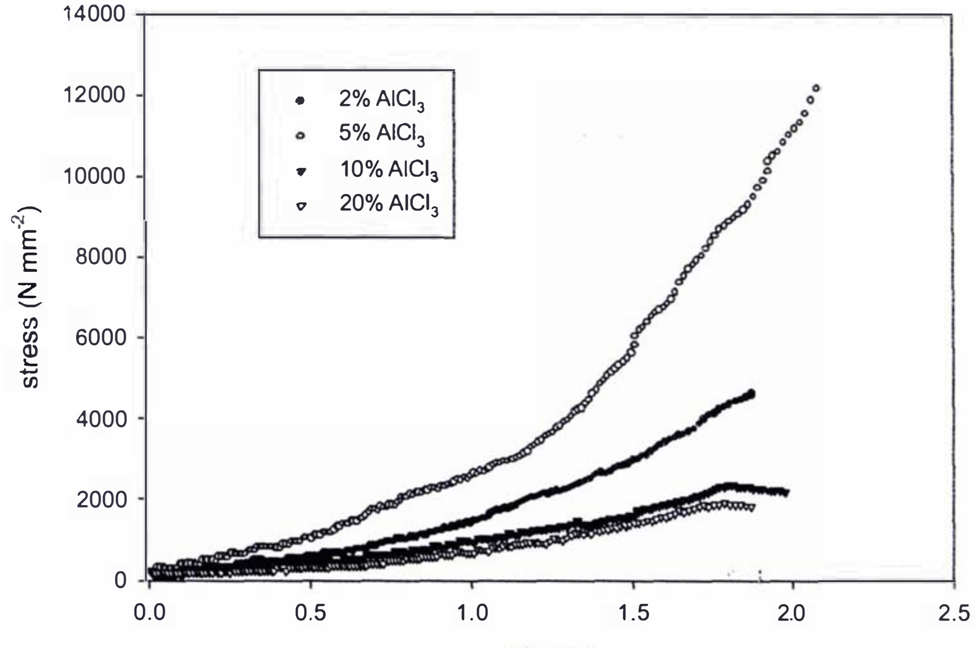

Figure 9.9. Stress *vs* extension ratio plot for gels at 20% *N*-MAM concentration with varying $AlCl_3$ concentration.

Table 9.2. Crosslink densities for 20% *N*-MAM gels with varying $AlCl_3$ concentration.

	2% $AlCl_3$	5% $AlCl_3$	10% $AlCl_3$	20% $AlCl_3$
ν_c (10^{-4} mol cm^{-3})	5.5	8.2	3.9	3.4

To investigate this anomalous behaviour further, PVAc/*N*-MAM formulations with and without addition of aluminium chloride were subjected to uniaxial compression and the results analysed in a similar fashion. Once more it appears that addition of aluminium chloride to the formulation has the effect of decreasing the crosslink density (Figure 9.10, Table 9.3). This runs counterintuitive to the reason for adding aluminium in the first place as it has long been held that addition of aluminium cation to PVAc formulations aided crosslinking. In fact the practical effect of aluminium addition is a *strength* improvement. Strength relates to the energy required to break the crosslinked structure whereas elasticity relates simply to the crosslink density. It is not necessary that these two mechanical parameters be directly related. For example, it may mean that aluminium addition has the effect of making fewer crosslinks but with stronger overall bonding. Certainly the results reported here suggest that some further investigation of the detailed nature of the physico-chemical effects of aluminium addition is warranted.

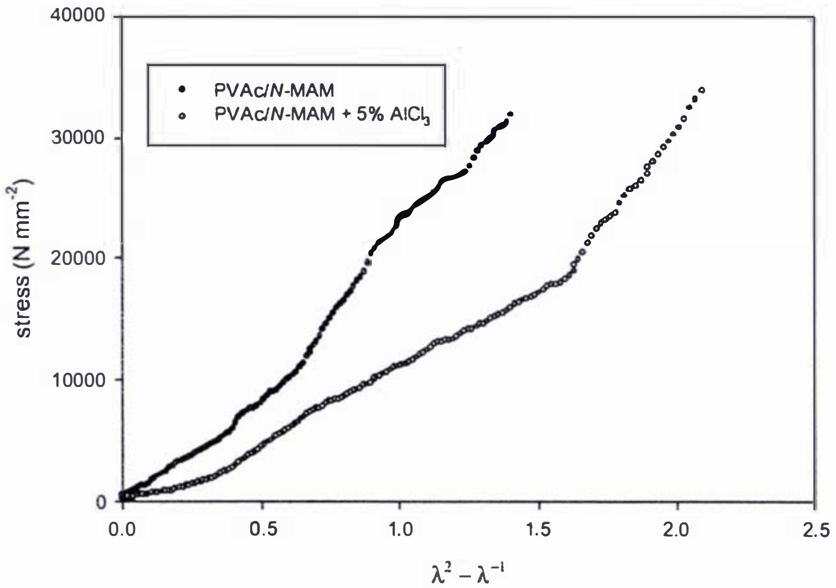

Figure 9.10. Stress *vs* extension ratio plot of PVAc/*N*-MAM gels with and without addition of 5% $AlCl_3$.

Table 9.3. Crosslink densities for PVAc/*N*-MAM gels with and without addition of $AlCl_3$.

	PVAc/*N*-MAM	**PVAc/*N*-MAM + 5% $AlCl_3$**
ν_c (10^{-4} mol cm^{-3})	55.6	19.4

In an attempt to further elucidate these results, analysis of the stress relaxation during constant strain was undertaken and the results presented in the following section.

9.2.2 RELAXATION BEHAVIOUR

Relaxation analysis was performed using the time dependence of the stress during the stress relaxation period, as shown in Figure 9.11. Force *vs* time plots are shown using a reduced number of data points in order to clarify the plot presentation. However, all data analysis was performed using the full range of available data (0.05 s intervals).

The compressive extension of cured *N*-MAM samples both with and without addition of $AlCl_3$ at varying concentrations of *N*-MAM can be seen in Figure 9.11. It shows that for low concentration of *N*-MAM (10%) very little force is required to cause flow in the cured polymer.

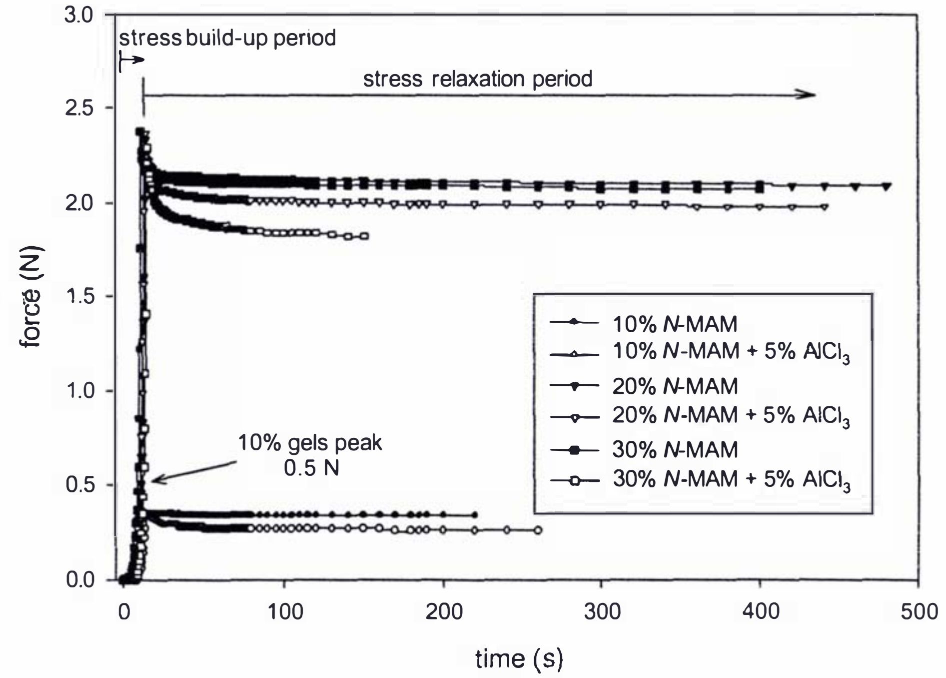

Figure 9.11. Force versus time plot for varying *N*-MAM concentration with and without addition of 5% $AlCl_3$. This plot also shows the stress build-up and relaxation periods referred to in the text.

In terms of the spring and Maxwell-Voigt dashpot model presented in section 9.1, this is explained in terms of the rapid initial relaxation of the shear stress followed by a slower relaxation. In all cases the addition of aluminium chloride enhances the rate of initial relaxation, suggesting that the crosslinks formed by the aluminium are weak and act as ball bearings to allow flow of adjacent polymer segments past one another.

The data have been fitted to a multi-exponential curve of the form:

$$\sigma(t) = \sum_n a_n \exp\left(-\frac{t}{\tau_n}\right) \qquad \text{eqn 9.22.}$$

In order to extract the time constants, τ_n, and amplitudes, a_n, the "inversion" of $\sigma(t)$ was performed using a regularised non-negative least squares procedure (Lawson and Hanson, 1974; Bates and Watts, 1988) with 100 time constants logarithmically spaced between the upper and lower bounds (which can be preset in the analysis).

In order to make sense of this analysis it is important to refer to the raw data. In particular we note that the materials tend to exhibit a very rapid initial decay ($\tau_R < 1$ s), a distinct intermediate decay (τ_R 1 - 10 s) and a weak and very slow final relaxation ($\tau_R > 10$ s). Clearly the relaxation is complex and, given the difficulties in inverting multi-exponential decay, it would be unwise to attempt to interpret the data in too much detail. However attention will be focussed on the distinct intermediate time scale decay.

The raw data showing relaxation of the gels with varying *N*-MAM concentration, with and without addition of aluminium chloride, is given in Figure 9.11. The corresponding exponential analysis is shown in Figure 9.12.

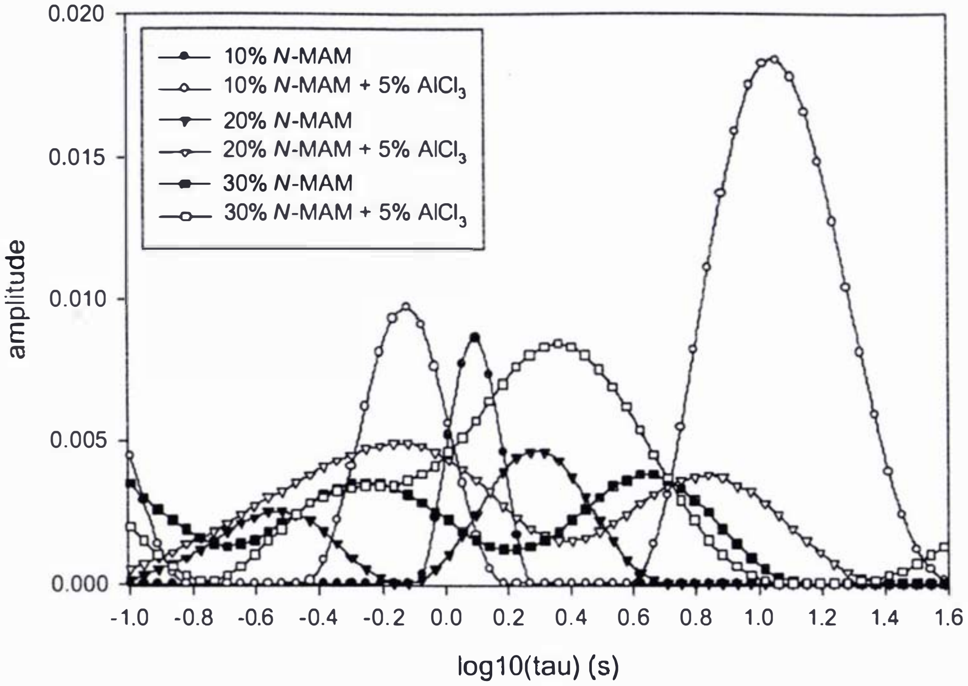

Figure 9.12. Relaxation time constant profile for varying *N*-MAM concentrations with and without addition of 5% $AlCl_3$.

All the gels show one or even two short time constants less than 1 second, while the 10% gel with added aluminium also shows a long time constant greater than 10 s. Figure 9.13 shows the expansion for the 10% and 30% gels for the range of time constants between 1 and 10 s. Addition of 5% $AlCl_3$ to 10% and 30% *N*-MAM gels, results in shorter intermediate relaxation time constants for the stress relaxation of the aluminium containing gel (Table 9.4). The arrows indicate the position of the dominant peaks. In particular for the 10% gel the time constant reduces from 1.3 to 0.8 s and for the 30% gel the time constant reduces from 4.6 to 1.9 s. In terms of the combined Maxwell-Voigt model described in Figure 9.6, this suggests a dashpot with a shorter (less viscous) time constant.

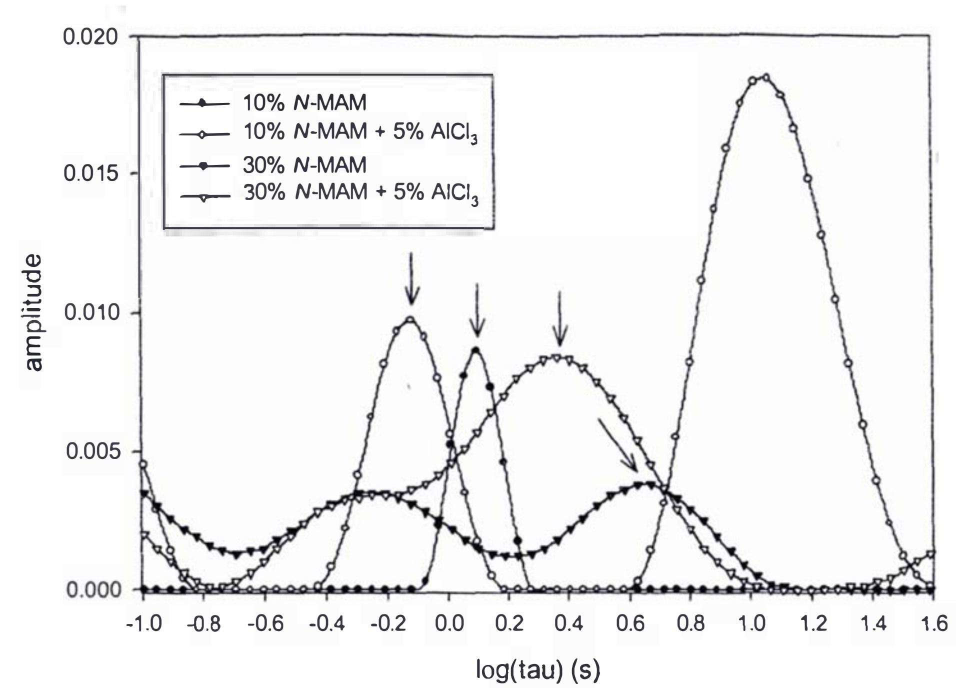

Figure 9.13. Expansion of relaxation time constant profile for 10% and 30% *N*-MAM concentrations with and without addition of 5% $AlCl_3$. The arrows indicate the peaks referred to in the text.

On a microscopic scale the very short time constants are due to rapid uncoiling of the polymer chain backbone. This is totally elastic in its behaviour. The processes giving rise to longer time constants however are visco-elastic in nature and require the breaking and formation of bonds. On the intermediate timescale this probably involves the breaking and formation of hydrogen bonds, which are characterised by weak van der Waal's forces. Addition of aluminium is believed to be involved in crosslink formation *via* solvation type complexes (Figure 2.13 1), which would also enable rapid bond breaking and formation. Interpreting the stress relaxation plots in terms of the increased relaxation afforded by addition of aluminium suggests that the aluminium acts like "ball-bearings" allowing adjacent polymer chains to slip past one another, enabling rapid reordering of the material in a response to compression.

Table 9.4. Relaxation time constants (in seconds) for *N*-MAM gels of varying *N*-MAM concentration with and without addition of $AlCl_3$ taken from Figures 9.12 and 9.13. The highlighted values refer to the peaks arrowed in Figure 9.13.

10% *N*-MAM	20% *N*-MAM	30% *N*-MAM	10% *N*-MAM + 5% $AlCl_3$	20% *N*-MAM + 5% $AlCl_3$	30% *N*-MAM + 5% $AlCl_3$
	0.10	0.10	0.10		0.10
	0.30	0.56			
1.25	**1.89**	**4.17**	**0.76**	**0.68**	**2.45**
			11.55	6.97	

When the level of *N*-MAM is held constant and the concentration of $AlCl_3$ is varied (Figure 9.14) it can be seen that a greater force can be applied to the gel when aluminium chloride is added at the 5% level. In the analysis of the relaxation however, this level of addition (5% $AlCl_3$) doesn't show evidence of a short relaxation time constant (Figure 9.15, Table 9.5).

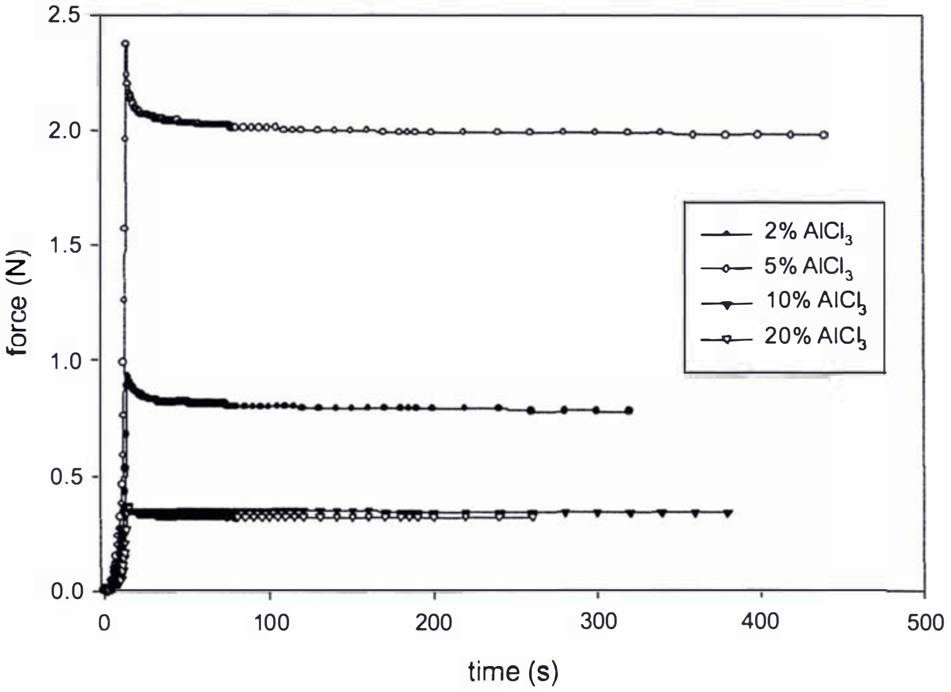

Figure 9.14. Force versus time plot for varying $AlCl_3$ concentration in gels at 20% *N*-MAM concentration.

The remaining gels exhibit a very short relaxation less than 1 s, and intermediate time constants in the range 1 – 10 s. While in Figure 9.14 they all appear to show longer time constants as evidenced by the long decay period, only the time constant for the gel containing 2% $AlCl_3$ was computed from the non-negative least squares fit. As previously mentioned this is one of the problems with curve fitting multi-exponential decay data.

The gel with the longest intermediate time constant is the gel with 5% addition of $AlCl_3$, corresponding to the gel with the highest density of crosslinking (Table 9.2). This suggests that 5% addition of aluminium chloride to the gel produces the most rigid gel whereas addition of either a higher or lower level of aluminium produces gels that are less rigid and relax more quickly.

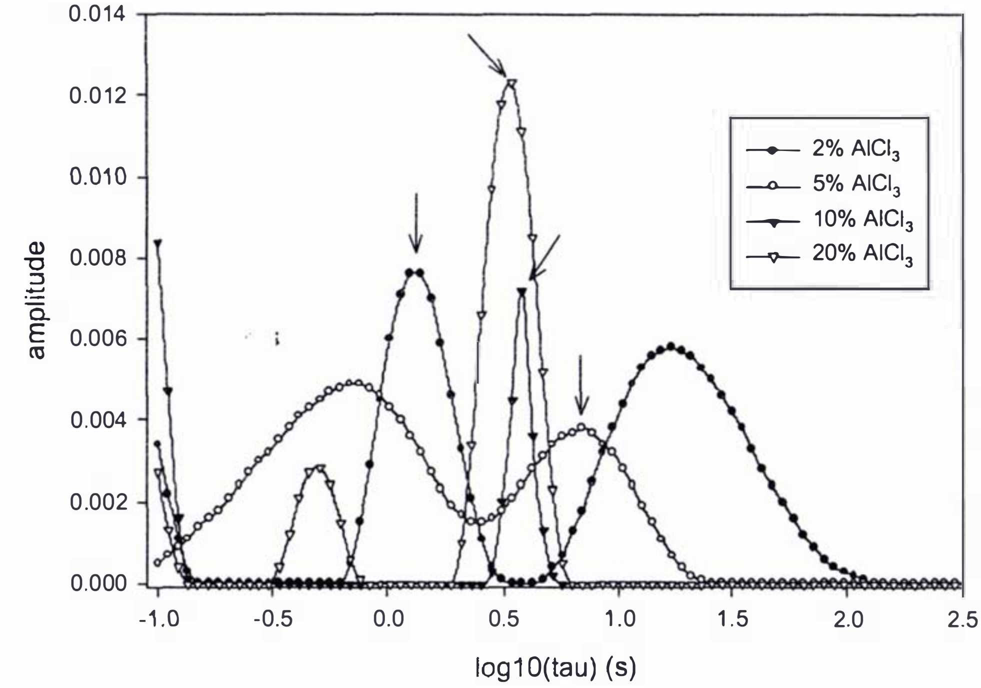

Figure 9.15. Relaxation time constant profile for varying $AlCl_3$ concentration at 20% *N*-MAM concentration.

Table 9.5. Relaxation time constants (in seconds) for 20% *N*-MAM gels with varying concentration of added $AlCl_3$ taken from Figure 9.15.

2% $AlCl_3$	5% $AlCl_3$	10% $AlCl_3$	20% $AlCl_3$
0.1		0.1	0.1
	0.72		0.51
1.31	**6.97**	**3.80**	**3.43**
19.19			

Analysis was also undertaken on fully formulated PVAc/*N*-MAM adhesives with and without addition of 5% $AlCl_3$. The force *vs* time plot for the two formulations is shown in Figure 9.16. As with previous samples the addition of $AlCl_3$ again results in greater stress relaxation, suggesting a greater structural reorganisation on application of a fixed strain.

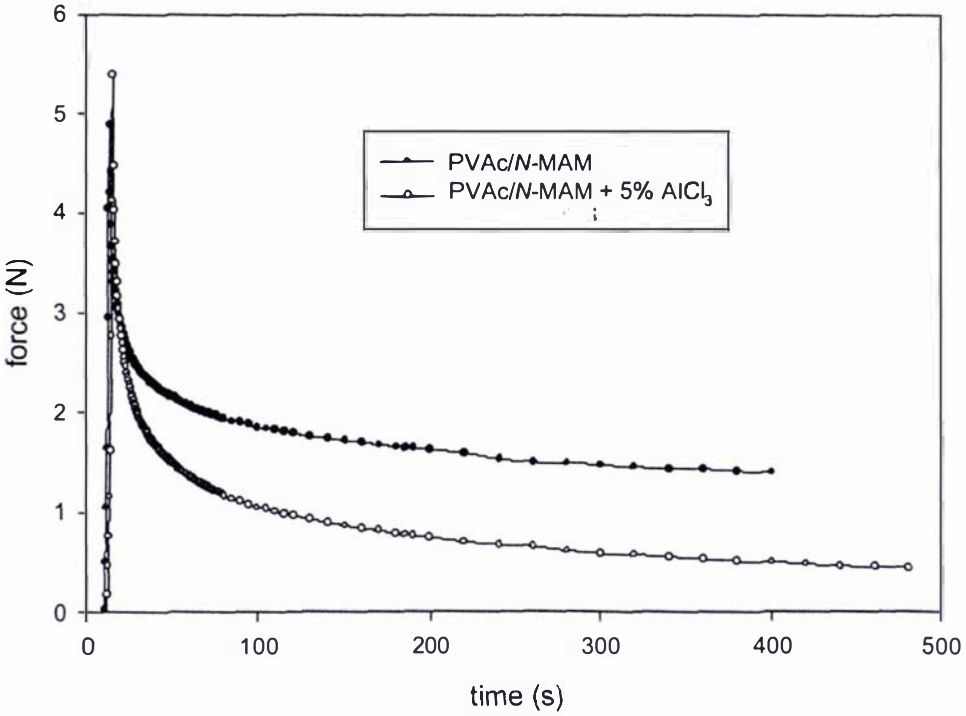

Figure 9.16. Force versus time plot for PVAc/*N*-MAM with and without addition of 5% $AlCl_3$.

The analysis of the time constants (Figure 9.17, Table 9.6) shows three distinct relaxation events with the time constants being shifted to longer periods with the addition of $AlCl_3$.

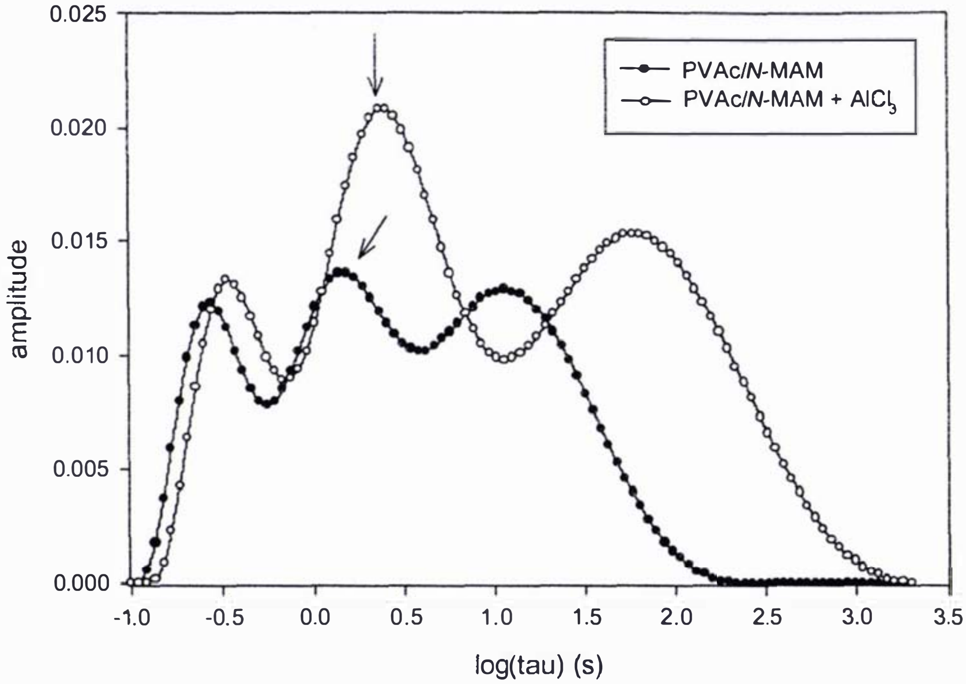

Figure 9.17. Relaxation time constant profile for PVAc/*N*-MAM adhesive with and without addition of 5% $AlCl_3$.

Table 9.6. Relaxation time constants (in seconds) for PVAc/*N*-MAM gels with and without addition of $AlCl_3$ taken from Figure 9.17.

PVAc/*N*-MAM	PVAc/*N*-MAM + 5% $AlCl_3$
0.27	0.34
1.38	**2.41**
10.44	64.3

Unlike the cured *N*-MAM gels whereby addition of aluminium decreased the observed time constants, addition of aluminium to fully formulated, cured *N*-

MAM/PVAc adhesives increases the time constants on all observable timescales. This is in fact what would be expected according to the intent of aluminium chloride addition, whereby the adhesive becomes more rigid and less prone to creep under load. This result can be contrasted with that of the previous section (§ 9.2.1) whereby the addition of aluminium chloride to PVAc appears to decrease the crosslink density of the cured polymer. As mentioned previously it is possible that while the addition of aluminium to PVAc formulations results in lower crosslink density the addition of aluminium in fact imparts strength to the cured gel rendering it more rigid and resilient to creep.

9.2.3 NMR SPECTROSCOPY OF GELS DURING COMPRESSION

In an attempt to observe any molecular change occurring in the gels during compression, multi-nuclear NMR spectra were acquired at stages during the compression. Any change in lineshape or chemical shift could be due to changes in chemical environment.

A manually operated version of "The Squisher" was available to insert into a 20 mm ID microimaging saddle coil. Originally tuned for ^{13}C operation (75.6 MHz) the coil was retuned to 78.2 MHz (^{27}Al) by judicious substitution of a capacitor. A series of ^{27}Al NMR spectra were recorded during an experiment whereby increasing force was applied to a cast cylindrical sample by screwing down the moveable piston turn by turn. Spectra were recorded at each 0.7 mm increment turn (Figure 9.18).

The signal shifts to high frequency by 4.6 ppm in comparing the spectrum recorded with no compression and that recorded at 3.5 mm compression (58% compression). This suggests that there could be a reordering at the aluminium site, which would correspond with formation of covalently bonded aluminium.

However when considering the shift experienced in the ^{1}H spectra under the same compression (Figure 9.19) it can be seen that a similar high frequency shift of 4.2 ppm occurs. Furthermore the change in lineshape is similar for the spectra of both nuclei. A similar high frequency shift of 4.3 ppm is also observed in the ^{13}C spectrum.

As the chemical shift difference is similar for the three nuclei, these observations are explained by changes in the diamagnetic susceptibility as the piston first comes into contact with the gel and then deforms it.

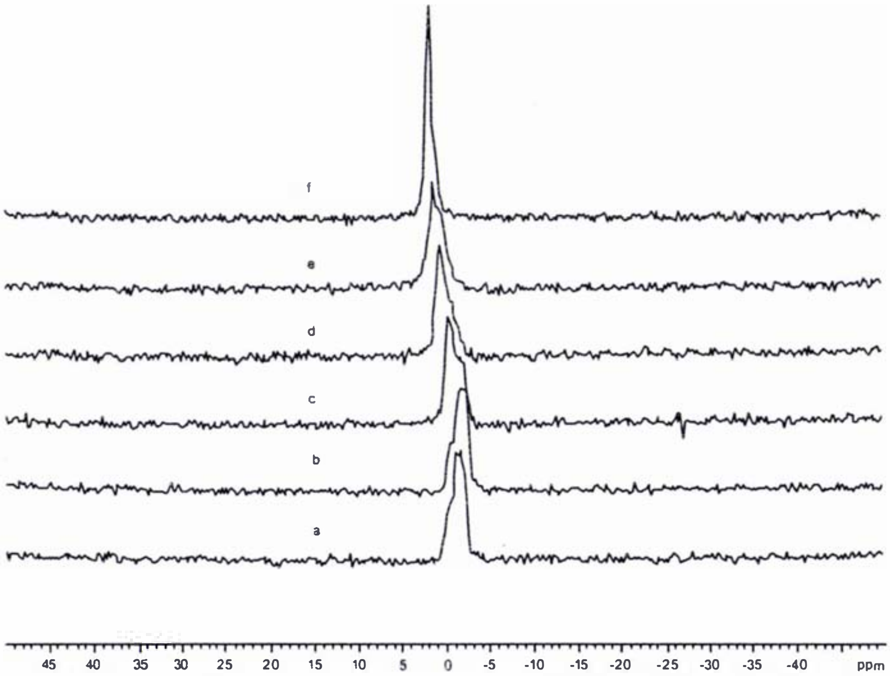

Figure 9.18. 78.2 MHz ^{27}Al NMR spectra of *N*-MAM/$AlCl_3$ cylindrical gels undergoing increased compression. (a) no compression, (b-f) increasingly compressed by 0.7 mm increments. [Conditions as per Figure 9.24].

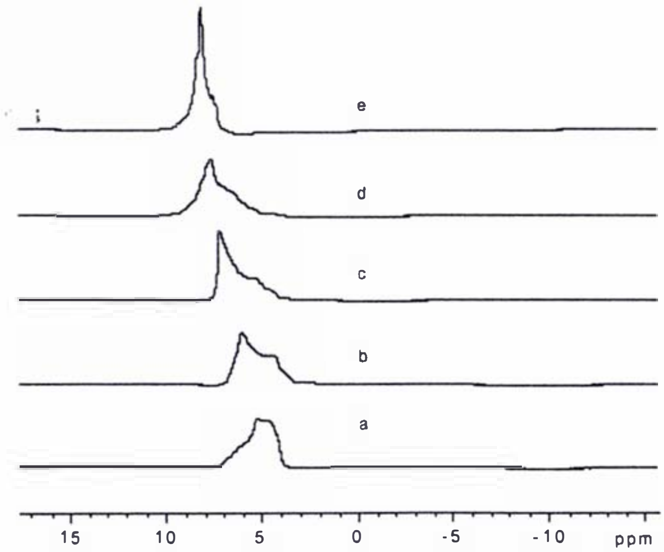

Figure 9.19. 300.1 MHz ^{1}H NMR spectra of cast *N*-MAM/$AlCl_3$ cylindrical gels undergoing increased compression. (a) no compression, (b-e) increasingly compressed by 0.7 mm increments. [AMX-300, single pulse, relaxation delay 2 s, 8.9 μs 90° pulse, LB 0.3 Hz].

9.3 FLOW RHEOLOGY

Rheology (Greek, *to flow*) is the study of deformation and flow in materials as a result of applied external force. Polymer emulsion adhesives such as those used to bond wood components are constantly subjected to shear forces in service and over time can be liable to creep-induced failure as the polymer "flows" infinitesimally over a prolonged period of time. Adhesives are continually being improved and engineered to overcome the incidence of failure due to such undesirable rheological properties.

In this section we analyse the simple shearing flow behaviour of PVAc emulsions using NMR to study the flow profile and the ^{27}Al spectra under shear. Several configurations exist for the study of shearing flow, from the simplest situation of flow through a pipe to more complex geometries such as Couette cells and cone-and-plate devices (Macosko, 1994).

It has previously been mentioned that NMR is able to study the translational motion of molecular systems *via* pulse field gradient spin echo (PFGSE) techniques (section 3.5). The combination of this ability to visualise flow in order to study rheological properties along with NMR spectroscopy to study molecular organisation has yielded the area of Rheo-NMR (Callaghan, 1991, 1999), a powerful tool to explore hitherto unobservable phenomena in fluid systems under shear. Systems such as flow through capillaries (Xia and Callaghan, 1991; Gibbs *et al.*, 1997) or rotational viscosities using Couette cells or cone and plate geometries on foodstuffs (Britton and Callaghan, 1997a) or polymer systems (Rofe *et al.*, 1994; Britton and Callaghan, 1997b; Callaghan and Gil, 2000) can readily be studied. In this section we will describe the rheo-NMR of PVAc liquids in a cone-and-plate device.

9.3.1 SHEARING FLOW IN A CONE-AND-PLATE RHEOMETER

Cone-and-plate rheometers have the advantage over Couette cells in that there is a constant rate of shear across the gap. The geometry of the cone-and-plate rheometer is shown schematically in Figure 9.20. The cone is described by the cone angle, α, which is generally less than 10°, and the angular frequency of rotation, Ω. Any point in the fluid can be described by it Cartesian (x, y, z), spherical polar (r, θ, ϕ) or cylindrical polar (ρ, z, ϕ) coordinates, where $y = r \sin \theta = \rho$ and $z = r \cos \theta$ (Lenk, 1978).

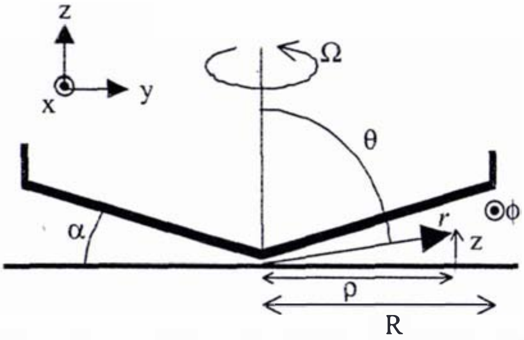

Figure 9.20. Schematic diagram of a cone and plate showing the relationship between the three coordinate systems described in the text. Note that the cone apex does not actually meet the plate.

The shear rate is given by:

$$\dot{\gamma} = \frac{\Omega}{\tan \alpha} \qquad \text{eqn 9.23.}$$

where Ω is the angular frequency of rotation, and α is the angle subtended by the cone and the plate.

The velocity at the wall is given by:

$$v_r = \Omega R \qquad \text{eqn 9.24.}$$

where R is the radius of the cone.

9.3.2 NMR VELOCIMETRY IN A CONE-AND-PLATE DEVICE

Velocity imaging of poly(vinyl acetate) polymer solutions under shear was undertaken using a 16 mm diameter, 4° cone-and-plate rheometer, which was fitted inside a 25 mm ^{1}H imaging coil on the AMX 300 spectrometer. A PFGSE edited spin echo imaging sequence was employed to image the flow across the gap in the cone-and-plate rheometer. To increase spatial resolution in the *z* axis (across the gap) the amplitude of the phase encoding gradient was increased by a factor of four. Spindle rotation frequencies of 0.085 – 0.250 Hz were employed, giving rise to shear rates in the range 7.6 – 22.5 s^{-1}, resulting in wall velocities of between 4.3 and 12.6 mm s^{-1}.

Solution state proton and ^{27}Al NMR spectra of the bulk solutions were also obtained during shear of the solutions in the rheometer, with shear rates in the range 7.6 – 85.2 s^{-1} (rotational frequencies 0.085 – 0.948 Hz).

For cone-and-plate study, the latex polymer solutions were used, with and without addition of $AlCl_3$ in order to investigate the role of aluminium in crosslinking the PVAc gel. The velocity images at varying shear rates are shown in Figure 9.21. Figure 9.21.e. shows the image of the polymer solution at rest and it shows the offset in images due to self diffusion of the polymer during the PGSE sequence.

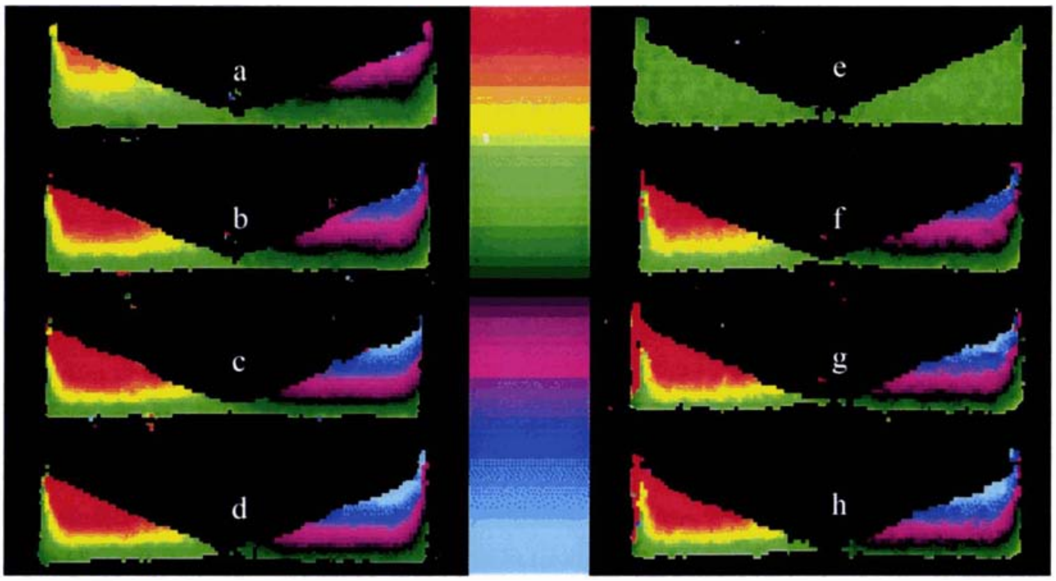

Figure 9.21. PFGSE velocity images of PVAc without addition of $AlCl_3$ at shear rates of (a) 7.6, (b) 12.4, (c) 17.3 and (d) 22.5 s^{-1} and PVAc with addition of 2.5% $AlCl_3$ at (e) rest and at shear rates of (f) 12.4, (g) 17.3 and (h) 22.5 s^{-1}. [AMX-300, DIFFSE, 128x128, FOV 20 mm, 1 mm slice, T_R 1000 ms, T_E 16.5 ms, Δ 12 ms, δ 3 ms, number of q-slices 8, *G* 0.35 mT/m, 4x expansion in phase gradient].

The velocity profile across the gap at a position 7.5 mm from the cone apex and at a shear rate of 17.3 s^{-1} for a solution of PVAc is shown in Figure 9.22 along with the velocity profile at zero shear rate. An offset of *ca.* 1.6 mm s^{-1} can be seen when no shear is present in the solution. All further velocity profiles have been recalculated to take into account this offset. Velocity profiles are shown for both the advancing and receding flow directions.

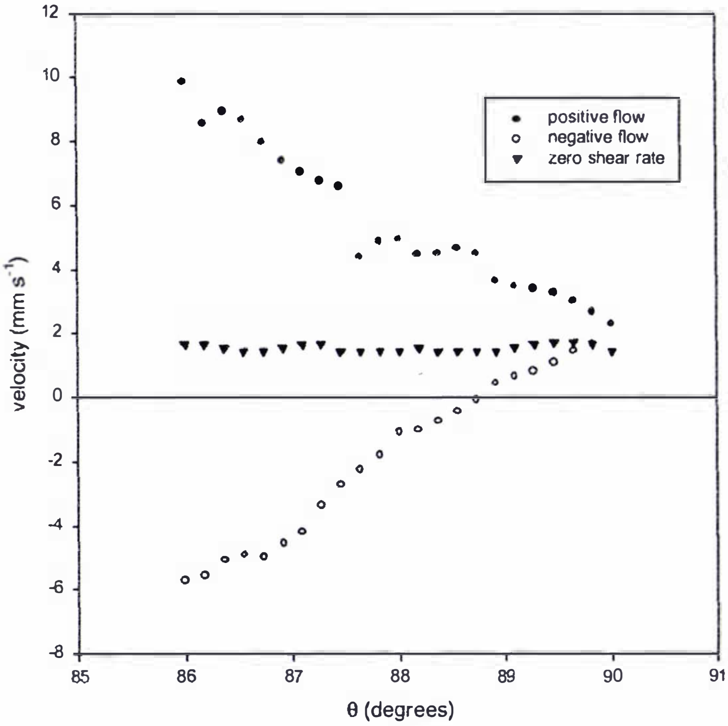

Figure 9.22. Velocity profile across the gap for PVAc at a shear rate of 17.3 s^{-1} and a distance of 7.5 mm from the cone apex. The velocity profiles are plotted for the advancing and receding flow directions as well as the steady state diffusion when no shear is experienced. Note the approximate 1.6 mm s^{-1} offset.

Figure 9.23 shows the corrected velocity profiles across the gap for PVAc solution at a range of shear rates. The velocities are approximately linear across the gap for both directions of flow, indicating a uniform shear rate.

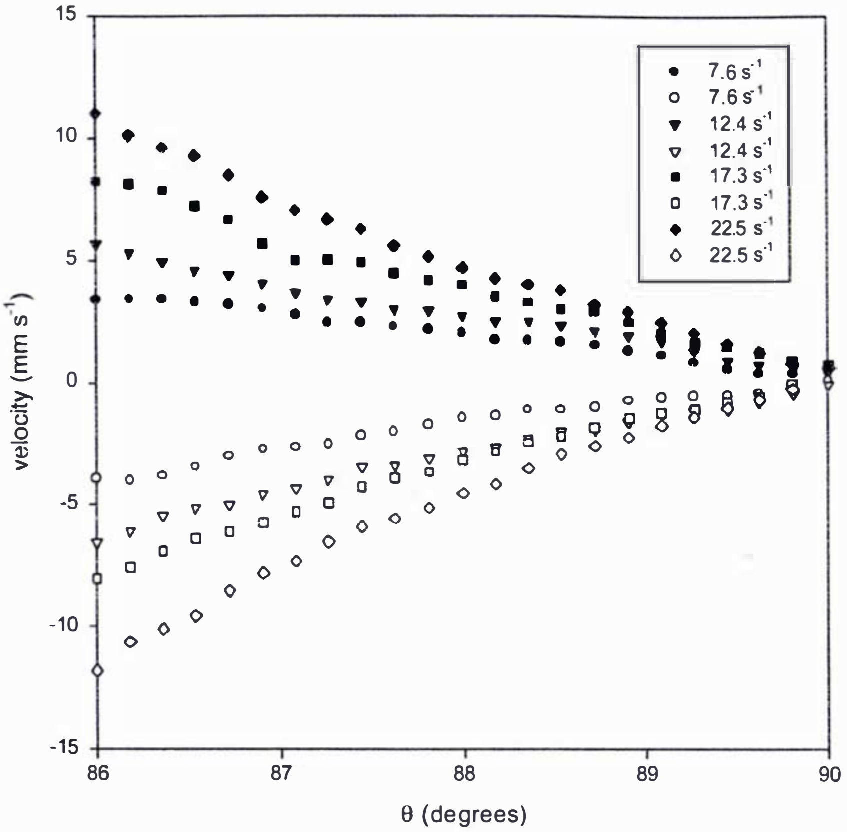

Figure 9.23. Velocity profile across gap for PVAc solution at varying shear rate.

The corrected velocity profiles for the PVAc solution with added aluminium is shown in Figure 9.24. Unlike the PVAc solution the velocity profile does not appear to be totally linear. This is shown more dramatically in Figure 9.25 by comparing the velocity profiles of PVAc and PVAc + $AlCl_3$ at a shear rate of 12.4 s^{-1}. There appears to be a region of anomalous flow at about mid-gap, which is observed at lower shear rates but becomes linear at higher shear rates (Figure 9.24).

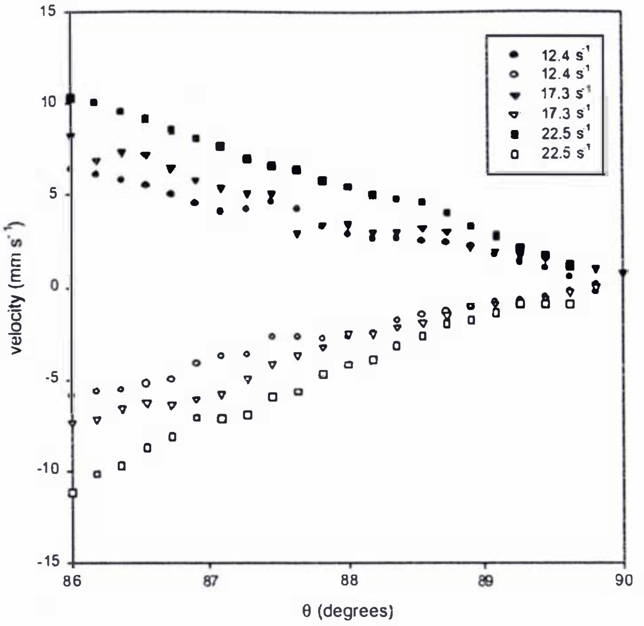

Figure 9.24. Velocity profile across gap for PVAc + $AlCl_3$ solution at varying shear rates.

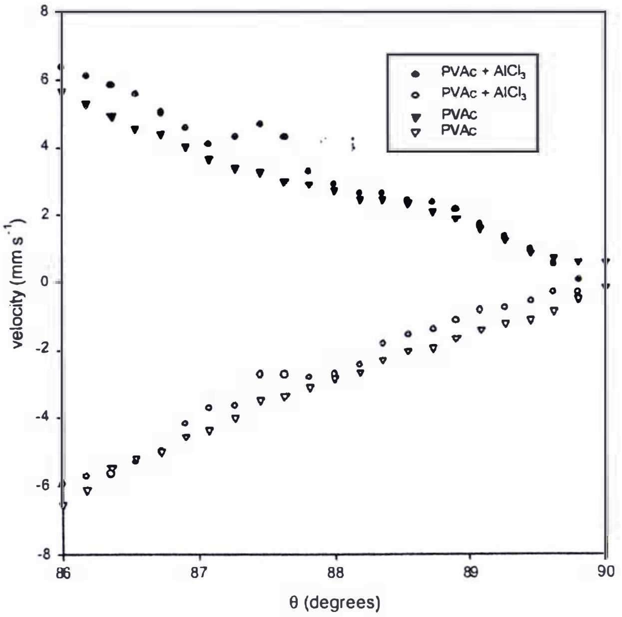

Figure 9.25. Velocity profile across gap for solutions of PVAc with and without added $AlCl_3$ at a shear rate of 12.4 s^{-1}.

The velocimetry study is preliminary in nature. The possible flow anomaly seen in Figure 9.25 is worthy of further investigation but has not been pursued in this study. For the purposes of rheo-NMR investigation the main conclusion is that approximately uniform shear occurs across the gap.

9.3.3 ^{27}Al NMR SPECTROSCOPY OF PVAC EMULSION UNDER SHEAR

Having confirmed the existence of approximately uniform shear of the PVAc emulsion in the cone-and-plate device, attention is now turned to investigating the NMR spectra under these shearing conditions.

Solution state ^{27}Al NMR spectra were acquired of the bulk solution at varying shear rates in the cone-and-plate rheometer and the results are shown in Figure 9.26. There is no observable shift in the resonance, which would suggest that shearing of the adhesive solution does not affect the aluminium cross-linking.

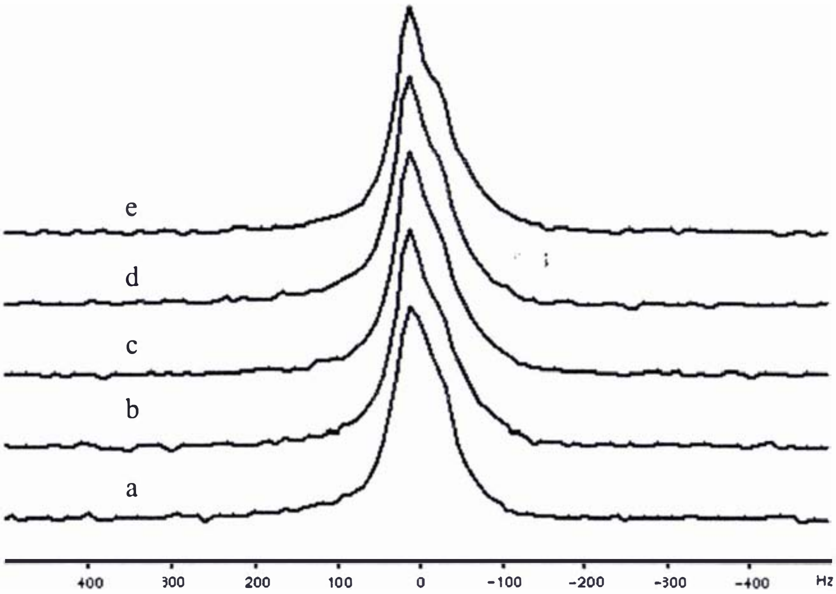

Figure 9.26. 78.2 MHz ^{27}Al NMR spectra of PVAc/AlCl$_3$ at shear rates of (a) 7.6 s^{-1}, (b) 12.4 s^{-1}, (c) 17.3 s^{-1}, (d) 22.5 s^{-1} and (e) 48.3 s^{-1}. [AMX-300, neat solution, single pulse, relaxation delay 2 s, 12.5 μs 90° pulse, LB 2 Hz].

9.4 SUMMARY OF CHAPTER

A novel instrument has been used to investigate the rheological properties of PVAc/*N*-MAM gels under compression, while a cone-and-plate rheometer has been used in combination with NMR imaging and spectroscopy to study PVAc emulsion polymers under conditions of constant shear.

Uniaxial compression of hydrogel cylinders formed from cured *N*-MAM and PVAc/*N*-MAM was performed while monitoring the force *vs* time relationship of the gel under conditions of constant strain. The data was analysed in terms of the stress-strain and stress relaxation relationships and these results interpreted with reference to a Maxwell-Voigt model of springs and dashpots for stress relaxation. In light of the problems associated with resolving multi-exponential data and the novel nature of the testing device, the results presented are open to discussion. However the results do suggest that:

- Addition of 5% $AlCl_3$ to *N*-MAM and *N*-MAM/PVAc hydrogels decreases the crosslink density by approximately a factor of two.

- Given that addition of $AlCl_3$ is known to improve adhesive strength, it would appear that this improvement must arise from fewer stronger crosslinks rather than simpler more crosslinks of the same strength.

When PVAc emulsion polymers, with and without addition of aluminium chloride, are subjected to constant shear in a cone-and-plate rheometer, the velocity across the gap appears uniform for the range of shear rates observed (7.6 – 22.5 s^{-1}) as evidenced by NMR imaging of velocity profiles *via* a PFGSE imaging sequence. Aluminium-27 NMR spectra obtained across an even greater range of shear rates (7.6 - 48.3 s^{-1}) show no distinguishable change in chemical shift or lineshape for the single resonance observed.

Corresponding attempts to obtain ^{27}Al NMR spectra from the aluminium-containing hydrogels under compression were thwarted by the occurrence of diamagnetic susceptibility due to the motion of the moving piston as it came into contact with the gel and continued compression. Spectra of three independent nuclei (^{1}H, ^{13}C and ^{27}Al) all showed a high frequency (low field) shift of *ca.* 4.2 ppm, confirming the susceptibility effect.

10. CONCLUDING REMARKS

> *If I have seen further, it is because I have stood on the shoulders of giants.*
> Isaac Newton

As the forest products industry moves from being a 20th century commodity supplier to producing engineered ligno-cellulosic products for the 21st century, there is an increasing requirement for understanding of both the changing raw material feedstock, resulting from changes in silvicultural and harvesting regimes, and the effects of processing on the long-term durability, serviceability and fitness of the final product. Consumer demand for uniform product performance means that sawmillers are having to extract value by better characterisation and knowledge of their feedstock in order to manufacture product that is fit-for-purpose while juggling the economic constraints of maximising recovery from the log and minimising product downgrade.

This thesis set out to investigate the application of magnetic resonance techniques to probe problems and questions that confront the forest products sector in New Zealand. In particular, use of magnetic resonance microimaging has assisted in providing *in situ* spatial information to the processes of timber drying and timber preservation, while magnetic resonance spectroscopy has provided chemical understanding to both timber preservation and adhesive formulation.

In particular, this work has shown that magnetic resonance imaging techniques can be used to determine the distribution of novel, boron-based preservative compounds in radiata pine wood. It showed that what was first thought to be an anomalous distribution on the basis of an apparent non-penetration into the latewood regions, was determined by ^{11}B MAS NMR spectroscopy of excised sections of latewood and earlywood, to in fact be a difference in the hydrolysis rates of trimethyl borate between the earlywood and latewood regions. The rate of hydrolysis was shown to occur very rapidly in the latewood (within 24 hours), and over a longer time scale of several days in the earlywood. It has also confirmed, *in situ*, the esterification of TBTO in radiata pine wood that was proposed to occur based on extracts of TBTO-treated wood (Archer and Meder, 1987; Blunden and Hill, 1988; Meder and Archer, 1991).

Before suggesting *carte blanche* that NMR will provide more detailed understanding of timber preservative retention, it must be noted however that magnetic resonance techniques only suit certain NMR-observable nuclei and even then conditions need to be suitable to allow images to be obtained. In particular the elements used in the Tanalith™ process (Cu, Cr and As) are all unsuitable to NMR observation as they are paramagnetic in nature. However, in light of the movement away from heavy metal preservatives towards preservatives based on group III elements (boron and aluminium), which lend themselves to NMR observation, there is considerable potential for magnetic resonance techniques to provide valuable insight into the nature and distribution of new generation timber preservatives.

By observing the distribution of water during the drying of softwood (*P. radiata*) timber it has been shown that there is an annual ring orientation and board thickness dependence on the movement of water during drying, confirming Olson's postulation (Olson *et al.*, 1990) that the orientation and thickness of timber has a marked effect on the water mass transport during drying. Due to a limitation in the experimental setup, only qualitative information could be obtained due to the samples being dried in a drying oven and removed at intervals for imaging, so that placement and alignment errors rendered superimposition of the time-course images impossible. However, even at a qualitative level there is evidence for anomalous behaviour in the mass transport of water for narrow flat-sawn boards. Rather than adopt the conventional core-shell drying behaviour whereby water is transported to the nearest drying face or edge, the narrow flat-sawn boards display directed movement of water where the latewood forms a barrier to movement, effectively channelling the water tangentially along the earlywood/latewood boundary to the board edge. For thicker boards and for quarter-sawn boards this phenomenon is not observed, possibly due to higher moisture content gradients forming in the thicker boards. Furthermore, preliminary results show that mass transport is considerably quicker using azeotropic drying techniques and that the water removal conforms to conventional core-shell drying behaviour.

To further support this observation of restricted movement in the radial direction, diffusion tensor imaging using a PFGSE imaging technique shows anisotropic diffusion to be present (as expected) and that the direction of greatest restriction to diffusion is in the radial direction.

An attempt to establish a rapid technique to screen radiata pine samples for their propensity to form internal checks on drying was only partially successful. It was originally thought that NMR relaxation parameters would provide sufficient correlation to allow sample screening for highly check-prone samples, however this was not to be the case with a coefficient of determination of 0.61 for T_2 being the best achievable. However, the PLS correlation of propensity for check formation with the full ^{13}C CP/MAS NMR spectra shows considerable potential to at least provide some fundamental understanding of the mechanism of check formation, as the primary latent variables indicate differences in the cellulose.

NMR spectroscopy has been an integral part of determining the reaction mechanism for a rapid curing phenol-resorcinol resin used for finger-jointing green lumber. Studies using model compounds further helped elucidate the mechanism, which is postulated to proceed *via* a methyleneimine intermediate to form benzylamine and aniline type bridge structures.

Aluminium chloride is added commercially to PVAc adhesive formulations, often according to “institutionalised” recipes, to aid crosslinking. No published information could be found in the scientific literature as to the role or nature of aluminium in the formation of crosslinks. It is assumed that this information too is institutionalised. Multinuclear magnetic resonance studies of modified and unmodified adhesives, show little evidence for an active role in crosslinking of PVAc. The single most noticeable effect was a low frequency shift of *ca.* 3 ppm for the ^{27}Al signal indicating a change in chemical environment from a solvated octahedral complex to a octahedral coordination complex on dehydration.

Uniaxial compression of *N*-MAM and PVAc gels provided a considerable amount of data, much of which is still uninterpreted due to the novel nature of the experiment. Tentative interpretation suggests that the addition of aluminium to PVAc formulations actually decreases the crosslink density of the cured material – which on first principles is contrary to the result intended. Interpreting the data obtained from the relaxation of stress for the gels under constant strain, suggests that while the addition of aluminium decreases the crosslink density, it imparts strength to the cured gel rendering it more resistant to shear-induced creep.

10.1 FUTURE DIRECTIONS

While the studies undertaken have provided answers to some questions and provided data in support of what was previously anecdotal evidence, during the course of the work several other questions have arisen. While this will not be an exhaustive summary of future work, it highlights some areas where there is still need for research and areas that the author maintains an interest in.

The movement of water during the drying of wood is still an area warranting further study. There are currently no three-dimensional models that describe the movement of water during drying. This requires further experimental work in the form of 3D imaging at stages during drying and in particular for varying ring orientations and surface area to volume ratios. In order to be successful this work would require the drying to occur *in situ* so as to be able to superimpose images without having to adjust for any repositioning errors as was experienced in this study.

A further area of application requiring understanding of the wood-water relationship is in the movement of water during stresses other than drying, namely redistribution during tension or compression or bending (combined tension and compression). It is likely that these processes would occur on reasonably short timescales of a few minutes, precluding use of lengthy spin echo imaging sequences. Fast imaging sequences such as FLASH (Haase *et al.*, 1986) could be used to generate a series of images or T_2 maps over a short timescale (Haase, 1989, Diechmann *et al.*, 1991) in order to visualise the redistribution of water or characterise any change in the nature of water relaxation as a response to 3-point bending.

Furthermore, magnetic resonance imaging could be used to follow the progress of novel dewatering processes such as extraction using supercritical CO_2. The additional advantage of these systems over conventional drying systems is that they have the potential to allow simultaneous impregnation of treatment chemicals for preservation. fire-retardancy or chemical modifiers (e.g. densifiers). A patent held by ***Forest Research*** describes dewatering of green wood using supercritical fluids (Franich *et al.*, 2001b) while Etesse *et al.*, (1993a,b) have studied the NMR spin-lattice relaxation of supercritical CO_2 at and around the critical point. Magnetic resonance imaging of supercritical CO_2 drying of wood, would however present some experimental obstacles. The critical point for carbon dioxide is 32 °C at 72 bar pressure. This would require a high pressure NMR cell capable of sustaining the high pressure required, while allowing a sufficient sample volume to be available for imaging. Furthermore the cell must be compatible with NMR systems in that it must be non-metallic in order to allow rf to penetrate and any metal fittings, such as gas line connections, must be non-magnetic. Such cells have been described as being built from sapphire (Roe, 1985) or a high tensile polymer such as poly(etheretherketone) (PEEK) (Wallen *et al.*, 2000). In order to image the drying it is necessary to be able to separately image the ^1H and ^{13}C distribution requiring a doubly tuned coil. In NMR spectroscopy, the NMR observable carbon isotope is the ^{13}C nucleus, which has a natural abundance of 1.1 %. For imaging, it would be normal practice to increase the concentration of ^{13}C by isotope enrichment. However, at the critical point, CO_2 has a density of 0.8-0.9 g cm^{-3} at 80-150 bar, and behaves like a solvent. At these higher densities there would be no necessity for the CO_2 to be isotope enriched with ^{13}C, making such a wood-water relationship studies readily amenable to NMR.

The preliminary results presented indicate a correlation between ^{13}C CP/MAS NMR spectra of earlywood samples and the propensity to form internal checks on drying. Due to the small number of samples, these results are however only indicative and would require considerable effort to significantly increase the number of samples and also to ensure sufficient coverage of other parameters such as geography, tree age, seasonal variation, soil nutrient status *etc.* It may also be that an increase in the number of samples would strengthen the tenuous correlation of propensity for internal check formation with the NMR spin-spin relaxation constant T_2.

The role of aluminium in crosslinked PVAc is still unclear. Preliminary indications are that the addition of $AlCl_3$ decreases the crosslink density of the cured adhesive.

This is not however to mean that the strength of the adhesive is any less. This aspect of emulsion polymer physics is worthy of further investigation and would require investigations using a broader range of rheometric techniques, some of which might be suitably miniaturised for use in NMR micro-imaging systems.

11. APPENDIX A

The difficulty lies, not in the new ideas, but in escaping the old ones.
John Maynard Keynes

11.1 PREPARATION OF *N*-MAM/PVAC

11.1.1 Preparation of ^{13}C-labelled N-MAM

The method used was an adaptation of one described in Warson, 1990. Rather than using an alkali solution to catalyse the condensation of acrylamide with formaldehyde, a strong-base ion exchange bead method was devised.

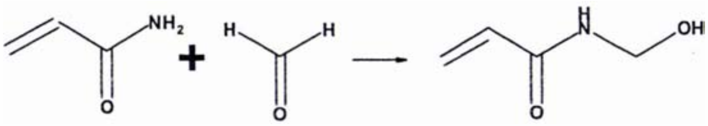

MW:	71	31	102
Wt:	0.88g	0.38g	1.26g
Mol:	0.0124	0.0124	0.0124

To a 40% w/v acrylamide solution was added 99 atom% ^{13}C formaldehyde (as 40% formalin solution) and freshly regenerated and washed Amberlite CG400 resin (OH-form). The mixture was stirred and warmed to 42-45 °C for 15 minutes. The mixture was cooled to 20 °C and then filtered under reduced pressure. The solution obtained was analysed directly by ^{13}C NMR.

^{13}C NMR:

δ_C formaldehyde (neat): 94.1, dihydroxymethane; 89.9, hydroxymethoxymethane; 82.5, oligomers.

δ_C acrylamide (acetone-d_6): 172.1, C=O; 131,5, $CH\underline{C}H_2$; 130.4 $\underline{C}HCH_2$.

δ_C N-methylolacrylamide (acetone-d_6): 168.9, C=O; 129.9, $CH\underline{C}H_2$; 128.4, $\underline{C}HCH_2$; 63.0, $HO\underline{C}H_2NH$.

δ_C ^{13}C *N*-methylolacrylamide (acetone-d_6): 70.6 (strong), $HO\underline{C}H_2NH$.

11.1.2 Preparation of N-MAM/PVAc

To water (13 g) was added polyvinylalcohol (BP05, 640 mg and BP25 350 mg) and a further charge of water (2.0 g) and the mixture stirred and heated to 80 °C. The headspace above the flask was purged with nitrogen and a nitrogen blanket maintained during the addition of components and polymerisation. Emulsifiers Rhodocal DS-10 and lanolubric 2 were added. The solution was cooled to 70 °C and then a vinyl acetate (0.9g) was added in one portion followed by potassium persulphate (5 mg) in water (150 mL) and ammonia solution (0.88 density, 50 mL).

The mixture was stirred and maintained at 80 °C while vinyl acetate (21.2 g) and a solution of *N*-methylolacrylamide (1.25 g) in water (3.5 g), ammonia (0.88 density, 25 mL) and Calfax DB45 emulsifier (0.16 g) and a solution of potassium persulphate (20 mg) in water (3.5 g) were each added separately over a 3 hour period while heating at 80 °C, stirring and nitrogen blanketing was maintained. To facilitate the delivery of the small volumes over the time period, syringes with long needles mounted on calibrated syringe pumps were used. At the end of the polymerisation period, an extra portion of potassium persulphate (5 mg) in water (150 mL) was added, and the mixture kept at 80 °C for a further 30 min. The creamy white emulsion was cooled while maintaining stirring and to the final product at 20 °C was added plasticiser (Chisso CS12) and water (1.0 g). The product was stirred for a further 15 minutes, then decanted and bottled.

The final product had a solids content of 46% and a viscosity of 5600 cps.

For preparation of a ^{13}C-labelled *N*-MAM/PVAc, the ^{13}C-labelled *N*-MAM prepared in § 11.1.1 above was substituted for the commercial *N*-MAM.

NMR δ_C (99% D_2O, acetone-d_6): 180.1–173.7, C=O; 68.1, $CO\underline{C}HCH_2$ (mm); 66.4-65.1, $CO\underline{C}HCH_2$ (mr); 41.8-37.0, $COCH\underline{C}H_2$; 20.9, $CO\underline{C}H_3$.

11.1.3 Curing of Hydrogels

Cylinders of *N*-MAM or *N*-MAM/PVAc were cured by casting inside 6 mm ID silicone tubing to a height of *ca.* 6-8 mm. Curing was undertaken at room temperature unless otherwise specified. Once cured the silicone tubing was removed affording a cylindrical sample of hydrogel or adhesive.

12. REFERENCES

To study, to finish, to publish.

Benjamin Franklin

Abragam, A. (1983) *The Principles of Nuclear Magnetism*. Oxford University Press, Oxford. ISBN 0-19-852014-X, 614 pp.

Alla, M. and Lippmaa, E. (1976) High resolution broad line ^{13}C NMR and relaxation in solid norbornadiene. *Chem. Phys. Lett.*, 37, 260-264.

Amram, B. and Laval, F. (1989) Graphitization studies of cured phenolic resins by high-resolution ^{13}C-cross-polarisation magic angle spinning solid-state NMR spectroscopy. *J. Appl. Polym. Sci.*, 37, 1-14.

Anderson, K.B., Franich, R.A., Kroese, H.W., Meder, R. and Rickard, C.E.F. (1995) The structure of biguanide complexes of boron. *Polyhedron*, 14, 1149-1153.

Anderson, K.B., Franich, R.A., Hedley, M.E., Kroese, H.W., Meder, R. and van der Waals, J. (1997) Synthesis, characterisation and effectiveness of biguanide derivatives of boric acid as potential fixed-boron wood preservatives. *Material u. Oragnismen,* 31, 63-75.

Andrew, E. R., Bradbury, A., Eades, R. G. and Jenks, G. J. (1960) Nuclear magnetic resonance [NMR] spectra of crystals rotated macroscopically: fine structure of the spectrum of phosphorus pentachloride. *Arch. Sci.*, 13, 371-373.

Araujo, C.D., MacKay, A.L., Hailey, J.R.T., Whittall, K.P. and Le, H. (1992) Proton magnetic resonance techniques for characterization of water in wood: Application to white spruce. *Wood Sci. Technol.*, 26, 101-113.

Araujo, C.D., MacKay. A.L., Whittall, K.P. and Hailey, J.R.T. (1993) A diffusion model for spin-spin relaxation of compartmentalized water in wood. *J. Magn. Reson.,* B101, 248-261.

Archer, K.J. and Meder, R. (1987) An investigation into the stability of TBTO in LOSP treated radiata pine. International Research Group on Wood Preservation, Honey Harbour, Ontario, Canada. Document IRG/WP/3459.

Aue, W.P., Bartholdi, E. and Ernst, R.R. (1976) Two-dimensional spectroscopy. Application to nuclear magnetic resonance. *J. Chem. Phys.*, 64, 2229-46.

Avramidis, S. and Siau, J.F. (1987) An investigation of the external and internal resistance to moisture diffusion in wood. *Wood Sci. Technol.*, 21, 249-256.

Backa, S. and Brolin, A. (1991) Determination of pulp characteristics by diffuse reflectance FTIR. *Tappi J.*, 74, 218-226.

Baekeland, L.H. (1907) US Patent 942,699.

Balcom, B.J.; MacGregor, R.P.; Beyea, S.D.; Green, D.P.; Armstrong, R.L.; Bremner, T.W. (2002) Single-point ramped imaging with T_1 enhancement. *J. Magn. Reson.*, 123, 131-134.

Barton II, F.E. (1991) New methods for the structural and compositional analysis of cell walls for quality determinations. *Anim. Feed Sci Technol.*, 32, 1-11.

Barton II, F.E. and Windham, W.R. (1988) Determination of acid-detergent fibre and crude protein in forages by near-infrared reflectance spectroscopy: Collaborative study. *J. Assoc. Off. Anal. Chem.*, 71, 1162-1167.

Barug, D. (1981) Microbial degradation of bis(tributyltin) oxide. *Chemosphere,* 10, 1145-1154.

Bates, D.M. and Watts, D.G. (1988) *Nonlinear Regression Analysis and its Applications*, J. Wiley & Sons, Bognor Regis. ISBN 0-471-81643-4, 384 pp.

Bax, A. and Subramanian, S. (1986) Sensitivity-enhanced two-dimensional heteronuclear shift correlated NMR spectroscopy. *J. Magn. Reson.*, 67, 565-569.

Bax, A. and Summers, M.F. (1986) Proton and carbon-13 assignments from sensitivity-enhanced detection of heteronuclear multiple-bond connectivity by 2D multiple quantum NMR. *J. Am. Chem. Soc.*, 108, 2093-2094.

Bendel P., Davis M., Berman E. and Kabelka G.W. (1990) A method for imaging nuclei with short T_2 relaxation and its application to boron-11 NMR imaging of BNCT agent in an intact rat. *J. Magn. Reson.*, 88, 369-375.

Bjorkman, A. (1956) Studies on finely divided wood. Part 1. Extraction of lignin with neutral solvents. *Svensk Pappst.*, 59, 477-85.

Bloch, F. (1946) Nuclear induction. *Phys. Rev.*, 70, 460-74.

Bloch, F., Hansen, W.W. and Packard, M. (1946) The nuclear induction experiment. *Phys. Rev.*, 70, 474-85.

Bloembergen, N., Purcell, E. M. and Pound, R. V. (1948) Relaxation effects in nuclear magnetic resonance absorption. *Phys. Rev.*, 73, 679-712.

Blumich, B. and Kuhn, W. (1992) *Magnetic Resonance Microscopy: Methods and Applications in Materials Science, Agriculture and Biomedicine.* VCH, Weinheim. ISBN 3-527-28403-6, 604 pp.

Blunden, S.J. and Hill, R. (1988) Bis(tributyltin)oxide as a wood preservative: its chemical nature in timber. *Organometal. Chem.*, 2, 251-256.

Bottomley, P. A., Hart, H. R., Edelstein, W. A., Schenck, J. F., Smith, L. S., Leue, W. M., Mueller, O. M. and Redington, R. W. (1983) NMR imaging/spectroscopy system to study both anatomy and metabolism. *Lancet*, 2(2834), 273-274.

Booker, R.E. (1991) Changes in transverse wood permeability during the drying of *Dacrydium cupressium* and *Pinus radiata*. *N.Z. J. Forest Sci.*, 20, 231-244.

Booker, R.E. (2001) *pers comm.*

Bramhall, G. (1979) Sorption diffusion in wood. *Wood Sci.*, 12, 3-13.

Braun, S., Kalinowski, H.-O. and Berger, S. (1996) *100 and More Basic NMR Experiments*. VCH, Weinheim. ISBN 3-527-29091-5, 418 pp.

Breitmaier, E. and Voelter, W. (1978) *^{13}C NMR Spectroscopy. Methods and Applications in Organic Chemistry*. 2nd ed. Verlag Chemie, Weinheim. 344 pp. ISBN 3-527-25780-2.

Brijnaresh, R.S., Blum, F.D. and O'Conner, D. (1989) Characterization of substituted phenol-formaldehyde resins using solid-state carbon-13 NMR. *J. Appl. Polym. Sci.*, 38, 163-171.

Britton, M.M. and Callaghan, P.T. (1997a) NMR microscopy and the non-linear rheology of food materials. *Magn. Reson. Chem.*, 35, S37-S46.

Britton, M.M. and Callaghan, P.T. (1997b) Nuclear magnetic resonance visualization of anomalous flow in cone-and-plate rheometry. *J. Rheol.*, 41, 1365-1385.

Bruker (1999) *Almanac 2000*. Bruker Analytik, Karlsruhe. p. 72.

Bryson, R.L., Hatfield, G.R., Early, T.A., Palmer, A.R. and Maciel, G.E. (1983) ^{13}C NMR studies of solid phenolic resins using cross polarisation and magic-angle spinning. *Macromol.*, 16, 1669-1672.

Burton, R.J., Bergevoet, A.J., Nasheri, K., Vinden, P. and Page, D.R. (1990) Gaseous preservative treatment of wood. 21st Annual Meeting International Research Group on Wood Preservation, Rotorua, New Zealand. Document IRG/WP3631.

Burton, R.J., Bergevoet, A.J., Nasheri, K., Vinden P. and Page D.R. (1991) Vapour phase preservation of wood. *Trans. Inst. Prof. Eng. N. Z.*, 18, 40-44.

Callaghan, P.T. (1991) *Principles of Nuclear Magnetic Resonance Microscopy.* Clarendon Press, Oxford. ISBN 0-19-853997-5, 492 pp.

Callaghan, P.T. (1999) Rheo-NMR: nuclear magnetic resonance and the rheology of complex fluids. *Rep. Prog. Phys.*, 62, 599-668.

Callaghan, P.T. and Gil, A.M. (2000) Rheo-NMR of semidilute polyacrylamide in water. *Macromol.*, 33, 4116-4124.

Carr, H.Y. and Purcell, E.M. (1954) Effects of diffusion on free precession in nuclear magnetic resonance experiments. *Phys. Rev.*, 94, 630-638.

Chang, S.J., Olson, J.R. and Wang, P.C. (1989) NMR imaging of internal features in wood. *Forest Prod. J.*, 39, 43-49.

Chuang, I-S. and Maciel, G.E. (1991) ^{13}C NMR investigation of the stability of a resol-type phenol-formaldehyde resin toward formalin, toward base and toward nonoxidising or oxidising acid. *Macromol.*, 24, 1025-1032.

Chuang, I-S. and Maciel, G.E. (1994) NMR characterization of complex organic resins. *Ann. Rep. NMR Spectrosc.*, 29, 169-286.

Clark, C.J., Drummond, L.N. and MacFall, J.S. (1998) Quantitative NMR imaging of kiwifuit (*Actinidia delicosa*) during growth and ripening. *J. Sci. Food Agric.*, 78, 349-358.

Coddington, J.M. and Taylor, M.J. (1989) High field ^{11}B and ^{13}C NMR investigations of aqueous borate solutions and borate-diol complexes. *J. Coord. Chem.*, 20, 27-38.

Côté, W.A. (1983) Wood as a substrate for coatings. *J. Coat. Technol.*, 55, 25-35.

Côté, W.A. (1967) *Wood Ultrastructure. An Atlas of Electron Micrographs.* University of Washington Press, Seattle.

Cown, D.J and Parker, M.L. (1978) Comparison of annual ring density profiles in hardwoods and softwoods by X-ray densitometry. *Can. J. Forest Res.*, 8, 442-449.

Deichmann, R., Adolf, H., Nöthe, U., Morrissey, S., Schwartzbauer, C. and Haase, A. (1995) Fast T_2-mapping with snapshot FLASH imaging. *Magn. Reson. Imag.*, 4, 633-639.

Derome, A.E. (1987) *Modern NMR Techniques for Chemistry Research.* Pergamon, Oxford. ISBN 0-08-032513-0, 280 pp.

de Souza, C.M.G. and Tavares, M.I.B. (1998) Nuclear magnetic resonance study of commercial poly(vinyl acetate). *J. Appl. Polym. Sci.*, 70, 2457-2461.

Diehl, P., Fluck, E., Günther, H., Kosfeld, R. and Seelig, J. (Eds) (1992) *NMR Basic Principles and Progress. 27. In-vivo Magnetic Resonance Spectroscopy II: Localization and Spectral Editing.* Springer Verlag, Berlin. ISBN 3-540-55022-4.

Diehl, P., Fluck, E., Günther, H., Kosfeld, R. and Seelig, J. (Eds) (1994a) *NMR Basic Principles and Progress. 30. Solid State NMR I: Methods.* Springer Verlag, Berlin. ISBN 3-540-57189-2

Diehl, P., Fluck, E., Günther, H., Kosfeld, R. and Seelig, J. (Eds) (1994b) *NMR Basic Principles and Progress. 31. Solid State NMR II: Inorganic Matter*. Springer Verlag, Berlin. ISBN 3-540-57190-6.

Doddrell, D.M., Pegg, D.T. and Bendall, M.R. (1982) Distortionless enhancement of NMR signals by polarisation transfer. *J. Magn. Reson.*, 48, 323-327.

Doi, M. (1993) Viscoelastic and rheological properties. In: *Materials Science and Technology. Volume 12. Structure and Properties of Polymers.* E.L. Thomas (Ed), VCH, Wienheim. ISBN 3-527-26813-8.

Doi, M. (1996) *Introduction to Polymer Physics.* Oxford University Press, London. ISBN 0-19-851789-0.

Easty, D.B., Berben, S.A., De Thomas, F.A. and Brimmer, P.J. (1990) Near-infrared spectroscopy for the analysis of wood pulp: quantifying heartwood-sapwood mixtures and estimating lignin content. *Tappi J.*, 73, 257-261.

Eccles, C.D. (1987) *Microscopic NMR Imaging.* PhD thesis, Massey University, New Zealand, 248 pp.

Eccles, C.D., Clark, C.J., Codd, S.L. and Dykstra, R. (1998) Construction of an MRI system for horticultural and materials science research. In: *Proceedings of the Fifth Electronics New Zealand Conference*, University of Otago, Dunedin, 45-50.

Einstein, A. (1905) Über die von der molekularkinetischen Theorie der Wärme geforderteBewegung von in ruhenden Flüssigkeiten suspendierten Teilchen. *Ann. Physik* 17, 549-560.

Einstein, A. (1908) Elementare theorie der Brownschen bewegung. *Z. Elektrochem.*, 13, 41-42 & 14, 235-239.

El-Aasser, M.S. and Vanderhoff, J.W. (1981) *Emulsion Polymerisation of Vinyl Acetate.* Applied Science Publishers, Essex. ISBN 0-85334-971-1, 290 pp.

Emst, R.R. (1966) Sensitivity enhancement in magnetic resonance. In: J.S. Waugh (Ed), *Advances in Magnetic Resonance.* Academic Press, New York.

Emst, R.R. (1975) Two-dimensional spectroscopy. *Chimica*, 29, 179-183.

Emst, R.R., Bodenhausen, G. and Wokaun, A. (1987) *Principles of Nuclear Magnetic Resonance in One and Two Dimensions.* Clarendon Press, Oxford. 610 pp. ISBN 0-19-855629-2.

Etesse, P., Chapman, W.G. and Kobayashi, R. (1993a) Nuclear magnetic resonance measurement of spin-lattice relaxation and self-diffusion in supercritical CO_2-*n*-hexadecane mixtures. *Molec. Phys.*, 80, 1145-1164.

Etesse, P., Ward, A.M., House, W.V. and Kobayashi, R. (1993b) Spin-lattice relaxation and self-diffusion near the critical point of carbon dioxide. *Physica B*, 183, 45-52.

Everitt, B.S. and Dunn, G. (1991) *Applied Multivariate Data Analysis.* Edward Arnold, London. 304 pp. ISBN 0-340-54529-1.

Fengel, D. and Wegener, G. (1983) *Wood. Chemistry, Ultrastructure, Reactions.* Walter de Gruyter, Berlin. 613 pp. ISBN 3-11-008481-3.

Fisher, T.H., Chao, P., Upton, C.G. and Day, A.J. (1995) One- and two-dimensional NMR study of resol phenol-formaldehyde prepolymer resins. *J. Magn. Reson.*, 33, 717-723.

Flibotte, S., Menon, R.S., MacKay, A.L. and Hailey, J.R.T. (1990) Proton magnetic resonance of Western red cedar. *Wood Fiber Sci.*, 22, 362-376.

Franich, R.A., Gallagher, S.S., Hedley, M., Kelly, B.D., Kroese, H.W. and Meder, R. (2001a) Preservative compounds and their use. NZ Patent applied for.

Franich, R.A., Gallagher, S.S. and Kreber, B. (2001b) Supercritical fluid dewatering of wood. New Zealand patent applied for.

Fyfe, C.A. (1983) *Solid State NMR for Chemists.* C.F.C. Press, Guelph, Ontario. ISBN 0-88955-038-7, 593 pp.

Fyfe, C.A., Rudin, A. and Tchir, W.J. (1980) Application of high-resolution carbon-13 NMR spectroscopy using magic angle spinning techniques to the direct investigation of solid cured phenolic resin. *Macromol.*, 13, 1320-1322.

Fyfe, C.A., McKinnon, M.S., Rudin, A. and Tchir, W.J. (1983) Investigation of the mechanisms of the thermal decomposition of cured phenolic resins by high-resolution ^{13}C CP/MAS solid-state NMR spectroscopy. *Macromol.*, 16, 1216-1219.

Gibbs, S.J., Haycock, D.E., Frith, W.J., Ablett, S. and Hall, L.D. (1997) Strategies for rapid NMR rheometry by magnetic resonance imaging velocimetry. *J. Magn. Reson.*, 125, 43-51.

Gil, A.M., Lopes, M.H., Neto, C.P. and Callaghan, P.T. (2000) An NMR microscopy study of water absorption in cork. *J. Mater. Sci.*, 35(8), 1891-1900.

Gu, H.-M., and Zink-Sharp, A. (1999) Measurement of moisture gradients during kiln-drying. *Forest Prod. J.*, 49, 77-86.

Haase, A. (1989) Snapshot FLASH MRI. Application to T1, T2, and chemical-shift imaging. *Magn. Reson. Med.*, 13, 77-89.

Haase, A., Frahm, D., Matthei, D. and Merbold, K.D. (1986) FLASH imaging: rapid NMR imaging using low flip angle pulses. *J. Magn. Reson.*, 104, 183-188.

Hahn, E.L. (1949) An accurate nuclear magnetic resonance method for measuring spin-lattice relaxation times. *Phys. Rev.*, 76, 145-146.

Hahn, E.L. (1950) Spin echoes. *Phys. Rev.*, 80, 580-594.

Hall, L.D. and Rajanayagam, V. (1986) Evaluation of the distribution of water in wood by use of three dimensional proton NMR volume imaging. *Wood Sci. Technol.*, 20, 329-333.

Hall, L.D., Rajanayagam, V., Stewart, W.A. and Steiner, P.R. (1986a) Magnetic resonance imaging of wood. *Can. J. Forest Res.*, 16, 423-426.

Hall, L.D., Rajanayagam, V., Stewart, W.A., Steiner, P.R. and Chow, S. (1986b) Detection of hidden morphology of wood by magnetic resonance imaging. *Can. J. Forest Res.*, 16, 684-687.

Harris, J.M. (1991) Structure of wood and bark. In: Kininnmonth, J.A. and Whitehouse, L.J. (Eds), *Properties and Uses of New Zealand Radiata Pine. Volume 1. Wood Properties.* NZ Ministry of Forestry, Rotorua, ISBN 0-47301181-6.

Harris, R.K. and Sebald, A. (1987) Experimental methodology for high-resolution solid-state NMR of heavy metal spin-1/2 nuclei. *Magn. Reson. Chem.*, 25, 1058-62.

Harrow K.M. (1955) Diffusion impregnation of building timbers with boron compounds. *N. Z. Timb. J. Forest Rev.*, 2, 28-29.

Hartmann, S.R. and Hahn, E.L. (1962) Nuclear double resonance in the rotating frame. *Phys. Rev.*, 128, 2042-53.

Hatfield, G.R. and Maciel, G.E. (1987) Solid-state NMR study of hexamethylenetetramine curing of phenolic resins. *Macromol.*, 20, 608-615.

Hayashi, S. and Hayamizu, K. (1989) Shift references in high-resolution solid-state NMR. *Bull. Chem. Soc. Jpn.*, 62, 2429-2430.

Hayes, C.E., Edelstein, W.A., Schenck, J.F., Mueller, O.M. and Eash, M. (1985) An efficient, highly homogeneous radiofrequency coil for whole-body NMR imaging at 1.5 T. *J. Magn. Reson.*, 63, 622-628.

Henshaw, B.G., Laidlaw, R.A., Orsler, R.J., Carey, J.K. and Savory J.G. (1978) The permanence of tributyltin oxide in timber. British Wood Preservers Association Annual Convention. 19-29.

Hill, B. (1998) *Magnetic Resonance Imaging in Food Science.* John Wiley & Sons, New York, 342 pp.

Hills, B.P. and Remigereau, B. (1997) NMR studies of changes in subcellular water compartmentation in parenchyma apple tissue during drying and freezing. *Int. J. Food Sci. Technol.*, 32, 51-61.

Hotelling, H. (1933) Analysis of a complex of statistical variables into principal components. *J. Educ. Psychol.*, 24, 417-441 and 498-520.

Hotelling, H. (1957) The relations of the newer multivariate statistical methods to factor analysis. *Brit. J. Stat. Psychol.*, 10, 69-79.

Hurd, R.E. (1990) Gradient-enhanced spectroscopy. *J. Magn. Reson.*, 87, 422-8.

Hurd, R.E. and John, B.K. (1991) Gradient-enhanced proton-detected heteronuclear multiple-quantum coherence spectroscopy. *J. Magn. Reson.*, 91, 648-53.

Ibrahim, B., Katritzky, A.R., Smith, A. and Weiss, D.E. (1974) Carbon-13 nuclear magnetic resonance spectroscopy of polymers. I. High resolution carbon-13 nuclear magnetic resonance spectroscopy. Tacticity studies on poly(vinyl acetate) and monomer distribution analysis in ethylene-vinyl acetate copolymers. *J. Chem. Soc., Perkin Trans. 2,* 13, 1537-1542.

Ishida, N., Kano, H. and Ogawa, H. (1994) Diffusive effect induced by a strong magnetic field gradient in 1H-NMR micro-imaging studies of plant tissues. *Biosci., Biotechnol., Biochem.*, 58, 9-13.

Jeener, J. (1971) Pulse pair techniques in high resolution NMR. *Ampère International Summer School*, Basko Polje, Yugoslavia.

Jenner, C.F., Xia, Y., Eccles, C.D. and Callaghan, P.T. (1988) Circulation of water within wheat grain revealed by nuclear magnetic resonance micro-imaging. *Nature*, 336, 399-402.

Jermer, J., Edlund, M-L., Henningson, B. and Hintze, W. (1983) Chemical and biological investigations of double vacuum treated windows after five years in service. International Research Group on Wood Preservation, 14th Annual Meeting, Document IRG/WP/2244.

Joliffe, I.T. (1982) A note on the use of principal components in regression. *Appl. Statist.*, 31, 300-303.

Kabalka, G.W., Cheng, G.Q and Bendel, P. (1992) Boron-11 MRI and MRS. In: Blümich, B. and Kuhn, W. (Eds) *Magnetic Resonance Microscopy: Methods and Applications in Materials Science, Agriculture and Biomedicine*. VCH Publishers, Cambridge. ISBN 1-56081-202-8.

Kelly, B.D. (1995) *The Synthesis and Characterisation of Novel Alumatrane Compounds for the Potential Use as New Wood Preservatives.* MSc (Tech.) Thesis, Waikato University, 111 pp.

Kendall, M.G. (1957) *A Course in Multivariate Analysis*, Griffin, London.

Kininmonth, J.A. (1991) Wood/Water Relationships. In: J.A. Kininmonth and L.J. Whitehouse (Eds), *Properties and Uses of New Zealand Radiata Pine. Volume 1. Wood Properties.*, NZ Ministry of Forestry, Rotorua. ISBN 0-47301181-6.

Knop, A. and Pilato, L. (1985) *Chemistry and Application of Phenolic Resins.* Springer-Verlag, Berlin ISBN 3-540-15039-0, 195 pp.

Köckenberger, W., Pope, J.M., Xia, Y., Jeffrey, K.R., Komor, E. and Callaghan, P.T. (1997) A non-invasive measurement of phloem and xylem water flow in castor bean seedlings by nuclear magnetic resonance microimaging. *Planta,* 201, 53-63.

Kuhn, W. (1990) NMR microscopy – fundamentals, limits and possible applications. *Angew. Chem. Int. Ed. Engl.*, 29, 1-19.

Labana, S.S. (1989) Cross-linking. In: H.F. Mark, N. Bikales, C.G. Overberger, G. Menges (Eds), *Encyclopedia of Polymer Science and Engineering, Volume 4.* J. Wiley and Sons, Chichester. 350-395. ISBN 0-471-88099-X.

Larsson, P.T., Westermark, U. and Iversen, T. (1995) Determination of the cellulose I_α allomorph content in a tunicate cellulose by CP/MAS ^{13}C-NMR spectroscopy. *Carb. Res.*, 278, 339-343.

Lauterbur, P.C. (1973) Image formation by induced local interactions: examples employing nuclear magnetic resonance. *Nature*, 242, 190-191.

Lawson, C.L. and Hanson, R.J. (1974) *Solving Least Squares Problems*, Prentice Hall, New Jersey.

Le Bihan, D. (1991) Molecular diffusion nuclear magnetic resonance imaging. *Magn. Reson. Q.*, 7, 1-30.

Lenk, R.S. (1978) *Polymer Rheology*. Applied Science Publishers, Essex. ISBN 0-85334-765-4, 375 pp.

Lennholm, H., Larsson, T. and Iversen, T. (1994) Determination of cellulose I_α and I_β in lignocellulosic materials. *Carb. Res.*, 261, 119-131.

Lindberg, O. (1992) *Medical CT-scanners for non-destructive wood density and moisture content measurements.* PhD thesis, Luleå University of Technology, Sweden.

Lockett, F.J. (1972) *Nonlinear Viscoelastic Solids.* Academic Press, London. ISBN 0-12454350-2.

Maciel, G.E., Chuang, I-S. and Gollob, L. (1984) Solid-state ^{13}C NMR study of resol-type phenol-formaldehyde resins. *Macromol.*, 17, 1081-1087.

MacKay, A.L. (2000) *pers comm.*

MacKay, A.L., Wallace, J.C., Sasaki, K. and Taylor, I.E.P. (1988) Investigation of the physical structure of the primary plant cell wall by proton magnetic resonance. *Biochem.*, 27, 1467-1473.

Macosko, C.W. (1994) *Rheology: Principles, Measurements and Applications.* VCH, Weinheim, ISBN 1-56081-579-5, 550 pp.

Man, P.P. (1995) Quadrupolar interactions. In: D.M. Grant and R.K. Harris (Eds), *Encyclopedia of Nuclear Magnetic Resonance,* J. Wiley and Sons, Chichester. 3838-3847. ISBN 0-471-93871-8.

Mansfield, P. and Grannell, P.K. (1973) NMR diffraction in solids. *J. Phys. C*, 6, L422-L426.

McConchie, D. and McConchie, M. (1999) Rapid disk drying assessment of internal check formation. Unpublished FRI Report.

MacMillan, M.B.; Schneider, M.H.; Sharp, A.R.; Balcom, B.J. (2002) Magnetic resonance imaging of water concentration in low moisture content wood. *Wood Fib. Sci.*, 34, 276-286.

Meder, R. and Archer, K.J. (1991) Degradation of TBTO preservative in *Pinus radiata. Holzforsch.*, 45, 103-108.

Meder, R., Gallagher, S.S., Kimberley, M.O., Uprichard, J.M. and Mackie, K.L. (1994) Prediction of wood chip and pulp and paper properties via multivariate analysis of spectral data. *Proceedings 48th Appita Annual General Conference,* Melbourne, Australia, 479-484.

Meder, R., Gallagher, S.S., Mackie, K.L., Böhler, H-P. and Meglen, R.R. (1999) Rapid determination of the chemical composition of *Pinus radiata* by PLS modelling of transmission and diffuse reflectance FTIR spectra. *Holzforsch.*, 53, 261-266.

Meder, R., Franich, R.A. and Callaghan, P.T. (1999) ^{11}B magnetic resonance imaging and MAS spectroscopy of trimethylborate-treated radiata pine wood. *Solid State Nucl. Magn. Reson.*, 15, 69-72.

Meder, R., Thumm, A. and Bier, H. (2002) Evaluation and prediction of veneer stiffness by NIR spectroscopy of mini-LVL test pieces. *Holz Roh Werkst.*, 60(3), 159-164.

Meglen, R.R. (1991) Examining large databases: A chemometric approach using principal component analysis. *J. Chemom.*, 5, 163-179.

Meglen, R.R. (1992) *Chemometrics. Lecture Notes.* University of Colorado at Denver.

Mehring, M. (1982) *Principles of High Resolution NMR in Solids, 2nd ed.* Springer-Verlag, Berlin. ISBN 3-540-11852-7, 342 pp.

Meiboom, S. and Gill, D. (1958) Modified spin-echo method for measuring nuclear relaxation times. *Rev. Sci. Instrum.*, 29, 688-691.

Menon, R.S., MacKay, A.L., Hailey, J.R.T., Bloom, M., Burgess, A.E. and Swanson, J.S. (1987) An NMR determination of the physiological water distribution in wood during drying. *J. Appl. Polym. Sci.*, 33, 1141-1155.

Menon, R.S., MacKay, A.L., Flibotte, S. and Hailey, J.R.T. (1989) Quantitative separation of NMR images of water in wood on the basis of T_2. *J. Magn. Reson.*, 82, 205-210.

Merboldt, K.D., Hänicke, W. and Frahm, J. (1987) NMR imaging of restricted diffusion. *Ber. Bunsen-Ges. Phys. Chem.*, 91, 1124-1126.

Michell, A.J. (1994) Vibrational spectroscopy - a rapid means of estimating plantation pulpwood quality? *Appita J.*, 47, 29-37.

Michell, A.J. (1995) Pulpwood quality estimation by near-infrared spectroscopic measurements on eucalypt woods. *Appita J.*, 48, 425-428.

Morris, P.G. (1986) *Nuclear Magnetic Resonance Imaging in Medicine and Biology.* Oxford University Press, Oxford, ISBN 0-19-855155-X, 388 pp.

Nanassy, A.J. (1973) Use of wide line NMR for measurement of moisture content in wood. *Wood Sci.*, 5, 187-193.

Nanassy, A.J. (1974) Water sorption in green and remoistened wood studied by the broad-line component of the wide-line NMR spectra. *Wood Sci.*, 7, 61-68.

Nanassy, A.J. (1976) True dry-mass and moisture content of wood by NMR. *Wood Sci.*, 9, 104-109.

Nanassy, A.J. (1978) Temperature dependence of NMR measurement of moisture content in wood. *Wood Sci.*, 11, 86-90.

Neilsen, A.T., Moore, D.W., Ogan, M.D. and Atkins, R.L. (1979) Structure and chemistry of the aldehyde ammonias. 3. Formaldehyde-ammonia reaction. 1,3,5-hexahydrotriazine. *J. Org. Chem.*, 44, 1678-1684.

Newman, R.H. (1991) Proton spin diffusion monitored by ^{13}C NMR. *Chem. Phys. Lett.*, 180, 301-304.

Newman, R.H. (1992) Nuclear magnetic resonance study of spatial relationships between chemical components in wood cell walls. *Holzforsch.*, 46, 205-210.

Newman, R.H. (1998) Evidence for assignment of ^{13}C NMR signals to cellulose crystallite surfaces in wood, pulp and isolated celluloses. *Holzforsch.*, 52, 157-159.

Newman, R.H. (1999) Estimation of the relative proportions of cellulose I_α and I_β in wood by carbon-13 NMR spectroscopy. *Holzforsch.*, 53, 335-340.

Newman, R.H. and Hemmingson, J.A. (1990) Determination of the degree of cellulose crystallinity in wood by carbon-13 nuclear magnetic resonance spectroscopy. *Holzforsch.*, 44, 351-355.

Newman, R.H. and Hemmingson, J.A. (1995) Carbon-13 NMR distinction between categories of molecular order and disorder in cellulose. *Cellulose*, 2, 95-110.

New Zealand Forest Owners Association - NZFOA (1999) *NZ Forestry Facts & Figures '99.* NZFOA/Ministry of Agriculture and Forestry, 22 pp.

Olson, J.R. (1986) Measurement of growth ring orientation in lumber. *Forest Prod. J.*, 36, 23-24.

Olson, J.R., Chang, S.J. and Wang, P.C. (1990) Nuclear magnetic resonance imaging: a noninvasive analysis of moisture distributions in white oak lumber. *Can. J. Forest Res.*, 20, 586-591.

Orendt, A.M. (1995) Chemical shift tensor measurement in solids. In: D.M. Grant and R.K. Harris (Eds), *Encyclopedia of Nuclear Magnetic Resonance*. J. Wiley and Sons, Chichester. 1282-1297. ISBN 0-471-93871-8.

Pang, S. (1996a) Moisture content gradient in a softwood board during drying: simulation from a 2-D model and measurement. *Wood Sci. Technol.*, 30, 165-178.

Pang, S. (1996b) Relationship between a diffusion model and a transport model for softwood drying. *Wood Fiber Sci.*, 29, 58-67.

Pang, S. and Wiberg, P. (1998) Model predicted and CT scanned moisture distribution in a *Pinus radiata* board during drying. *Holz Roh Werkst.*, 56, 9-14.

Parker, JR., Taylor, J.M.B., Plackett, D.V. and Lomax, T.D. (1997) Method for joining wood. US Patent 5,674,338, NZ Patent 226,022

Peck, T.L., Magin, R.L. and Lauterbur, P.C. (1995) Design and analysis of microcoils for NMR microscopy. *J. Magn. Reson.*, 108, 114-124.

Peurière, C. (2000) *Matlab Analysis of Stress, Strain and Time Relationships in Bi-axial Extension.* Massey University/INSA Honours Report.

Peuke, A.D., Rokitta, M., Zimmermann, U., Schreiber, L. and Haase, A. (2001) Simultaneous measurement of water flow velocity and solute transport in xylem and phloem of adult plants of *Ricinus communis* over a daily time course by nuclear magnetic resonance spectrometry. *Plant, Cell Environ.*, 24, 491-503.

Pham, Q.-T., Petiaud, R. and Waton, H. (1983) *Proton and Carbon NMR Spectra of Polymers*. John Wiley & Sons, Chicester. ISBN 0-471-26263-3. pp. 410-411.

Pizzi, A. and Teleky, P. (1996) Hardening mechanisms by hexamethylenetetramine of fast-reacting phenolic wood adhesives – A CP-MAS ^{13}C NMR study. *Holzforsch.*, 50, 277-281.

Pope, J.M., Jonas, J. and Walker, R.R. (1993) Applications of NMR micro-imaging to the study of water, lipid and carbohydrate distribution in grape berries. *Protoplasma*, 173, 177-186.

Purcell, E.M., Torrey, H.C. and Pound, R.V. (1946) Resonance absorption by nuclear magnetic moments in a solid. *Phys. Rev.*, 69, 37-38.

Quick, J.J., Hailey, J.R.T. and MacKay, A.L. (1990) Radial moisture profiles of cedar sapwood during drying: a proton magnetic resonance study. *Wood Fiber Sci.*, 22, 404-412.

Richards, R. and Packer, K.J. (eds) (1981) *Nuclear Magnetic Resonance Spectroscopy in Solids. A Royal Society Discussion.* University Press, Cambridge. ISBN 0-85403-160-X, 686 pp.

Riggin, M.T., Sharp, A.R. and Kaiser, R. (1979) Transverse relaxation of water in wood. *J. Appl. Polym. Sci.*, 23, 3147-3154.

Roe, D.C. (1985) Sapphire NMR tube for high-resolution studies at elevated pressure. *J. Magn. Reson.*, 63, 388-391.

Rofe, C.J., Lambert, R.K. and Callaghan, P.T. (1994) Nuclear magnetic resonance imaging of flow for a shear-thinning polymer in cylindrical Couette geometry. *J. Rheol.*, 38, 875-887.

Rokitta, M., Zimmermann, U. and Haase, A. (1999a) Fast NMR flow measurements in plants using FLASH imaging. *J. Magn. Reson.*, 137, 29-32.

Rokitta, M., Peuke, A.D., Zimmermann, U. and Haase, A. (1999b) Dynamic studies of phloem and xylem flow in fully differentiated plants by fast nuclear-magnetic-resonance microimaging. *Protoplasma*, 209, 126-131.

Rosenkilde, A. and Jesper, A. (1997) Measurement and evaluation of moisture transport coefficients during drying of wood. *Holzforsch.*, 51, 372-380.

Ruan, R.R. and Chen, P.L. (1998) *Water in Foods and Biological Materials: A Nuclear Magnetic Resonance Approach.* Technomic, Basel. ISBN 1-56676-589-7, 298 pp.

Samuelsson, A. and Arfvidsson, J. (1994) Measurement and calculation of moisture contents during drying. Proceedings of the 4th IUFRO International Wood Drying Conference, Rotorua, New Zealand, 79-86.

Schaafsma, T.J., Van As, H., Palstra, W.D., Snaar, J.E.M. and de Jager, P.A. (1992) Quantitative measurement and imaging of transport processes in plants and porous media by ^{1}H NMR. *Magn. Reson. Imag.*, 10, 827-836.

Scheenen, T.W.J., van Dusschoten, D., de Jager, P.A. and Van As, H. (2000) Quantification of water transport in plants with NMR imaging. *J. Exp. Bot.*, 51, 1751-1759.

Shaka, A.J., Keeler, J. and Freeman, R. (1983) Evaluation of a new broadband decoupling sequence: WALTZ-16. *J. Magn. Reson.*, 53, 313-340.

Shaka, A.J., Barker, P.B. and Freeman, R. (1985) Computer-optimized decoupling scheme for wideband applications and low-level operation. *J. Magn. Reson.*, 64, 547-552.

Sharp, A.R., Riggin, M.T., Kaiser, R. and Schneider, M.H. (1978) Determination of moisture content of wood by pulsed nuclear magnetic resonance. *Wood Fiber Sci.*, 10, 74-81.

Singh, A.P., Dawson, B.S.W., Franich, R.A., Cowan, F. and Warnes, J. (1999) The relationship between pit membrane ultrastucture and chemical impregnability of wood. *Holzforsch.*, 53, 341-346.

Singh, A.P. (2001) *pers comm.*

Skaar, C. (1984) Wood Water Relationships. In: R. Rowell (Ed) *The Chemistry of Solid Wood. Am. Chem. Soc., Adv. Chem. Ser.,* American Chemical Society, Washington, DC. ISBN 0065-2393-207.

Smith, P.J. and Tupciauskas, A.P. (1978) Chemical shifts of ^{119}Sn nuclei in organotin compounds. *Ann. Rep. NMR Spectrosc.*, 8, 291-370.

Smoluchowski, M. (1917) Mathematical theory of the kinetics of the coagulation of colloidal solutions. *Z. Physik. Chem.*, 92, 129-168.

Spolek, G.A. and Plumb, O.A. (1981) Capillary pressure in softwoods. *Wood Sci. Technol.*, 15, 189-199.

Stamm, A.J. (1959) Bound-water diffusion into wood in the fiber direction. *Forest Prod. J.*, 9, 27-32.

Stamm, A.J. (1960) Bound-water diffusion into wood in across-the-fiber direction. *Forest Prod. J.*. 10, 524-528.

Stanish, M.A. (1986) The roles of bound water chemical potential and gas phase diffusion in moisture transport through wood. *Wood Sci. Technol.*, 20, 53-70.

Stejskal, E.O. and Tanner, J.E. (1965) Spin diffusion measurement: spin echoes in the presence of a time-dependent field gradient. *J. Chem. Phys.*, 42(1), 288-92.

Summers, M.F., Marzilli, L.G. and Bax, A. (1986) Complete proton and carbon-13 assignments of coenzyme B_{12} through the use of new two-dimensional NMR experiments. *J. Am. Chem. Soc.*, 108, 4285-94.

Sun, X., Zhu, J., Wu, H., Jiang, L., Wu, G., Wu, Y. and Lu, K. (1986) ^{11}B NMR and quantum chemistry studies of boratrane compounds. *Scientia Sinica, Series B,* 29(12), 1261-1266.

Sung, H.N. and Noggle, J.H. (1981) Carbon-13 NMR of poly(vinyl acetate) and ethylene-vinyl acetate copolymer. *J. Polym. Sci., Polym. Phys. Ed.,* 19, 1593-1602.

Tabachnik, B.G. and Fidel, L.S. (1989) *Using Multivariate Statistics. 2nd ed.* Harper Collins, ISBN 0-06-046571-9, 746 pp

Talagala, S.L. and Lowe, I.J. (1991) Introduction to magnetic resonance imaging. *Concept Magn. Reson.*, 3, 145-159.

Timell, T.E. (1986) *Compression Wood in Gymnosperms, Vol. 1: Bibliography, Historical Background, Determination, Structure, Chemistry, Topochemistry, Physical Properties, Origin, and Formation of Compression Wood.* Springer Verlag, Berlin. ISBN 3-540-15715-8, 706 pp.

Thomas, E.V. (1994) A primer on multivariate calibration. *Anal. Chem.*, 66, 795A–804A.

Thumm, A. and Meder, R. (2001) Stiffness prediction of radiata pine clearwood test pieces using NIR spectroscopy. *J. Near Infrared Spectrosc.*, 9, 117-122.

Thygesen, L.G. (1996) PLS calibration of pulse NMR free induction decay for determining moisture content and basic density of softwood above fiber saturation. *Holzforsch.*, 50, 434-436.

Treloar, L.R.G. (1971) Rubber elasticity. *Contemp. Phys.*, 12, 33-56.

Vega, A. (1995) Quadrupolar nuclei in solids. In: D.M. Grant and R.K. Harris (Eds). *Encyclopedia of Nuclear Magnetic Resonance,* J. Wiley and Sons, Chichester. 3888-3900. ISBN 0-471-93871-8.

Vinden, P. (1990) Gaseous or vapour phase treatment of wood with boron preservatives. NZ Patent 220,816.

Walker, J.C.F. (1993) The drying of timber. In: J.C.F Walker (Ed) *Primary Wood Processing. Principles and Practice.* Chapman & Hall, London. ISBN 0-412-54840-2.

Wallbäcks, L., Edlund, U. and Nordén, B. (1989) Multivariate data analysis of in situ pulp kinetics using ^{13}C CP/MAS NMR. *J. Wood Chem. Technol.*, 9, 235-249.

Wallbäcks, L. (1991) *Pulp Characterization Using Spectroscopy and Multivariate Analysis.* PhD thesis, University of Umeå, Sweden. ISBN 91-7174-5768-5.

Wallbäcks, L., Edlund, U., Nordén, B. and Iversen, T. (1991a) Multivariate characterisation of pulp. Part 1. Spectroscopic characterization of physical and chemical differences between pulps using ^{13}C CP/MAS NMR, FTIR NIR and multivariate data analysis. *Nordic Pulp Paper Res. J.*, 2, 74-80,94.

Wallbäcks, L., Edlund, U., Nordén, B., Iversen, T. and Mohlin, U-B. (1991b) Multivariate characterisation of pulp. Part 2. Interpretation and prediction of beating processes. *Nordic Pulp Paper Res. J.*, 3, 104-109.

Wallbäcks, L., Edlund, U., Nordén, B. and Berglund., I (1991c) Multivariate characterisation of pulp using solid state ^{13}C NMR, FTIR and NIR. *Tappi J.*, 74, 201-206.

Wallen, S., Schoenbachler, L.K., Dawson, E.D. and Blatchford, M. (2000) A polymer NMR cell for the study of high pressure and supercritical fluid solutions. *Anal. Chem.*, 72, 4230-4234

Wang, P.C. and Chang, S.J. (1986) Nuclear magnetic resonance imaging of wood. *Wood Fiber Sci.*, 18, 308-314.

Wang, Y., Simonsen, J., Neto, C.P., Rocha, J., Rials, T.G. and Hart, E. (1996) The reaction of boric acid with wood in a polystyrene matrix. *J. Appl. Polym. Sci.*, 62, 501-508.

Warson, H. (1990). Preparation of derivatives of acrylamide. *Paint and Resin*, June, 26-30.

Watson, P.A. and Franich R.A. (1996) Report on the synthesis of a protected resorcinol model compound. Unpublished FRI report.

Whittaker, A.K. (1997) NMR studies of crosslinked polymers. *Ann. Rep. NMR Spectrosc.*, 34, 105-182.

Wiberg, P. (1995) Moisture distribution changes during drying. *Holz Roh Werkst.*, 53, 402.

Winter, H.H. (1989) Gel Point. In: H.F. Mark, N. Bikales, C.G. Overberger, G. Menges (Eds), *Encyclopedia of Polymer Science and Engineering, Supplement Volume*. J. Wiley and Sons, Chichester. 343-351. ISBN 0-471-80948-9.

Witanowski, M and Januszewski, H. (1969) Nitrogen-14 nuclear magnetic resonance: amines and ammonium ions. *Can. J. Chem.*, 47, 1321-1325.

Witanowski, M. and Webb, G.A. (1972) Nitrogen NMR spectroscopy. *Ann. Rep. NMR Spectrosc.*, 5A, 395-464.

Wold, S., Martens, H. and Wold, H. (1983) A multivariate calibration problem in analytical chemistry solved by partial least-squares models in latent variables. *Anal. Chim. Acta*, 150, 61-70.

Wu, T.K. and Ovenall, D.W. (1974) Proton and carbon-13 nuclear magnetic resonance studies of poly(vinyl acetate). *Macromol.*, 7, 776-779.

Wrackmeyer, B. (1985) ^{119}Sn NMR Parameters. *Ann. Rep. NMR Spectrosc.*, 16, 73-186.

Wrackmeyer, B. (1999) Application of ^{119}Sn NMR Parameters. *Ann. Rep. NMR Spectrosc.*, 38, 203-265.

Xia, Y. and Callaghan, P.T. (1991) Study of shear thinning in high polymer solution using dynamic NMR microscopy. *Macromol.*, 24, 4777-4786.

Xia, Y., Sarafis, V., Campbel, E.O. and Callaghan, P.T. (1993) Non invasive imaging of water flow in plants by NMR microscopy. *Protoplasma*, 173, 170-176.

Xu, Y., Araujo, C.D., MacKay, A.L. and Whittall, K.P. (1996) Proton spin-lattice relaxation in wood – T_1 related to local specific gravity using a fast-exchange model. *J. Magn. Reson. B*, 110, 55-64.

Zhang, X., Looney, M.G., Solomon, D.H. and Whittaker, A.K. (1997) The chemistry of novolac resins: 3. ^{13}C and ^{15}N n.m.r studies of curing with hexamethylenetetramine. *Polym.*, 38, 5835-5848.

Ziessow, D. (1990) Understanding multiple-pulse experiments – An introduction to the product operator description I. Starting with the vector model. *Concepts Magn. Reson.*, 2, 81-100.